



**UNIVERSIDAD
DE GRANADA**

TESIS DOCTORAL

**PROGRAMA DE DOCTORADO EN FÍSICA Y CIENCIAS DEL
ESPACIO**

**Nanoestructuras híbridas y
anisotrópicas para aplicaciones
biomédicas**

Marina Lázaro Callejón

Directores

Guillermo Iglesias Salto

Silvia Ahualli Yapur

Departamento de Física Aplicada, Universidad de Granada

**GRUPO DE FÍSICA DE INTERFASES Y SISTEMAS COLOIDALES
DEPARTAMENTO DE FÍSICA APLICADA**

—
Granada, 2024

Editor: Universidad de Granada. Tesis Doctorales
Autor: Marina Lázaro Callejón
ISBN: 978-84-1195-677-2
URI: <https://hdl.handle.net/10481/102200>

La doctoranda / *The doctoral candidate* Marina Lázaro Callejón y los directores de la tesis / *and the tesis supervisors* Guillermo Ramón Iglesias Salto, Profesor Titular del Departamento de Física Aplicada de la Universidad de Granada y Silvia Ahualli Yapur, Catedrática del Departamento de Física Aplicada de la Universidad de Granada.

Garantizamos, al firmar esta tesis doctoral, que el trabajo ha sido realizado por la doctoranda bajo la dirección de los directores de la tesis y hasta donde nuestro conocimiento alcanza, en la realización del trabajo, se han respetado los derechos de otros autores a ser citados, cuando se han utilizado sus resultados o publicaciones.

Guarantee, by signing this doctoral thesis, that the work has been done by the doctoral candidate under the direction of the supervisors and, as far as our knowledge reaches, in the performance of the work, the rights of other authors to be cited (when their results or publications have been used) have been respected.

Granada, 26 de septiembre de 2024

Doctorando / *Doctoral candidate*

Fdo: Marina Lázaro Callejón

Los Directores de la Tesis / *Thesis supervisors*

Fdo: Guillermo Ramón Iglesias Salto

Fdo: Silvia Ahualli Yapur

A mis padres.

*Con el tiempo comprendí que la alegría
era un arma superior al odio, las sonrisas
más útiles, más feroces que los gestos de
rabia y desaliento.*

Almudena Grandes

Agradecimientos

En primer lugar, quisiera agradecer de corazón a Guillermo por confiar en mí desde el primer momento, ayudarme a ver las cosas desde otra perspectiva, y enseñarme a mantener la calma. A Silvia, por su infinita paciencia, sus valiosos consejos y por mostrarme la importancia de relativizar los problemas. Y, por supuesto, a Ángel, gracias por tu inagotable paciencia y por tener siempre las puertas de tu despacho abiertas, dispuesto a ayudar. A los tres, gracias por introducirme y guiarme en el mundo de la investigación. Siempre os estaré agradecida por hacer que lo complicado pareciera sencillo. Gracias por vuestra infinita dedicación, tiempo, esfuerzo y apoyo, y sobre todo, por acompañarme en cada paso.

En segundo lugar, me gustaría dar las gracias a todas las personas del Departamento de Física Aplicada, y en particular, del grupo de Física de Interfaces y Sistemas Coloidales, que me acogieron dentro de la gran familia que forman. A Fran, por ser el mejor compañero de despacho, por su optimismo constante y por transmitir siempre tranquilidad. A Sergio, por su infinita paciencia para escuchar y por su comprensión. Estoy convencida de que la tesis que estás preparando será excepcional. A Alfredo, por su alegría contagiosa en el laboratorio. A Ana Belén, por sus consejos, tanto científicos como personales. Por estar siempre dispuesta a echar una mano, y por enseñarme la química que sé. Y sobre todo a Ana, que empezó este camino conmigo y se ha convertido en amiga. Quisiera hacer una mención especial a Gracia. Aunque nos conocimos al inicio de esta tesis doctoral, fue al final cuando nos reencontramos. Gracias por tu constante apoyo y compartir tus experiencias. Haber tenido la oportunidad de conocerte mejor en estos últimos meses ha sido una de las mayores alegrías de este doctorado. A Alberto, Juan Antonio y todos los demás compañeros que han pasado por este grupo de investigación, que han hecho más entretenidos los días de trabajo.

También quisiera agradecer a Jose y Migue, por tantos momentos divertidos, descansos de café y cervezas, y a Javi y Óscar. Sin vosotros esta tesis no hubiese sido la misma.

Dado el carácter multidisciplinar de esta tesis, quiero agradecer también a todo el equipo de bio: MariPaz, Conchi, Alberto, Tamara, y a todos aquellos que han formado

parte de este grupo. Quisiera expresar un agradecimiento especial a Mónica, a quien, desde aquel viaje a Zaragoza, ya considero amiga.

A mis compañeros de NeptunLab, en especial a Santiago, quien me acogió e hizo que me sintiera como en casa. Junto a los amigos que allí encontré, fuisteis la mejor parte de mi estancia.

A mis amigos, del instituto, de la carrera y del pueblo, donde escribí parte de esta tesis, por haberme acompañado a lo largo de este camino. A Carmen y Mar, con quienes, a pesar de la distancia, siempre he encontrado la manera de sentirme cerca.

A mi familia, muchísimas gracias. A mi tita Dioni, siempre dispuesta a leer todo lo que le mando, y a mi abuelo Pepe, que sé que estaría muy orgulloso. A mi hermano Javier. Aunque somos muy distintos, siempre te esfuerzas por comprenderme. Gracias por tu interés, tu paciencia y por ser el autor de la portada de esta tesis, que sé que leerás.

A mis padres; esta tesis es tan mía como vuestra. Nada de esto sería posible sin vosotros. Siempre habéis dado todo para que mi hermano y yo nos formemos, aprendamos, viajemos y disfrutemos. Gracias por brindarme vuestro apoyo incondicional en cada paso y por valorar siempre nuestros logros. Sois un ejemplo para mí.

A Juan, por siempre darme impulso y acompañarme en este viaje. Gracias por compartir tu vida conmigo.

Financiación

La investigación que ha conducido a la realización de esta tesis doctoral se ha llevado a cabo gracias al proyecto P20_00346 financiado por la Junta de Andalucía y al Fondo Europeo de Desarrollo Regional (FEDER), y al proyecto TED2021-131855B-I00, financiado por MCIN/AEI 10.13039/501100011033 y por la Unión Europea *Next Generation EU/PRTR*. Gracias a ellos ha sido posible la asistencia y presentación de comunicaciones en 14 conferencias, así como la participación en 9 artículos científicos.

La estancia de investigación realizada en el *Institut für Mikrosystemtechnik de la Universidad de Friburgo, Alemania*, ha sido financiada por el Programa de Ayudas para Realizar Estancias Breves en Centros de Investigación Nacionales y Extranjeros (P10) del Plan Propio de la Universidad de Granada



**UNIVERSIDAD
DE GRANADA**

Resumen

El cáncer es una de las principales causas de mortalidad a nivel mundial y representa un gran desafío para mejorar la esperanza de vida. En este contexto, la nanotecnología ofrece nuevas y prometedoras soluciones, como las relacionadas con las nanopartículas magnéticas (NPMs), que se presentan como herramientas de gran interés en el campo de la biomedicina. Estas partículas destacan por su capacidad de respuesta magnética, lo que les permite ser dirigidas hacia áreas específicas del cuerpo, desempeñando funciones terapéuticas diversas.

El núcleo de esta investigación se centra en el estudio, caracterización y aplicación de terapias térmicas utilizando NPMs, así como su rol como agentes transportadores de fármacos, permitiendo tratamientos más eficaces con dosis menores. Entre las terapias térmicas destaca la hipertermia magnética, que consiste en la generación localizada de calor mediante la aplicación de campos magnéticos alternos. Se ha demostrado que, al aumentar la temperatura de las células tumorales en el rango de 41-46°C, es posible inducir apoptosis celular. Otra opción es la fototermia, que utiliza radiación láser a una longitud de onda específica para generar calor. Además, una alternativa menos explorada es el uso de campos magnéticos rotantes de baja frecuencia, los cuales no generan calor, pero pueden romper membranas celulares de forma magneto-mecánica o favorecer la difusión de fármacos.

Para estas aplicaciones se han sintetizado nanoestructuras híbridas que responden a múltiples estímulos, tanto físicos como biológicos. Desde el punto de vista físico, se busca optimizar su rendimiento y propiedades. En el aspecto biológico, estas nanoestructuras están diseñadas para minimizar efectos secundarios y maximizar la efectividad del tratamiento.

En este trabajo se han diseñado cuatro tipos de nanoestructuras: (i) nanoesferas de magnetita recubiertas de oro, (ii) nanovarillas magnéticas de 40 nm de longitud, (iii) nanovarillas magnéticas de 550 nm, con y sin semillas de oro en la superficie, y (iv) partículas de carbón activo con magnetita. Se realizó una caracterización completa de cada estructura y se recubrieron con polímeros catiónicos (polietilénimina) y aniónicos (poliestireno sulfonato), mostrando ser biocompatibles hasta concentraciones de 300 µg/mL en diversas líneas celulares. Además, se

evaluó su eficiencia como agentes de calentamiento frente a diferentes estímulos. Específicamente, en las nanovarillas de menor tamaño, se observó que la aplicación tanto de hipertermia magnética como de fototermia redujo la viabilidad celular en más del 60% en ambos casos.

En cuanto al comportamiento fototérmico de las partículas recubiertas de oro, se observó un menor calentamiento en el rango del infrarrojo, pero con longitudes de onda en el espectro azul-verde, la temperatura aumentó hasta 10 veces más. Aunque estas longitudes de onda son menos penetrantes, podrían ser útiles para tratar tumores superficiales o accesibles mediante fibra óptica.

Uno de los resultados más relevantes obtenidos fue la terapia dual, que combina la aplicación de un campo magnético alterno con la irradiación láser simultánea. Este enfoque permite reducir tanto la intensidad del campo magnético ($\sim 20\%$, de 21 kA/m a 17 kA/m) como la densidad de potencia del láser (en un 70%), ofreciendo un tratamiento potencialmente menos dañino, pero igualmente eficaz.

En cuanto a las estructuras de carbón activo con magnetita, se alcanzó una adsorción del 80% del fármaco antitumoral en 2 horas, mejorando su liberación con técnicas fototérmicas y campos magnéticos rotantes de baja frecuencia.

Por último, gracias a los experimentos *in vitro*, se demostró que la localización intracelular de las NPMs es crucial para mejorar la eficacia del tratamiento fototérmico, ya que es necesario que las nanopartículas se encuentren dentro de las células tumorales para maximizar la muerte celular.

Abstract

Cancer is one of the main causes of mortality worldwide and represents a great challenge to improve life expectancy. In this context, nanotechnology offers new and promising solutions, such as those related to magnetic nanoparticles (MNPs), which are tools of great interest in the field of biomedicine. These particles stand out for their magnetic responsiveness, which allows them to be directed to specific areas of the body, performing diverse therapeutic functions.

The core of this research focuses on the study, characterization and application of thermal therapies using MPNs, as well as their role as drug transporting agents, allowing more effective treatments with lower doses. Among the thermal therapies, magnetic hyperthermia stands out, which consists of the localized generation of heat through the application of alternating magnetic fields. It has been shown that, by increasing the temperature of tumor cells in the range of 41-46°C, it is possible to induce cell apoptosis. Another option is photothermia, which uses laser radiation at a specific wavelength to generate heat. In addition, a less explored alternative is the use of low-frequency rotating magnetic fields, which do not generate heat, but can magneto-mechanically rupture cell membranes or enhance drug diffusion.

For these applications hybrid nanostructures capable of responding to multiple stimuli, both physical and biological, have been synthesized. From the physical point of view, the objective is to optimize their performance and properties. From the biological perspective, these nanostructures are designed to minimize side effects and maximize treatment efficacy.

In this work four types of nanostructures have been designed: (i) gold-coated magnetite nanospheres, (ii) magnetic nanorods of 40 nm in length, (iii) magnetic nanorods of 550 nm, with and without gold seeds on the surface, and (iv) activated carbon particles with magnetite. A complete characterization of each structure was carried out and they were coated with cationic (polyethylenimine) and anionic (poly(styrenesulfonate)) polymers, showing to be biocompatible up to concentrations of 300 µg/mL in diverse cell lines. In addition, their efficiency as heating agents against different stimuli was evaluated. Specifically, in the smaller size nanorods, it was observed that the application of both magnetic hyperthermia and photothermia

reduced cell viability by more than 60% in both cases.

Regarding the photothermal behavior of the gold-coated particles, lower heating was observed in the infrared range, but with wavelengths in the blue-green spectrum, the temperature increased up to 10 times higher. Although these wavelengths are less penetrating, they could be useful for treating superficial or fiber-optically accessible tumors.

One of the most relevant results obtained was dual therapy, which combines the application of an alternating magnetic field with simultaneous laser irradiation. This approach makes it possible to reduce both the intensity of the magnetic field ($\sim 20\%$, from 21 kA/m to 17 kA/m) and the laser power density (by 70%), offering a potentially less damaging but equally effective treatment.

Concerning the activated carbon structures with magnetite, an adsorption of 80% of the antitumor drug was achieved in 2 hours, improving its release with photothermal techniques and low-frequency rotating magnetic fields.

Finally, through *in vitro* experiments, it was shown that the intracellular localization of NPMs is crucial to improve the efficacy of photothermal treatment, since it is necessary for the nanoparticles to be inside the tumor cells to maximize cell death.

Contents

Contents	15
I Introduction	19
1. Background	21
1.1. Biomedical applications of nanotechnology	21
1.2. Magnetic nanoparticles	22
1.3. Magnetic nanoparticles from a biomedical perspective	24
1.4. Targeted therapies	28
Bibliography	33
2. Justification	41
2.1. Motivation	41
2.2. Outline of the thesis	43
Bibliography	45
II Physical principles and experimental methods	49
3. Fundamentals of magnetic hyperthermia, photothermia and low-frequency magnetic rotating fields	51
3.1. Magnetic hyperthermia	51
3.2. Photothermia	54

3.3. Thermal evaluation	56
3.4. Low-frequency magnetic rotating fields	57
3.5. Experimental methods	58
Bibliography	63
III Results and discussion	65
4. Magneto-photothermal synergy applied to gold-coated magnetic nanoparticles	67
4.1. Introduction	69
4.2. Materials and methods	71
4.3. Results and discussion	75
4.4. Conclusions	84
Bibliography	85
5. The role of biocompatible coatings of magnetic nanorods on their thermal response in hyperthermia. Consequences on tumor cell survival.	95
5.1. Introduction	97
5.2. Materials and methods	100
5.3. Results and discussion	105
5.4. Conclusions	115
Appendix. Supplementary Information	116
Bibliography	119
6. Combined magnetic hyperthermia and photothermia with polyelectrolyte/gold-coated magnetic nanorods	127
6.1. Introduction	129
6.2. Materials and methods	133
6.3. Results and discussion	137
6.4. Conclusions	150

Appendix. Supplementary Information	151
Bibliography	157
7. Magnetic activated carbon as stimuli-responsive vehicles for methotrexate	167
7.1. Introduction	169
7.2. Materials and methods	171
7.3. Results and discussion	176
7.4. Conclusions	184
Appendix. Supplementary Information	186
Bibliography	191
8. The importance of cell uptake in photothermal treatments mediated by biomimetic magnetic nanoparticles	199
8.1. Introduction	201
8.2. Materials and methods	203
8.3. Results and discussion	208
8.4. Conclusions	215
Appendix. Supplementary Information	216
Bibliography	217
IV Summary and conclusions	223
9. Conclusions	225
10. Resumen	229
10.1. Introducción	229
10.2. Resultados	233
10.3. Conclusiones	246
Bibliografía	249

Part I

Introduction

Chapter 1

Background

1.1. Biomedical applications of nanotechnology

Cancer is one of the leading causes of death and a major obstacle to improving the quality of life and life expectancy worldwide. It is estimated that in 2022 there were 19.3 million new cases of cancer worldwide and almost 10 million deaths from cancer. In the case of the European Union, cancer is the most lethal disease in people under the age of 65, surpassing any other illness in the Member States [1.1]. Moreover, estimates continue to rise. According to the European Network of Cancer Registries (ENCR, <http://https://www.encre.eu/>), more than 1.5 million cancer deaths are expected by 2040, 26.9% higher than in 2022. Focusing on Spain, cancer is already the main cause of mortality. In 2023, tumors were responsible for 26.6% of all registered losses, surpassing deaths due to diseases of the circulatory system for the first time (according to the National Institute of Statistics <https://www.ine.es/>).

To deal with this major problem some of the conventional treatments of cancer include surgery, radiotherapy and chemotherapy. However, despite the advances made, these approaches have major limitations due to their toxicity and aggressiveness. In this context, nanotechnology offers promising new alternatives. Its application in biomedicine includes both early detection and treatment of diseases [1.2].

The history of nanotechnology has its beginnings in 1959, when the renowned physicist Richard Feynman gave a lecture exploring the idea of manipulating and controlling materials at the atomic level [1.3]. However, its real growth and development began in the 1980s. Despite this, in 1954, physician Paul Ehrlich introduced the concept of targeted drug delivery using nanoparticles, calling them "Zauberkugeln" or "magic bullets." This concept gained popularity during the 1950s and 1960s, focusing on the controlled release of drugs [1.4]. In 1973, Professor Peter

Paul Speiser developed the first nanoparticles (NPs) for drug and vaccine delivery [1.2, 1.4]. Subsequently, albumin and magnetic NPs were developed by the Johns Hopkins Medical Institutions and Kramer, respectively, for medical applications, such as cancer detection and treatment. NPs demonstrated their ability to deliver anti-infective drugs, DNA fragments and genes, and to cross the blood-brain barrier with the help of antibodies [1.2].

Nanotechnology has transformed medical diagnostics, immunization, treatment and medical devices, using a variety of techniques to link biological agents with NPs [1.2]. This emerging field encompasses areas such as diagnostics, drug delivery, tissue engineering, gene and cell therapies, as well as applications in antivirals and vaccines.

1.2. Magnetic nanoparticles

Magnetic nanoparticles (MNPs) have been used broadly in various fields, such as contaminant removal in environmental applications [1.5, 1.6], and also in industries such as petroleum and textiles [1.7, 1.8]. However, their properties are particularly outstanding in biomedicine, especially in cancer research and treatment [1.9–1.11]. Moreover, their responsiveness to magnetic fields that guides them to specific areas of the body and keeps them there while they perform their therapeutic function, is another property that underlines their importance in this field.

Various methods exist for producing MNPs, including physical approaches like pyrolysis and laser ablation, chemical techniques such as co-precipitation, thermal decomposition, and hydrothermal or solvothermal synthesis [1.12], as well as biomimetic strategies that use microorganisms and bacteria for synthesis [1.13].

These nanosystems, in addition to being functional, must be biocompatible [1.14]. Materials such as magnetite (Fe_3O_4) and maghemite ($\gamma\text{-Fe}_3\text{O}_4$) are the most widely used due to their excellent magnetic properties and low toxicity [1.15, 1.16]. In general, both tend to coexist within the same nanoparticle, due to the ease with which magnetite oxidizes to maghemite, especially if the synthesis is carried out under ambient conditions.

Focusing on magnetite, the most commonly used of these two iron oxide phases, let us emphasize that it is a ferrimagnetic material, which is characterized by an inverse cubic spinel structure and a cell parameter of 8.39 Å. It is based on 32 oxygen ions located in the interstices. Moreover, two types of ions can be also found, Fe^{2+} occupying half of the octahedral sites (4), and Fe^{3+} occupying both octahedral (4) and tetrahedral (16) sites in a unit cell (being the stoichiometry $\text{Fe}^{3+}/\text{Fe}^{2+} = 0.5$, Figure 1.1) [1.17].

The Curie temperature of magnetite is observed at 850 K, which marks the critical point where the magnetization changes from ferrimagnetic to paramagnetic.

Below this temperature, the magnetic moment originates mainly in Fe^{2+} ($\approx 4\mu_B$), since the magnetic moments of Fe^{3+} cancel each other out through antiferromagnetic exchange [1.17]. As the temperature increases toward the Curie temperature, thermal fluctuations destroy the ferromagnetic alignment of the magnetic moments at the tetrahedral sites, thus decreasing the ferrimagnetic strength. Upon reaching the Curie temperature, the net magnetization becomes zero and paramagnetic behavior is observed. Therefore, at room temperature, magnetite exhibits ferrimagnetic behavior. The coercivity, which represents the magnetic field strength required to revert the magnetization to zero after magnetic saturation, varies between 2.4 (typical of recording media in disk drives) and 20.0 kAm^{-1} (characteristic of real permanent magnets) [1.17].

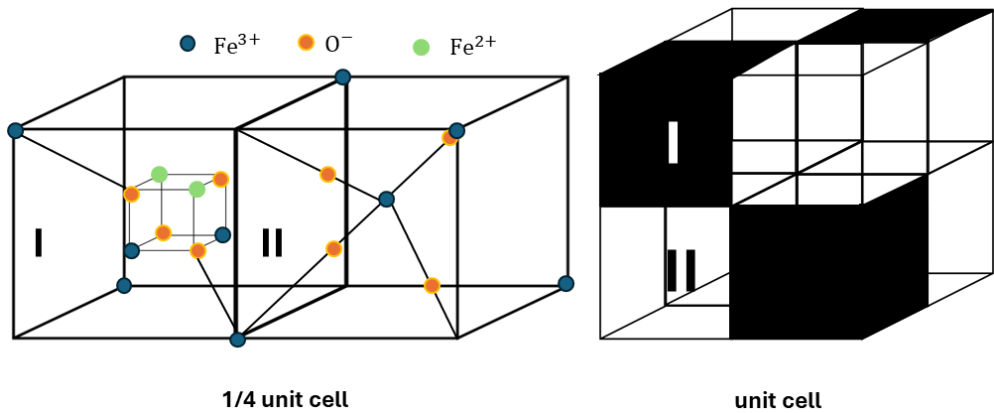


Figure 1.1: Representation of the structure of magnetite. Blue spheres represent Fe^{+3} atoms, orange spheres oxygen atoms, green spheres Fe^{+2} .

For particle diameters above a certain value (128 nm in magnetite [1.18]), we must take into account the existence of magnetic domains, due to different energy contributions. These contributions include the energy of the magnetic field, spin orientation anisotropy, and exchange energy. Although dipole interactions between spins are initially negligible, their importance increases with multiple spin alignment, being long-range but low energy. Domains are formed to reduce the exchange energy, although abrupt changes in spin orientation between neighboring domains carry an energetic cost, mitigated in part by the thickness of the domain walls (Bloch/Néel walls).

Moreover, the orientation of the spins with respect to the crystallographic axes (easy axes) also influences the energy [1.17]. It is important to note that the direction of easy magnetization of magnetite is $[111]$, when a magnetic field is applied. Small crystals, comparable in size to domain walls, tend to be single-domain and behave like permanent magnets with magnetization in a privileged direction.

Magnetite (in bulk) is characterized by having a high saturation magnetization (around 92-100 emu/g), while magnetite nanoparticles have slightly lower magnetization. An example of this are the results obtained in the synthesis of monodisperse magnetite nanoparticles by Kemp *et al.* [1.19], with saturation magnetization of up to 80 emu/g (92% of bulk magnetite)*. In addition, it is important to mention that the relationship between magnetization and size has been extensively studied by several authors [1.16, 1.18, 1.20], observing that the saturation magnetization increases with size, regardless of the crystal structure and particle shape [1.18].

1.3. Magnetic nanoparticles from a biomedical perspective

Some of the previously described specific magnetic properties of MNPs have important biological implications. In the following, they will be described by considering the fate of particles entering the human body.

The first step is their administration. This can be done intravenously, subcutaneously or locally injected (very useful for non-metastatic lymphatic tumors, since the particles can infiltrate and be adsorbed by the lymphatic capillaries), or even orally. The problem in this last case is that for certain applications they may be degraded by gastric acids or the adsorption may be low [1.21].

In second place, the nanoparticles must reach the target organ or tissue, and in order to do so escape from the bloodstream. To counteract blood flow, from a physical perspective, it is essential to use an inhomogeneous magnetic field with a high field gradient, which is detailed further below. But also, from a physiological point of view, there are two key factors that facilitate these interactions: the nature of the tumor and also the particle size. In this context, it is important to take into account the Enhanced Permeability and Retention Effect (EPR). This effect is due to the fact that rapid tumor growth increases the demand for nutrients and oxygen, which leads cancer cells to form new blood vessels. This process, called neo-angiogenesis in malignant tumors, is more rapid and abundant, and the accelerated formation of hypervasculation results in defective vascular architecture, inefficient lymphatic drainage, and the production of permeable vessels [1.22]. Nanoparticles that are considered optimal are in the range up to 100-200 nm, to achieve the EPR effect in solid tumors [1.23], although they can be around the micron [1.24].

*Recall that $1 \text{ emu/g} = 1 \text{ A} \cdot \text{m}^2/\text{kg}$

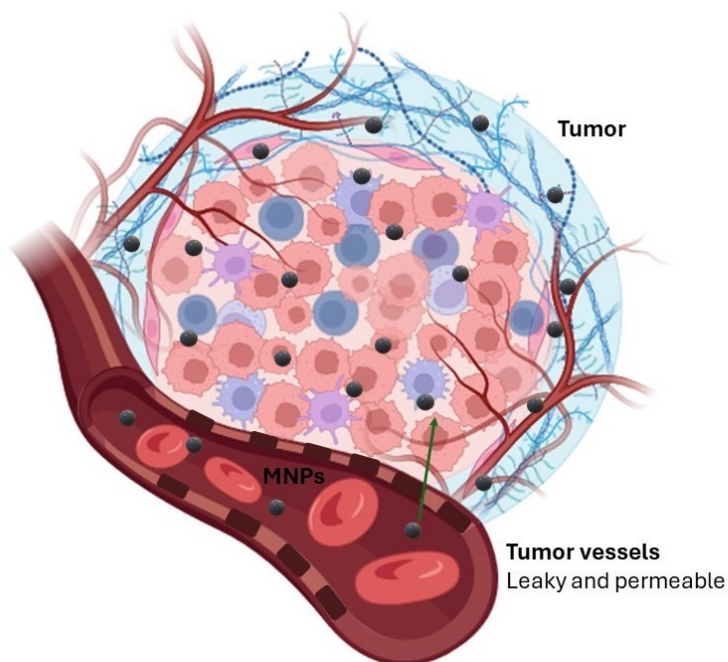


Figure 1.2: Schematic representation of Enhanced Permeability and Retention effect. Figure created with BioRender.com.

Once they escape from the bloodstream, the nanoparticles should interact with the cells, and if possible, be internalized. The uptake of nanoparticles by cells occurs in two stages: binding to the cell membrane, influenced by the surface charge of the nanoparticles, and internalization through various mechanisms such as pinocytosis and endocytosis, depending on both the surface charge and the cell type [1.24]. Thus, with internalization in the target cell, the effectiveness of the treatments is increased, as will be demonstrated in this doctoral thesis.

Finally, it is also important to know what happens to the particles that remain in the bloodstream, or what happens to those that have already achieved their function. After an NP enters the bloodstream, the reticuloendothelial system is activated through opsonization processes. MNPs are taken up by cells such as Kupffer macrophages in the bone marrow, liver and spleen, where they can be degraded [1.21]. Depending on their size and biodegradation capacity, some nanoparticles are excreted in the bile and eliminated in the feces, while others are filtered by the kidneys and eliminated in the urine. Smaller particles are rapidly eliminated by the kidneys, while larger particles are retained in the liver, spleen and bone marrow. Phagocytic cells such as macrophages and dendritic cells eliminate large particles, whereas small particles can be taken up by cells that perform endocytosis, such as lymphocytes. Lastly, the breakdown products of biodegradable magnetic nanoparticles can be taken up by any cell by pinocytosis [1.21] (Figure 1.3).

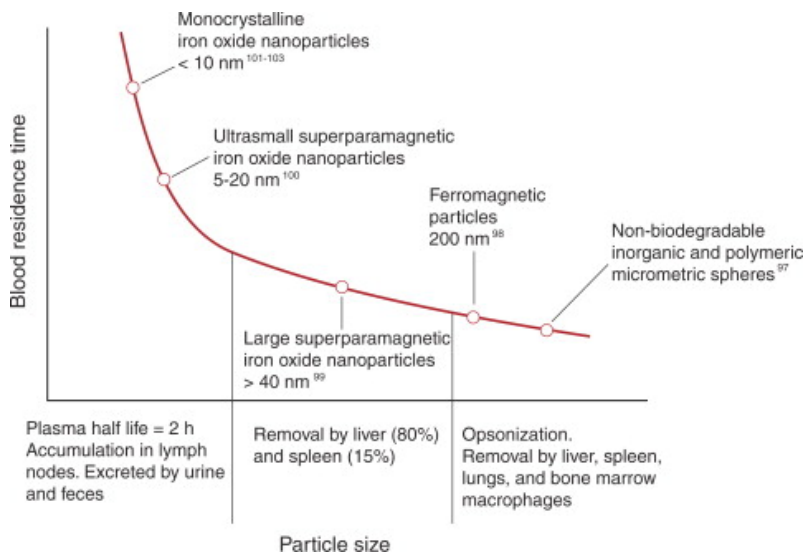


Figure 1.3: Schematic of the evolution of blood residence time versus particle size. Figure extracted from [1.21].

An additional aspect linked to size is the superparamagnetic property of the nanoparticles. Recall that superparamagnetism is the magnetic behavior of single-domain particles (depending on the frequency of the magnetic field if it is alternating and also on the temperature) characterized by negligible remanence in their magnetization cycle. The ascending and descending branches on the M - M are practically coincident (no hysteresis) and the particle is magnetized only in the presence of a magnetic field. This feature ensures both safety and effectiveness, as it prevents magnetic interactions between the nanoparticles, as well as maintaining colloidal stability and prevents their aggregation. This reduces the possibility of aggregate formation after intravenous administration, which in turn minimizes the risk of thrombus formation in the capillaries.

Another important factor to highlight is their surface charge [1.25]. After intravenous injection, MNPs are in an environment with a slightly basic physiological pH (\sim pH 7.4) and high ionic strength. Under these conditions, the surface charge is low, and therefore aggregation is difficult to avoid. To maintain particle stability both *in vitro* and *in vivo*, it is crucial to counteract these effects by:

- Electrostatic repulsion between appropriately charged surfaces.
- A suitable envelope on the particle surface (steric barrier) [1.25].

In this context, the coating of the nanoparticle surface improves the colloidal and physical stability of the nanoparticles, their dispersion in water and allows their functionalization for subsequent conjugation with bioactive molecules or specific

ligands, thus obtaining multifunctional nanoparticles [1.25]. Among the different methods to obtain MNPs coatings, the following stand out:

- Creation of polymeric shells that prevent the growth of clusters after initial formation and keep particle separate against attractive forces. In this case, the composite particles can be made of previously formed monomers or polymers. These polymeric stabilizers, in addition to stabilizing the colloidal solution, can offer other advantages such as providing biocompatibility to the system [1.25]. Some of them are described in Table 1.1, which can be either synthetic, such as PEG (poly(ethyleneglycol), or natural, like chitosan [1.25].
- Another technique is the formation of lipid shells (such as liposomes/lipid NPs) around magnetic cores to modify particle properties [1.25].
- Deposition of metals, such as gold, or oxide surfaces [1.25].

Polymer	Advantages	References
Dextran	Improves blood circulation time.	[1.26, 1.27]
PVA	Prevents coagulation of particles, resulting in monodisperse particles.	[1.26, 1.28]
PEG	Improves internalization efficiency of MNPs.	[1.26, 1.29]
Chitosan	Used as a non-viral gene delivery system, prolongs the blood circulation of the MNP, and improves internalization.	[1.30, 1.31]
PCL	Applied in drug delivery due to its adsorption and sustained or biphasic release profiles.	[1.30, 1.32]
PLGA	Biodegradable and controlled drug release capabilities.	[1.33, 1.34]

Table 1.1: Polymers used for the coating of MNPs. Abbreviations: PVA (poly(vinyl alcohol)), PEG (poly(ethylene glycol)), PCL (poly(ϵ -caprolactone)) and PLGA (poly(lactic-*co*-glycolic acid)).

In the context of this doctoral thesis, the use of polyethylenimine (PEI) as a coating agent for inorganic NPs is highlighted, since the coating process is simple, and provides biocompatibility and stability to the system [1.35]. It is a cationic polymer with a high positive charge density, which forms a positive surface particularly useful for the delivery of cancer treatments [1.36]. Moreover, this property enhances biological interactions with cells, facilitating their uptake, as

well as with proteoglycans in tumor blood vessels, which could improve treatment effectiveness [1.37].

In this scope, biomimetic magnetic particles are noteworthy. As previously mentioned, these particles can be synthesized by microorganisms or bacteria, and an example of this are the magnetic biomimetic nanoparticles mediated by the MamC protein from *Magnetococcus marinus*. These particles are designed to mimic natural biological structures, which makes them highly compatible with biological systems. They do not require additional polymeric coatings for biocompatibility or to enhance interaction with cells. [1.38, 1.39].

1.4. Targeted therapies

MNPs as drug carriers

As mentioned previously, the origin of nanoparticle delivery techniques dates back to the 1950's. However, focusing on magnetic nanoparticles, before being used for drug delivery, magnetic microparticles were initially proposed for radiation therapy and vascular occlusion of tumors [1.21]. In 1960, authors such as Freeman proposed to transport the MNPs through the vascular system and concentrate them in a specific part of the body with the help of a magnetic field [1.40]. The concept of using magnetic micro- and nanoparticles as carriers for therapeutic drugs at specific sites in the body began in the late 1970s. Widder described in animal models the target of magnetic albumin microspheres encapsulating an anticancer drug [1.41]. In 1994, Häfeli developed biodegradable polylactic acid microspheres incorporating magnetite and the ^{90}Y beta emitter for targeted radiotherapy [1.42].

Nevertheless, these approaches used microscopic-sized particles. Lübbe and his team pioneered the use of MNPs in animal models. In 1996, they conducted the first phase of a clinical trial using epirubicin-loaded MNPs in patients with advanced cancer who had not responded to other treatments. However, in this initial trial, more than 50% of the nanoparticles accumulated in the liver [1.43, 1.44].

Currently, this field of research holds considerable interest due to the numerous benefits of targeted therapies, mainly because of the reduction of systemic distribution and improving uptake in the target area, allowing effective treatment with lower doses [1.45, 1.46]. However, practical implementation still presents challenges, primarily due to factors such as magnetic properties, particle size, magnetic field configuration, capacity for drug or gene transport, and various physiological parameters including target depth, vascular perfusion, blood flow dynamics, or patient conditions [1.45, 1.46].

Therefore, it is of great importance to know the adsorption, as well as how to guide the particles to the area of interest, and even more, the release of drugs using MNPs as vehicles. In this context, although it is true that porous particles such as mesoporous silica [1.47] or graphene oxide present better adsorption capacities [1.48], numerous studies have been carried out using MNPs as nanoplatforams for drug adsorption due to the unique characteristics of magnetite and its ability to be functionalized with other agents [1.49–1.51]. In addition, it is possible to combine both structures (magnetic and porous, as will be discussed below), creating hybrid structures [1.52, 1.53].

Once the drug-carrier complex is administered, then a magnetic field is used to guide and concentrate the particles on specific areas, such as tumors [1.54]. Regarding the physical principles to capture MNPs in a given area and to be able to manipulate them, the basis consists in the application of a high-gradient external magnetic fields, which exerts a translational force on the particle/drug in the field of the target area and attracts it towards the [1.54, 1.55] magnet. This magnetic force is governed by:

$$\mathbf{F}_{\text{mag}} = (\chi_2 - \chi_1) V \frac{1}{\mu_0} (\mathbf{B} \cdot \nabla) \mathbf{B} \quad (1.1)$$

being χ_1 the magnetic susceptibility of the medium (which in the case of biological systems is negligible), χ_2 the magnetic susceptibility of the MNP, V is the volume of the particle, and \mathbf{B} is the magnetic field [1.54, 1.55]. Some research suggests that hydrodynamic conditions for magnetic nanoparticle targeting should employ magnetic field strength of 200-700 mT, with gradients of approximately 8-100 T/m, depending on blood flow [1.56, 1.57].

As expected, the goal of drug delivery systems is to ensure a controlled release that maintains a constant dose over time (zero-order kinetics), a high initial dosage to achieve a constant level (first-order kinetics), or a gradual release over a prolonged period (sustained release) [1.58]. Traditional drug delivery systems have limitations such as poor absorption, low bioavailability, high metabolism and the need for frequent dosing. In the nanosystems presented, a controlled and localized drug delivery is pursued, which maintain stable therapeutic levels for prolonged periods of time [1.58].

Once at the target site, the drug is released from the magnetic carrier controlled by enzymatic activity or physiological changes (pH, osmolality or temperature, or therapies based on electromagnetic stimuli, among others) [1.54, 1.59]. Similar principles have been applied for therapeutic gene delivery [1.45, 1.46].

Finally, since the present thesis is mostly focus in the use of MNPs in cancer treatments, some of the most commonly used drugs for different cancer cell models are highlighted in Table 1.2.

Cancer cell line	Type of cancer	Drug loaded	Ref.
HepG2	Liver	Doxorubicin	[1.49]
		Sorafenib	[1.60]
		Crocetin	[1.61]
HeLa	Cervical	Doxorubicin	[1.62]
		Curcumin	[1.63]
MCF-7	Breast	Doxorubicin	[1.64]
		Methotrexate	[1.65]
		Gemcitabine	[1.50]
HT-29	Colon	5-fluorouracil	[1.51]

Table 1.2: Some of the drugs for which MNPs act as vehicles, and cell lines on which they have been applied.

MNPs as heating agents

Another possibility to combat diseases such as cancer in a targeted way is to use nanoparticles as localized heating agents. In this case, they become hyperthermia agents [1.66]. It has been shown that by raising the temperature of tumor cells to a range of 41-46°C, they do not survive after a certain time of application [1.67]. Tumor cells have an accelerated metabolism and as mentioned above, a disorganized vascular structure. When they are subjected to heat, the blood flow is not efficient enough to dissipate the heat evenly, which can induce apoptosis by increasing the temperature without significantly affecting the surrounding healthy tissue. It is worth mentioning that the use of temperatures above 50°C can cause irreversible damage, such as damage to DNA or proteins, and above 60°C almost instantaneous coagulation of proteins [1.67]. For this reason, it is necessary to modulate the desired temperature increases and to know the characteristics of the heating agents.

Although it can be considered a modern therapy against cancer, the use of thermal therapies is not a novelty, as they have been applied since ancient times. There are evidences that the Egyptians already used this type of therapy to treat superficial wounds. However, the core of the present contribution consists of the study and application of thermal therapies based on MNPs. In first place, we highlight magnetic hyperthermia, a treatment that has been relied upon for two decades. This treatment consists of generating localized heat through the application of alternating magnetic fields to a suspension of MNPs [1.68].

Another possibility is the application of the therapy known as photothermia, which consists of increasing the temperature by means of irradiation with a laser of a specific wavelength [1.69]. It is important to mention that, while magnetic hyperthermia depends on long-range magnetic fields, in the case of photothermia, its limitation lies in the location of the tumor mass, being the penetration of the wavelengths limited in the human body. However, it is possible to take advantage of certain ranges of the spectrum, called biological windows, in which the optical transmittance is much higher through tissue, water and hemoglobin. Specifically, this occurs in the 650-1350 nm region [1.70]. This type of therapy can be of great interest for superficial cancers, such as basal cell carcinoma tumors, which have a depth of invasion of 0.68 mm on average [1.71].

Finally, a less studied possibility is the use of low-frequency rotating magnetic fields. These fields do not generate heat, but can break membranes or cells in a magneto-mechanical way, or enhance drug diffusion [1.72–1.74]. In other words, the three techniques presented can be used together or separately, not only to trigger cancer cell death by temperature increase (in the case of magnetic hyperthermia and photothermia), but also to release drugs, thus acting as multifunctional agents.

In the following chapter, the advantages of using certain types of hybrid nanostructures (magnetic-metallic or magnetic-porous), as well as those of anisotropic geometry, to optimize the aforementioned therapies are presented.

Bibliography

- [1.1] Tadeusz Dyba, Giorgia Randi, Freddie Bray, Carmen Martos, Francesco Giusti, Nicholas Nicholson, Anna Gavin, Manuela Flego, Luciana Neamtii, Nadya Dimitrova, et al. The european cancer burden in 2020: Incidence and mortality estimates for 40 countries and 25 major cancers. *European Journal of Cancer*, 157:308–347, 2021.
- [1.2] Shariqsrijon Sinha Ray and Jayita Bandyopadhyay. Nanotechnology-enabled biomedical engineering: Current trends, future scopes, and perspectives. *Nanotechnology Reviews*, 10(1):728–743, 2021.
- [1.3] Richard Feynman. There’s plenty of room at the bottom. In *Feynman and Computation: Exploring the Limits of Computers*, pages 63–76. CRC Press, 1959.
- [1.4] Jörg Kreuter. Nanoparticles—a historical perspective. *International Journal of Pharmaceutics*, 331(1):1–10, 2007.
- [1.5] Leena Mohammed, Hassan G Gomaa, Doaa Ragab, and Jesse Zhu. Magnetic nanoparticles for environmental and biomedical applications: A review. *Particuology*, 30:1–14, 2017.
- [1.6] Saurabh Shukla, Ramsha Khan, and Achlesh Daverey. Synthesis and characterization of magnetic nanoparticles, and their applications in wastewater treatment: A review. *Environmental Technology & Innovation*, 24:101924, 2021.
- [1.7] Sheila Shahidi. Magnetic nanoparticles application in the textile industry—a review. *Journal of Industrial Textiles*, 50(7):970–989, 2021.
- [1.8] Kaibo Zhou, Xiang Zhou, Jie Liu, and Zhen Huang. Application of magnetic nanoparticles in petroleum industry: A review. *Journal of Petroleum Science and Engineering*, 188:106943, 2020.

- [1.9] Seipati Rosemary Mokhosi, Wendy Mdlalose, Amos Nhlapo, and Moganavelli Singh. Advances in the synthesis and application of magnetic ferrite nanoparticles for cancer therapy. *Pharmaceutics*, 14(5):937, 2022.
- [1.10] D Stanicki, T Vangijzegem, I Ternad, and S Laurent. An update on the applications and characteristics of magnetic iron oxide nanoparticles for drug delivery. *Expert Opinion on Drug Delivery*, 19(3):321–335, 2022.
- [1.11] Hung-Vu Tran, Nhat M Ngo, Riddhiman Medhi, Pannaree Srinnoi, Tingting Liu, Supparesk Rittikulsittichai, and T Randall Lee. Multifunctional iron oxide magnetic nanoparticles for biomedical applications: A review. *Materials*, 15(2):503, 2022.
- [1.12] Laís Salomão Arias, Juliano Pelim Pessan, Ana Paula Miranda Vieira, Taynara Maria Toito de Lima, Alberto Carlos Botazzo Delbem, and Douglas Roberto Monteiro. Iron oxide nanoparticles for biomedical applications: a perspective on synthesis, drugs, antimicrobial activity, and toxicity. *Antibiotics*, 7(2):46, 2018.
- [1.13] C Valverde-Tercedor, M Montalbán-López, T Perez-Gonzalez, MS Sanchez-Quesada, T Prozorov, E Pineda-Molina, MA Fernandez-Vivas, AB Rodriguez-Navarro, D Trubitsyn, Dennis A Bazylnski, et al. Size control of in vitro synthesized magnetite crystals by the MamC protein of *Magnetococcus marinus* strain MC-1. *Applied Microbiology and Biotechnology*, 99:5109–5121, 2015.
- [1.14] Raquel GD Andrade, Sérgio RS Veloso, and Elisabete MS Castanheira. Shape anisotropic iron oxide-based magnetic nanoparticles: Synthesis and biomedical applications. *International Journal of Molecular Sciences*, 21(7):2455, 2020.
- [1.15] Lokesh Srinath Ganapathe, Mohd Ambri Mohamed, Rozan Mohamad Yunus, and Dilla Duryha Berhanuddin. Magnetite nanoparticles (Fe_3O_4) in biomedical application: From synthesis to surface functionalisation. *Magnetochemistry*, 6(4):68, 2020.
- [1.16] Kirill D Petrov and Alexey S Chubarov. Magnetite nanoparticles for biomedical applications. *Encyclopedia*, 2(4):1811–1828, 2022.
- [1.17] Lee Blaney. Magnetite (Fe_3O_4): Properties, synthesis, and applications. *Lehigh Preserve*, 15, 2007.
- [1.18] Qing Li, Christina W Kartikowati, Shinji Horie, Takashi Ogi, Toru Iwaki, and Kikuo Okuyama. Correlation between particle size/domain structure and magnetic properties of highly crystalline Fe_3O_4 nanoparticles. *Scientific Reports*, 7(1):9894, 2017.

- [1.19] Scott J Kemp, R Matthew Ferguson, Amit P Khandhar, and Kannan M Krishnan. Monodisperse magnetite nanoparticles with nearly ideal saturation magnetization. *RSC Advances*, 6(81):77452–77464, 2016.
- [1.20] Arati G Kolhatkar, Andrew C Jamison, Dmitri Litvinov, Richard C Willson, and T Randall Lee. Tuning the magnetic properties of nanoparticles. *International Journal of Molecular Sciences*, 14(8):15977–16009, 2013.
- [1.21] Manuel Arruebo, Rodrigo Fernández-Pacheco, M Ricardo Ibarra, and Jesús Santamaría. Magnetic nanoparticles for drug delivery. *Nano Today*, 2(3):22–32, 2007.
- [1.22] Rakesh K Jain. Normalization of tumor vasculature: an emerging concept in antiangiogenic therapy. *Science*, 307(5706):58–62, 2005.
- [1.23] Jun Wu. The enhanced permeability and retention (EPR) effect: the significance of the concept and methods to enhance its application. *Journal of Personalized Medicine*, 11(8):771, 2021.
- [1.24] Xiaopin Duan and Yaping Li. Physicochemical characteristics of nanoparticles affect circulation, biodistribution, cellular internalization, and trafficking. *Small*, 9(9-10):1521–1532, 2013.
- [1.25] L Harivardhan Reddy, José L Arias, Julien Nicolas, and Patrick Couvreur. Magnetic nanoparticles: design and characterization, toxicity and biocompatibility, pharmaceutical and biomedical applications. *Chemical Reviews*, 112(11):5818–5878, 2012.
- [1.26] Ajay Kumar Gupta and Mona Gupta. Synthesis and surface engineering of iron oxide nanoparticles for biomedical applications. *Biomaterials*, 26(18):3995–4021, 2005.
- [1.27] Zhila Shaterabadi, Gholamreza Nabiyouni, and Meysam Soleymani. High impact of in situ dextran coating on biocompatibility, stability and magnetic properties of iron oxide nanoparticles. *Materials Science and Engineering: C*, 75:947–956, 2017.
- [1.28] Ting-Yu Liu, Shang-Hsiu Hu, Kun-Ho Liu, Dean-Mo Liu, and San-Yuan Chen. Study on controlled drug permeation of magnetic-sensitive ferrogels: effect of Fe₃O₄ and PVA. *Journal of Controlled Release*, 126(3):228–236, 2008.
- [1.29] Murali Mohan Yallapu, Susan P Foy, Tapan K Jain, and Vinod Labhasetwar. PEG-functionalized magnetic nanoparticles for drug delivery and magnetic resonance imaging applications. *Pharmaceutical research*, 27:2283–2295, 2010.

- [1.30] Gracia García-García, Marina Lázaro-Callejón, Fátima Fernández-Álvarez, Guillermo R Iglesias, and José L Arias. (magnetite/poly (ϵ -caprolactone))/chitosan (core/shell)/shell nanocomposites with potential applications in hyperthermia cancer therapy. *Journal of Magnetism and Magnetic Materials*, 588:171500, 2023.
- [1.31] Gracia García-García, Marina Lázaro, Alejandro Cenalmor, Isabel García-Álvarez, Guillermo R Iglesias, and José L Arias. Cluster/shell citrate- Fe_3O_4 /chitosan nanoparticles for enhancing heating efficiency in combined magnetic and photothermal therapy. *Ceramics International*, 2024.
- [1.32] Esperanza Díaz, María Blanca Valle, Sylvie Ribeiro, Senentxu Lanceros-Mendez, and José Manuel Barandiarán. 3D Cytocompatible Composites of PCL/magnetite. *Materials*, 12(23):3843, 2019.
- [1.33] Fátima Fernández-Álvarez, Gracia García-García, Guillermo R Iglesias, and José L Arias. A maghemite/PLGA (core/shell) nanostructure that may facilitate chemotherapy and antitumor hyperthermia. *Journal of Magnetism and Magnetic Materials*, 589:171574, 2024.
- [1.34] Jaime Ibarra, Julio Melendres, Mario Almada, María G Burboa, Pablo Taboada, Josué Juárez, and Miguel A Valdez. Synthesis and characterization of magnetite/PLGA/chitosan nanoparticles. *Materials Research Express*, 2(9):095010, 2015.
- [1.35] Ritu Goyal, Sushil K Tripathi, Esther Vazquez, Pradeep Kumar, and Kailash C Gupta. Biodegradable poly (vinyl alcohol)-polyethylenimine nanocomposites for enhanced gene expression in vitro and in vivo. *Biomacromolecules*, 13(1):73–83, 2012.
- [1.36] María del Mar Ramos-Tejada, Julian L Viota, Katarzyna Rudzka, and Angel V Delgado. Preparation of multi-functionalized Fe_3O_4 /Au nanoparticles for medical purposes. *Colloids and Surfaces B: Biointerfaces*, 128:1–7, 2015.
- [1.37] Beata Chertok, Allan E David, and Victor C Yang. Polyethyleneimine-modified iron oxide nanoparticles for brain tumor drug delivery using magnetic targeting and intra-carotid administration. *Biomaterials*, 31(24):6317–6324, 2010.
- [1.38] Michael T Klem, Mark Young, and Trevor Douglas. Biomimetic magnetic nanoparticles. *Materials Today*, 8(9):28–37, 2005.
- [1.39] Ylenia Jabalera, Alberto Sola-Leyva, María P Carrasco-Jiménez, Guillermo R Iglesias, and Concepcion Jimenez-Lopez. Synergistic photothermal-chemotherapy based on the use of biomimetic magnetic nanoparticles. *Pharmaceutics*, 13(5):625, 2021.

- [1.40] MW Freeman, A Arrott, and JHL Watson. Magnetism in medicine. *Journal of Applied Physics*, 31(5):S404–S405, 1960.
- [1.41] Kenneth J Widder, Andrew E Senyei, and Dante G Scarpelli. Magnetic microspheres: a model system for site specific drug delivery in vivo. *Proceedings of the Society for Experimental Biology and Medicine*, 158(2):141–146, 1978.
- [1.42] Urs O Häfeli, Siobhan M Sweeney, Beverly A Beresford, Edward H Sim, and Roger M Macklis. Magnetically directed poly (lactic acid) ^{90}Y -microspheres: Novel agents for targeted intracavitary radiotherapy. *Journal of Biomedical Materials Research*, 28(8):901–908, 1994.
- [1.43] Andreas Stephan Lübbe, Christian Bergemann, Winfried Huhnt, Thomas Fricke, Hanno Riess, Jeffery Walter Brock, and Dieter Huhn. Preclinical experiences with magnetic drug targeting: tolerance and efficacy. *Cancer Research*, 56(20):4694–4701, 1996.
- [1.44] Andreas Stephan Lübbe, Christian Bergemann, Winfried Huhnt, Thomas Fricke, Hanno Riess, Jeffery Walter Brock, and Dieter Huhn. Preclinical experiences with magnetic drug targeting: tolerance and efficacy. *Cancer Research*, 56(20):4694–4701, 1996.
- [1.45] Daisuke Kami, Shogo Takeda, Yoko Itakura, Satoshi Gojo, Masatoshi Watanabe, and Masashi Toyoda. Application of magnetic nanoparticles to gene delivery. *International Journal of Molecular Sciences*, 12(6):3705–3722, 2011.
- [1.46] Jon Dobson. Gene therapy progress and prospects: magnetic nanoparticle-based gene delivery. *Gene Therapy*, 13(4):283–287, 2006.
- [1.47] Miguel Manzano and María Vallet-Regí. Mesoporous silica nanoparticles for drug delivery. *Advanced Functional Materials*, 30(2):1902634, 2020.
- [1.48] Jingquan Liu, Liang Cui, and Dusan Losic. Graphene and graphene oxide as new nanocarriers for drug delivery applications. *Acta Biomaterialia*, 9(12):9243–9257, 2013.
- [1.49] Ndumiso Vukile Mdlovu, Kuen-Song Lin, Meng-Tzu Weng, and You-Sheng Lin. Design of doxorubicin encapsulated ph-/thermo-responsive and cationic shell-crosslinked magnetic drug delivery system. *Colloids and Surfaces B: Biointerfaces*, 209:112168, 2022.
- [1.50] Gracia García-García, Fátima Fernández-Álvarez, Laura Cabeza, Ángel V Delgado, Consolación Melguizo, José C Prados, and José L Arias. Gemcitabine-loaded magnetically responsive poly (ϵ -caprolactone) nanoparticles against breast cancer. *Polymers*, 12(12):2790, 2020.

- [1.51] Samira Eynali, Samideh Khoei, Sepideh Khoee, and Elaheh Esmaelbeygi. Evaluation of the cytotoxic effects of hyperthermia and 5-fluorouracil-loaded magnetic nanoparticles on human colon cancer cell line HT-29. *International Journal of Hyperthermia*, 33(3):327–335, 2017.
- [1.52] Hasan Keshavarz, Alireza Khavandi, Somaye Alamolhoda, and M Reza Naimi-Jamal. pH-Sensitive magnetite mesoporous silica nanocomposites for controlled drug delivery and hyperthermia. *RSC Advances*, 10(64):39008–39016, 2020.
- [1.53] Hoang V Tran, Tuong L Tran, Truong D Le, Thu D Le, Hang MT Nguyen, and Le T Dang. Graphene oxide enhanced adsorption capacity of chitosan/magnetite nanocomposite for Cr (VI) removal from aqueous solution. *Materials Research Express*, 6(2):025018, 2018.
- [1.54] Jon Dobson. Magnetic nanoparticles for drug delivery. *Drug Development Research*, 67(1):55–60, 2006.
- [1.55] Quentin A Pankhurst, J Connolly, Stephen K Jones, and JJopDAp Dobson. Applications of magnetic nanoparticles in biomedicine. *Journal of physics D: Applied physics*, 36(13):R167, 2003.
- [1.56] PA Voltairas, DI Fotiadis, and LK Michalis. Hydrodynamics of magnetic drug targeting. *Journal of biomechanics*, 35(6):813–821, 2002.
- [1.57] EK Ruuge and AN Rusetski. Magnetic fluids as drug carriers: Targeted transport of drugs by a magnetic field. *Journal of Magnetism and Magnetic Materials*, 122(1-3):335–339, 1993.
- [1.58] Joanna Kurczewska and Bernadeta Dobosz. Recent progress and challenges regarding magnetite-based nanoparticles for targeted drug delivery. *Applied Sciences*, 14(3):1132, 2024.
- [1.59] Salvatore Calogero Gaglio, Ylenia Jabalera, Manuel Montalbán-López, Ana Cristina Millán-Placer, Marina Lázaro-Callejón, Mercedes Maqueda, María Paz Carrasco-Jimenez, Alejandro Laso, José A Aínsa, Guillermo R Iglesias, et al. Embedding biomimetic magnetic nanoparticles coupled with peptide AS-48 into PLGA to treat intracellular pathogens. *Pharmaceutics*, 14(12):2744, 2022.
- [1.60] Mona Ebadi, Ahmad Rifqi Md Zain, Tengku Hasnan Tengku Abdul Aziz, Hossein Mohammadi, Clarence Augustine TH Tee, and Muhammad Rahimi Yusop. Formulation and characterization of Fe₃O₄@ PEG nanoparticles loaded sorafenib; molecular studies and evaluation of cytotoxicity in liver cancer cell lines. *Polymers*, 15(4):971, 2023.

- [1.61] Sulafa Ibrahim, Badriya Baig, Soleiman Hisaindee, Hussein Darwish, Ashraf Abdel-Ghany, Hesham El-Maghraby, Amr Amin, and Yaser Greish. Development and evaluation of crocetin-functionalized pegylated magnetite nanoparticles for hepatocellular carcinoma. *Molecules*, 28(7):2882, 2023.
- [1.62] Qinfu Zhao, Peiyu Xie, Xian Li, Yue Wang, Ying Zhang, and Siling Wang. Magnetic mesoporous silica nanoparticles mediated redox and pH dual-responsive target drug delivery for combined magnetothermal therapy and chemotherapy. *Colloids and Surfaces A: Physicochemical and Engineering Aspects*, 648:129359, 2022.
- [1.63] Marzieh Ramezani Farani, Maryam Azarian, Hamid Heydari Sheikh Hossein, Zohreh Abdolvahabi, Zahra Mohammadi Abgarmi, Arash Moradi, Seyyede Maedeh Mousavi, Milad Ashrafizadeh, Pooyan Makvandi, Mohammad Reza Saeb, et al. Folic acid-adorned curcumin-loaded iron oxide nanoparticles for cervical cancer. *ACS Applied Bio Materials*, 5(3):1305–1318, 2022.
- [1.64] Elisa Parceró Hernández, Raquel Dosciatti Bini, Karina Midori Endo, Vercy Alves de Oliveira Junior, Igor Vivian de Almeida, Gustavo Sanguino Dias, Ivair Aparecido dos Santos, Paula Nunes de Oliveira, Verónica Elisa Pimenta Vicentini, and Luiz Fernando Cotica. Doxorubicin-loaded magnetic nanoparticles: enhancement of doxorubicin's effect on breast cancer cells (MCF-7). *Magnetochemistry*, 8(10):114, 2022.
- [1.65] Ehab MM Ali, Aya A Elashkar, Hala Y El-Kassas, and Elsayed I Salim. Methotrexate loaded on magnetite iron nanoparticles coated with chitosan: Biosynthesis, characterization, and impact on human breast cancer MCF-7 cell line. *International Journal of Biological Macromolecules*, 120:1170–1180, 2018.
- [1.66] Zhila Shaterabadi, Ángel Delgado, and Guillermo R Iglesias. Solvothermally synthesized magnetite nanorods for application in magnetic hyperthermia and photothermia. *Journal of Magnetism and Magnetic Materials*, 596:171990, 2024.
- [1.67] Daniel Jaque, L Martínez Maestro, Blanca del Rosal, P Haro-Gonzalez, Antonio Benayas, JL Plaza, E Martín Rodríguez, and J García Solé. Nanoparticles for photothermal therapies. *Nanoscale*, 6(16):9494–9530, 2014.
- [1.68] Daniel Ortega and Quentin A Pankhurst. Magnetic hyperthermia. *Nanoscience*, 1(60):e88, 2013.
- [1.69] Anouchka Plan Sangnier, Sandra Preveral, Alberto Curcio, Amanda KA Silva, Chistopher T Lefèvre, David Pignol, Yoann Lalatonne, and Claire Wilhelm. Targeted thermal therapy with genetically engineered magnetite

- magnetosomes@ RGD: Photothermia is far more efficient than magnetic hyperthermia. *Journal of Controlled Release*, 279:271–281, 2018.
- [1.70] Louise Finlayson, Isla RM Barnard, Lewis McMillan, Sally H Ibbotson, C Tom A Brown, Ewan Eadie, and Kenneth Wood. Depth penetration of light into skin as a function of wavelength from 200 to 1000 nm. *Photochemistry and Photobiology*, 98(4):974–981, 2022.
- [1.71] Megan Wetzel, John Strickley, M Tye Haeberle, and Timothy S Brown. Depth of invasion of aggressive and nonaggressive basal cell carcinoma. *The Journal of Clinical and Aesthetic Dermatology*, 12(3):12, 2019.
- [1.72] Yajing Shen, Congyu Wu, Taro QP Uyeda, Gustavo R Plaza, Bin Liu, Yu Han, Maciej S Lesniak, and Yu Cheng. Elongated nanoparticle aggregates in cancer cells for mechanical destruction with low frequency rotating magnetic field. *Theranostics*, 7(6):1735, 2017.
- [1.73] Sara Lopez, Nicolas Hallali, Yoann Lalatonne, Arnaud Hillion, Joana C Antunes, Nizar Serhan, Pascal Clerc, Daniel Fourmy, Laurence Motte, Julian Carrey, et al. Magneto-mechanical destruction of cancer-associated fibroblasts using ultra-small iron oxide nanoparticles and low frequency rotating magnetic fields. *Nanoscale Advances*, 4(2):421–436, 2022.
- [1.74] Silvia Nappini, Francesca Baldelli Bombelli, Massimo Bonini, Bengt Nordèn, and Piero Baglioni. Magnetoliposomes for controlled drug release in the presence of low-frequency magnetic field. *Soft Matter*, 6(1):154–162, 2010.

Chapter 2

Justification

2.1. Motivation

Study of hybrid and anisotropic nanostructures for biomedical applications

Considering the literature review conducted in the previous chapter, the use of hybrid nanostructures capable of responding to multiple stimuli simultaneously is of great interest. This interest not only from the physical perspective, which involves understanding and applying the different materials available and their particular properties to optimize the structural and functional characteristics of nanoparticles, thus maximizing their performance in specific applications. Equally important is the biological perspective, which focuses on minimizing side effects and enhancing the safety and efficacy of treatments, crucial for their clinical application. To achieve this, efforts are directed towards reducing the required dose of nanoparticles and the necessary stimulus rate, aiming to develop advanced therapies that are both effective and safe. And it is in this context that this doctoral thesis is situated.

However, before focusing on the sought objectives, the importance of developing this type of nanostructures is discussed below:

- First, the use of multifunctional nanoparticles, coated with metals or other materials that improve their optical properties, is highlighted.
- Next, the use of anisotropic nanoparticles is described.
- Finally, nanostructures composed of different porous and magnetic materials as drug vehicles are discussed.

This set of properties and improvements is crucial to advance the techniques and nanoparticles available so far.

Following the outlined structure, magnetite is known to act as an agent in both magnetic hyperthermia and photothermia [2.1,2.2]. However, there are other materials with a better optical response, such as gold and silver [2.2,2.3] due to their plasmonic properties [2.4]. In particular, gold stands out for its high biocompatibility, proving to be a highly effective photothermia agent [2.2, 2.5]. For this reason, obtaining nanoparticles that combine both characteristics is of special relevance. Several authors have studied the use of these nanostructures by applying them to both electromagnetic stimuli separately [2.2,2.6–2.9]. One question that this doctoral thesis seeks to answer is what happens when both stimuli are applied simultaneously.

In addition to the improvement in optical properties by metallic coatings, it is important to consider particle anisotropy. In particular, there is a growing interest in such geometries, since in general, they show a higher magnetization than symmetric particles such as nanospheres [2.10, 2.11]. Another determining factor in shape is the aspect ratio. Mohapatra *et al.* [2.10] showed that as the aspect ratio of nanoparticles increases (spheres < cubes < octahedrons < rods < wires), the thermal efficiency increases, despite having a lower magnetic susceptibility (wires < rods < spheres < cubes < octahedrons), probably due to the high anisotropy of nanowires, which significantly increases the hysteresis loss, thus improving the heating efficiency [2.10]. In addition, another desired feature of this type of anisotropic nanoparticles is their ability to exert a magnetomechanical action on cells. A recent study by Nikitin *et al.* [2.12] demonstrates that, upon application of a low-frequency magnetic field (31 Hz), rod-shaped CoFe_2O_4 nanoparticles succeed in inducing breast cancer cell death even at low concentrations (6 $\mu\text{g/mL}$).

One of the possibilities mentioned is the combination of different structures, such as porous materials that serve as a basis for drug adsorption and magnetic materials that allow drug targeting. Among the most studied so far are magnetic composites with silica [2.13–2.16], but also those with activated carbon [2.17, 2.18]

Finally, it is important to remember that, as mentioned previously, these nanostructures present multiple response capabilities. They act not only as heating agents in magnetic hyperthermia and/or photothermia therapies, but can also act as magneto-mechanical agents and as efficient drug vehicles. Their versatility allows them to perform several therapeutic functions simultaneously, making them valuable tools in the field of nanomedicine. In short, multifunctional capabilities are sought that not only improve treatment efficacy, but can also reduce side effects by allowing more targeted and controlled drug delivery.

2.2. Outline of the thesis

The objectives of this thesis can be summarized as follows.

1. Study and characterization of magnetic hyperthermia and photothermia equipment. Possibility of using rotating magnetic fields and not only oscillating ones.
2. Synthesis methods of MNPs of different sizes and morphologies, aimed at obtaining high magnetic response (initial susceptibility, saturation magnetization) and thermal efficiency.
3. Functionalization of the MNPs by adsorption of suitable molecules to: (i) make them biocompatible and avoid immune response; (ii) facilitate drug release in the organism.
4. *In vitro* study of cell viability after the application of different electromagnetic stimuli.
5. Study of the release kinetics of drugs adsorbed on the surface of the synthesized MNPs, with and without the application of hyperthermia, photothermia or rotating fields.

With these objectives in mind, this thesis is divided into ten chapters. The first two correspond to the introduction of the thesis. Chapter 3 is dedicated to a review of the fundamental physical concepts of the techniques on which this thesis focuses: magnetic hyperthermia, photothermia and rotating fields, related to Objective 1, which is also developed in the Results and Discussion part of the thesis. As argued in the previous section, the common thread is the production of nanoparticles with different sizes and geometries (Objective 2, developed in Chapters 4-7), coated with biocompatible polymers (Objective 3, Chapters 4-7). These nanoparticles act as heating agents, making it possible to evaluate cell death following the application of electromagnetic stimuli (Objective 4, carried out in Chapters 5 and 8), and also behave as drug carriers with controlled release in response to various stimuli (Objective 5, developed in Chapters 6 and 7).

Chapters 4, 5, 6 and 8 contain work already published, while Chapter 7 is work pending publication. The following is a brief description of the main points to be covered in each of them:

- Chapter 4: Related to obtaining spherical particles of a size suitable for biomedical applications, high magnetic properties and optimal heating rate. The MNPs are coated with a biocompatible polymeric layer, which allows the incorporation of gold nanospheres, improving their optical response in

the visible, and therefore, acting as magnetic hyperthermia and photothermia agents.

- Chapter 5: Dedicated to the synthesis of magnetite nanorods 40 nm in length, coated with a triple polymeric layer that makes them biocompatible with MCF7 cells and ensures a high percentage of internalization (higher than 80%). It is verified that both magnetic hyperthermia and photothermia application induce a cell death rate higher than 60%.
- Chapter 6: Focused on the synthesis of biocompatible magnetic rods (550 nm of length), coated with gold seeds, that act as drug carriers and behave as hyperthermia agents. This work demonstrates that the simultaneous application of both stimuli results in safer and more effective treatments by reducing both the power of the irradiation and the intensity of the magnetic field.
- Chapter 7: Centered on the production of biocompatible porous/magnetic structures made of activated carbon and magnetite. Due to their high specific surface area, these structures can adsorb large quantities of drugs. The goal is to enhance drug release following the application of photothermia or low-frequency rotating magnetic fields.
- Chapter 8: Emphasizing the biological application in using biomimetic magnetic particles as hyperthermia agents. This work determines that cellular internalization is necessary to achieve cell death when applying photothermia, while maintaining irradiation powers that are safe for the human body.

Finally, Chapters 9 and 10 are dedicated to the conclusions and summary of the work carried out.

Bibliography

- [2.1] Agnieszka Włodarczyk, Szymon Gorgoń, Adrian Radoń, and Karolina Bajdak-Rusinek. Magnetite nanoparticles in magnetic hyperthermia and cancer therapies: Challenges and perspectives. *Nanomaterials*, 12(11):1807, 2022.
- [2.2] Ana Espinosa, Jelena Kolosnjaj-Tabi, Ali Abou-Hassan, Anouchka Plan Sangnier, Alberto Curcio, Amanda KA Silva, Riccardo Di Corato, Sophie Neveu, Teresa Pellegrino, Luis M Liz-Marzán, et al. Magnetic (hyper) thermia or photothermia? progressive comparison of iron oxide and gold nanoparticles heating in water, in cells, and in vivo. *Advanced Functional Materials*, 28(37):1803660, 2018.
- [2.3] Karthikeyan Manivannan, Chih-Chia Cheng, Rajeshkumar Anbazhagan, Hsieh-Chih Tsai, and Jem-Kun Chen. Fabrication of silver seeds and nanoparticle on core-shell Ag@SiO₂ nanohybrids for combined photothermal therapy and bioimaging. *Journal of Colloid and Interface Science*, 537:604–614, 2019.
- [2.4] Yingjie Hang, Anyang Wang, and Nianqiang Wu. Plasmonic silver and gold nanoparticles: shape- and structure-modulated plasmonic functionality for point-of-care sensing, bio-imaging and medical therapy. *Chemical Society Reviews*, 2024.
- [2.5] Rua J Kadhim, Esraa H Karsh, Zainab J Taqi, and Majid S Jabir. Biocompatibility of gold nanoparticles: In-vitro and in-vivo study. *Materials Today: Proceedings*, 42:3041–3045, 2021.
- [2.6] Mohamed F Sanad, Bianca P Meneses-Brassea, Dawn S Blazer, Shirin Pourmiri, George C Hadjipanayis, and Ahmed A El-Gendy. Superparamagnetic Fe/Au nanoparticles and their feasibility for magnetic hyperthermia. *Applied Sciences*, 11(14):6637, 2021.
- [2.7] Evangelia Christou, John R Pearson, Ana M Beltrán, Yilian Fernández-Afonso, Lucía Gutiérrez, Jesús M de la Fuente, Francisco Gámez, María L García-Martín, and Carlos Caro. Iron-gold nanoflowers: A promising tool for

- multimodal imaging and hyperthermia therapy. *Pharmaceutics*, 14(3):636, 2022.
- [2.8] Beatrice Muzzi, Martin Albino, Alessio Gabbani, Alexander Omelyanchik, Elena Kozenkova, Michele Petrecca, Claudia Innocenti, Elena Balica, Alessandro Lavacchi, Francesca Scavone, et al. Star-shaped magnetic-plasmonic Au@ Fe₃O₄ nano-heterostructures for photothermal therapy. *ACS Applied Materials & Interfaces*, 14(25):29087–29098, 2022.
- [2.9] Olga Yu Griaznova, Iaroslav B Belyaev, Anna S Sogomonyan, Ivan V Zelepukin, Gleb V Tikhonowski, Anton A Popov, Aleksei S Komlev, Petr I Nikitin, Dmitry A Gorin, Andrei V Kabashin, et al. Laser synthesized core-satellite Fe-Au nanoparticles for multimodal in vivo imaging and in vitro photothermal therapy. *Pharmaceutics*, 14(5):994, 2022.
- [2.10] Jeotikanta Mohapatra, Meiyang Xing, Julian Beatty, Jacob Elkins, Takele Seda, Sanjay R Mishra, and J Ping Liu. Enhancing the magnetic and inductive heating properties of Fe₃O₄ nanoparticles via morphology control. *Nanotechnology*, 31(27):275706, 2020.
- [2.11] Felisa Reyes-Ortega, Ángel V Delgado, and Guillermo R Iglesias. Modulation of the magnetic hyperthermia response using different superparamagnetic iron oxide nanoparticle morphologies. *Nanomaterials*, 11(3):627, 2021.
- [2.12] Aleksey A Nikitin, Victor A Arkhipov, Nelly S Chmelyuk, Anna V Ivanova, Stepan S Vodopyanov, Anastasiia S Garanina, Mikhail A Soldatov, Maksim A Gritsai, Valeriy M Cherepanov, Natalia N Barbotina, et al. Multifunctional Anisotropic Rod-Shaped CoFe₂O₄ Nanoparticles for Magnetic Resonance Imaging and Magnetomechanical Therapy. *ACS Applied Nano Materials*, 6(15):14540–14551, 2023.
- [2.13] Yuan Gao, Ming-Wei Chang, Zeeshan Ahmad, and Jing-Song Li. Magnetic-responsive microparticles with customized porosity for drug delivery. *RSC Advances*, 6(91):88157–88167, 2016.
- [2.14] Shanshan Huang, Chunxia Li, Ziyong Cheng, Yong Fan, Piaoping Yang, Cuimiao Zhang, Kuiyue Yang, and Jun Lin. Magnetic Fe₃O₄@mesoporous silica composites for drug delivery and bioadsorption. *Journal of Colloid and Interface Science*, 376(1):312–321, 2012.
- [2.15] Cuilian Tao and Yufang Zhu. Magnetic mesoporous silica nanoparticles for potential delivery of chemotherapeutic drugs and hyperthermia. *Dalton Transactions*, 43(41):15482–15490, 2014.
- [2.16] Baisong Chang, Jia Guo, Congying Liu, Ji Qian, and Wuli Yang. Surface functionalization of magnetic mesoporous silica nanoparticles for controlled drug release. *Journal of Materials Chemistry*, 20(44):9941–9947, 2010.

-
- [2.17] RV Ramanujan, S Purushotham, and MH Chia. Processing and characterization of activated carbon coated magnetic particles for biomedical applications. *Materials Science and Engineering: C*, 27(4):659–664, 2007.
- [2.18] Zhanna K Nazarkina, Tatyana A Savostyanova, Boris P Chelobanov, Irina V Romanova, Pavel A Simonov, Ren I Kvon, Andrey A Karpenko, and Pavel P Laktionov. Activated carbon for drug delivery from composite biomaterials: The effect of grinding on sirolimus binding and release. *Pharmaceutics*, 14(7):1386, 2022.

Part II

Physical principles and experimental methods

Chapter 3

Fundamentals of magnetic hyperthermia, photothermia and low-frequency magnetic rotating fields

3.1. Magnetic hyperthermia

As mentioned in the previous chapter, magnetic nanoparticles act as thermal agents. This therapy has its beginnings in the late 1950s, when Gilchrist first reported the heating of micrometre-sized magnetite particles by alternating magnetic fields, known as hyperthermia [3.1]. Then, in 1993, research by Jordan and his team, drove the development of magnetic hyperthermia, which uses alternating magnetic fields of frequencies between kHz and MHz [3.2]. To this day, this is still being researched for greater effectiveness, and fewer side effects. One example is the european NoCanTher project, which in 2022 began clinical trials in patients with locally advanced pancreatic tumours at the Vall d'Hebron hospital (Barcelona). Thus, when considering local heating, the first question that rises is how to achieve it. Therefore, the principles of magnetic hyperthermia are explained in detail below.

For heating to occur, it is essential that there is a mechanism capable of generating energy losses, which in turn produces sufficient heat to induce cell death. Furthermore, it is important to mention that due to the small size of the magnetic particles and their low electrical conductivity, eddy currents are discarded. Therefore, the observed increase in temperature is attributed to hysteresis [3.3].

If the nanoparticles acting as hyperthermic agents are ferromagnetic, they exhibit magnetic remanence, resulting in an open hysteresis cycle. This is due to the energy consumed by the displacement of the magnetic domain walls, and a coercive field is required to demagnetize the material. In this case, the power density dissipated (P) as heat in an alternating magnetic field of frequency (f) is defined in terms of the

magnetic permeability of the vacuum (μ_0), magnetization (M) and the field strength (H) as follows:

$$P = \mu_0 f \oint M(H) dH. \quad (3.1)$$

However, if these nanoparticles are assumed to be superparamagnetic and single-domain, which is favourable because of the biological advantages already described, the hysteresis is not related to the Bloch wall displacement, but to the phase lag between the magnetization and the applied field. In this context, and in order to go a little deeper into the mechanisms of temperature increase, the Stoner-Wohlfarth model is known to adequately describe the behavior of single-domain particles. However, for highly anisotropic particles, such as those to be studied in this thesis, and under the application of moderately low fields, typically used in magnetic hyperthermia, the linear response theory (LRT) is applicable. In this theory, the magnetization is assumed to vary linearly with the field, although the susceptibility is complex ($\chi = \chi' + i\chi''$) [3.4]. This is due to the finite time required for the magnetic moment to reverse under the influence of the field, resulting in a time lag between magnetic moment and field. This phase lag results in a hysteresis cycle with a finite area, which implies a release of energy in the form of heat [3.4]. In this case the power dissipated is:

$$P = 2\mu_0 f H_0^2 \chi'' \int_0^{1/f} \sin^2(2\pi ft) dt \quad (3.2)$$

being H_0 the amplitude of the magnetic field. Therefore, the thermal energy release is attributed to the processes or relaxation of the magnetic moments of the MNPs under the influence of the magnetic field, known as Néel and Brown relaxations [3.3].

We speak of Néel relaxation (Figure 3.1), when the magnetic moment rotates inside the nanoparticle to align with the easy magnetization direction. In this process, the energy is transferred to the lattice and absorbed by phonons, and therefore this mechanism is intrinsically related to the properties of the MNP [3.3]. The equation describing the Néel relaxation time is given by:

$$\tau_N = \tau_0 e^{\frac{T_B}{T}} = \tau_0 e^{\frac{KV}{k_B T}} \quad (3.3)$$

where K is the anisotropy constant, V the particle volume, and k_B the Boltzmann constant. The relaxation time (τ_0) for a non-interacting magnetic moment, generally varies between 10^{-9} and 10^{-13} s. The blocking temperature, represented by T_B , is the parameter that distinguishes between stable or blocked states and rapid changes in spin. If $T > T_B$, the magnetic behavior is close to paramagnetism. However, when $T < T_B$, the Néel time becomes significant, leading to magnetic moment blocking.

However, since the particles are immersed in a fluid, it is also relevant to consider Brown relaxation. In this case, it is the whole particle that rotates when the field

changes direction (Figure 3.1). Heat transfer occurs directly to the fluid through the viscosity at the particle surface. The expression for Brown relaxation time is given by:

$$\tau_B = \frac{3\eta V_H}{k_B T} \quad (3.4)$$

where η is the viscosity and V_H is the hydrodynamic volume [3.3].

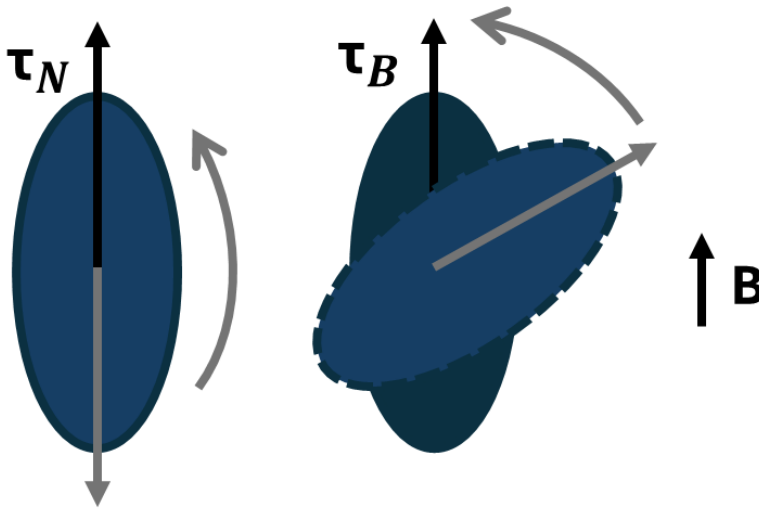


Figure 3.1: Sketch of Néel (left) and Brown (right) relaxation processes.

Both effects occur at the same time, and therefore the reciprocal effective time of the system (τ_{eff}) is the sum of the inverses of the Brown and Néel relaxations:

$$\frac{1}{\tau_{eff}} = \frac{1}{\tau_B} + \frac{1}{\tau_N}. \quad (3.5)$$

However, as Figure 3.2 details, Néel relaxation predominates for small particles ($R < 18$ nm), while Brown relaxation predominates for larger particles ($R > 22$ nm).

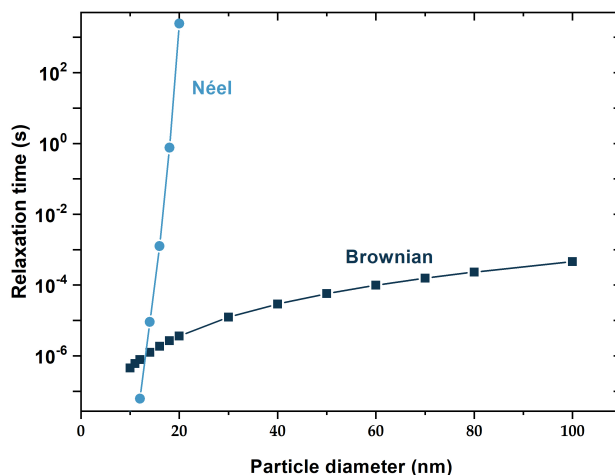


Figure 3.2: Brown and Néel relaxation times for a suspension of magnetite NPs of different diameters in water.

It is significant to mention that maximum values of $H_0 \cdot f$ have been delimited for application to humans, minimising the discomfort due to eddy current enhancement. The most famous, the Atkinson-Brezovich limit, which is given by $H_0 \cdot f = 4.85 \times 10^8 \text{ A m}^{-1} \text{ s}^{-1}$ [3.5]. Less strict is the limit proposed by Hergt and Dutz, where for a reduced exposed region of the body, and depending on the severity of the disease, a weaker criterion can be assumed ($H_0 \cdot f = 5 \times 10^9 \text{ A m}^{-1} \text{ s}^{-1}$) [3.6].

Finally, it is crucial to note that, although magnetic hyperthermia offers many advantages for localized cancer treatments, its practical application, both *in vitro* and *in vivo*, often results in lower than expected temperature increments. This is due to the high viscosity of the media, which limits particle rotation and mainly affects Brown relaxation time, as mentioned above, especially for larger particles. Therefore, it is of great interest to adjust controllable factors, such as the size of the MNPs or the anisotropy constant, by modifying their morphology, composition and other aspects.

3.2. Photothermia

Photothermia, although less studied than magnetic hyperthermia, is a technique of growing interest in the biomedical field. Nowadays, lasers are used in a variety of treatments, such as the removal of vascular lesions, scars, in ophthalmological and urological surgeries, and even for cutting and coagulating tissues. In oncology, thermal laser ablation is used for some types of cancer, but faces limitations due to heat

scattering and energy absorption by healthy tissues [3.7]. To improve laser precision and efficacy, photothermal agents that generate localized heat by absorbing light are used, overcoming these limitations.

In this context, photothermia emerges as an extension of photodynamic therapy, which uses photothermal agents on tumour tissues. Furthermore, it is important to remember that, as mentioned above, the radiation used in photothermia is in the near infrared (NIR) range, whose wavelength allows deeper penetration into biological tissues. There are two wavelength ranges known as biological windows. The first NIR biological window spans the wavelengths from 650 to 900 nm, where both haemoglobin and water, the main absorbers of visible and infrared light, have their lowest absorption coefficients. The second window extends from 1000 to 1350 nm, which allows even greater penetration, favouring more effective and less invasive localized treatments [3.7, 3.8].

In general, efficient photothermal agents require biocompatibility and adequate size, as well as absorbance in the NIR, and high absorption cross-section to maximize the conversion of light into heat. The following describes the heating mechanisms for magnetite and gold materials, focus of this work [3.7, 3.9].

As mentioned in previous chapters, iron oxide particles are effective photothermal agents, although they have a low molar absorption coefficient in the NIR region [3.7]. The key factor to the temperature rise mechanism is how much light the heat mediators can absorb, determining the subsequent heat generated. Fe_3O_4 nanoparticles, when immersed in water, exhibit light absorption behavior that resembles that of a black body in the visible and NIR spectra. The real part of the complex refractive index ($n = n' + in''$) of magnetite relative to water ($n' \geq 1.6$) facilitates transparency and moderate refractive power [3.10]. On the other hand, for MNPs the value of $n'' \approx 0.4$ (relative to water), is low, but significant as it allows a high penetration of the electromagnetic waves into the material at the same time as increasing energy absorption [3.10, 3.11].

Furthermore, it should be noted that the behavior of magnetite is not as influenced by wavelength in the visible and near-infrared ranges. This can be seen in its absorption cross-section, which tends to remain constant without showing Mie resonances [3.10, 3.11].

To conclude with MNPs as photothermal agents, it is worth noting that other studies justify the use of magnetic nanoparticles, arguing that their molar absorption coefficient improves when they are clustered in a controlled manner due to their magnetic character. This results in higher absorption of specific radiation, as well as much more efficient energy-to-heat conversion compared to individual nanoparticles [3.7].

On the other hand, the mechanism of heat generation in gold particles is much better studied. In this case, a temperature rise occurs due to the phenomenon of local

surface plasmon resonance (LSPR). This effect occurs when the valence electrons of a metal oscillate at a specific resonance frequency when irradiated with a specific wavelength (Figure 3.3). Thus, photons are emitted and absorbed in all directions at the same frequency [3.12]. As a result, these photothermal agents can efficiently convert the electromagnetic energy of the exciting light into dissipated heat. In addition, it is important to note that the plasmon depends on both the size of the nanoparticles as well as their geometry. For example, spherical particles of 10 nm diameter have their LSPR at 520 nm, and particles of the same type but of larger size (100 nm) find it at 580 nm. Other types of geometries such as nanorods or nanostars stand out for having the LSPR in the NIR [3.7].

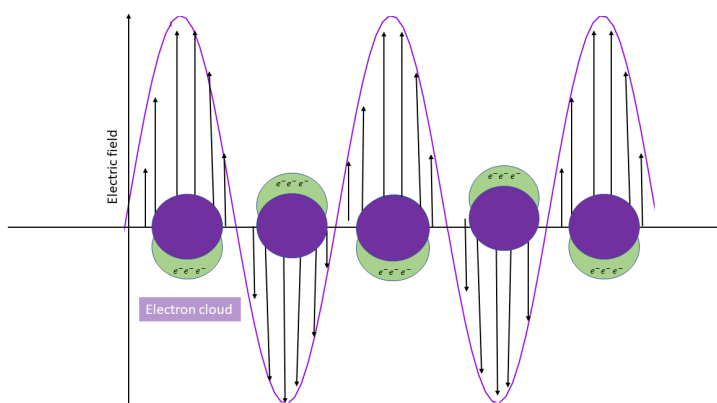


Figure 3.3: Diagram of the local surface plasmon resonant effect

3.3. Thermal evaluation

The Specific Absorption Rate (SAR) is the magnitude that determines the heating rate per unit mass of the MNPs, expressed in W/g [3.13]. As will be demonstrated throughout this doctoral thesis, it is most commonly determined experimentally from calorimetric methods. That is, from a priori known parameters of the sample, such as the mass specific heat (C_{liq}), the density of the suspension (ρ_{liq}), and the concentration (w/v) of MNPs (ϕ), as well as from the recording of the temperature increase as a function of time (dT/dt), from thermometric probes (magnetic hyperthermia) or cameras (in the case of photothermia). The expression is given by:

$$SAR = \frac{C_{liq}\rho_{liq}}{\phi} \frac{dT}{dt}. \quad (3.6)$$

Different models can be used to calculate $\frac{dT}{dt}$. The first, linear, consists of linearly

fitting the heating curve during the first 30 seconds, thus obtaining $\frac{dT}{dt}$ as the slope of the fit [3.14].

The second model uses the phenomenological Box-Lucas equation proposed in 1959. It is based on the fact that hyperthermia experiments should be performed adiabatically, with no losses to the surroundings, implying a linear increase in temperature. However, conducting such experiments is complicated, and the temperature increase does not follow a linear function with time. Therefore, the model must consider heat exchange with the medium and heat absorption from the sample support materials. To obtain reproducible results, the temperature rise of a water sample under the conditions is subtracted from the MNPs sample [3.14]. This allows an asymptotic thermal equilibrium to be reached over a prolonged period. The following expression results:

$$T(t) = (T_0 - T_{eq})e^{-\frac{t}{\tau}} + T_{eq} \quad (3.7)$$

being $T(t = 0) = T_0$ and $T(t = \infty) = T_{eq}$, and $\frac{1}{\tau}$ is the characteristic heating time [3.14]. Thus the heating rate can be defined as:

$$\left. \frac{dT}{dt} \right|_{t=0} = \frac{(T_{eq} - T_0)}{\tau}. \quad (3.8)$$

Finally, the Intrinsic Loss Power (ILP) is defined for the case of magnetic hyperthermia. It is a magnitude that allows the characteristics of the equipment to be standardized and compared with other equipment. It is defined as:

$$ILP = \frac{SAR}{H^2 f}. \quad (3.9)$$

3.4. Low-frequency magnetic rotating fields

This section ends with considerations on the application of rotating magnetic fields, in this case of low frequency (approximately 0.1 to 5 kHz) [3.15], a technique that does not seek a local temperature increase.

For this purpose, it is necessary to design equipment capable of rotating nanometric particles. Then, systems of magnets or electromagnets are designed to enable the trapping and movement, both translational and rotational. This technique, much less developed than the two previous ones, is very promising for magnetomechanical action. The aim is that, by applying rotating fields to anisotropic MNPs or those that are prone to self-assembly in chains or aggregates, it is possible

to provoke movements of the particles, eventually inside cells, disturbing the cell cytoplasm and possibly destroying it [3.16, 3.17]. Another possibility is the use of such rotating fields to enhance the diffusion of transported drugs in MNPs [3.15].

3.5. Experimental methods

Magnetic hyperthermia device

The magnetic hyperthermia device was designed in the research group, allowing sweeps of frequency and field strength by varying the system parameters. The system consists of a user-switchable coil for the application of the magnetic field and a series of capacitors to vary the frequency of the latter.

The maximum alternating current flowing through the coil can be up to 40 A. To minimize the effect of Joule heating on the samples, the coils are constructed of copper tubing and water from a thermostated bath is pumped through the coil as the current passes through.

The field frequency is determined by the resonant frequency of a parallel LC circuit, with the device having a capacitor bank that allows frequencies between 100 and 300 kHz to be selected (Figure 3.4A). The sample is placed centered within the coil and the thermostatic bath at a specified temperature so that the operating temperature of the coil does not exceed $20 \pm 1^\circ\text{C}$.

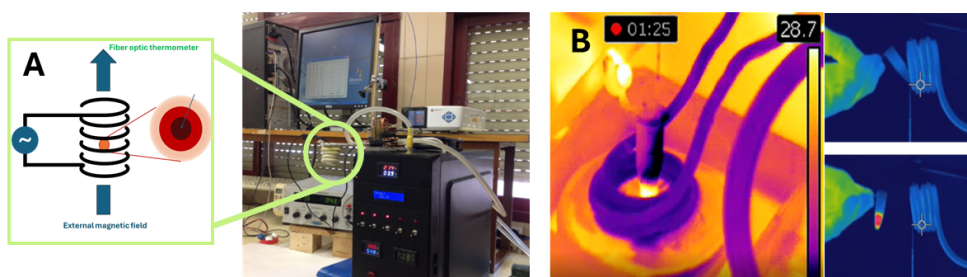


Figure 3.4: Experimental device to carry out magnetic hyperthermia experiments (A). Thermographic camera images taken of the samples (B).

The temperature increase in the sample can be recorded using fibre optic sensors with a resolution of 0.01°C , and the use of thermal imaging cameras is also possible. The use of fibre optic sensors or IR cameras are essential as they are not affected by the induced magnetic field, unlike conventional thermocouples, which are usually sensitive to electromagnetic fields. Figure 3.4B , centre and right, shows some thermal images of the experiment.

The research group has several alternating field generation devices, both desktop and portable, for use in *in vitro* systems, such as the experiments performed in this doctoral thesis, but which could also be used for *in vivo* assays. Some of the devices described are shown in Figure 3.5.

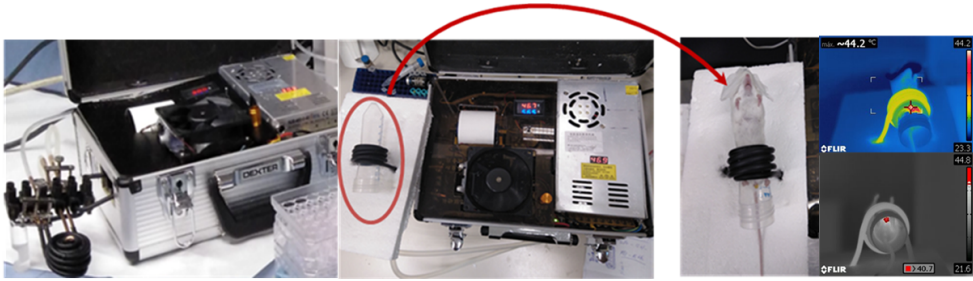


Figure 3.5: Portable device to perform magnetic hyperthermia *in vitro* and *in vivo*.

Photothermia setup

Two types of devices were used to perform the photothermia experiments. The first, simpler, was used for photothermal characterization of the samples. This system consists of an infrared laser of 850 nm and 1.6 W, which irradiates from above towards a support where an Eppendorf tube with the sample is located (Figures 3.6A, B). It is also possible to irradiate with wavelengths in the visible spectrum and lower power, using an RGB laser with the following characteristics: $\lambda_{red}=638$ nm (100 mW), $\lambda_{blue}=450$ nm (100 mW) and $\lambda_{green}=505$ nm (100 mW) (RGB Combined White Laser, Laserland, China). In both cases, the temperature is measured with a thermal camera (Flir, USA), which records the temperature every 0.0625 s with an accuracy of 10^{-6} °C, and the laser power can be adjusted as desired.

The second device, used in *in vitro* experiments, consists of a set of six lasers, arranged in such a way that they can be directed to a 96-well cell culture plate. This system reduces the application time in these experiments by a factor of six compared to a single sample. Moreover, the device has a microcontrolled system that enables the programming of the experiment in real time.

This whole setup is placed in a thermostatic chamber at 37°C to maintain optimal cell culture conditions. The temperature of the irradiated wells is controlled from above with the same thermal chamber mentioned above. Figures 3.6C and D, show the multi-laser device and the arrangements for the *in vitro* experiment.

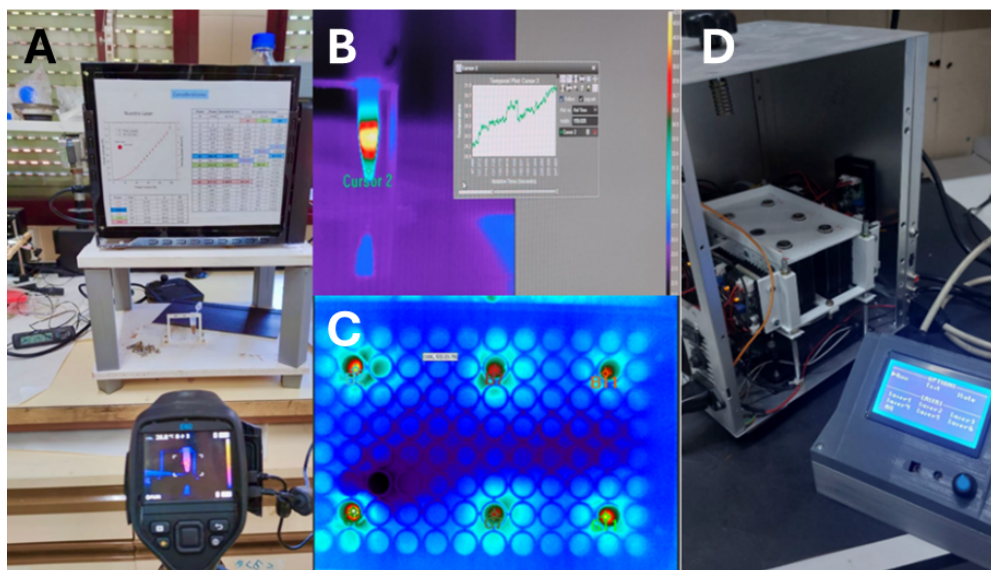


Figure 3.6: Experimental devices to carry out photothermia experiments as part of the characterization of a sample (A, B), and *in vitro* (C, D).

Finally, it is worth mentioning that magneto-photothermal device also was designed for performing dual therapy determinations. It consists of two devices similar to those previously described for magnetic hyperthermia and photothermia, which are coupled and work simultaneously (Figure 3.7A). The temperature is measured through an orifice arranged in the center of the coil, as can be seen in Figure 3.7B. The temperature measurement is performed with an infrared camera similar to that of the independent photothermia experiments.

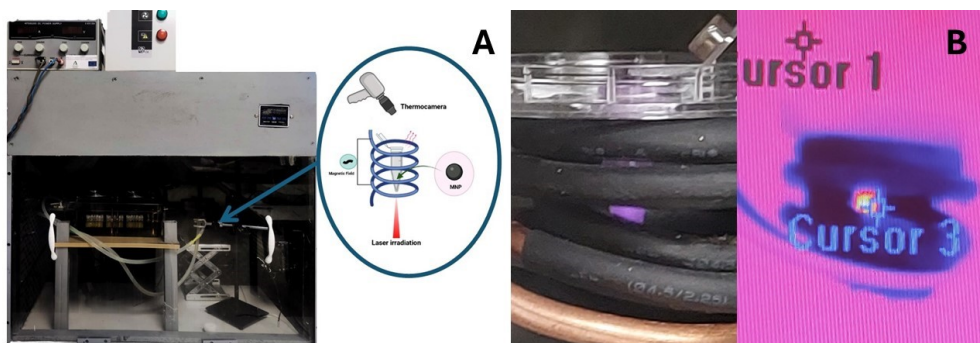


Figure 3.7: Experimental devices to carry out dual therapy assays. Figure created with BioRender.com.

Low-frequency rotating magnetic fields

Two different systems were designed for the application of low frequency rotating magnetic fields. The one used for this work consists of four permanent NIB magnets placed opposite to each other. The magnets, of opposite polarities, rotate around the sample at a speed preset by the user (Figure 3.8 A, B). The synchronized rotation of the magnetic field induces a corresponding rotation of the magnetic particles within the sample producing a mechanical torque 3.8B. The intensity of this magnetic field at the point where the sample is placed is 65 mT and the speed can be controlled up to a maximum of 300 rpm.

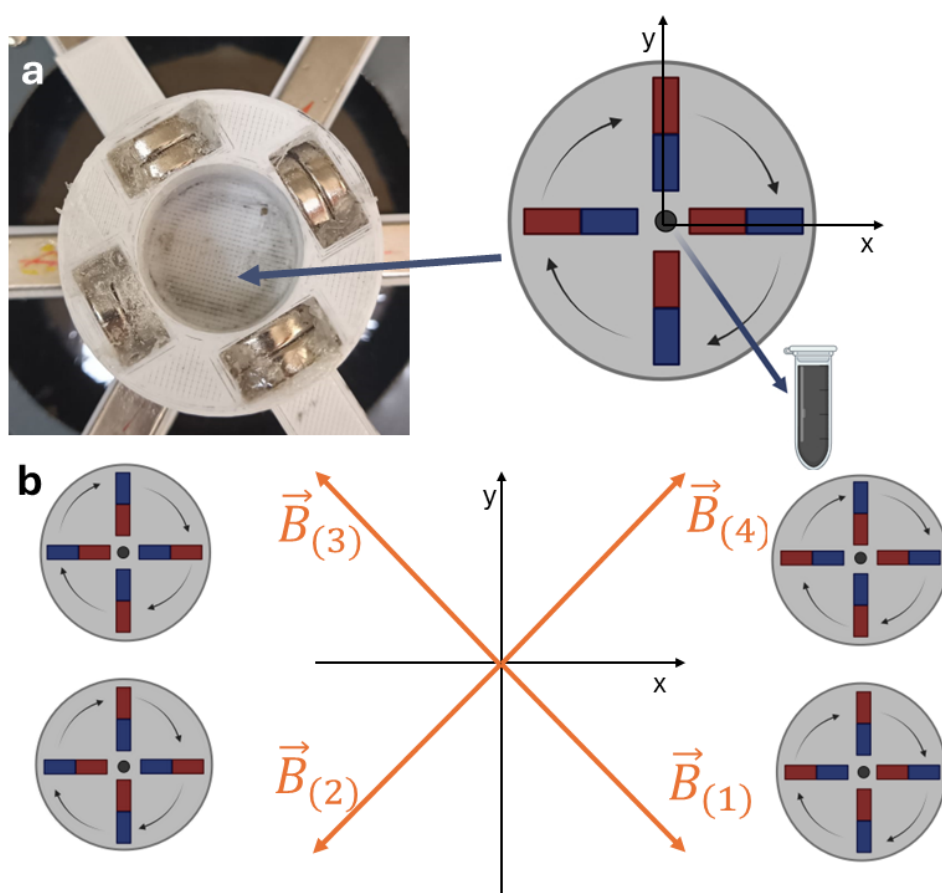


Figure 3.8: Experimental device to carry out low-frequency magnetic rotating field assays (A). Plot of the direction of the magnetic field at different positions (B).

The other device designed in the group consists of four coils fed by signal amplifiers that produce sine or square fields depending on the excitation source. The signal supplied to the amplifiers is phase shifted at will by the user and allows to

control the direction of the field in the sample. This device is designed not only to apply magnetic fields to samples, but also to allow their visualisation through an optical microscope. The use of coils makes it possible to turn the magnetic field on and off at will. Figures 3.9A,B show two designed prototypes (6 and 4 coils) and a series of images of the rotation observed in a sample of magnetic nanoparticles (Figures 3.9 C).

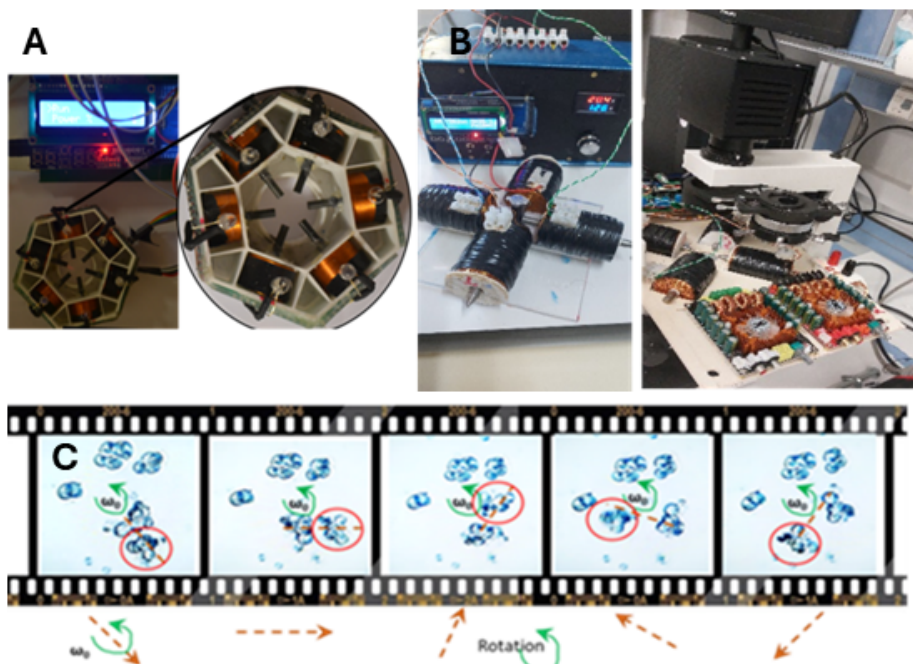


Figure 3.9: Experimental devices to carry out low-frequency magnetic rotating field assays with 6 coils (A) and 4 coils (B). Example of images obtained from particle rotation (C).

Bibliography

- [3.1] RK Gilchrist, Richard Medal, William D Shorey, Russell C Hanselman, John C Parrott, and C Bruce Taylor. Selective inductive heating of lymph nodes. *Annals of Surgery*, 146(4):596–606, 1957.
- [3.2] Andreas Jordan, P Wust, H Fählin, W John, A Hinz, and R Felix. Inductive heating of ferrimagnetic particles and magnetic fluids: physical evaluation of their potential for hyperthermia. *International Journal of Hyperthermia*, 9(1):51–68, 1993.
- [3.3] Daniel Ortega and Quentin A Pankhurst. Magnetic hyperthermia. *Nanoscience*, 1(60):e88, 2013.
- [3.4] Cindi L Dennis and Robert Ivkov. Physics of heat generation using magnetic nanoparticles for hyperthermia. *International Journal of Hyperthermia*, 29(8):715–729, 2013.
- [3.5] William J Atkinson, Ivan A Brezovich, and Dev P Chakraborty. Usable frequencies in hyperthermia with thermal seeds. *IEEE Transactions on Biomedical Engineering*, (1):70–75, 1984.
- [3.6] Rudolf Hergt and Silvio Dutz. Magnetic particle hyperthermia—biophysical limitations of a visionary tumour therapy. *Journal of Magnetism and Magnetic Materials*, 311(1):187–192, 2007.
- [3.7] Joan Estelrich and Maria Antònia Busquets. Iron oxide nanoparticles in photothermal therapy. *Molecules*, 23(7):1567, 2018.
- [3.8] Ralph Weissleder. A clearer vision for in vivo imaging. *Nature Biotechnology*, 19(4):316–317, 2001.
- [3.9] Jilian R Melamed, Rachel S Edelstein, and Emily S Day. Elucidating the fundamental mechanisms of cell death triggered by photothermal therapy. *ACS Nano*, 9(1):6–11, 2015.

- [3.10] Héctor Rodríguez-Rodríguez, Gorka Salas, and J Ricardo Arias-Gonzalez. Heat generation in single magnetic nanoparticles under near-infrared irradiation. *The Journal of Physical Chemistry Letters*, 11(6):2182–2187, 2020.
- [3.11] Alejandro G Roca, José Francisco López-Barbera, Aritz Lafuente, Fatmahan Özel, Elvira Fantechi, Javier Muro-Cruces, Miryana Hémadi, Borja Sepúlveda, and Josep Nogués. Iron oxide nanoparticles (Fe_3O_4 , $\gamma\text{-Fe}_2\text{O}_3$ and FeO) as photothermal heat mediators in the first, second and third biological windows. *Physics Reports*, 1043:1–35, 2023.
- [3.12] Mohammad Zaki Ahmad, Sohail Akhter, Ziyaur Rahman, Shabib Akhter, Mohammed Anwar, Neha Mallik, and Farhan Jalees Ahmad. Nanometric gold in cancer nanotechnology: current status and future prospect. *Journal of Pharmacy and Pharmacology*, 65(5):634–651, 2013.
- [3.13] Elio Alberto Perigo, Gauvin Hemery, Olivier Sandre, Daniel Ortega, Eneko Garaio, Fernando Plazaola, and Francisco Jose Teran. Fundamentals and advances in magnetic hyperthermia. *Applied Physics Reviews*, 2(4), 2015.
- [3.14] Beatriz Sanz, M Pilar Calatayud, Nicolás Cassinelli, M Ricardo Ibarra, and Gerardo F Goya. Long-term stability and reproducibility of magnetic colloids are key issues for steady values of specific power absorption over time. *European Journal of Inorganic Chemistry*, 2015(27):4524–4531, 2015.
- [3.15] Silvia Nappini, Francesca Baldelli Bombelli, Massimo Bonini, Bengt Nordèn, and Piero Baglioni. Magnetoliposomes for controlled drug release in the presence of low-frequency magnetic field. *Soft Matter*, 6(1):154–162, 2010.
- [3.16] Yu Cheng, Megan E Muroski, Dorothée CMC Petit, Rhodri Mansell, Tarun Vemulkar, Ramin A Morshed, Yu Han, Irina V Balyasnikova, Craig M Horbinski, Xinlei Huang, et al. Rotating magnetic field induced oscillation of magnetic particles for in vivo mechanical destruction of malignant glioma. *Journal of Controlled Release*, 223:75–84, 2016.
- [3.17] Andrew O Fung, Vishal Kapadia, Erik Pierstorff, Dean Ho, and Yong Chen. Induction of cell death by magnetic actuation of nickel nanowires internalized by fibroblasts. *The Journal of Physical Chemistry C*, 112(39):15085–15088, 2008.

Part III

Results and discussion

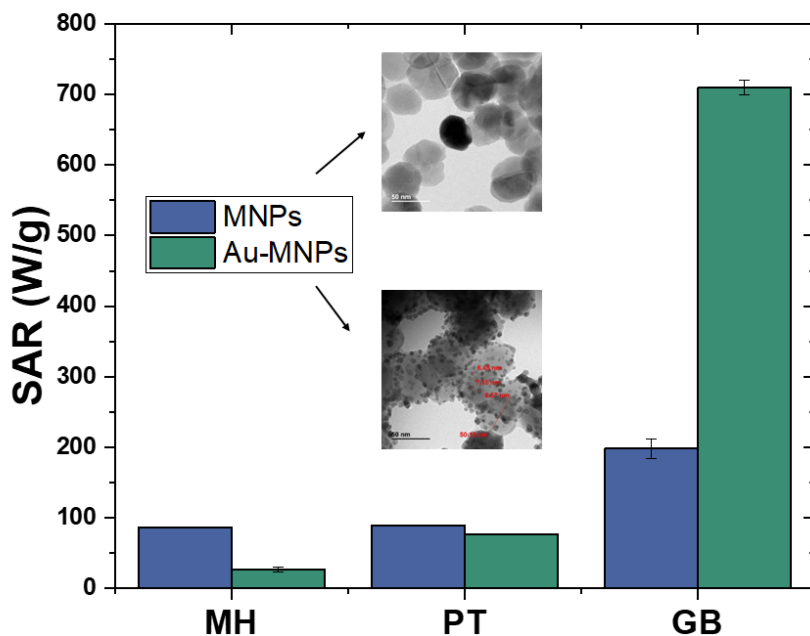
Chapter 4

Magneto-photothermal synergy applied to gold-coated magnetic nanoparticles

M. Lázaro, ÁV. Delgado, GR. Iglesias, *J. Magn. Magn. Mater.* **2024**, *591*, 171718.

Abstract

In this work, we describe the synthesis of magnetic nanoparticles with a suitable size for easy cellular internalization, avoiding their rapid renal excretion (less than 5 nm) and accumulation in the liver (more than 100 nm). The nanoparticles are functionalized with a biocompatible polymer (low molecular weight, branched polyethylenimine, PEI), and this treatment allows their functionalization with a shell of gold particles in order to improve their ability to absorb electromagnetic radiation in the visible and near infrared wavelength regions. As a result, the magnetic nanostructures are potential agents of local heating (hyperthermia) by exposing them to alternating magnetic fields (magnetic hyperthermia) or to light of the suitable wavelength (photothermia). Magnetic hyperthermia experiments demonstrate that both types of particles can reach the desired temperature range for cell apoptosis, with the difference of a shorter time needed when gold is absent. The released thermal energy is measured by the SAR (specific absorption rate, in W/g), and the values found are promising, up to 600 W/g in the case of uncoated particles. Regarding the photothermia response under the IR radiation, it is comparable for gold-coated and uncoated magnetic particles, but it is enhanced by a factor of almost 10 when the incident light is visible (blue-green) and the particles are provided with their gold shell. Improvements related to the selection of gold particles with resonant absorbance in the infrared are under investigation.



4.1. Introduction

The special properties of magnetic nanoparticles (MNPs) have made them an object of intense investigation during the last decades. Interest has been accentuated by their many applications, particularly, but not exclusively, in the biomedical field. Uses ranging from contrast agents in magnetic resonance imaging [4.1–4.3] or magnetic particle imaging [4.4, 4.5], in magnetic particle spectroscopy for the characterization of materials [4.6–4.9], to the design of drug vehicles or controlled drug release nanostructures [4.10–4.14], or to the production of local temperature increase by the action of alternating magnetic fields (hyperthermia [4.15–4.17]) or of IR lasers (photothermia [4.18–4.21]) have been deeply studied. Less developed but equally exciting is their application as an option to surgical nerve grafting in neuroscience [4.22], or to the detection and separation of proteins [4.23], or their catalytic properties [4.24].

Some of these properties are focussed on their potential use in cancer treatment. As it is well known, solid tumors have a disorganized and compact vascular structure, as well as an accelerated metabolism, performing quick mitosis [4.25]. Therefore, heat generated in the tumor for any reason is difficult to dissipate, with the additional feature of tumor cells that they can undergo apoptosis in direct response to heating in the temperature range 40–48 °C, although the optimum interval has been proposed to be between 42 and 46 °C [4.26].

As mentioned, one of the proposed therapies based on temperature elevation is called magnetic hyperthermia: when an alternating magnetic field (AMF) of suitable frequency and amplitude is applied to a suspension of MNPs, heat is generated which increases the temperature of the suspension. This results in the death of tumour cells [4.27, 4.28], which, as mentioned above, are more sensitive to this increase in temperature than healthy cells [4.29]. Mechanisms by which energy losses occur and produce have been widely investigated. For highly anisotropic particles and moderate to low fields (precisely in the range of fields applied in hyperthermia) the so-called linear response theory (LRT) is applicable [4.7, 4.8]. In this model, it is supposed that the magnetization is linearly dependent on the field, but the susceptibility is a complex quantity, as the finite time needed for the magnetic moment to revert under the action of the field means a phase lag between \mathbf{M} and \mathbf{H} [4.30–4.33]. This is equivalent to a finite-area hysteresis cycle, hence a release of energy in the form of heat. This is the Néel mechanism, but in our case, we will be dealing with non-interacting particles in suspension in a fluid, where they are somewhat free to move or rotate when acted by the field, subject to the viscous friction with the fluid. This is known as Brown relaxation; in the first phenomenon the energy is transmitted to the lattice being absorbed by phonons, whereas in the case of Brown relaxation, heat is transferred directly to the fluid by the viscous friction on the surface of the particle [4.30–4.33]. Broadly speaking, Néel relaxation dominates for small particles (characteristic size

$R < 18$ nm), while Brown relaxation prevails for larger ones ($R > 22$ nm) [4.34].

MNPs either bare or, more often, properly coated, can produce local heating through an entirely different mechanism, widely known as photothermia. Numerous studies have been carried out using various types of nanoparticles in this technique, based on iron oxide particles with different coatings such as PEG [4.35, 4.36], silica [4.37, 4.38] or others [4.39–4.41]. It is also important to note that not only iron oxides can act as photothermal agents, but other entities such as carbon nanostructures [4.42], quantum dots [4.42, 4.43] or photoluminescent nanoparticles doped with rare earth ions have been extensively studied [4.44].

Typically, MNPs become photosensitive materials when they are coated with metallic particles capable of absorbing light of a certain wavelength, subsequently releasing energy in the form of heat, contributing again to tumor cell death. In recent years, numerous studies have been carried out with different conducting coatings, particularly gold-covered MNPs in different forms: with a gold layer [4.21, 4.45, 4.46], in the form of Janus MNPs [4.47, 4.48] and in other types of nanosystems that implement both materials [4.49]. Other metals that have been studied in photothermia include a layer of silver or a combination of gold and silver on MNPs [4.50, 4.51]. These coatings may provide the additional advantages of biocompatibility, optimal optical properties, and high absorption efficiency. The latter has been related to the surface plasmon resonance (SPR) phenomenon: photons are emitted and absorbed at the same frequency in all directions [4.19, 4.52–4.54], and therefore, gold-coated particles are capable of effectively converting the electromagnetic energy of the light excitation into dissipated heat.

The heating achieved inside the tumour is determined by the specific absorption rate (SAR, usually expressed in W/g), which is a measure of the released energy per unit time and per unit mass of MNPs when exposed to the AMF. The SAR depends on the environment, extrinsic parameters such as the frequency and amplitude of the applied field, medium viscosity, as well as on the characteristics of the particles themselves: anisotropy energy, rate of magnetic relaxation, stability, or saturation magnetization [4.55, 4.56]. Some of the most relevant parameters will be discussed below.

The MNPs of interest for use inside living organisms are in a size range around 15–100 nm, given the capillary size and considering the tumour enhanced permeability and retention effect (EPR). In general, it is preferred to use particles smaller than 100 nm, in order to approach the single-domain condition, to have a lower tendency to sedimentation, and, at the same time, improved tissue diffusion and higher effective surface areas [4.24].

The mentioned approach based on the combination of MNPs with metallic coatings, adding an optical response to the magnetic one [4.41, 4.45–4.47, 4.49, 4.57] is particularly interesting, as it enables the independent or simultaneous application

of both stimuli. This, in turn, makes it possible to reduce the safe limits used in magnetic hyperthermia and photothermia for application on the human body. In addition, the nanoparticles presented in this study are within the previously mentioned ideal size range for biological application (70 nm). Consequently, their combination with gold makes them multifunctional nanoparticles. The advantages of the combined application of magnetic hyperthermia and photothermia have been little explored, mainly with the purpose of reducing well below admitted safety limits the strength of the applied external fields. The purpose of this work is the synthesis and characterization of MNPs (magnetite/maghemite) and to explore their use in magnetic hyperthermia and photothermia procedures. Additionally, we describe the preparation of composite MNP/gold nanostructures. For this purpose, a biocompatible polymer (polyethylenimine) is incorporated into the synthesis process, which in addition prevents the formation of large aggregates and can make the system biocompatible, due to the low cytotoxicity offered by the low molecular weight and branched structure of the polyethylenimine [4.58].

All of them will be characterized in terms of size, shape, electrical surface state, magnetization and finally they will be tested regarding the specific heating power that they can achieve when subjected to alternating magnetic fields or to lasers in the visible and near IR regions of the electromagnetic spectrum. While magnetic hyperthermia with iron oxide nanoparticles has been widely investigated before, the same phenomenon when the particles are coated by metallic gold nanoparticles has been less studied. Likewise, the photothermia of the magnetic particles alone or in combination with the gold coating is also a less investigated methodology. The consequences on the thermal response of the bare or coated particles under any of the excitations described, on the applicability of these nanostructures will also be addressed.

4.2. Materials and methods

Materials

All reactants used were commercially available: iron (II) sulphate heptahydrate ($\text{FeSO}_4 \cdot 7\text{H}_2\text{O}$), potassium nitrate (KNO_3), sodium hydroxide (NaOH), branched polyethyleneimine (PEI, $M_w \approx 2000$ g/mol), chloroauric acid (HAuCl_4), sodium citrate tribasic dihydrate ($\text{HOC}(\text{COONa})(\text{CH}_2\text{COONa})_2 \cdot 2\text{H}_2\text{O}$), sodium borohydride (NaBH_4) were purchased from Sigma-Aldrich (Saint Louis, MO, USA). The water used was deionized and filtered through a 0.2 μm filter in a Milli-Q Academic equipment (Millipore, Spain).

Methods

Synthesis of gold-coated magnetic nanoparticles

In order to achieve the coating by gold, the originally negative surface obtained from magnetite NPs synthesis had to be changed into positive. Coating with the cationic polyelectrolyte poly(ethylene imine) (PEI) was the method chosen, as will be described below. For this reason, the sample was synthesized following a procedure in which PEI coating was produced in one pot during the synthesis of the MNPs themselves [4.59]. The procedure involved the following steps: 280 mL Milli-Q water was bubbled with N_2 in a Pyrex bottle. Subsequently, in the oxygen-free environment, 1.280 g of $FeSO_4$, 10 mL of KNO_3 2 M, 0.6 g of PEI and 10 mL of NaOH 1 M were added, obtaining a green gel. 100 mL of the formed $Fe(OH)_2$ gel were heated in a closed bottle during 2 hours at 90 °C. With this, $Fe(OH)_2$ was oxidized to PEI-coated MNPs nanoparticles. Finally, the particles were magnetically decanted and redispersed in Milli-Q water several times [4.59].

It is worth mentioning that using PEI as coating prevents the formation of large aggregates by electrosteric repulsion between particles. Furthermore, the choice of this polymer (PEI, low molecular weight and branched) is justified, as it makes the nanoparticles fulfil the double objective of setting a positive charge on the particles, while they remain non-toxic [4.58].

For gold-coating of the MNPs, gold nano-spheres were first synthesized as follows: 0.1 mL of $HAuCl_4$ 0.05 M were mixed with 0.5 mL of 0.01 M Na-citrate solution, adding 18 mL of Milli-Q water under stirring. Then 0.5 mL of 0.1 M $NaBH_4$ freshly prepared in an ice bath was added. Afterwards the solution was left in a thermostatic bath at 30 °C for 15 minutes [4.60].

Subsequently, the MNPs suspension was coated with gold seeds. For that purpose, the gold particles suspension was diluted by adding 10 mL of water to 30 mL of the suspension. Then, 20 mL of 0.25 mg/mL MNPs were added dropwise to the diluted gold seeds under ultrasonication. The resulting suspension was further ultrasonicated for 15 minutes and left unperturbed for 30 minutes. Finally, the particles were decanted, and redispersed in 2 mL of Milli-Q water [4.60].

HRTEM Characterization: Morphology

The morphology and size of the particles was determined using a high-resolution transmission electron microscope (HRTEM) (Thermo Fisher Scientific TALOS F200X, USA), provided by the CIC-UGR Microscopy Service. The radii of the nano-spheres were determined using JImage software (University of Wisconsin, Madison, WI, USA).

Electrophoretic mobility

The measurement of the electrophoretic mobility of dilute MNP suspensions were carried out using a Zetasizer Nano-ZS (from Malvern Instruments, Worcestershire, UK). This same instrument also allowed to evaluate the hydrodynamic diameter through Dynamic Light Scattering (DLS) measurements.

Structural Characterization

The structural characterization of the sample was performed by X-ray powder diffraction (XRD) with a Bruker D8 Advance diffractometer (Berlin, Germany) equipped with a Bruker LINXEYE detector and a $\text{CuK}\alpha$ radiation source. Micro-Raman spectroscopy was performed using a JASCO NRS-5100 Dispersive Micro-Raman (Tokyo, Japan) equipped with a green diode laser of 532 nm, with 30 mW power (Elforlight G4-30; Nd: YAG), and a spectral range of 50 to 8000 cm^{-1} .

Thermogravimetric analysis

In order to estimate the thickness of the PEI layer, a thermogravimetric evaluation was carried out on the PEI/MNPs nanostructures. Weight variations were measured in a Mettler Toledo (Switzerland) differential scanning calorimeter, in a nitrogen atmosphere, at 10.0 °C/min, up to 950 °C.

Magnetic properties

Magnetization cycles were measured at room temperature using an AC Hyster Series magnetometer (Spain). This device operates at a frequency of 1 kHz and is capable of applying magnetic field strengths (H), within the range of -1.5 to +1.5 kOe (-119.4 to +119.4 kA/m, $\mu_0\text{H}$ from -150 to 150 mT).

Optical absorbance

UV/VIS optical absorbance of the samples was determined with a Jenway Series 67 (UK) spectrophotometer, working in the range 190-1100 nm, using a quartz cuvette with 1 cm path length.

Magnetic hyperthermia

The magnetic hyperthermia device has been designed in the group's laboratory [4.61, 4.62] and allows for performing frequency and field sweeps (100-200 kHz and 12-24 kA/m) by varying circuit parameters. It consists of a double four-turn coil 24.90 ± 0.05 mm in diameter, made of copper tube, and an AC current generator. A ferrite nucleus is placed below the sample to increase the field. Cooling water at 20°C from a thermostatic bath is circulated in the copper tube during the experiment; this is important, since Joule heating can be very significant (currents as high as 40 A are passed through the coil) and could easily mask any temperature changes associated with true magnetic hyperthermia.

To perform magnetic hyperthermia experiments, an Eppendorf tube containing the sample (200 μL) is placed in the center of the coil on top of the ferrite bar. Field strength and frequency measurements at this point are determined with a NanoScience Laboratories Ltd. Probe (UK), with 10 μT instrumental sensitivity. Sample and bath temperatures are recorded using two optical fiber sensors (Optocon AG, Germany) every 3 seconds with 0.01°C resolution.

Photothermia

The device used to perform photothermia consists of an infrared laser (850 nm, 1 W power) pointing towards the support where the Eppendorf with the sample (200 μL) is located. A thermal imaging camera (Flir, USA) capable of taking temperature measurements every 0.0625 s with a resolution is used to record temperature changes. In order to compare with the results obtained from optical absorbance determinations, less powerful red, green, and blue lasers (RGB Combined White Laser, Laserland (China)), with $\lambda_{red} = 638$ nm (100 mW), $\lambda_{blue} = 450$ nm (100 mW), and $\lambda_{green} = 505$ nm (100 mW) were also used [4.63].

Thermal efficiency evaluation

As mentioned above, the most useful parameter for reporting magnetic heating properties is the Specific Absorption Rate (SAR), calculated as:

$$SAR = \frac{C_{liq}\rho_{liq}}{\phi} \frac{dT}{dt} \quad (4.1)$$

where C_{liq} and ρ are, respectively, the mass specific heat and the density of the magnetic carrier suspension. ϕ is the mass concentration of MNPs, and $\frac{dT}{dt}$ is the rate of temperature increase in the sample [4.57]. This heating rate can be calculated following two different procedures.

The first method consists of determining it as the slope of the initial linear portion (typically, the first 20 s of heating) of the heating curve. The Box-Lucas method provides another way to calculate the slope [4.64]. In this case, the equation for the non-adiabatic temperature increase is given by:

$$T(t) = (T_0 - T_{eq})e^{\frac{t}{\tau}} + T_{eq} \quad (4.2)$$

where $T_0(T_{eq})$ is the initial (final, steady) temperature, and τ is a characteristic time. From this, the slope is now calculated as:

$$\frac{dT}{dt} = \frac{T_{eq} - T_0}{\tau}. \quad (4.3)$$

4.3. Results and discussion

Size and shape characterization

To carry out a geometrical characterization of the nanoparticles, the images obtained from HRTEM in Figure 4.1 were analyzed by measuring diameters of at least 150 nanospheres (the size distribution histogram is plotted in Figure 4.2). The value obtained (mean diameter \pm S.D.) was 70 ± 12 nm for polymer-coated MNPs. Pictures show their quasi-spherical geometry. It can also be observed some particle aggregation unavoidable in the process of drying for HRTEM. Moreover, it should be noted that gold nanoparticles are very uniform in size, with their radius determined by DLS being 6.00 ± 0.10 nm.

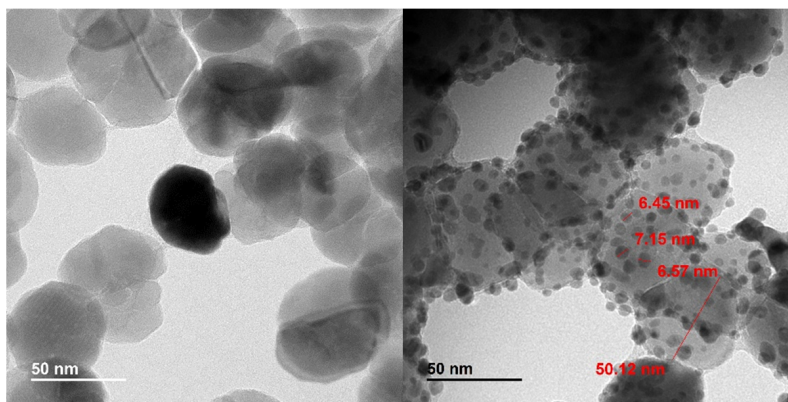


Figure 4.1: HRTEM images of MNPs before (left) and after (right) gold coating.

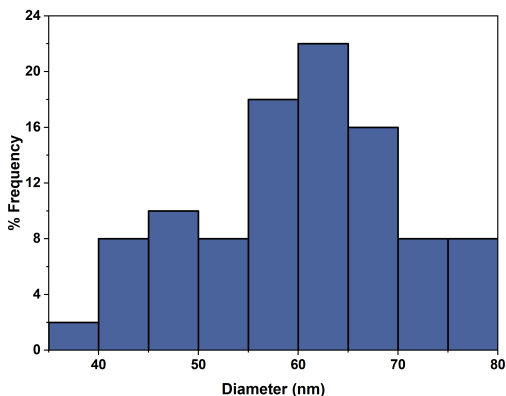


Figure 4.2: Size distribution of PEI-coated MNPs.

Structural characterization

The XRD pattern of the MNPs obtained (Figure 4.3a) corresponds very well with that of magnetite. However, since the diffraction patterns of the two main magnetic iron oxides, magnetite and maghemite, are very similar, they cannot be differentiated by this technique, so our particles might instead be maghemite or a mixture of the two phases. A possible procedure for distinguishing between them (XPS can also be mentioned) is Raman spectroscopy. Figure 4.3b shows the results: by comparing the spectra obtained with those of the RRUFF database [4.65], we can establish correlations between the 276, 385, and 496 cm^{-1} peaks and those of magnetite (at 283, 376, and 502 cm^{-1} , RRUFF ID: R060656.3), given that the position of these peaks varies slightly depending on the orientation of the sample. However, it is important to note that the peak at 594 cm^{-1} shows a shift of approximately 100 cm^{-1} which could be attributed to the presence of maghemite (which is generally located around 670 cm^{-1} , RRUFF ID: R14071).

Moreover, in order to estimate the average size of crystallites (D), the Scherrer equation was applied:

$$D = \frac{K\lambda}{\beta \cos(\theta)} \quad (4.4)$$

being K a constant depending on the crystal shape (0.9 was used), λ the wavelength of X-rays (0.154 nm), β is the full width at half maximum (FWHM) of the diffraction peak, and θ the diffraction angle. Maxima with Miller indices (220), (311), (400), (422), (511), (440) were used for the calculation. The average (\pm S.D.) crystallite size was found to be 21.8 ± 2.8 nm, so that the particles are formed by 2-3 domains on average.

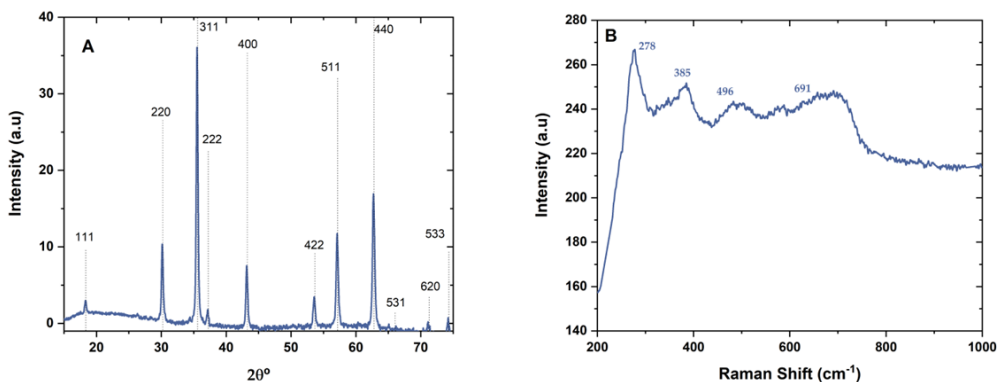


Figure 4.3: XRD (A) and micro-Raman spectroscopy (B) of PEI-coated MNPs. The dashed lines in A correspond to the x-ray diffraction data in RRUFF database [4.65]

Electrophoretic mobility

Figure 4.4 shows the electrophoretic mobility as a function of pH in water for the samples investigated. Recall that the MNPs are coated with positive PEI. For this reason, the PEI-coated MNPs show positive values for all pH values below 11 (in contrast with bare magnetite, whose isoelectric point is around $\text{pH} \approx 6$). Coating with gold nanoparticles (negatively charged) reduces the positive mobility and even changes its sign, providing additional proof of the efficient gold-coating achieved.

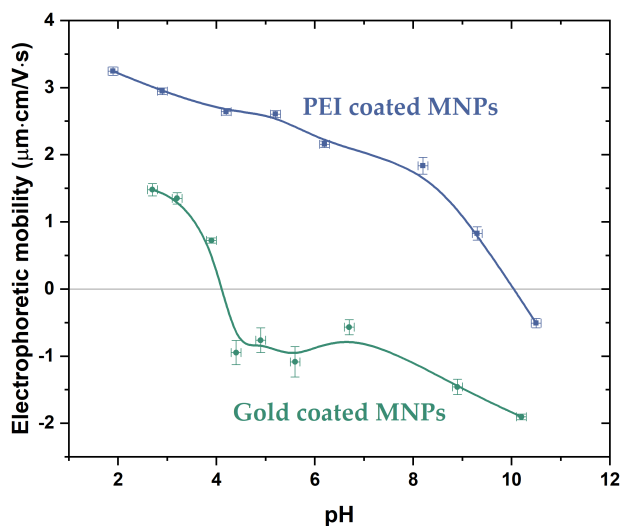


Figure 4.4: Electrophoretic mobility of PEI coated MNPs and gold coated MNPs

Thermogravimetric analysis

A thermogravimetric analysis was performed in order to estimate the percentage of polymer incorporated on the surface of the magnetic nanoparticles (Figure 4.5). It can be observed that up to 189 °C the first mass loss occurs due to the loss of water in the sample [4.66]. Then, from 189 °C to 550 °C a mass loss spread is observed, which is attributed to the degradation of the PEI [4.67]. Let us mention that the mass increase above 550 °C can be attributed to slight oxidation (0.7 mg/1.6%). Its possible causes are that the nitrogen used is 99.99% grade. Also, a large amount of mass has been used (43 mg), so it is possible that some air may have been retained between the solid particles. Taking the density of PEI as 1.08 g/cm³ and that of magnetite as 5.2 g/cm³, and assuming a radius of the composite particle of 35 nm, it is estimated that the thickness of the polymer layer is around 2.2 nm. Note that this agrees well with the few cases in Figure 4.1 where some detail of the layer can be observed (recall that the gold diameter is 6 nm).

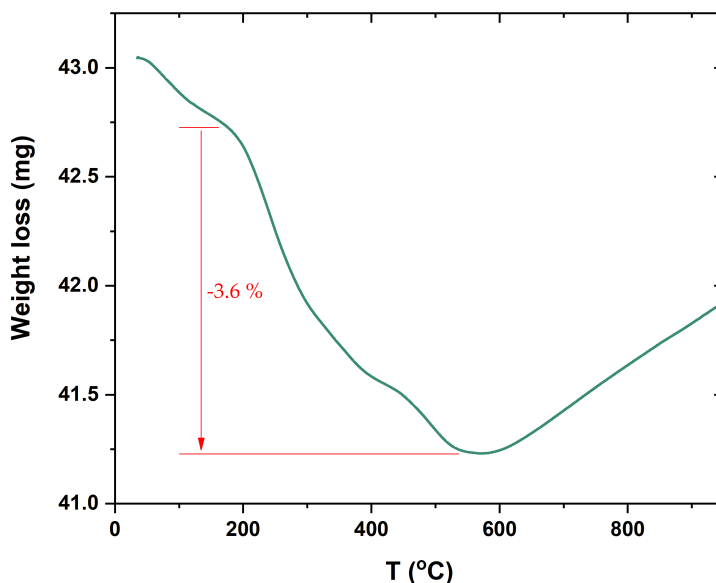


Figure 4.5: Thermogravimetric analysis of polymer-coated MNPs

Magnetic characterization

The magnetic characterization of the particles was carried out by AC magnetometry, since, despite providing magnetic saturation values slightly lower than

those obtained by other techniques (in addition to the opening in the hysteresis cycle), it allows us to perform fast and effective measurements in liquid. In Figure 4.6, it can be seen that the nanoparticles exhibit good magnetic properties, even when coated with the polymeric layer. Thus, the maximum magnetization ($M_{\max} = 81.3 \pm 2.2$ emu/g) is close to values obtained by other authors for pure magnetite nanoparticles [4.68–4.70]. Furthermore, this result, in addition to the micro-Raman spectroscopy analysis, is another proof that the nanoparticles obtained are mainly composed of magnetite, as maghemite has a lower magnetic saturation value (in bulk within the range of 56–74 emu/g [4.68, 4.71]).

For gold-coated nanoparticles, the maximum value is $M_{\max} = 36.1 \pm 1.7$ emu/g. As expected, the gold coating reduces the magnetic saturation, but we are still in the presence of sufficient magnetic response for the pursued application in hyperthermia. This reduction in the magnetization obtained has been previously observed by other authors. For example, Iglesias-Silva *et al.* [4.72] noted a decrease in the magnetization of silver-coated magnetite particles, yielding values approximately 20 times lower compared to uncoated particles. Similar results were obtained by Wang *et al.* [4.73] when studying magnetite nanoparticles coated with a gold shell, where the maximum magnetization was 66 emu/g for the uncoated particles and 15 emu/g for those with the gold shell.

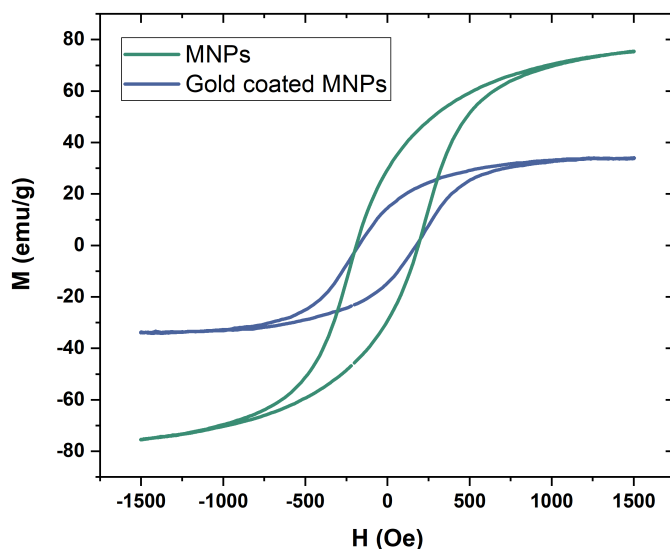


Figure 4.6: Magnetization of PEI-coated MNPs ($M_{\max} = 81.3 \pm 2.2$ emu/g) and gold-coated MNPs ($M_{\max} = 36.1 \pm 1.7$ emu/g).

In addition, the coercivity obtained is $H_c = 14.8 \pm 0.1$ kA/m for polymer coated

nanoparticles and $H_c = 15.6 \pm 0.2$ kA/m for those with gold on the surface. The higher coercivity observed in the gold-coated nanoparticles could be attributed to their slightly larger size. This could lead to less efficient coupling of magnetic dipole moments compared to PEI-coated nanoparticles [4.73]. It must be pointed out that this field is below that applied in magnetic hyperthermia experiments (23 kA/m maximum), so that the particles will not remain permanently magnetized during the heating cycles, as expected for MH. Regarding the remanence, values at 1 kHz were 29.4 ± 0.2 emu/g, and 14.5 ± 0.3 emu/g for uncoated and PEI-coated MNPs, respectively.

Optical characterization

Optical spectra (Figure 4.7) were measured for both the gold coated and uncoated samples, and with the subsequent incorporation of the nanoparticles on the surface. The plasmon resonance of the bare gold particles is well identified and located around 510 nm. In the case of the coated particles the plasmon band is only slightly appreciated, extending in the 530–620 nm range, so that the resonance is wider and red-shifted, as reported in [4.59]. The density of the coating is not high enough for a clearer expression of the gold SPR.

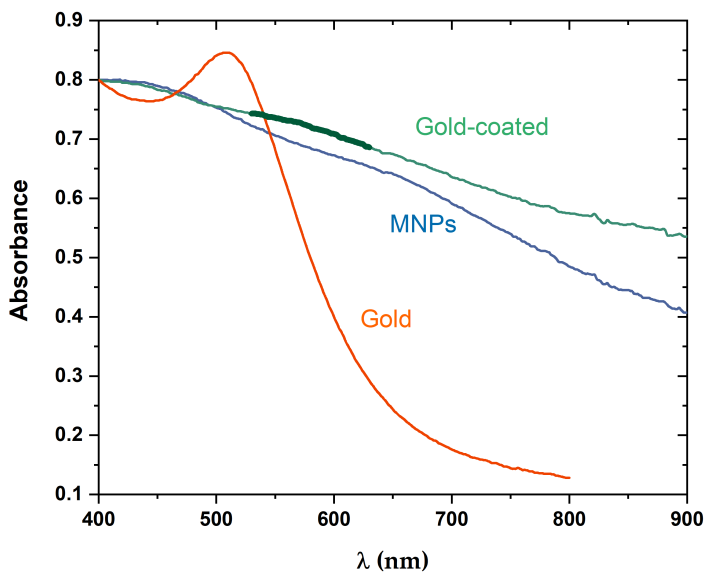


Figure 4.7: Optical absorbance spectra of PEI-coated MNPs, gold-coated MNPs, and gold nanospheres. The curvature of the absorbance of the coated samples in the 520–620 nm range of wavelengths has been remarked.).

Magnetic hyperthermia and photothermia results

In the case of magnetic hyperthermia, as a first step, we proceeded to evaluate the response of the particles with just the polymer coating. As detailed in Figure 4.8A, the maximum thermal efficiency was reached at a frequency of 150 kHz and 20 kA/m.

The thermal efficiency of nanoparticles depends on multiple factors, including magnetic anisotropy, which relies on the size, shape, arrangement, and dipolar interactions of the nanoparticles [4.56]. The SAR values obtained in this work (Figure 4.8) are comparable to those reported by other authors. For example, Nemati *et al.* [4.56] carried out a detailed study on magneto-thermal efficiency, addressing various geometries. For nanospheres ranging in size from 7 to 97 nm, they achieved a SAR of approximately 100 W/g for 52 nm spheres at 15.9 kA/m and 300 kHz. Even applying higher fields than those used in this work (63.7 kA/m and 300 kHz), they obtained comparable results, the maximum being 650 W/g [4.56]. In another analysis, Vergés *et al.* [4.74] also reported SAR values close to 100 W/g for 30 nm particles, with a frequency of 249 kHz and a magnetic field of 10 kA/m. In addition, for smaller particles (around 10 nm) SAR values around 60-240 W/g were obtained by different authors [4.75–4.79].

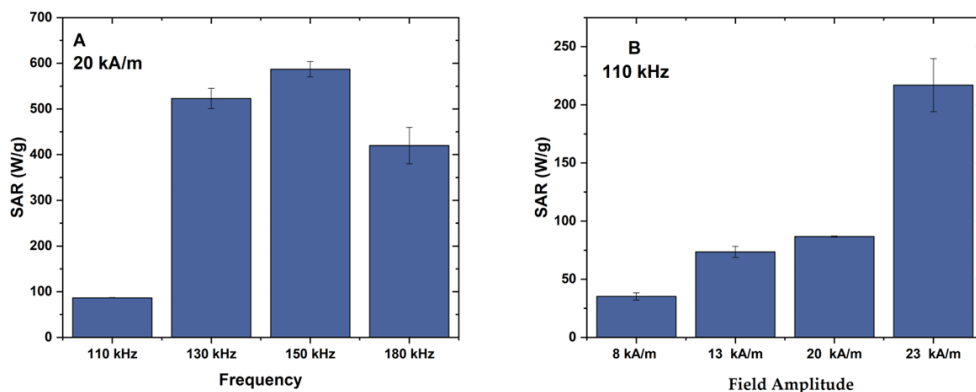


Figure 4.8: SAR determination of PEI coated MNPs at constant field amplitude (A) and at constant frequency (B).

According to the Rosensweig [4.32] thermodynamic model, assuming a Debye-type relaxation of the complex susceptibility with frequency, the power released is expected to increase with frequency until reaching a plateau. Our data in Figure 4.8A do not allow to fully confirm the model, as the SAR at 180 kHz is lower than at 150 kHz, but the decrease is modest and a qualitative agreement with Rosensweig calculations can be admitted. In any case, our device allows to reach higher fields for lower frequencies it was decided to select 110 kHz to carry out an additional magnetic field sweep. In this analysis, as expected, SAR values were found to improve significantly with the application of higher magnetic field amplitudes (Figure 4.8B), in

agreement with results published in other studies and with model predictions [4.19], since there is a quadratic dependence with magnetic field amplitude (H) according to the linear response theory (LRT) [4.32, 4.80].

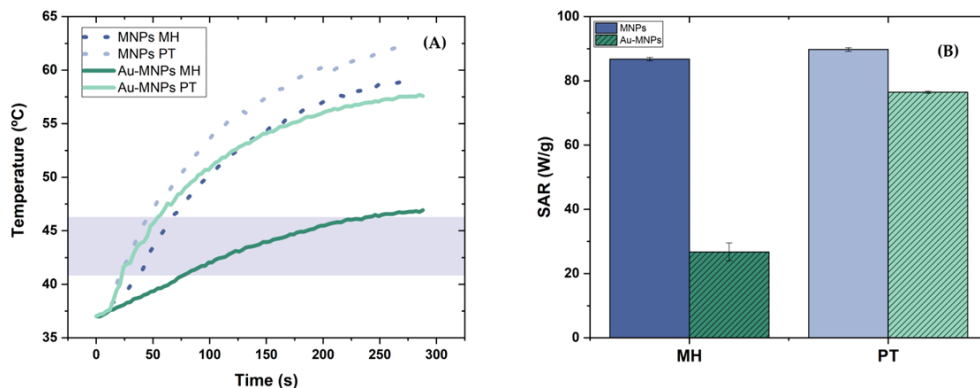


Figure 4.9: Temperature increment of PEI (“MNPs”) and gold (“Au-MNPs”) coated MNPs. (A) Magnetic hyperthermia (“MH”) under the application of 110 kHz and 20 kA/m alternating magnetic field and photothermia (“PT”) by laser irradiation of 850 nm (1 W/cm^2) power. (B) SAR values for the situations presented in (A). The particle concentration used was 10 mg/mL.

Figure 4.9A demonstrates that, although the temperature elevation achieved with gold-coated MNPs reaches the desired range for antitumor activity, it takes longer than with particles carrying the PEI shell.

In the case of magnetic hyperthermia (MH) this effect was expected considering the better magnetic response of the PEI-coated particles. This manifests in SAR calculations (Figure 4.9B) whereby a SAR value of 87 W/g (MNP-PEI) must be compared with 27 W/g (MNP-PEI-gold). These SAR estimations are comparable to results previously reported by other researchers using other types of MNPs under similar frequencies and field strengths [4.81]. Moreover, it is important to highlight that with the application of 110 kHz, and field with 20 kA/m amplitude, in both samples the hyperthermia regime is reached before 5 minutes of treatment (in the case of the sample coated with polyelectrolyte before the first 40 seconds), while keeping the field amplitude and application frequencies below safe limits for the human body [4.79]. This demonstrates the potential utility of these MNPs as MH tools, although it is true that the gold coating worsens the performance in magnetic hyperthermia, as the SAR obtained is lower. However, despite this, the magnetic hyperthermia region (42-46 °C) is still reached in less than two minutes. This is really the aim of this type of technique, i.e., reaching these temperatures while keeping the field amplitude and application frequencies below safe limits for the human body [4.8]. Furthermore, the aim of synthesising this type of hybrid nanoparticles is to be able to use them for both stimuli.

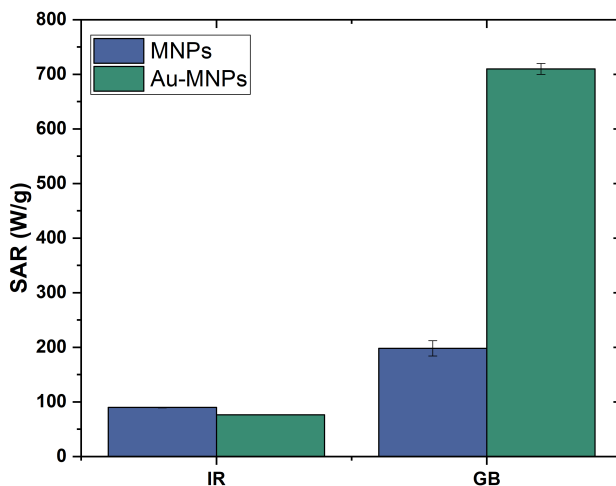


Figure 4.10: SAR determination of PEI- and gold-coated MNPs at 0.2 W laser irradiation using a NIR laser (850 nm, IR), and an RGB laser (green blue-GB, 0.65 mW of $\lambda_{green}=505$ nm, and 0.35 mW of $\lambda_{blue}=450$ nm).

Regarding results with the photothermia technique (PT, with an infrared laser of specific power 1 W/cm^2 or 0.2 W nominal power), similar temperature elevations (Figure 4.9A) and SAR values (Figure 4.9B) were achieved with both samples, although those not coated perform slightly better. This may be due to two factors: firstly, since the density of gold is considerably higher than that of magnetite, at the same nominal particle concentration, fewer nanoparticles will be present in a given volume. Secondly, and more remarkable, it is that the increase in absorbance when gold nanospheres are glued together is not observed in the NIR (Figure 4.6), but in the visible (where the surface plasmon is located). The SAR achieved in PT under IR laser (89.8 W/g in terms of total particle mass) can be rescaled using the iron mass in order to compare to published results. The result is 129 W/gFe, which is comparable to that reported by Espinosa *et al.* [4.82] for iron oxide nanospheres in similar conditions (190 W/g_{Fe}). It is when nanocubes are tested that the SAR in photothermia can reach values around 5 times higher. Results obtained for composite iron oxide/gold nanostructures (Janus geometry) were recently reported in [4.48]: in that work it was found that SAR can be as high as 18 kW/g_{magnetite+gold}, decreasing to values similar to those shown here when the iron concentration is increased above 0.3 mM (around 24 $\mu\text{g/mL}$ of iron oxide particles).

It is for this reason that particles were also irradiated with the RGB laser, with green (0.65 W) and blue (0.35 W) wavelengths (GB in Figure 4.10). Interestingly, the thermal efficiency, as measured by the SAR, increases by almost a factor 10 (in

the case of gold coating) and of 2 (PEI coating) as compared to the results under IR laser (IR in Figure 4.10). While these wavelengths are outside the first biological window [4.83], and have more limited penetration than an IR laser (up to 1 mm vs. 3 mm penetration), they may be useful for some superficial diseases [4.84]. This is the case of basal cell carcinoma cell tumours, where the overall median depth of invasion of 0.68 mm [4.85]. Furthermore, optical fibers could be used to significantly increase penetration. Alternatively, the future therapeutic use of these hybrid magnetite/gold nanoparticles in photothermia using IR could be designed with other types of plasmonic structures (gold nanorods, nanostars...), which can shift the plasmon resonance to the NIR.

4.4. Conclusions

In this work it has been described the synthesis of magnetite/maghemite nanospheres incorporating PEI in situ, with a diameter of 70 nm. In addition, it has also found feasible to incorporate gold spheres 7 nm in size, electrostatically bound to the surface of the polymer-coated magnetite. Finally, the capabilities of these MNPs as local heating tools, both in magnetic hyperthermia and photothermia, have also been tested. In the case of magnetic hyperthermia application, it has been found that, as expected, the particles without metal coating show higher efficiency for the same particle concentration. The particles are also responsive to photothermia, under the action of a near-infrared light. The gold nanoparticles shell does not significantly affect the photothermia SAR value, a result mostly related to the location of the surface plasmon resonance in the visible region of the spectrum. This explains that when irradiating with wavelengths corresponding to blue and green, SAR values almost ten times larger are obtained. Hence, for efficient irradiation with more penetrating lasers (NIR), it is necessary to shift the plasmon of the hybrid nanostructures by incorporating other types of metallic particles, with different geometries onto the MNPs.

Acknowledgements

Financial support of this investigation by Ministerio de Economía y Competitividad TED2021-131855BI00/Unión Europea Next Generation EU/PRTR. FEDER/Junta de Andalucía- Consejería de Transformación Económica, Industria, Conocimiento y Universidades, Spain (Grant No. P20_00346 and P20_00233) and Consejería de Conocimiento, Investigación y Universidad, Junta de Andalucía, Spain (A-FQM492-UGR20). European Union's Horizon 2020 research and innovation programme under the Marie Skłodowska-Curie grant agreement No 10106426.

Bibliography

- [4.1] Xianguang Ding, Haitao Zhao, Chunyan Li, Qiangbin Wang, and Jiang Jiang. All-in-one theranostic nanoplatfrom with controlled drug release and activated MRI tracking functions for synergistic NIR-II hyperthermia-chemotherapy of tumors. *Nano Research*, 12:2971–2981, 2019.
- [4.2] Nahideh Gharehaghaji and Baharak Divband. PEGylated Magnetite/Hydroxyapatite: A Green Nanocomposite for T2-Weighted MRI and Curcumin Carrying. *Evidence-Based Complementary and Alternative Medicine*, 2022(1):1337588, 2022.
- [4.3] Harald Unterweger, Christina Janko, Marc Schwarz, László Dézsi, Rudolf Urbanics, Jasmin Matuszak, Erik Órfi, Tamás Fülöp, Tobias Bäuerle, János Szebeni, et al. Non-immunogenic dextran-coated superparamagnetic iron oxide nanoparticles: a biocompatible, size-tunable contrast agent for magnetic resonance imaging. *International Journal of Nanomedicine*, pages 5223–5238, 2017.
- [4.4] Hamed Arami, Eric Teeman, Alyssa Troksa, Haydin Bradshaw, Katayoun Saatchi, Asahi Tomitaka, Sanjiv Sam Gambhir, Urs O Häfeli, Denny Liggitt, and Kannan M Krishnan. Tomographic magnetic particle imaging of cancer targeted nanoparticles. *Nanoscale*, 9(47):18723–18730, 2017.
- [4.5] Lorena Moor, Subas Scheibler, Lukas Gerken, Konrad Scheffler, Florian Thieben, Tobias Knopp, Inge K Herrmann, and Fabian HL Starsich. Particle interactions and their effect on magnetic particle spectroscopy and imaging. *Nanoscale*, 14(19):7163–7173, 2022.
- [4.6] Kai Thode, Rainer H Müller, and Mayk Kresse. Two-time window and multiangle photon correlation spectroscopy size and zeta potential analysis—highly sensitive rapid assay for dispersion stability. *Journal of Pharmaceutical Sciences*, 89(10):1317–1324, 2000.
- [4.7] Patrick Vogel, Martin Andreas Rückert, Bernhard Friedrich, Rainer Tietze, Stefan Lyer, Thomas Kampf, Thomas Hennig, Lars Dölken, Christoph Alexiou,

- and Volker Christian Behr. Critical offset magnetic particle spectroscopy for rapid and highly sensitive medical point-of-care diagnostics. *Nature Communications*, 13(1):7230, 2022.
- [4.8] Kai Wu, Jinming Liu, Vinit Kumar Chugh, Shuang Liang, Renata Saha, Venkatramana D Krishna, Maxim CJ Cheeran, and Jian-Ping Wang. Magnetic nanoparticles and magnetic particle spectroscopy-based bioassays: a 15 year recap. *Nano Futures*, 6(2):022001, 2022.
- [4.9] Kai Wu, Diqing Su, Renata Saha, Jinming Liu, Vinit Kumar Chugh, and Jian-Ping Wang. Magnetic particle spectroscopy: a short review of applications using magnetic nanoparticles. *ACS Applied Nano Materials*, 3(6):4972–4989, 2020.
- [4.10] Liron L Israel, Anna Galstyan, Eggehard Holler, and Julia Y Ljubimova. Magnetic iron oxide nanoparticles for imaging, targeting and treatment of primary and metastatic tumors of the brain. *Journal of Controlled Release*, 320:45–62, 2020.
- [4.11] Sumera Khizar, Nasir M Ahmad, Naveed Ahmed, Sadia Manzoor, and Abdelhamid Elaissari. Encapsulation of doxorubicin in magnetic-polymer hybrid colloidal particles of Eudragit E100 and their hyperthermia and drug release studies. *Polymers for Advanced Technologies*, 31(8):1732–1743, 2020.
- [4.12] Peng Mi. Stimuli-responsive nanocarriers for drug delivery, tumor imaging, therapy and theranostics. *Theranostics*, 10(10):4557, 2020.
- [4.13] Marina V Novoselova, Sergei V German, Tatiana O Abakumova, Stanislav V Perevoschikov, Olga V Sergeeva, Mikhail V Nesterchuk, Olga I Efimova, Kirill S Petrov, Vasiliy S Chernyshev, Timofei S Zatsepin, et al. Multifunctional nanostructured drug delivery carriers for cancer therapy: Multimodal imaging and ultrasound-induced drug release. *Colloids and Surfaces B: Biointerfaces*, 200:111576, 2021.
- [4.14] Chin-Hao Su, Andree Soendoro, Shinya Okayama, Fitriani Jati Rahmania, Takashi Nagai, Toyoko Imae, Kaname Tsutsumiuchi, and Noriyasu Kawai. Drug release stimulated by magnetic field and light on magnetite-and carbon dot-loaded carbon nanohorn. *Bulletin of the Chemical Society of Japan*, 95(4):582–594, 2022.
- [4.15] Michele Ammendola, Giuseppe Currò, Riccardo Memeo, Lucia Stella Curto, Maria Luposella, Valeria Zuccalà, Patrick Pessaux, Giuseppe Navarra, Cosmo Damiano Gadaleta, and Girolamo Ranieri. Targeting stem cells with hyperthermia: Translational relevance in cancer patients. *Oncology*, 98(11):755–762, 2020.

- [4.16] Jobin Jose, Rajesh Kumar, Seetha Harilal, Githa Elizabeth Mathew, Della Grace Thomas Parambi, Ankitha Prabhu, Md Sahab Uddin, Lotfi Aleya, Hoon Kim, and Bijo Mathew. Magnetic nanoparticles for hyperthermia in cancer treatment: an emerging tool. *Environmental Science and Pollution Research*, 27:19214–19225, 2020.
- [4.17] Xiaoli Liu, Yifan Zhang, Yanyun Wang, Wenjing Zhu, Galong Li, Xiaowei Ma, Yihan Zhang, Shizhu Chen, Shivani Tiwari, Kejian Shi, et al. Comprehensive understanding of magnetic hyperthermia for improving antitumor therapeutic efficacy. *Theranostics*, 10(8):3793, 2020.
- [4.18] H Belkahla, R Boudjema, V Caorsi, D Pineau, A Curcio, JS Lomas, P Decorse, A Chevillot-Biraud, T Azaïs, C Wilhelm, et al. Carbon dots, a powerful non-toxic support for bioimaging by fluorescence nanoscopy and eradication of bacteria by photothermia. *Nanoscale Advances*, 1(7):2571–2579, 2019.
- [4.19] Ana Espinosa, Jelena Kolosnjaj-Tabi, Ali Abou-Hassan, Anouchka Plan Sangnier, Alberto Curcio, Amanda KA Silva, Riccardo Di Corato, Sophie Neveu, Teresa Pellegrino, Luis M Liz-Marzán, et al. Magnetic (hyper) thermia or photothermia? progressive comparison of iron oxide and gold nanoparticles heating in water, in cells, and in vivo. *Advanced Functional Materials*, 28(37):1803660, 2018.
- [4.20] Marina Lázaro, Pablo Lupiáñez, José L Arias, María P Carrasco-Jiménez, Ángel V Delgado, and Guillermo R Iglesias. Combined magnetic hyperthermia and photothermia with polyelectrolyte/gold-coated magnetic nanorods. *Polymers*, 14(22):4913, 2022.
- [4.21] Mikel Rincón-Iglesias, Irati Rodrigo, Leixuri B. Berganza, Esraa Samy Abu Serea, Fernando Plazaola, Senentxu Lanceros-Méndez, Erlantz Lizundia, and Javier Reguera. Core-shell $\text{Fe}_3\text{O}_4@ \text{Au}$ nanorod-loaded gels for tunable and anisotropic magneto-and photothermia. *ACS Applied Materials & Interfaces*, 14(5):7130–7140, 2022.
- [4.22] M Pilar Calatayud, Cristina Riggio, Vittoria Raffa, Beatriz Sanz, Teobaldo E Torres, M Ricardo Ibarra, Clare Hoskins, Alfred Cuschieri, Lijun Wang, Josephine Pinkernelle, et al. Neuronal cells loaded with PEI-coated Fe_3O_4 nanoparticles for magnetically guided nerve regeneration. *Journal of Materials Chemistry B*, 1(29):3607–3616, 2013.
- [4.23] Xi Zhou, Wenlong Xu, Yan Wang, Qin Kuang, Yanfeng Shi, Lubin Zhong, and Qiqing Zhang. Fabrication of cluster/shell $\text{Fe}_3\text{O}_4/\text{Au}$ nanoparticles and application in protein detection via a SERS method. *The Journal of Physical Chemistry C*, 114(46):19607–19613, 2010.

- [4.24] Abolfazl Akbarzadeh, Mohammad Samiei, and Soodabeh Davaran. Magnetic nanoparticles: preparation, physical properties, and applications in biomedicine. *Nanoscale Research Letters*, 7:1–13, 2012.
- [4.25] Douglas Hanahan and Robert A Weinberg. Hallmarks of cancer: the next generation. *Cell*, 144(5):646–674, 2011.
- [4.26] Daniel Jaque, L Martínez Maestro, Blanca del Rosal, P Haro-Gonzalez, Antonio Benayas, JL Plaza, E Martín Rodríguez, and J García Solé. Nanoparticles for photothermal therapies. *Nanoscale*, 6(16):9494–9530, 2014.
- [4.27] Francesca Oltolina, Ana Peigneux, Donato Colangelo, Nausicaa Clemente, Annarita D’Urso, Guido Valente, Guillermo R Iglesias, Concepcion Jiménez-Lopez, and Maria Prat. Biomimetic magnetite nanoparticles as targeted drug nanocarriers and mediators of hyperthermia in an experimental cancer model. *Cancers*, 12(9):2564, 2020.
- [4.28] Ylenia Jabalera, Alberto Sola-Leyva, Ana Peigneux, Federica Vurro, Guillermo R Iglesias, Jesus Vilchez-Garcia, Inmaculada Pérez-Prieto, Francisco J Aguilar-Troyano, Luisa C López-Cara, María P Carrasco-Jiménez, et al. Biomimetic magnetic nanocarriers drive choline kinase alpha inhibitor inside cancer cells for combined chemo-hyperthermia therapy. *Pharmaceutics*, 11(8):408, 2019.
- [4.29] Xiaoli Zhang, Qingli Qu, Weixia Cheng, Aying Zhou, Yankang Deng, Wenjing Ma, Miaomiao Zhu, Ranhua Xiong, and Chaobo Huang. A Prussian blue alginate microparticles platform based on gas-shearing strategy for antitumor and antibacterial therapy. *International Journal of Biological Macromolecules*, 209:794–800, 2022.
- [4.30] Cindi L Dennis and Robert Ivkov. Physics of heat generation using magnetic nanoparticles for hyperthermia. *International Journal of Hyperthermia*, 29(8):715–729, 2013.
- [4.31] Julian Carrey, Boubker Mehdaoui, and Marc Respaud. Simple models for dynamic hysteresis loop calculations of magnetic single-domain nanoparticles: Application to magnetic hyperthermia optimization. *Journal of Applied Physics*, 109(8), 2011.
- [4.32] Ronald E Rosensweig. Heating magnetic fluid with alternating magnetic field. *Journal of Magnetism and Magnetic Materials*, 252:370–374, 2002.
- [4.33] RR Wildeboer, P Southern, and QA Pankhurst. On the reliable measurement of specific absorption rates and intrinsic loss parameters in magnetic hyperthermia materials. *Journal of Physics D: Applied Physics*, 47(49):495003, 2014.

- [4.34] Daniel Ortega and Quentin A Pankhurst. Magnetic hyperthermia. *Nanoscience*, 1(60):e88, 2013.
- [4.35] Joan Estelrich and Maria Antònia Busquets. Iron oxide nanoparticles in photothermal therapy. *Molecules*, 23(7):1567, 2018.
- [4.36] Gang Yuan, Yongjie Yuan, Kan Xu, and Qi Luo. Biocompatible PEGylated Fe₃O₄ nanoparticles as photothermal agents for near-infrared light modulated cancer therapy. *International Journal of Molecular Sciences*, 15(10):18776–18788, 2014.
- [4.37] Alexandre Adam and Damien Mertz. Iron oxide@ mesoporous silica Core-Shell nanoparticles as multimodal platforms for magnetic resonance imaging, magnetic hyperthermia, near-infrared light photothermia, and drug delivery. *Nanomaterials*, 13(8):1342, 2023.
- [4.38] FH Mustafa and MS Jaafar. Comparison of wavelength-dependent penetration depths of lasers in different types of skin in photodynamic therapy. *Indian Journal of Physics*, 87:203–209, 2013.
- [4.39] Sérgio RS Veloso, Eva S Marta, Pedro V Rodrigues, Cacilda Moura, Carlos O Amorim, Vítor S Amaral, Miguel A Correa-Duarte, and Elisabete MS Castanheira. Chitosan/alginate nanogels containing multicore magnetic nanoparticles for delivery of doxorubicin. *Pharmaceutics*, 15(9):2194, 2023.
- [4.40] Barbara Freis, Maria De Los Angeles Ramirez, Céline Kiefer, Sébastien Harlepp, Cristian Iacovita, Céline Henoumont, Christine Affolter-Zbarszczuk, Florent Meyer, Damien Mertz, Anne Boos, et al. Effect of the size and shape of dendronized iron oxide nanoparticles bearing a targeting ligand on MRI, magnetic hyperthermia, and photothermia properties—from suspension to in vitro studies. *Pharmaceutics*, 15(4):1104, 2023.
- [4.41] Anilkumar Thaghalli Shivanna, Banendu Sunder Dash, and Jyh-Ping Chen. Functionalized magnetic nanoparticles for alternating magnetic field-or near infrared light-induced cancer therapies. *Micromachines*, 13(8):1279, 2022.
- [4.42] Kaiming Shen, Yunfei Yan, Zongguo Xue, Shuo Wu, Jingxiang You, Lixian Li, and Wen Siang Lew. Multiwalled carbon nanotubes decorated with Mn₀. 5Zn₀. 5Fe₂O₄ nanoparticles for magneto-photothermal cancer therapy. *ACS Applied Nano Materials*, 6(14):13330–13341, 2023.
- [4.43] Dandan Ding, Wei Guo, Chongshen Guo, Jianzhe Sun, Nannan Zheng, Fei Wang, Mei Yan, and Shaoqin Liu. MoO 3- x quantum dots for photoacoustic imaging guided photothermal/photodynamic cancer treatment. *Nanoscale*, 9(5):2020–2029, 2017.

- [4.44] Erving C Ximendes, Uéslen Rocha, Carlos Jacinto, Kagola Upendra Kumar, David Bravo, Fernando J López, Emma Martín Rodríguez, José García-Solé, and Daniel Jaque. Self-monitored photothermal nanoparticles based on core-shell engineering. *Nanoscale*, 8(5):3057–3066, 2016.
- [4.45] Beatrice Muzzi, Martin Albino, Alessio Gabbani, Alexander Omelyanchik, Elena Kozenkova, Michele Petrecca, Claudia Innocenti, Elena Balica, Alessandro Lavacchi, Francesca Scavone, et al. Star-shaped magnetic-plasmonic Au@ Fe₃O₄ nano-heterostructures for photothermal therapy. *ACS Applied Materials & Interfaces*, 14(25):29087–29098, 2022.
- [4.46] Nihal S Elbially, Mohamed M Fathy, AL-Wafi Reem, Reem Darwesh, Umama A Abdel-Dayem, Musab Aldhahri, Abdulwahab Noorwali, and Attieh A Al-Ghamdi. Multifunctional magnetic-gold nanoparticles for efficient combined targeted drug delivery and interstitial photothermal therapy. *International journal of pharmaceutics*, 554:256–263, 2019.
- [4.47] Esraa Samy Abu Serea, Inñaki Orue, José Ángel García, Senentxu Lanceros-Meéndez, and Javier Reguera. Enhancement and tunability of plasmonic-magnetic hyperthermia through shape and size control of Au: Fe₃O₄ janus nanoparticles. *ACS Applied Nano Materials*, 6(19):18466–18479, 2023.
- [4.48] Ana Espinosa, Javier Reguera, Alberto Curcio, Álvaro Muñoz-Noval, Christian Kuttner, Aurore Van de Walle, Luis M Liz-Marzán, and Claire Wilhelm. Janus magnetic-plasmonic nanoparticles for magnetically guided and thermally activated cancer therapy. *Small*, 16(11):1904960, 2020.
- [4.49] Esther Cazares-Cortes, Claire Wilhelm, Jose Efrain Perez, Ana Espinosa, Sandra Casale, Aude Michel, Ali Abou-Hassan, and Christine Ménager. Tuning the load of gold and magnetic nanoparticles in nanogels through their design for enhanced dual magneto-photo-thermia. *Chemical Communications*, 57(48):5945–5948, 2021.
- [4.50] Nguyen Thi Ngoc Linh, Le The Tam, Ha Minh Nguyet, Ngo Thanh Dung, Nguyen Hoa Du, Le Thi Thanh Tam, Pham Hong Nam, Nguyen Dinh Vinh, Nguyen Thien Vuong, Ngo Dai Quang, et al. Combination of photothermia and magnetic hyperthermia properties of Fe₃O₄@ Ag hybrid nanoparticles fabricated by seeded-growth solvothermal reaction. *Vietnam Journal of Chemistry*, 59(4):431–439, 2021.
- [4.51] Adam Y Lin, Joseph K Young, Ariel V Nixon, and Rebekah A Drezek. Encapsulated Fe₃O₄/Ag complexed cores in hollow gold nanoshells for enhanced theranostic magnetic resonance imaging and photothermal therapy. *Small*, 10(16):3246–3251, 2014.

- [4.52] Juan J Giner-Casares, Malou Henriksen-Lacey, Marc Coronado-Puchau, and Luis M Liz-Marzán. Inorganic nanoparticles for biomedicine: where materials scientists meet medical research. *Materials Today*, 19(1):19–28, 2016.
- [4.53] Luis M Liz-Marzán. Nanometals: formation and color. In *Colloidal synthesis of plasmonic nanometals*, pages 1–13. Jenny Stanford Publishing, 2020.
- [4.54] Mohammad Zaki Ahmad, Sohail Akhter, Ziyaur Rahman, Shabib Akhter, Mohammed Anwar, Neha Mallik, and Farhan Jalees Ahmad. Nanometric gold in cancer nanotechnology: current status and future prospect. *Journal of Pharmacy and Pharmacology*, 65(5):634–651, 2013.
- [4.55] Sheng Tong, Christopher A Quinto, Linlin Zhang, Priya Mohindra, and Gang Bao. Size-dependent heating of magnetic iron oxide nanoparticles. *ACS Nano*, 11(7):6808–6816, 2017.
- [4.56] Zohreh Nemati, Javier Alonso, Irati Rodrigo, Raja Das, Eneko Garaio, José Ángel García, Iñaki Orue, Manh-Huong Phan, and Hariharan Srikanth. Improving the heating efficiency of iron oxide nanoparticles by tuning their shape and size. *The Journal of Physical Chemistry C*, 122(4):2367–2381, 2018.
- [4.57] L León Félix, B Sanz, V Sebastián, TE Torres, Marcelo Henrique Sousa, JAH Coaquira, MR Ibarra, and Gerardo Fabian Goya. Gold-decorated magnetic nanoparticles design for hyperthermia applications and as a potential platform for their surface-functionalization. *Scientific Reports*, 9(1):4185, 2019.
- [4.58] Ritu Goyal, Sushil K Tripathi, Esther Vazquez, Pradeep Kumar, and Kailash C Gupta. Biodegradable poly (vinyl alcohol)-polyethylenimine nanocomposites for enhanced gene expression in vitro and in vivo. *Biomacromolecules*, 13(1):73–83, 2012.
- [4.59] Ian Y Goon, Leo MH Lai, May Lim, Paul Munroe, J Justin Gooding, and Rose Amal. Fabrication and dispersion of gold-shell-protected magnetite nanoparticles: systematic control using polyethyleneimine. *Chemistry of Materials*, 21(4):673–681, 2009.
- [4.60] María del Mar Ramos-Tejada, Julian L Viota, Katarzyna Rudzka, and Angel V Delgado. Preparation of multi-functionalized Fe₃O₄/Au nanoparticles for medical purposes. *Colloids and Surfaces B: Biointerfaces*, 128:1–7, 2015.
- [4.61] Felisa Reyes-Ortega, Blanca Luna Checa Fernández, Angel V Delgado, and Guillermo R Iglesias. Hyperthermia-triggered doxorubicin release from polymer-coated magnetic nanorods. *Pharmaceutics*, 11(10):517, 2019.
- [4.62] G Iglesias, AV Delgado, M Kujda, and MM Ramos-Tejada. Magnetic hyperthermia with magnetite nanoparticles: Electrostatic and polymeric stabilization. *Colloid and Polymer Science*, 294:1541–1550, 2016.

- [4.63] Ylenia Jabalera, Alberto Sola-Leyva, María P Carrasco-Jiménez, Guillermo R Iglesias, and Concepcion Jimenez-Lopez. Synergistic photothermal-chemotherapy based on the use of biomimetic magnetic nanoparticles. *Pharmaceutics*, 13(5):625, 2021.
- [4.64] Beatriz Sanz, M Pilar Calatayud, Nicolás Cassinelli, M Ricardo Ibarra, and Gerardo F Goya. Long-term stability and reproducibility of magnetic colloids are key issues for steady values of specific power absorption over time. *European Journal of Inorganic Chemistry*, 2015(27):4524–4531, 2015.
- [4.65] Barbara Lafuente, Robert T Downs, Hexiong Yang, Nate Stone, Thomas Armbruster, Rosa Micaela Danisi, et al. The power of databases: the RRUFF project. *Highlights in mineralogical crystallography*, 1:25, 2015.
- [4.66] Jane Cathleen Gabunada, Mohanraj Vinothkannan, Dong Hee Kim, Ae Rhan Kim, and Dong Jin Yoo. Magnetite nanorods stabilized by polyaniline/reduced graphene oxide as a sensing platform for selective and sensitive non-enzymatic hydrogen peroxide detection. *Electroanalysis*, 31(8):1507–1516, 2019.
- [4.67] Jinjin Shi, Hongling Zhang, Lei Wang, Lulu Li, Honghong Wang, Zhenzhen Wang, Zhi Li, Chengqun Chen, Lin Hou, Chaofeng Zhang, et al. Pei-derivatized fullerene drug delivery using folate as a homing device targeting to tumor. *Biomaterials*, 34(1):251–261, 2013.
- [4.68] Mei Fang, Valter Ström, Richard T Olsson, Lyubov Belova, and K Venkat Rao. Particle size and magnetic properties dependence on growth temperature for rapid mixed co-precipitated magnetite nanoparticles. *Nanotechnology*, 23(14):145601, 2012.
- [4.69] C Ravikumar and Rajdip Bandyopadhyaya. Mechanistic study on magnetite nanoparticle formation by thermal decomposition and coprecipitation routes. *The Journal of Physical Chemistry C*, 115(5):1380–1387, 2011.
- [4.70] Roberto Valenzuela, María Cecilia Fuentes, Carolina Parra, Jaime Baeza, Nelson Duran, SK Sharma, Marcelo Knobel, and Juanita Freer. Influence of stirring velocity on the synthesis of magnetite nanoparticles (Fe_3O_4) by the coprecipitation method. *Journal of Alloys and Compounds*, 488(1):227–231, 2009.
- [4.71] CJ Goss. Saturation magnetisation, coercivity and lattice parameter changes in the system Fe_3O_4 - γ - Fe_2O_3 , and their relationship to structure. *Physics and Chemistry of Minerals*, 16(2):164–171, 1988.
- [4.72] E Iglesias-Silva, J Rivas, LM León Isidro, and MA López-Quintela. Synthesis of silver-coated magnetite nanoparticles. *Journal of Non-Crystalline Solids*, 353(8-10):829–831, 2007.

- [4.73] Wang, Jin Luo, Quan Fan, Masatsugu Suzuki, Itsuko S Suzuki, Mark H Engelhard, Yuehe Lin, Nam Kim, Jian Q Wang, and Chuan-Jian Zhong. Monodispersed core-shell $\text{Fe}_3\text{O}_4@ \text{Au}$ nanoparticles. *The Journal of Physical Chemistry B*, 109(46):21593–21601, 2005.
- [4.74] M Andrés Vergés, R Costo, AG Roca, JF Marco, GF Goya, CJ Serna, and MdP Morales. Uniform and water stable magnetite nanoparticles with diameters around the monodomain–multidomain limit. *Journal of Physics D: Applied Physics*, 41(13):134003, 2008.
- [4.75] Agnieszka Włodarczyk, Szymon Gorgoń, Adrian Radoń, and Karolina Bajdak-Rusinek. Magnetite nanoparticles in magnetic hyperthermia and cancer therapies: Challenges and perspectives. *Nanomaterials*, 12(11):1807, 2022.
- [4.76] Venkatesha Narayanaswamy, Sangaraju Sambasivam, Alam Saj, Sulaiman Alaabed, Bashar Issa, Imaddin A Al-Omari, and Ihab M Obaidat. Role of magnetite nanoparticles size and concentration on hyperthermia under various field frequencies and strengths. *Molecules*, 26(4):796, 2021.
- [4.77] Yolanda Piñeiro-Redondo, Manuel Bañobre-López, Iván Pardiñas-Blanco, Gerardo Goya, M Arturo López-Quintela, and José Rivas. The influence of colloidal parameters on the specific power absorption of PAA-coated magnetite nanoparticles. *Nanoscale Research Letters*, 6:1–7, 2011.
- [4.78] Miloš Ognjanović, Dalibor M Stanković, Željko K Jaćimović, Milica Kosović-Perutović, Biljana Dojčinović, and Bratislav Antić. The effect of surface-modifier of magnetite nanoparticles on electrochemical detection of dopamine and heating efficiency in magnetic hyperthermia. *Journal of Alloys and Compounds*, 884:161075, 2021.
- [4.79] Rudolf Hergt and Silvio Dutz. Magnetic particle hyperthermia—biophysical limitations of a visionary tumour therapy. *Journal of Magnetism and Magnetic Materials*, 311(1):187–192, 2007.
- [4.80] Venkatesha Narayanaswamy, Jayalakshmi Jagal, Hafsa Khurshid, Imaddin A Al-Omari, Mohamed Haider, Alexander S Kamzin, Ihab M Obaidat, and Bashar Issa. Hyperthermia of magnetically soft-soft core-shell ferrite nanoparticles. *International Journal of Molecular Sciences*, 23(23):14825, 2022.
- [4.81] Lucía Vizcaíno-Anaya, Carlos Herreros-Lucas, José M Vila-Fungueiriño, and María del Carmen Giménez-López. Magnetic hyperthermia enhancement in iron-based materials driven by carbon support interactions. *Chemistry—A European Journal*, 28(67):e202201861, 2022.
- [4.82] Ana Espinosa, Riccardo Di Corato, Jelena Kolosnjaj-Tabi, Patrice Flaud, Teresa Pellegrino, and Claire Wilhelm. Duality of iron oxide nanoparticles in

- cancer therapy: amplification of heating efficiency by magnetic hyperthermia and photothermal bimodal treatment. *ACS Nano*, 10(2):2436–2446, 2016.
- [4.83] Andrew M Smith, Michael C Mancini, and Shuming Nie. Second window for in vivo imaging. *Nature Nanotechnology*, 4(11):710–711, 2009.
- [4.84] Pinar Avci, Asheesh Gupta, Magesh Sadasivam, Daniela Vecchio, Zeev Pam, Nadav Pam, and Michael R Hamblin. Low-level laser (light) therapy (lllt) in skin: stimulating, healing, restoring. In *Seminars in cutaneous medicine and surgery*, volume 32, page 41. NIH Public Access, 2013.
- [4.85] Megan Wetzel, John Strickley, M Tye Haeberle, and Timothy S Brown. Depth of invasion of aggressive and nonaggressive basal cell carcinoma. *The Journal of Clinical and Aesthetic Dermatology*, 12(3):12, 2019.

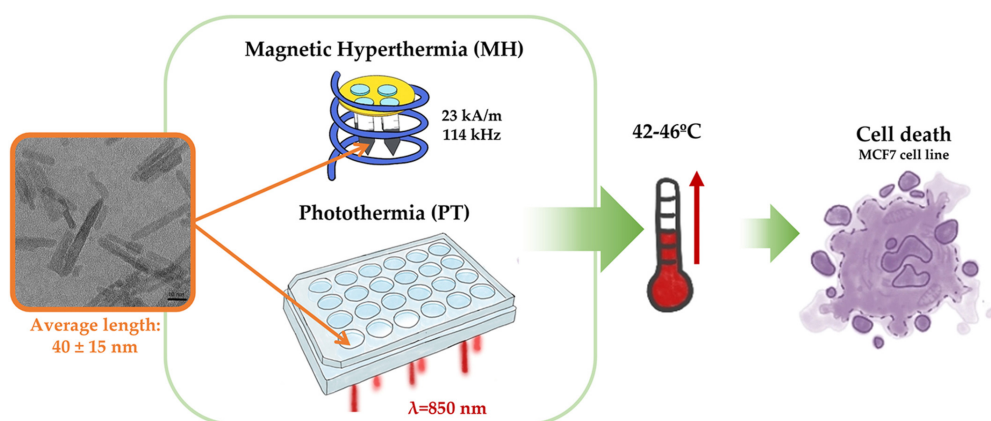
Chapter 5

The role of biocompatible coatings of magnetic nanorods on their thermal response in hyperthermia. Consequences on tumor cell survival.

M. Lázaro, A. Sola-Leyva, M. Jimenez-Carretero, MP. Carrasco Jiménez, ÁV. Delgado, GR. Iglesias, *J. Drug. Deliv. Sci. Technol.* **2024**, *95*, 105622.

Abstract

There are so many hopes for nanoscience as a tool in the fight against various diseases, notably cancer, that the problem can be approached from many different points of view. In this paper, we focus on two essential aspects. One is the preparation of non-spherical and superparamagnetic magnetic particles, with the right size to be able to exit the blood vessels and be incorporated by cells. The second is their use as agents of hyperthermia. For the first purpose, a two-step method was followed, in which hematite templates with the desired shape and size were first prepared, and these were subsequently reduced by heat treatment. As a result, nanorods with a length of 40 nm and an axis ratio of 1:8 were obtained. The bare particles were coated with a triple layer of cationic/anionic/cationic polymers. Electrophoretic mobility, thermogravimetric analysis, x-ray photoelectron spectroscopy and Fourier-transform infrared spectroscopy evaluations confirmed the presence of the coating and the positive charge of the last polymeric layer, while x-ray diffraction and micro-Raman spectroscopy indicated that the crystal structure of the core particles was magnetite/maghemite. The magnetization cycles of the particles showed that they were superparamagnetic, with a saturation magnetization of 82 emu/g in the case of the bare particles. For concentrations up to 300 $\mu\text{g/mL}$, they were found to be compatible with MCF7 (Michigan Cancer Foundation-7) breast cancer cell line, for cell uptakes higher than 80%. Both bare and polymer-coated particles produced heating by magnetic hyperthermia and laser-light irradiation. Finally, cytotoxicity against the cancer cells was evaluated, and it was found that photothermia and, above all, magnetic hyperthermia applied to the coated particles could induce more than 50% cell death.



5.1. Introduction

In recent decades, nanotechnology has emerged as a multidisciplinary discipline with promising results in a multitude of fields. Magnetic nanoparticles (MNPs) appear to have found a niche in the area, considering their obvious field-responsiveness and the varied applications where they are considered especially useful (drug delivery, magnetic resonance imaging, magnetic particle spectroscopy, hyperthermia. . .) [5.1, 5.2]. This is partly explained by the fact that they can be synthesized in a variety of shapes, dimensions, or compositions and also by the generally accepted limited toxicity of the particles mostly used (magnetite or maghemite), mainly if applied at low doses and for short periods of time [5.3]. Although most studies on MNPs have used (quasi)spherical geometries, interest in other shapes has increased, considering such aspects as transport in the blood stream or mechanisms of cell internalization. Hence, nanocubes, nanoflowers, octahedra, rods, wires. . . have been investigated [5.4]. Among these various nanoscale structures, magnetic nanorods stand out due to their excellent magnetic properties and their tunable size, which can go from a few nanometers to microns [5.5]. Additionally, this type of nanostructures has a wide variety of applications, from the design of magnetic memories (given their high magnetic coercivity, [5.6]), to their use in the communication and information industry [5.7], as well as their application for energy storage [5.1].

Like other magnetic particles [5.2], the use of nanorods in biomedicine is increasingly explored. Fields like drug transport [5.8,5.9], magnetic particle imaging [5.10], diagnostic nanosensors utilizing biomarkers [5.11], magnetofection to enhance the efficiency of gene therapy for introducing genetic material into cells, etc. are just some examples [5.12]. They can also function as contrast agents in magnetic resonance imaging (MRI), as it has been shown that magnetite nanorods have a high R_2 relaxivity value in comparison with other geometries [5.13,5.14]. The advantages of the elongated geometry have been discussed by several authors. Thus Gubanov *et al.* [5.15] demonstrated by numerical simulation that such geometry is preferred over the spherical one in achieving high performance in magnetic hyperthermia. This was experimentally confirmed by Bautoin *et al.* [5.16]. Shen *et al.* [5.17] found that rod-like particles are ideal for mechanical destruction of tumor cells by application of rotating magnetic fields, and this is also an optimal shape for cell internalization [5.18]. Lisjak and Mertelj [5.19] have also reviewed applications in imaging or drug delivery.

The present study will focus on a specific area, namely, the heating of a system of dispersed nanorods by application of an alternating magnetic field (magnetic hyperthermia, MH) of proper frequency and amplitude. This is based on the fact that reaching the hyperthermia regime, comprising temperatures of 42-46°C during a few minutes, can lead to cell death [5.20,5.21]. This can happen to both healthy and tumor cells, but the latter are more prone to undergo apoptosis because of the deficient blood

vessels of tumours [5.21–5.24]. To achieve this goal, stimuli are applied by means of external fields. In the case of magnetic hyperthermia, the sample is subjected to field frequencies of approximately 100–200 kHz and strengths of about 20 kA/m [5.25]. These conditions make it possible to obtain localized temperature increases in the sample.

An alternative or complementary local heating technique is hyperthermia induced by light irradiation (i.e., photothermia, PT). In this case, the sample is subjected to electromagnetic radiation of specific wavelength for which absorbance is maximum, preferably resonant, in the infrared (IR) range of the spectrum, since wavelengths in this region undergo greater penetration into the skin due to the existence of a biological window [5.26]. It is important to mention that magnetite, the material used in this research, presents good absorption in the aforementioned region of the spectrum, which ensures temperature increases by photothermia [5.27].

For the implementation of the two mentioned techniques, it is essential to have nanoparticles of adequate dimensions for biomedical applications. That is, they must have a size greater than 15 nm and less than 100 nm, since the magnetic moment decreases as the size of the particles decreases [5.28]. It is also crucial that these nanoparticles can be internalized by cells to achieve the desired effect of cell death. In addition, it is highly beneficial that they exhibit superparamagnetic behaviour, so that they do not undergo aggregation by dipolar magnetic interactions under conditions in which an external magnetic field is not applied. Recall that the magnetic behaviour is denominated superparamagnetic when the size of the particles and the frequency of the magnetic field is such that the magnetic moments of the (monodomain) particles can follow the field oscillations without appreciable phase lag. As a consequence, no hysteresis will be found when magnetization cycles are performed. This behaviour ensures that the particles remain stable and avoid possible adverse effects on the human body [5.29].

However, there is still much to be improved in the use of these new techniques. One of the objectives is to obtain nanoparticles with the highest possible thermal efficiency. It has been proven that the use of anisotropic geometries is more efficient in magnetic hyperthermia [5.30, 5.31]. For example, Geng *et al.* [5.32] have shown that the use of magnetite nanorods with an aspect ratio of 4.5 provides higher thermal efficiency compared to 15 nm magnetite nanoparticles. The choice of nanorods instead of other geometries, such as cubic or spherical, offers several significant advantages. For example, nanorods have a larger surface area, resulting in dramatic changes in their physicochemical properties [5.33]. This feature is especially beneficial for their use as drug-carrying vehicles, as it allows for greater drug incorporation. A highlight for the applications addressed in this work is that anisotropic particles, such as nanorods, have been shown to improve circulation time in the bloodstream and have higher retention in tumour areas compared to spherical nanoparticles [5.34]. In addition, the shape of the nanorods allows them to be

manipulated with external magnetic fields, broadening their possible applications. For example, as above mentioned, they can be directed with a rotating magnetic field, potentially damaging cell membranes, enhancing drug diffusion or inducing an active flow to improve thrombolysis efficiency [5.35–5.37].

There are different methods for the synthesis of magnetic nanorods, depending on the size and the properties that one wishes to obtain for their application [5.12]. Some of these methods are thermal decomposition [5.38], hydrothermal synthesis [5.39], use of templates [5.40], or hydrolysis techniques, among others. However, in this work we will focus on producing magnetic nanorods by a two-step method: the first one will be the transformation of a $\text{Fe}(\text{OH})_3$ gel phase to $\beta\text{-FeOOH}$ by dissolution, and the growth by the dissolution-crystallization mechanism to $\alpha\text{-Fe}_2\text{O}_3$, previously described by Sugimoto *et al.* [5.41, 5.42]. In addition, the presence of a shape-controlling agent, such as phosphate or sulfate ions, favors predirectional aggregation processes. This means that, through this mechanism, and once hematite nucleation occurs, phosphate or sulphate ions are adsorbed on the planes parallel to the *c*-axis, due to better matching between the O-O interatomic distance of these anions and the Fe-Fe distance in the crystal lattice (compared to the perpendicular planes), and hence the particle growth is hindered in directions perpendicular to the *c* direction [5.43, 5.44]. The advantage of this method over the others is that it allows very reproducible results to be obtained, and that by changing parameters such as the concentrations of reagents used, the size and aspect ratio of the desired particles can be reduced or increased [5.44].

On the other hand, we cannot forget to guarantee the biocompatibility of the synthesized nanorods for their future bio applications. For this purpose, different polymeric coatings have been studied. Among them, polyethylene glycol stands out, due to the easy renal excretion that it presents, showing neither autoimmunogenic nor antigenic properties [5.45]. Also, other polymers such as chitosan, dextran, alginate, poly acid polyetherimide can be used [5.30]. In this work, the nanorods will be coated by low molecular weight, branched poly(ethyleneimine) or PEI. This coating guarantees cell viability and prevents the formation of large aggregates [5.46]. Hence, this paper presents the synthesis of magnetic nanorods, and their coating with (PEI) to make them biocompatible.

The nanorods will be tested as magnetic hyperthermia and photothermia agents, and their action on tumor cells will be tested both in the absence and in the presence of the external stimuli used for hyperthermia, that is, alternating magnetic fields or laser irradiation. To the authors' knowledge, this is the first time that magnetic nanorods are used jointly for magnetic hyperthermia and photothermia, and that these techniques and these particles are tested as antitumoral tools.

5.2. Materials and methods

Materials

All chemicals used were commercially available: sodium hydroxide, iron (III) chloride hexahydrate, anhydrous sodium sulfate, perchloric acid, hydrochloric acid, hydrogen peroxide, potassium thiocyanate, branched polyethyleneimine (PEI, $M_w \approx 2000$ g/mol) and poly(styrenesulfonate) (PSS, $M_w \approx 7 \times 10^4$ g/mol) were purchased from Merck Sigma-Aldrich (Spain). Absolute ethanol was provided by Scharlau, Germany. The water used was deionized and filtered through a 0.2 μm filter in a Milli-Q Academic equipment (Millipore, Spain). Fetal Bovine Serum (FBS) and RPMI-1640 (Roswell Park Memorial Institute 1640) were obtained from Biowest (Nuaillé, France). Resazurin was also acquired from Sigma-Aldrich (Madrid, Spain).

The breast cancer cell line MCF7 (Michigan Cancer Foundation-7) was provided by the European Collection of Animal Cell Cultures (Salisbury, UK). RPMI-1640, used to culture MCF7, was supplemented with 10% (v/v) heat-inactivated FBS, 2 mM L-glutamine, 100 IU/mL penicillin and 100 $\mu\text{g}/\text{mL}$ streptomycin. Cells were incubated at 37 °C in a humidified atmosphere with 5% CO_2 .

Methods

5.2.1 Synthesis of magnetic nanorods

The synthesis of nanorods was carried out in two steps: first, hematite nanorods were synthesized, and then they were transformed by high-temperature reduction. Hematite seeds were obtained by following the sol-gel method proposed by Sugimoto and Muramatsu [5.42]: in a Pyrex bottle sealed with Teflon, 6 mol NaOH and 2 mol FeCl_3 were added to 1 L of Milli-Q water. The solution was kept at 100 °C for 24 h. Subsequently, the seeds were centrifuged 3 times for 20 minutes at 21000 rpm and dried overnight. The resulting sample was ground in an agate mortar and later in a planetary ball mill. Finally, the powder obtained was resuspended in 0.01 M HClO_4 and centrifuged again at 10000 rpm for 30 minutes. In order to keep the size of the smallest particles around a few nm, the supernatant of this centrifugation was centrifuged again at 21000 rpm for 30 minutes and redispersed in 0.01 M HClO_4 several times. The final seed size obtained in acid was 18 nm.

Once the desired seed size was achieved, 100 mL NaOH 4.8 M were added slowly under stirring to 100 mL $\text{FeCl}_3 \cdot 6\text{H}_2\text{O}$ 2 M. The resulting solution was stirred additionally for 5 minutes. Then a 20 mL aliquot was extracted, to which 2 mL of the seed solution and 40 mL of a solution 3 mM Na_2SO_4 were added. This suspension was kept at 100 °C for 3 days in a Pyrex bottle sealed with Teflon. Subsequently the

resulting particles were cleaned by centrifugation, redispersed in water several times, and dried overnight.

Finally, it was necessary to carry out the transformation of the hematite nanoparticles into magnetite by means of a high-temperature reduction process. To achieve this, a tube furnace (Hobersal, Spain) was employed, operating at a constant temperature of 350 °C, while nitrogen bubbled in pure ethanol was passed through the furnace tube at a flow rate of 3.83 L/h. At this temperature, ethanol was oxidized, reducing the hematite powder to magnetite. The hematite powder was introduced into the furnace and kept in the ethanol/N₂ atmosphere for a duration of 6 hours to allow for complete and effective reduction to magnetite [5.36].

5.2.1 Polymer coating of magnetite nanorods

First, 5 mL of MNPs (1g/L) were added drop by drop into 5 mL of PEI (2 g/L) with ultrasonic agitation. The resulting mixture was maintained in the ultrasonic bath for another 90 minutes, followed by a 30-minute rest period without any disturbance. The final step involved multiple rounds of magnetic decantation and redispersion in 5 mL Milli-Q water, while maintaining the initial concentration. This process was repeated for both PSS and PEI coatings.

The convenience of carrying out the triple-layer coating was suggested by our previous results on the coating of magnetite by PEI [5.47]. There it was found that a one-layer coating by this cationic polymer was unstable: the electrostatic interaction was not sufficient to keep the layer attached beyond a few days, and electrophoretic determinations showed that the surface behaviour was progressively approaching that of bare magnetite.

In contrast, using a negatively charged polymer (poly(styrene sulphonate), PSS) as second layer and support for the final PEI coating demonstrated that the pH dependence of the electrophoresis of the multiply-coated particles remained constant by at least two weeks, and probably longer.

5.2.1 HRTEM Characterization: Morphology

The morphology of MNPs was examined using high-resolution transmission electron microscopy (HRTEM) (Thermo Fisher Scientific TALOS F200X, USA) at CIC UGR. JImage software (University of Wisconsin, Madison, WI, USA) was utilized to determine the size distribution.

5.2.1 Structural characterization

The structural evaluation of the nanorods was carried out using X-ray diffraction. Additionally, micro-Raman spectroscopy was performed to confirm the results. X-ray powder diffraction patterns (XRD) were obtained from the dry samples using a Bruker D8 Advance diffractometer (Germany) with a Bruker LINXEYE detector and a $\text{CuK}\alpha$ radiation source ($\lambda = 1.5406 \text{ \AA}$).

An issue with XRD is its inability to differentiate between the crystal structures of magnetite and maghemite due to the identical structure of both minerals (inverse spinel) and the similar interatomic distances in all three directions. Micro-Raman spectroscopy was conducted using a JASCO NRS-5100 Dispersive Micro-Raman (Japan) at CIC-UGR. The device was equipped with a green diode laser of 532 nm and 30 mW power (Elforlight G4-30; Nd: YAG). The spectral range for the analysis was from 50 to 8000 cm^{-1} . This technique will enable us to differentiate between both magnetic phases.

X-ray photoelectron spectroscopy determinations were carried out with both bare and polymer-coated nanoparticles. A PHI 5000 VersaProbe II (from Physical Instruments USA) was used. The presence of the polymer layer was also evaluated through infrared spectroscopy (FTIR JASCO 6200, Japan).

The surface area of the solids was measured by BET nitrogen adsorption using a Micromeritics TriStar 3000 (USA).

5.2.1 Thermogravimetric analysis

Thermogravimetric analysis was performed using a Shimadzu TGA-50H (Japan). The mass changes were measured with 0.001 mg accuracy, and the temperature range was from 25 °C to 950 °C.

5.2.1 Electrophoretic mobility measurements

Electrophoretic mobility measurements were carried out by dynamic light scattering (PALS) with a Zetasizer Nano-ZS (Malvern Instruments, UK).

5.2.1 Magnetic properties

The magnetization cycles of the samples were obtained using two different methods. One was the Quantum Design MPMS XL magnetometer (USA). Measurements were performed at 292 K, using magnetic fields in the range of -5 to +5 T. The second technique allows measuring the magnetization when the particles

are suspended in a liquid. In this case, magnetization cycles were acquired using an inductive magnetometer AC Hyster Series (Spain). The experiments were performed at room temperature (20 °C) using a 40 μL suspension of MNPs in water with a concentration of up to 20 mg/mL; the device operates with a field frequency of 1.5 kHz, and a field strength of 120 kA/m.

5.2.1 Cytotoxicity and cell uptake determinations

To determine cytotoxicity of the nanorods, MCF7 cells were seeded at a density of 10,000 cells/well into 96-well black plates with clear bottoms. The plates were then incubated at 37 °C and 5% CO₂ for 24 hours to allow for cell adhesion. The magnetite solutions, denominated NR2s hereafter, were prepared (100-500 $\mu\text{g/mL}$) and 100 μL of each magnetite solution was added to the corresponding well. The plates were incubated at 37 °C and 5% CO₂ for an additional 24 hours. After this, 10 μL of resazurin 1 mM in PBS was added to each well. The reaction was incubated in the dark for 2 hours and the fluorescence intensity was measured at $\lambda_{ex} = 535 \text{ nm}/\lambda_{em} = 590 \text{ nm}$ using a microplate reader (HTX Microplate Reader BioTek Instruments, Vermont, USA).

To determine cytotoxicity of the nanorods upon application of magnetic hyperthermia and photothermia, MCF7 cells were seeded onto 12 well-plates at 300,000 cells/well in a volume of 1 mL. Then, 9 wells were treated with 300 $\mu\text{g/mL}$ of NR2s and 3 wells with medium RPMI-1640/10% FBS, this experiment acting as control. After the 24 hours treatment, cells were trypsinized and resuspended in 200 μL of fresh medium RPMI-1640/10% FBS, and then transferred to Eppendorf tubes (0.5 mL), obtaining a final cell concentration of 1.5 million cells/mL. Then, 3 samples were irradiated for 10 minutes from the top with the NIR laser set at 0.7 W cm⁻², and other 3 samples were exposed to AMF (frequency = 114 kHz, H = 23 kA/m). In parallel, the same experimental conditions were tested without exposing the cells to either the laser or AMF. After exposure, 180 μL of each sample was transferred to each well of a 96-well black plate and 18 μL of resazurin 1 mM in PBS was added. The reaction was incubated in the dark for 2 h and the fluorescence intensity was measured at $\lambda_{ex} = 535 \text{ nm}/\lambda_{em} = 590 \text{ nm}$ as described above.

Cell uptake experiments were carried out by triplicate using MCF7 cell line too, and the procedure previously described in [5.48]. For this, 3×10^5 cells/well were seeded in RPMI-1640/10% FBS, using 12-well plates. After 24 hours of seeding, 1 mL of the chosen treatment was added, resulting in: a) control groups (cells alone + RPMI-1640/10% FBS medium), b) treatment groups (cells + 300 $\mu\text{g/mL}$ NR2s in RPMI-1640/10% FBS), and c) reference groups (NR2s 300 $\mu\text{g/mL}$ in RPMI-1640/10% FBS without cells). Following 24 hours in the cell culture incubator, the cells were washed twice with 1 mL PBS and trypsinized. Then, they were centrifuged for 5 min at 6500 rpm and the pellet was resuspended in 100 μL of 37% HCl and

10 μL of 10% H_2O_2 . The mixture was vortexed and incubated for 20 minutes at room temperature. Finally, we added 1 mL of 1% potassium thiocyanate, and the absorbance at 490 nm was measured.

To obtain the endogenous iron of the cells, a standard calibration curve was used. To determine internalization, we utilized the following expression for percent cell uptake, UPT:

$$UTP = \frac{\bar{T} - \bar{C}}{\bar{R}} \times 100 \quad (5.1)$$

where \bar{T} is the average of the treatments, \bar{C} is the average in control samples, and \bar{R} is the reference average.

5.2.1 Magnetic hyperthermia

The hyperthermia equipment used in these experiments has been designed and manufactured in our laboratory, and allows frequency sweeps between 114 and 208 kHz, and field amplitudes from 10 to 25.2 kA/m [5.49].

The field is applied to the samples by placing them (sample volume 100 μL) in the centre of a double four-turn copper coil with a diameter of 24.90 ± 0.05 mm, with $L = 2.48 \pm 0.01$ mH, and resistance $R = 300 \pm 1$ m Ω . Thermostated water at 15 $^\circ\text{C}$ is passed while the coil is energized (maximum AC current in the coil is 50 A). Cooling is essential because the high currents used generate a significant amount of Joule heating, which may interfere with or even surpass the magnetic heating effect.

Field strength and frequency measurements were taken using a NanoScience Laboratories Ltd. Probe (UK), which has a sensitivity of 10 μT . Temperature rise is registered using an optical fiber thermometer (Optocon AG, Germany) every 3 seconds with 0.01 $^\circ\text{C}$ resolution.

5.2.1 Photothermia

The equipment uses a laser (with a wavelength of 850 nm and a power of 1.6 W) that is directed towards a support where a sample (200 μL in an Eppendorf) is placed.

For cell experiments, a laser of the same wavelength will be used, but allowing up to 6 triplicates to be performed at the same time. Moreover, a thermal imaging camera (Flir 60 with 320×240 pixels, IR resolution, and thermal sensitivity of 0.045 $^\circ\text{C}$; FLIR Systems, Inc., USA) records temperature every 0.067 s [5.50].

5.2.1 Thermal efficiency evaluation

To determine the thermal efficiency of the nanoparticles, the SAR (Specific Absorption Rate) parameter is used. It characterizes the heating power per unit mass of the MNPs, and it is defined in terms of the rate of temperature increase with time, as follows:

$$\text{SAR} = \frac{C_{\text{liq}} \cdot \rho_{\text{liq}}}{\phi} \cdot \frac{dT}{dt} \quad (5.2)$$

where C_{liq} and ρ_{liq} are, respectively, the mass specific heat and the density of the suspension, and ϕ is the nanoparticle mass concentration. These parameters are, a priori, known in the sample preparation. To determine the temperature-time slope in magnetic hyperthermia use was made of the phenomenological Box Lucas equation, and in photothermia we performed the linear fit to the first 30 seconds of temperature increase [5.51].

5.2.1 Statistical analysis

To evaluate the differences between experiments, we employed the Student's *t* test. This test was conducted using a two-tailed approach with a 95% confidence level. Differences are considered statistically significant at $*p < 0.05$ and $***p < 0.001$. The data are shown as mean \pm standard error of the mean (SEM).

5.3. Results and discussion

Size and shape characterization

The size and morphology of the magnetic nanorods (NR2) can be observed in Figure 5.1 A, B, C. As can be seen, they have an elongated shape with an aspect ratio of 1:8. The average length size of the nanorods is 40 ± 15 nm (Figure 5.1D). There is polydispersity in the sample which is due to the fact that in order to obtain monodisperse particles, generally the stages of nucleation and subsequent growth must be totally separated. However, in this case another type of mechanism has been used, in which the seeds (previously preformed particles), present certain probability of coagulation between the nuclei that are generated simultaneously, and the growing particles. Therefore, some deviation in the monodispersity of the sample following this procedure is inevitable [5.42]. The BET surface area of the particles resulted to be $12 \text{ m}^2/\text{g}$, much smaller than the geometrical surface area, indicating significant aggregation upon drying.

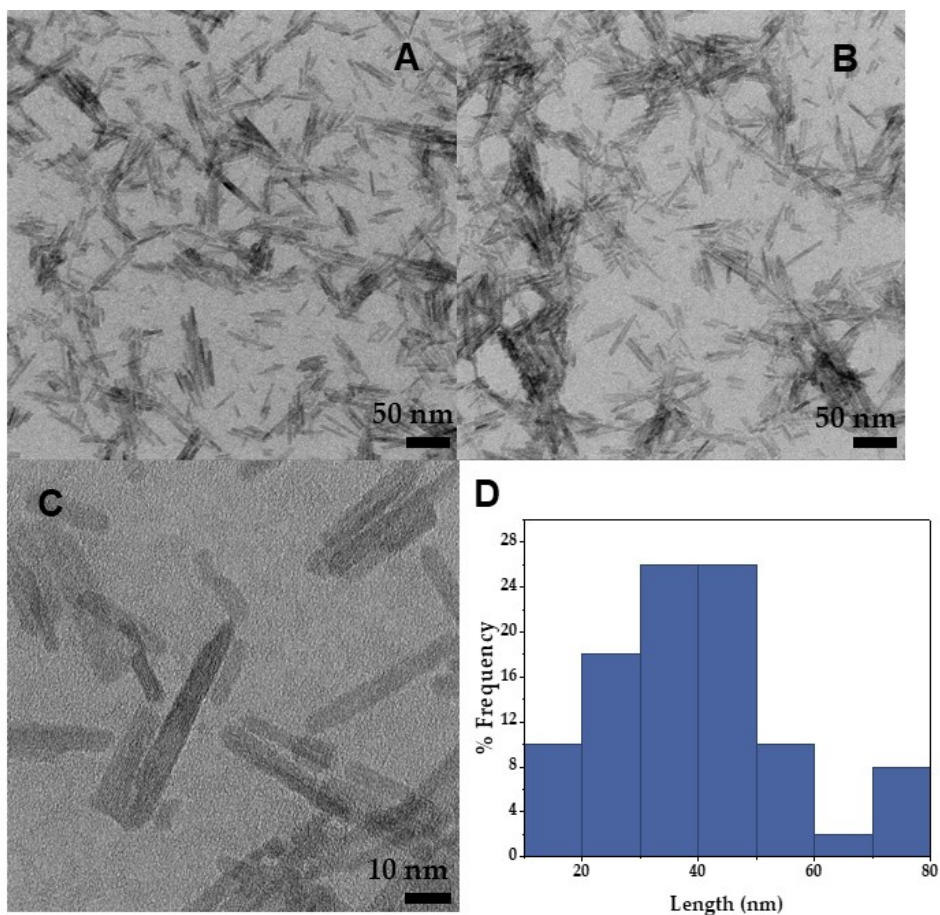


Figure 5.1: (A, B and C) HRTEM images of NR2 sample. Length distribution of NR2 (D).

Structural characterization

As shown in Figure 5.2A, the XRD patterns confirm the conversion of hematite to magnetite, by comparing with the reference data from the RRUFF database [5.52]. However, this technique does not allow us to differentiate between magnetite and maghemite, and both magnetic phases might be present.

For this reason, we also used Micro-Raman spectroscopy. The results (Figure 5.2B), reveal that the observed bands correspond to both maghemite (300 cm⁻¹ reference data, RRuff ID R140712 [5.52]) and magnetite (378, 515, and 718 cm⁻¹, RRuff ID R060656.3 [5.52]), suggesting that the particles are a mixture of maghemite and magnetite.

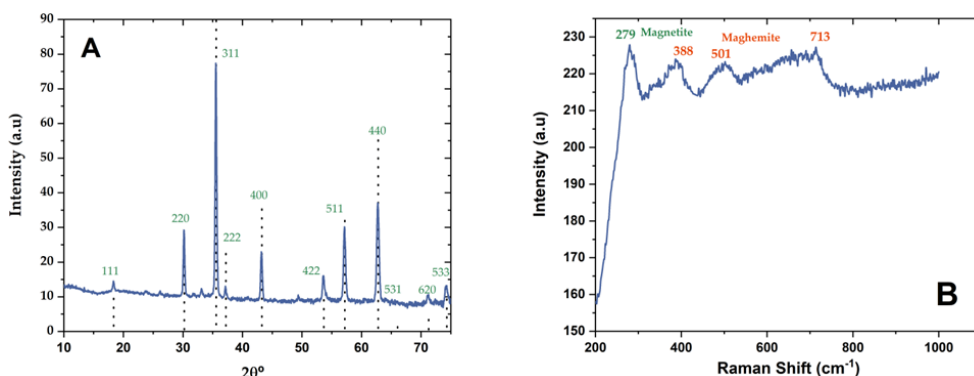


Figure 5.2: XRD pattern of NR2 (A; the dashed lines indicate the reference spectrum of magnetite, RRuff database) and Micro Raman spectrum of the sample (B).

Evaluation of the polymer coating

In order to use these nanoparticles in bio-applications, it is necessary for them to be biocompatible and for this biocompatibility to be stable over time. Therefore, the particles are coated with a triple polymer layer (polyethyleneimine, PEI/Poly(styrene sulfonate), PSS/PEI). To verify the successful particle coating in successive layers, the electrophoretic mobility was determined over a pH range of 3-9.5. As shown in Figure 5.3A, the isoelectric point (pH of zero electrophoretic mobility) of naked NR2 is around pH 4.65, slightly below the typical values for magnetite [5.53]. However, with the different coatings, it shifts according to their charge (towards the right for the cationic PEI polymer and towards the left for the anionic PSS polymer). In the final step, the coating with PEI, it is observed that the particle has a positive surface charge throughout the pH range. A significant stability can be foreseen for these particles, considering the electrosteric repulsion between them. Figure 5.10 of the Supplementary Information file shows that the dry coated particles are in fact formed by individual rods encapsulated by the polymer, with average size around 250 nm.

Moreover, thermogravimetric analysis was performed as a double check that the polymer coating has been successfully achieved (Figure 5.3B). First, we focus on the NR2 naked sample. We can observe that up to 207 °C the sample mass is reduced by 6.66%, a decrease associated with adsorbed water evaporation [5.54]. However, an appreciable mass gain is observed at 382 °C, followed by a mass decrease of 1.4% around 443°C. It is worth noting that this phenomenon is also observed in the case of polymer-coated nanorods. Regarding the weight increment, it can be associated with partial oxidation of the particles. Although the nitrogen used in the analyzer is 99.99% pure, the small amount of oxygen, together with the possibility of air being entrapped between the powder particles while preparing the samples, can explain some degree of oxidation of the core particles. The high concentration of Fe^{2+} and the relatively

small mass gain (around 1%) suggest, in any case, that the amount of oxygen must be very low, and it should not lead to any significant mistake in the interpretation of the TGA data.

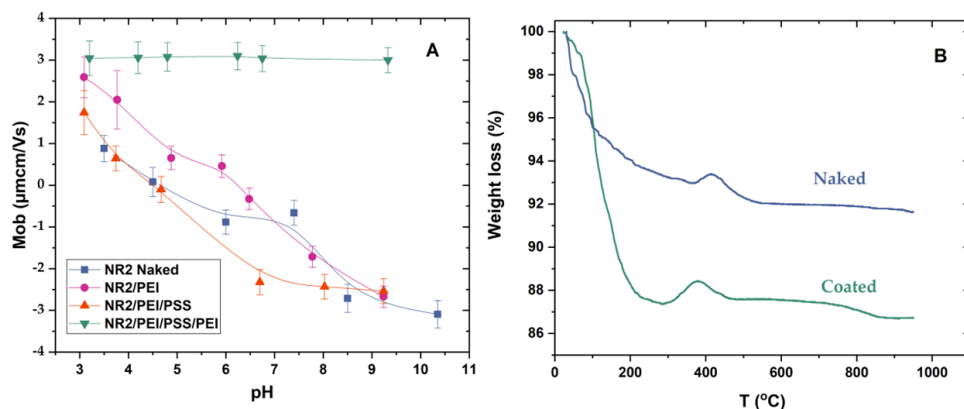


Figure 5.3: (A) Electrophoretic mobility as a function of pH, of naked, PEI, PEI/PSS, and PEI/PSS/PEI coatings. Ionic strength: 1 mM KCl. (B) TGA determinations of naked and polymer coated NR2 samples.

Secondly, we will focus on the polymer triple-layer coated nanorods. Similar to the bare nanorods, we can observe the evaporation of water molecules, which extends up to 156 $^{\circ}\text{C}$, and overlaps with the peak of PSS polymer degradation at around 230 $^{\circ}\text{C}$ [5.55]. These two processes result in a 10.5% mass loss, indicating the successful achievement of the polymer coating. On the other hand, a significant mass increase is observed as in the case of bare particles in the temperature range between 298-462 $^{\circ}\text{C}$ (1.041%), followed now by a subsequent loss (0.812%). It can also be observed a final weight loss due to PEI polymer degradation (0.870%). This degradation begins around 650 $^{\circ}\text{C}$ and extends up to 870 $^{\circ}\text{C}$, with the maximum weight loss occurring at 781 $^{\circ}\text{C}$. These values are slightly higher than those reported in the literature [5.56, 5.57].

As an additional test of the coating, FTIR spectra of the two kinds of particles were also performed, as shown in Fig. S2. Note that the differences between the spectra of naked and coated particles are barely distinguishable, but some absorption bands are observed in the coated particles, which are absent in the magnetic nanorods. These are located at wavenumbers (cm^{-1}) 836 (N-H bending), 1038, 1126, 1221 (C-N stretching), 1646 (N-H bending together with CH_2 scissors) [5.58].

Finally, XPS spectra are depicted in Fig. S3. It can be observed that NKLL, N1s and N2s electrons coming from the PEI coating, and S2s and S2p from the PSS substrate of the last PEI layer are emitted from PEI-coated samples, further confirming the presence of the polymer shell.

Magnetization results

As mentioned earlier, magnetic characterization is carried out in two different ways: first, by means of the SQUID magnetometer, and it has also been determined through AC magnetization. As can be seen in Figure 5.4A, the bare NR2 sample exhibits excellent magnetic properties, with a magnetic saturation of 81.7 emu/g. In addition, it can be verified that they do not exhibit hysteresis, a behavior typical of superparamagnetic materials, making them ideal for use in biomedical applications. This fact will guarantee that the temperature increases observed later when applying magnetic hyperthermia are due only to Neel and Brown relaxation (the latter predominating due to the size of the nanorods) [5.59].

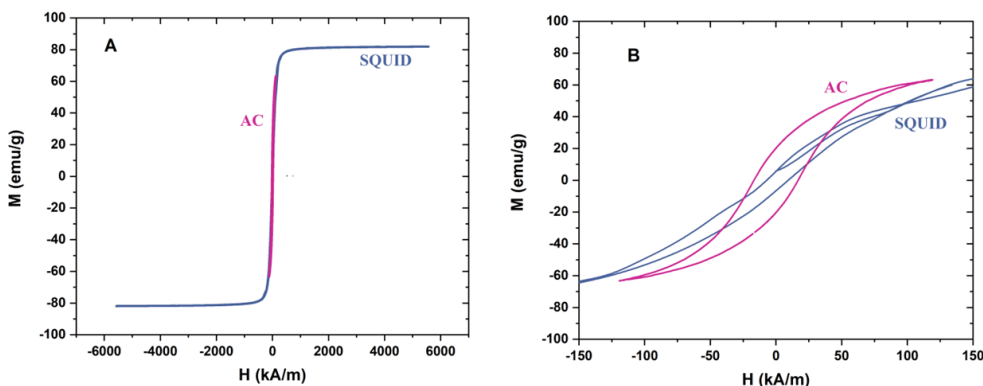


Figure 5.4: (A) Magnetization measurements (SQUID and AC magnetometry) at 292 K of naked NR2 particles. (B) Low-field detail of the plots in (A).

Furthermore, focusing on the H region between -150 kA/m to 150 kA/m (Figure 5.4B), we can observe differences between the two techniques used. These differences may be due to two factors: firstly, the minor cycles observable in AMF determinations are more affected by dipolar interactions than those obtained with the quasistatic SQUID method [5.60]. Additionally, according to the linear response theory, for a given temperature, the field frequency ω must be compared with the reciprocal of the relaxation time τ for magnetic moment orientation [5.61]: if $\omega\tau \ll 1$ (or in DC measurements), the moment of the particle will follow the field oscillations and no hysteresis will occur; if $\omega\tau$ is comparable to 1, the magnetization will lag behind the field, and hysteresis will be produced. This must be the case for the cycles presented in Figure 5.4B.

Cell viability and cell uptake assays

The viability and cellular internalization experiments of polymer-coated nanorods were conducted on the cell line MCF7. Figure 5.5 shows the cell viability as a function of the magnetic particle concentration. It can be observed that no toxicity was found up to 300 $\mu\text{g/mL}$. Above this concentration, for 400 and 500 $\mu\text{g/mL}$, a slight decrease in cell viability (down to 91% and 73%, respectively) was measured.

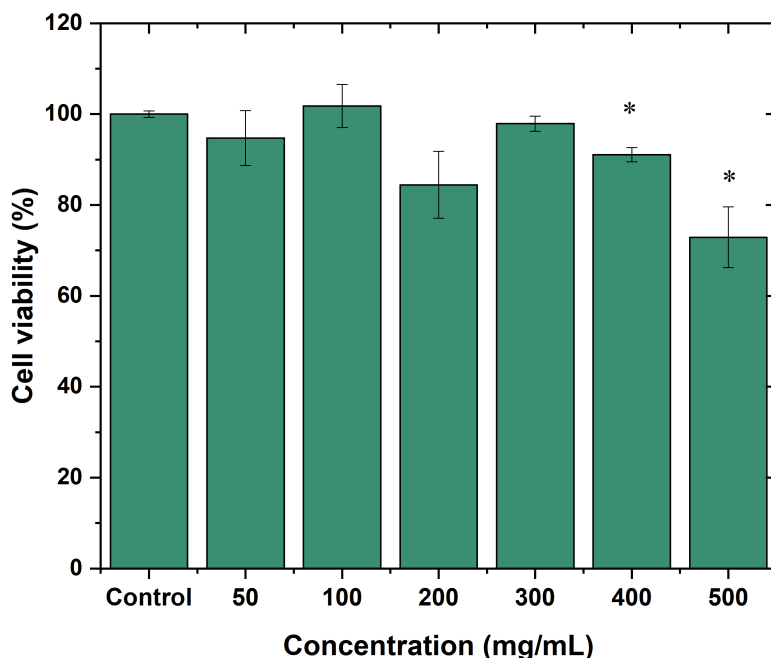


Figure 5.5: Cellular viability of the MCF7 cell line as a function of the concentration of polymer-coated NR2 particles. Data represent the mean \pm SEM of three independent experiments performed in triplicate; $p \leq 0.05$ (*).

The results of this experiment led us to choose for the next assays the maximum concentration of nanorods that does not produce toxicity in the cell, namely, 300 $\mu\text{g/mL}$. Next, we determine the percentage of internalization of NR2s in cells MCF7. In total, $82.41 \pm 0.99\%$ of NR2s were internalized when cells were incubated with 300 $\mu\text{g/mL}$ suspensions of NR2 particles coated by the three layers of polyelectrolyte for 24 hours. The findings demonstrate promising outcomes, as it has been demonstrated that high cellular internalization is crucial and necessary to achieve cell death in therapies such as hyperthermia or photothermia.

Magnetic hyperthermia

Next, we consider the evaluation of the thermal efficiency of these particles in magnetic hyperthermia. To characterize the particles for future bio-applications, frequency and field sweeps were performed, allowing us to determine the optimal parameters for these samples. Figure 5.6A shows the temperature elevations achieved as a function of time for fields of increasing amplitude and fixed frequency (114 kHz). The effect of frequency for constant amplitude (17 kA/m) is plotted in Figure 5.6B. All the data presented in this figure correspond to 5 mg/mL particle concentration. Results for other concentrations can be found in the Supplementary Information (SI) file (Figure 5.13, varying field strength; Figure 5.14, varying frequency; and Figure 5.15, SAR values obtained).

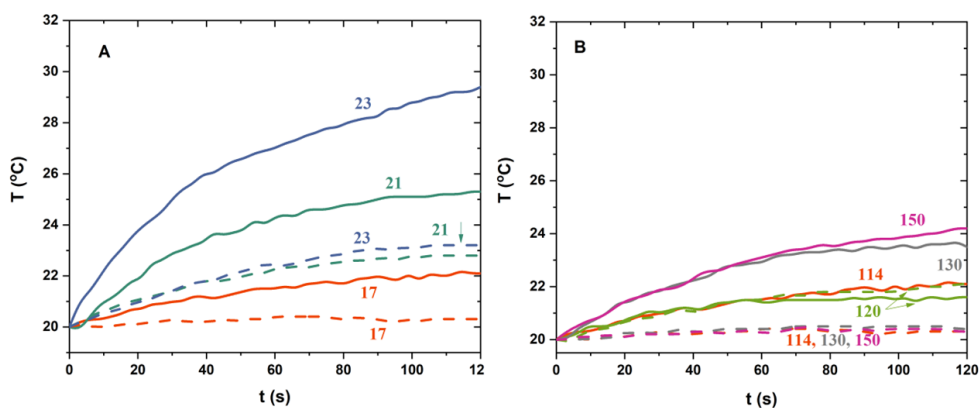


Figure 5.6: Temperature as a function of time in magnetic hyperthermia of naked (solid lines) and coated (dashed lines) nanorod suspensions of 5 mg/mL concentration. (A): constant frequency (114 kHz) and increasing field amplitude (indicated in kA/m); (B) constant field (17 kA/m) and increasing frequency (indicated in kHz).

As expected, the thermal efficiency in magnetic hyperthermia decreases slightly for coated particles as compared to bare ones, due to the presence of the magnetically inert polymer, for the same concentration of nanoparticles. In other words, at the same nanoparticle concentration, we will find a slightly lower iron concentration (which can be extracted from the TGA results). Table 1 shows the results. Note that, on average, the polymer coated particles contain about 85 % magnetic material. For this reason, in magnetic hyperthermia, we observe that the particles coated with polymer achieve lower temperatures, as shown in Figure 5.6A, B. This apparent disadvantage is compensated for to a large extent when one considers that the coating makes the particles biocompatible and quite stable, so an increased concentration of particles might be considered for a given bio-application, without risk of particle aggregation in the body fluids.

Figure 5.6A demonstrates that both the heating rate and the maximum temperature reached increase with the field amplitude, as expected for fields much lower than that corresponding to saturation. The study for varying frequencies presented in Figure 5.6B shows that while for bare NR2 increasing the frequency improves the thermal response, for the polymer-coated sample the maximum response occurs at 120 kHz. This indicates that the polymer has some effect on the relaxation time of the nanorods, probably reducing the overall anisotropy by quenching the orientation of surface magnetic moments.

The response is quantified by calculation of the SAR values, detailed in Figure 5.7. It is worth mentioning that the SAR calculation has taken into account the mass of magnetic material, obtained from the TGA result, data available in Table 5.1. When normalizing each of the samples by the amount of magnetic material, we observe that there are still differences between those not coated with polymer (exhibiting lower SAR values) compared to bare ones. The polymer coating thus has a measurable effect on the thermal efficiency of the particles.

C (mg/mL)	$C_{magnetite}$ (mg/mL) Naked particles	$C_{magnetite}$ (mg/mL) Polymer coated particles
2.5	2.3	2.2
5	4.6	4.3
10	9.2	8.7

Table 5.1: Magnetite concentration in suspensions of magnetic particles of the nominal concentrations C indicated.

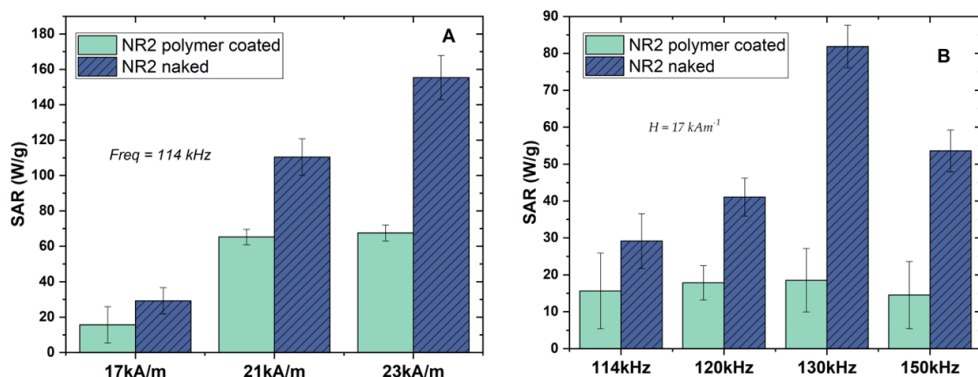


Figure 5.7: SAR evaluation for the bare NR2 particles, and for polymer-coated nanorods, at a frequency of 114 kHz and the field amplitudes indicated. (A): constant frequency; (B): constant field amplitude (17 kA/m).

From the data in Figure 5.7, it can be predicted that the best conditions for magnetic hyperthermia application would be 114 kHz and 23 kA/m, naked particles better than coated ones. In fact, in the case of bare nanorods, at concentrations of 5 mg/mL and a frequency of 114 kHz with a field intensity of 21 kA/m, we can enter the hyperthermia range and achieve cell death within 3 minutes. However, for polymer-coated nanorods, we would need to increase the concentration to 10 mg/mL (Figures 5.12-5.14) to achieve hyperthermia under the same time frame.

Regarding the effect of concentration on SAR, Figure 5.6 demonstrates that increasing the concentration does not mean a larger hyperthermia response, but rather the reverse: particle interactions and formation of possible aggregates reduce the SAR, as found in other works, where particle stability is demonstrated to be of utmost importance [5.62].

Photothermia

The evolution of temperature when heating of the systems is performed by photothermia is plotted in Figure 5.8A, for 5 mg/mL suspensions of bare and coated nanorods, and different specific powers of the 850 nm laser. The corresponding SAR values (in this case the total mass of the particles is used, not just their magnetic component) are depicted in Figure 5.8B.

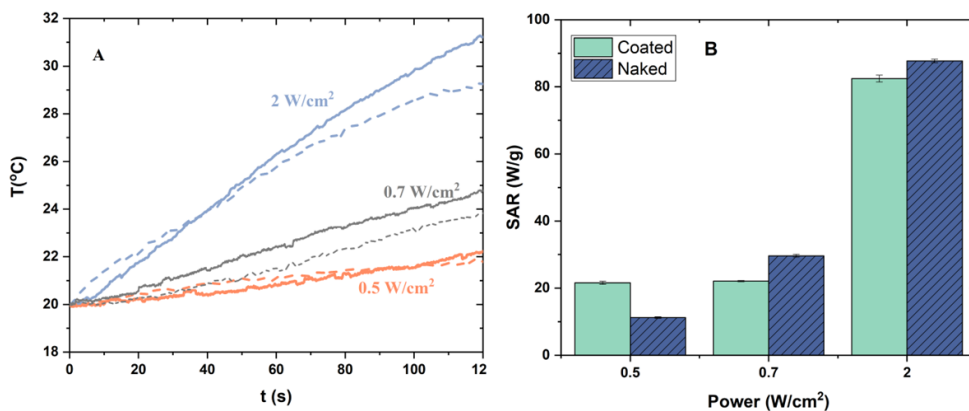


Figure 5.8: Temperature increases for bare and polymer-coated NR2 samples when irradiated by a laser (850 nm) (A); SAR evaluation (B). Three specific laser powers are tested (0.5, 0.7, and 2 W/cm²).

The (expected) improved heating efficiency (as represented by SAR values) achieved for higher laser powers is clearly demonstrated, although, in contrast to magnetic hyperthermia, it is not immediately clear that naked particles are better photothermia agents. It appears as if the polymer coating contributes to IR light

absorption, while the magnetic core means a lesser contribution except when the laser power is highest.

Cytotoxicity of treatments

Finally, the effectiveness of the two techniques (magnetic hyperthermia and photothermia) as treatments against MCF7 tumor cells will be discussed. In the case of magnetic hyperthermia treatment, triplicates were maintained for 2 hours in an alternating magnetic field of 23 kA/m and 114 kHz. By working with lower concentrations of nanoparticles *in vitro*, we have reduced the concentration used in the characterization of magnetic hyperthermia from 5 mg/mL to 300 $\mu\text{g/mL}$. This concentration reduction implies the need to prolong the treatment application time to reach the optimal temperatures needed to induce tumor cell death, as demonstrated in previous research [5.63, 5.64].

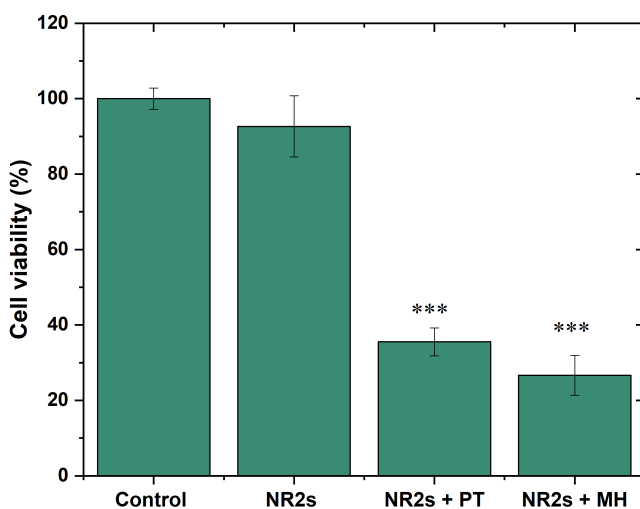


Figure 5.9: Cell viability of MCF7 cells following treatment with EMEM medium (control) and NR2s polymer coated nanorods (300 $\mu\text{g/mL}$) in the absence or upon application of magnetic hyperthermia (MH) and photothermia (PT). Data represent the means \pm SEM of three independent experiments performed in triplicate; $p \leq 0.001$ (***)

On the other hand, in the case of photothermia, the cells were maintained in the hyperthermia range (42–46 $^{\circ}\text{C}$) for 10 minutes, irradiating the triplicates with a wavelength of 850 nm and a power of 0.7 W/cm^2 , which is within tolerable limits and in the range used by other authors [5.64–5.66]. Moreover, as shown in Figure 5.5,

the sample NR2 coated with the polymeric layer did not show cytotoxicity up to 300 $\mu\text{g/mL}$, which is why this concentration was chosen for the experiments.

As can be seen in Figure 5.9, after exposing NR2s to AMF of 23 kA/m and 114 kHz, a significant reduction in MCF7 cell viability (down to $73.3 \pm 5.3\%$) is achieved. Through the implementation of photothermia, temperatures within the range of 42-46 $^{\circ}\text{C}$ were attained for a duration of 10 minutes, resulting in a cell death of $64.4 \pm 3.7\%$. It is evident that there is significant cell death when cells are incubated with 300 $\mu\text{g/mL}$ and treated with MH or PT, with no differences observed in cell death between both strategies.

5.4. Conclusions

In this work we have first described the synthesis of superparamagnetic nanorods, with magnetite + maghemite composition, length around 40 nm and axial ratio of 1:8. The saturation magnetization of the particles is high, above 80 emu/g, and they are susceptible to polymer coating (PEI(+)/PSS(-)/PEI(+)), demonstrating their excellent biocompatibility up to concentrations of 300 $\mu\text{g/mL}$. Breast tumor cells, MCF7, were used throughout the study. Electrophoretic mobility determinations and thermogravimetric analysis demonstrate the quality of the coating, with approximately 5 % by mass of polymer. By applying alternating magnetic fields of amplitude up to 23 kA/m and frequency up to 150 kHz, it could be demonstrated that both bare and coated particles (especially the former) behave as excellent magnetic hyperthermia agents, with specific heating power (SAR) exceeding 100 W/g. If the suspensions (in all cases containing 5 mg/mL of particles) are irradiated with an IR laser of 850 nm and specific power up to 2 W/cm^2 , photothermal heating is also observed, generally more efficient for the polymer-coated particles. Both treatments demonstrate the capacity to produce cell death.

Acknowledgments

FEDER/Junta de Andalucía-Consejería de Transformación Económica, Industria, Conocimiento y Universidades, Programa Operativo FEDER 2014-2020, Spain (Grant No. P20_00346 and A-FQM492-UGR20) is gratefully acknowledged. G.R.I, Á.V.D and M.L, thank also the financial assistance of the grant TED2021-131855BI00/Unión Europea Next Generation EU/PRTR and European Union's Horizon 2020 research and innovation programme under the Marie Skłodowska-Curie grant agreement No 10106426. G.R.I, Á.V. D and M.L thanks Instituto de Investigación Biosanitaria ibs. GRANADA, España. M.J.-C. wishes to acknowledge a FPU2021 grant (ref. FPU21_01529) from the Ministerio de Universidades (Spain).

Appendix. Supplementary Information

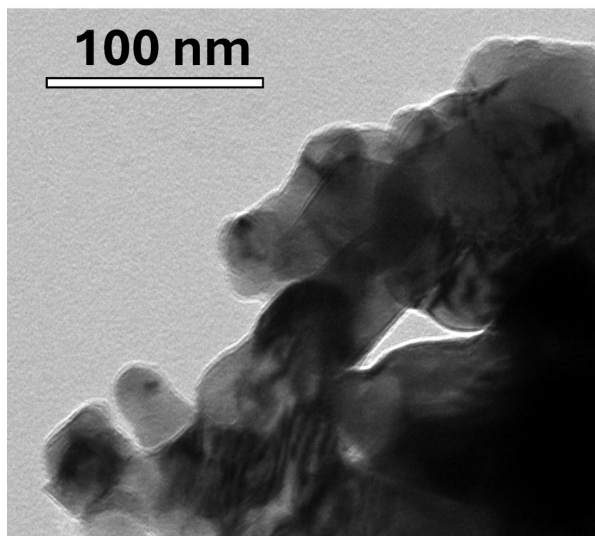


Figure 5.10: HRTEM picture of PEI-coated nanorods.

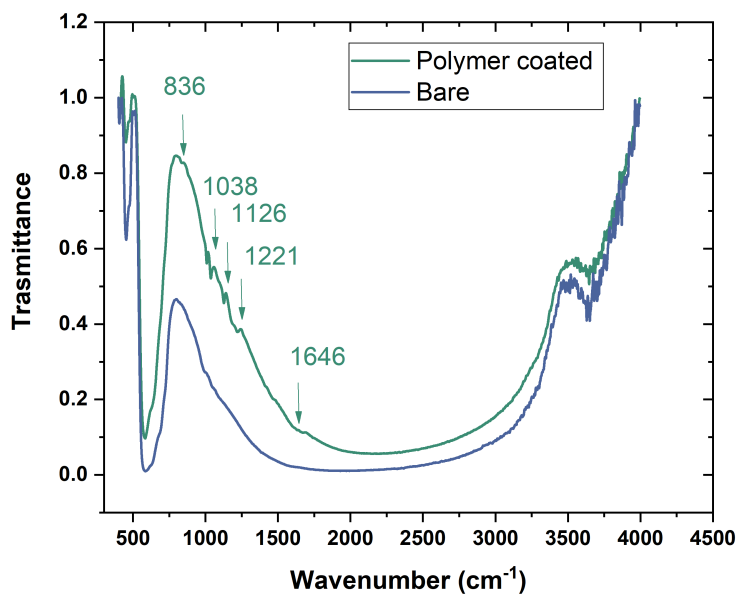


Figure 5.11: FTIR spectra of bare and polymer-coated samples.

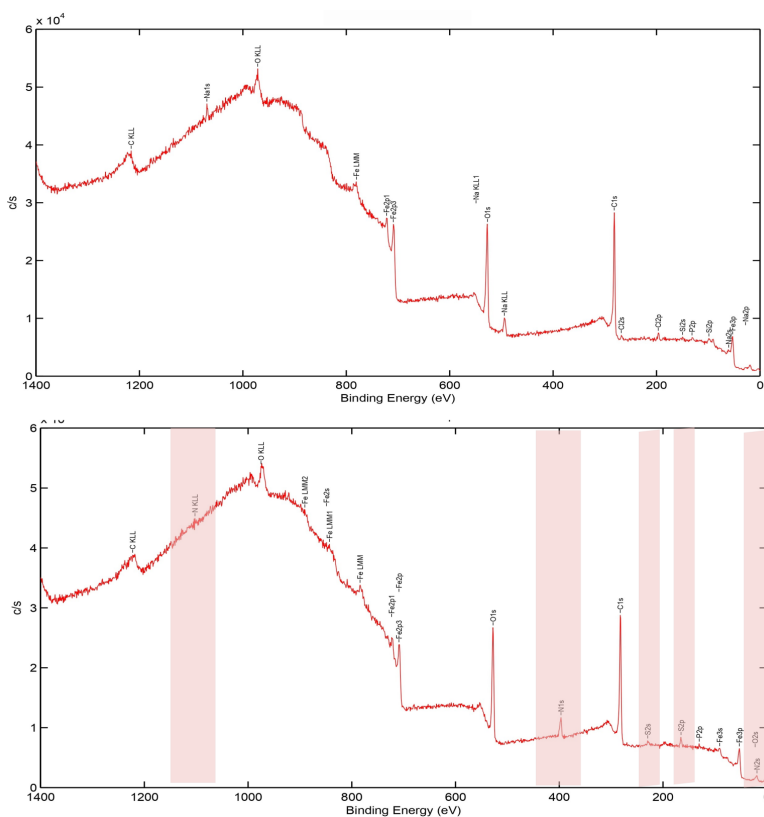


Figure 5.12: XPS spectra of bare (above) and polymer-coated samples (below). The electrons corresponding to the PEI or PSS coatings are marked in the bottom panel.

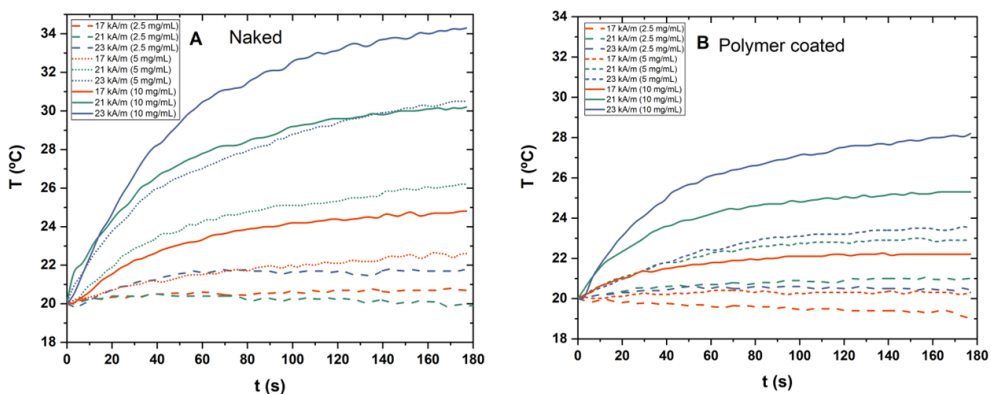


Figure 5.13: Temperature increases as a function of time for naked particles (A) and particles coated with a triple polymer layer (B), at a given frequency of 114 kHz, and different field amplitudes of 17 kA/m, 21 kA/m, and 23 kA/m. Additionally, for both cases, a concentration sweep is also shown at 2.5 mg/mL, 5 mg/mL, and 10 mg/mL.

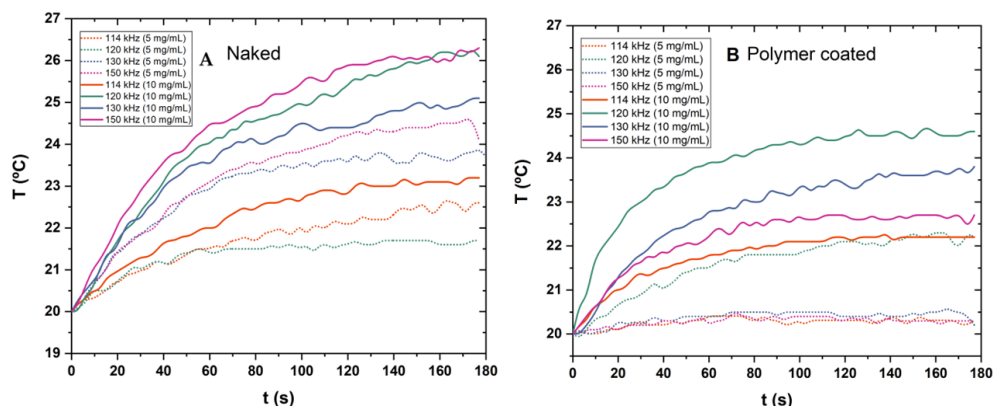


Figure 5.14: Temperature increases as a function of time for naked particles (A) and particles coated with a triple polymer layer (B), at a given field amplitude of 17 kA/m, and different frequencies in the range of 114-150 kHz, using two different concentrations of NR2 samples: 5 and 10 mg/mL.

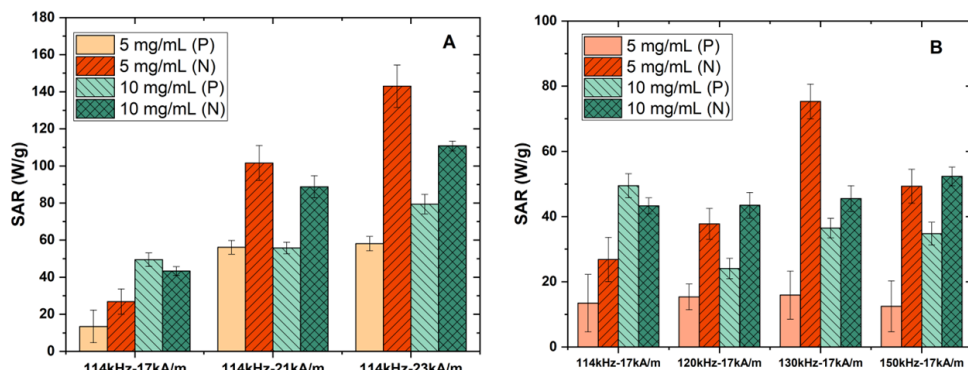


Figure 5.15: SAR values for suspensions of naked (N) and polymer coated (P) particles. (A): constant frequency; (B) constant field.

Bibliography

- [5.1] An-Hui Lu, E emsp14L Salabas, and Ferdi Schüth. Magnetic nanoparticles: synthesis, protection, functionalization, and application. *Angewandte Chemie International Edition*, 46(8):1222–1244, 2007.
- [5.2] Deanna D Stueber, Jake Villanova, Itzel Aponte, Zhen Xiao, and Vicki L Colvin. Magnetic nanoparticles in biology and medicine: past, present, and future trends. *Pharmaceutics*, 13(7):943, 2021.
- [5.3] Vanessa Valdiglesias, Natalia Fernández-Bertólez, Gözde Kiliç, Carla Costa, Solange Costa, Sonia Fraga, Maria Joao Bessa, Eduardo Pásaro, João Paulo Teixeira, and Blanca Laffon. Are iron oxide nanoparticles safe? Current knowledge and future perspectives. *Journal of Trace Elements in Medicine and Biology*, 38:53–63, 2016.
- [5.4] Jeotikanta Mohapatra, Meiyang Xing, Julian Beatty, Jacob Elkins, Takele Seda, Sanjay R Mishra, and J Ping Liu. Enhancing the magnetic and inductive heating properties of Fe₃O₄ nanoparticles via morphology control. *Nanotechnology*, 31(27):275706, 2020.
- [5.5] Suoyuan Lian, Zhenhui Kang, Enbo Wang, Min Jiang, Changwen Hu, and Lin Xu. Convenient synthesis of single crystalline magnetic Fe₃O₄ nanorods. *Solid State Communications*, 127(9-10):605–608, 2003.
- [5.6] Xiong Wang, Xiangying Chen, Lisheng Gao, Huagui Zheng, Mingrong Ji, Chenming Tang, Tao Shen, and Zude Zhang. Synthesis of β-FeOOH and α-Fe₂O₃ nanorods and electrochemical properties of β-FeOOH. *Journal of Materials Chemistry*, 14(5):905–907, 2004.
- [5.7] Rainer Birringer, Helmut Wolf, Christian Lang, Andreas Tschöpe, and Andreas Michels. Magnetic nanorods: Genesis, self-organization and applications. *Zeitschrift für Physikalische Chemie*, 222(2-3):229–255, 2008.
- [5.8] C Gispert, A Serrà, ME Alea, M Rodrigues, Elvira Gómez, M Mora, M Ll Sagristá, L Pérez-García, and E Vallés. Electrochemical preparation and

- characterization of magnetic core–shell nanowires for biomedical applications. *Electrochemistry Communications*, 63:18–21, 2016.
- [5.9] Muhammad Shahbaz Beg, Jeotikanta Mohapatra, Lina Pradhan, D Patkar, and D Bahadur. Porous $\text{Fe}_3\text{O}_4\text{-SiO}_2$ core-shell nanorods as high-performance MRI contrast agent and drug delivery vehicle. *Journal of Magnetism and Magnetic Materials*, 428:340–347, 2017.
- [5.10] Liron L Israel, Anna Galstyan, Eggehard Holler, and Julia Y Ljubimova. Magnetic iron oxide nanoparticles for imaging, targeting and treatment of primary and metastatic tumors of the brain. *Journal of Controlled Release*, 320:45–62, 2020.
- [5.11] E Celeste Welch, Jessica M Powell, Tobias B Clevinger, Alexis E Fairman, and Anita Shukla. Advances in biosensors and diagnostic technologies using nanostructures and nanomaterials. *Advanced Functional Materials*, 31(44):2104126, 2021.
- [5.12] Ali Ramzannezhad, Pooria Gill, and Ali Bahari. Fabrication of magnetic nanorods and their applications in medicine. *BioNanoMaterials*, 18(3-4):20170008, 2017.
- [5.13] Jeotikanta Mohapatra, Arijit Mitra, Himanshu Tyagi, D Bahadur, and M Aslam. Iron oxide nanorods as high-performance magnetic resonance imaging contrast agents. *Nanoscale*, 7(20):9174–9184, 2015.
- [5.14] Raja Das, Javier Alonso, Zohreh Nemati Porshokouh, Vijaysankar Kalappattil, David Torres, Manh-Huong Phan, Eneko Garaio, José Ángel García, Jose Luis Sanchez Llamazares, and Hariharan Srikanth. Tunable high aspect ratio iron oxide nanorods for enhanced hyperthermia. *The Journal of Physical Chemistry C*, 120(18):10086–10093, 2016.
- [5.15] Elizaveta M Gubanova, Nikolai A Usov, and Vladimir A Oleinikov. Heating ability of elongated magnetic nanoparticles. *Beilstein Journal of Nanotechnology*, 12(1):1404–1412, 2021.
- [5.16] Vasily A Bautin, Ruslan A Rytov, Yulia A Nalench, Nelly S Chmelyuk, Irina A Antoshina, and Nikolai A Usov. Specific absorption rate in quasispherical and elongated aggregates of magnetite nanoparticles: Experimental characterization and numerical simulation. *Ceramics International*, 49(10):16379–16384, 2023.
- [5.17] Yajing Shen, Congyu Wu, Taro QP Uyeda, Gustavo R Plaza, Bin Liu, Yu Han, Maciej S Lesniak, and Yu Cheng. Elongated nanoparticle aggregates in cancer cells for mechanical destruction with low frequency rotating magnetic field. *Theranostics*, 7(6):1735, 2017.

- [5.18] Matteo Avolio, Helena Gavilán, Eva Mazario, Francesca Brero, Paolo Arosio, Alessandro Lascialfari, and M Puerto Morales. Elongated magnetic nanoparticles with high-aspect ratio: a nuclear relaxation and specific absorption rate investigation. *Physical Chemistry Chemical Physics*, 21(34):18741–18752, 2019.
- [5.19] Darja Lisjak and Alenka Mertelj. Anisotropic magnetic nanoparticles: A review of their properties, syntheses and potential applications. *Progress in Materials Science*, 95:286–328, 2018.
- [5.20] WC Dewey, LE Hopwood, SA Sapareto, and LE Gerweck. Cellular responses to combinations of hyperthermia and radiation. *Radiology*, 123(2):463–474, 1977.
- [5.21] Agnieszka Włodarczyk, Szymon Gorgoń, Adrian Radoń, and Karolina Bajdak-Rusinek. Magnetite nanoparticles in magnetic hyperthermia and cancer therapies: Challenges and perspectives. *Nanomaterials*, 12(11):1807, 2022.
- [5.22] Bert Hildebrandt, Peter Wust, Olaf Ahlers, Annette Dieing, Geetha Sreenivasa, Thoralf Kerner, Roland Felix, and Hanno Riess. The cellular and molecular basis of hyperthermia. *Critical reviews in oncology/hematology*, 43(1):33–56, 2002.
- [5.23] Takeshi Kobayashi. Cancer hyperthermia using magnetic nanoparticles. *Biotechnology Journal*, 6(11):1342–1347, 2011.
- [5.24] Ihab M Obaidat, Bashar Issa, and Yousef Haik. Magnetic properties of magnetic nanoparticles for efficient hyperthermia. *Nanomaterials*, 5(1):63–89, 2015.
- [5.25] Felisa Reyes-Ortega, Ángel V Delgado, and Guillermo R Iglesias. Modulation of the magnetic hyperthermia response using different superparamagnetic iron oxide nanoparticle morphologies. *Nanomaterials*, 11(3):627, 2021.
- [5.26] Pinar Avci, Asheesh Gupta, Magesh Sadasivam, Daniela Vecchio, Zeev Pam, Nadav Pam, and Michael R Hamblin. Low-level laser (light) therapy (lllt) in skin: stimulating, healing, restoring. In *Seminars in cutaneous medicine and surgery*, volume 32, page 41. NIH Public Access, 2013.
- [5.27] Jing Tang, Matt Myers, Ken A Bosnick, and Louis E Brus. Magnetite Fe_3O_4 nanocrystals: spectroscopic observation of aqueous oxidation kinetics. *The Journal of Physical Chemistry B*, 107(30):7501–7506, 2003.
- [5.28] Eric D Smolensky, Hee-Yun E Park, Yue Zhou, Gabriele A Rolla, Małgorzata Marjańska, Mauro Botta, and Valérie C Pierre. Scaling laws at the nanosize: the effect of particle size and shape on the magnetism and relaxivity of iron oxide nanoparticle contrast agents. *Journal of Materials Chemistry B*, 1(22):2818–2828, 2013.

- [5.29] Abolfazl Akbarzadeh, Mohammad Samiei, and Soodabeh Davaran. Magnetic nanoparticles: preparation, physical properties, and applications in biomedicine. *Nanoscale Research Letters*, 7:1–13, 2012.
- [5.30] Lijo P Mona, Sandile P Songca, and Peter A Ajibade. Synthesis and encapsulation of iron oxide nanorods for application in magnetic hyperthermia and photothermal therapy. *Nanotechnology Reviews*, 11(1):176–190, 2021.
- [5.31] Carlos Martinez-Boubeta, Konstantinos Simeonidis, Antonios Makridis, Makis Angelakeris, Oscar Iglesias, Pablo Guardia, Andreu Cabot, Lluís Yedra, Sonia Estradé, Francesca Peiró, et al. Learning from nature to improve the heat generation of iron-oxide nanoparticles for magnetic hyperthermia applications. *Scientific Reports*, 3(1):1652, 2013.
- [5.32] Sai Geng, Haitao Yang, Xiao Ren, Yihao Liu, Shuli He, Jun Zhou, Na Su, Yongfeng Li, Chunming Xu, Xiangqun Zhang, et al. Anisotropic magnetite nanorods for enhanced magnetic hyperthermia. *Chemistry—An Asian Journal*, 11(21):2996–3000, 2016.
- [5.33] Poornima Kolhar, Aaron C Anselmo, Vivek Gupta, Kapil Pant, Balabhaskar Prabhakarandian, Erkki Ruoslahti, and Samir Mitragotri. Using shape effects to target antibody-coated nanoparticles to lung and brain endothelium. *Proceedings of the National Academy of Sciences*, 110(26):10753–10758, 2013.
- [5.34] YAN Geng, Paul Dalhaimer, Shenshen Cai, Richard Tsai, Manorama Tewari, Tamara Minko, and Dennis E Discher. Shape effects of filaments versus spherical particles in flow and drug delivery. *Nature nanotechnology*, 2(4):249–255, 2007.
- [5.35] Rui Cheng, Weijie Huang, Lijie Huang, Bo Yang, Leidong Mao, Kunlin Jin, Qichuan ZhuGe, and Yiping Zhao. Acceleration of tissue plasminogen activator-mediated thrombolysis by magnetically powered nanomotors. *ACS Nano*, 8(8):7746–7754, 2014.
- [5.36] Weijie Huang, Fengchang Yang, Lu Zhu, Rui Qiao, and Yiping Zhao. Manipulation of magnetic nanorod clusters in liquid by non-uniform alternating magnetic fields. *Soft Matter*, 13(20):3750–3759, 2017.
- [5.37] Yuri I Golovin, Sergey L Gribanovsky, Dmitry Y Golovin, Natalia L Klyachko, Alexander G Majouga, Tlyssa M Master, Marina Sokolsky, and Alexander V Kabanov. Towards nanomedicines of the future: Remote magneto-mechanical actuation of nanomedicines by alternating magnetic fields. *Journal of Controlled Release*, 219:43–60, 2015.
- [5.38] Jongnam Park, Bonil Koo, Yosun Hwang, Chejin Bae, Kwangjin An, Je-Geun Park, Hyun Min Park, and Taeghwan Hyeon. Novel synthesis of magnetic Fe₂P

- nanorods from thermal decomposition of continuously delivered precursors using a syringe pump. *Angewandte Chemie*, 116(17):2332–2335, 2004.
- [5.39] Trevor P Almeida, Michael W Fay, Yanqiu Zhu, and Paul D Brown. Hydrothermal growth mechanism of α -Fe₂O₃ nanorods derived by near in situ analysis. *Nanoscale*, 2(11):2390–2399, 2010.
- [5.40] Hauke Kloust, Robert Zierold, Jan-Philip Merkl, Christian Schmidtke, Artur Feld, Elmar Poñselt, Andreas Kornowski, Kornelius Nielsch, and Horst Weller. Synthesis of iron oxide nanorods using a template mediated approach. *Chemistry of Materials*, 27(14):4914–4917, 2015.
- [5.41] Tadao Sugimoto, Yinsheng Wang, Hiroyuki Itoh, and Atsushi Muramatsu. Systematic control of size, shape and internal structure of monodisperse α -Fe₂O₃ particles. *Colloids and Surfaces A: Physicochemical and Engineering Aspects*, 134(3):265–279, 1998.
- [5.42] Tadao Sugimoto and Atsushi Muramatsu. Formation Mechanism of Monodispersed α -Fe₂O₃ Particles in Dilute FeCl₃ Solutions. *Journal of Colloid and Interface Science*, 184(2):626–638, 1996.
- [5.43] Manuel Ocaña, Maria P Morales, and Carlos J Serna. The growth mechanism of α -Fe₂O₃ ellipsoidal particles in solution. *Journal of Colloid and Interface Science*, 171(1):85–91, 1995.
- [5.44] Masataka Ozaki, Stanka Kratochvil, and Egon Matijević. Formation of monodispersed spindle-type hematite particles. *Journal of Colloid and Interface Science*, 102(1):146–151, 1984.
- [5.45] Anisha A D’souza and Ranjita Shegokar. Polyethylene glycol (PEG): a versatile polymer for pharmaceutical applications. *Expert Opinion on Drug Delivery*, 13(9):1257–1275, 2016.
- [5.46] Ritu Goyal, Sushil K Tripathi, Esther Vazquez, Pradeep Kumar, and Kailash C Gupta. Biodegradable poly (vinyl alcohol)-polyethylenimine nanocomposites for enhanced gene expression in vitro and in vivo. *Biomacromolecules*, 13(1):73–83, 2012.
- [5.47] María del Mar Ramos-Tejada, Julian L Viota, Katarzyna Rudzka, and Angel V Delgado. Preparation of multi-functionalized Fe₃O₄/Au nanoparticles for medical purposes. *Colloids and Surfaces B: Biointerfaces*, 128:1–7, 2015.
- [5.48] Salvatore Calogero Gaglio, Ylenia Jabalera, Manuel Montalbán-López, Ana Cristina Millán-Placer, Marina Lázaro-Callejón, Mercedes Maqueda, María Paz Carrasco-Jimenez, Alejandro Laso, José A Aínsa, Guillermo R Iglesias, et al. Embedding biomimetic magnetic nanoparticles coupled with

- peptide AS-48 into PLGA to treat intracellular pathogens. *Pharmaceutics*, 14(12):2744, 2022.
- [5.49] Felisa Reyes-Ortega, Ángel V Delgado, Elena K Schneider, BL Checa Fernández, and GR Iglesias. Magnetic nanoparticles coated with a thermosensitive polymer with hyperthermia properties. *Polymers*, 10(1):10, 2017.
- [5.50] Ylenia Jabalera, Alberto Sola-Leyva, María P Carrasco-Jiménez, Guillermo R Iglesias, and Concepcion Jimenez-Lopez. Synergistic photothermal-chemotherapy based on the use of biomimetic magnetic nanoparticles. *Pharmaceutics*, 13(5):625, 2021.
- [5.51] Beatriz Sanz, M Pilar Calatayud, Nicolás Cassinelli, M Ricardo Ibarra, and Gerardo F Goya. Long-term stability and reproducibility of magnetic colloids are key issues for steady values of specific power absorption over time. *European Journal of Inorganic Chemistry*, 2015(27):4524–4531, 2015.
- [5.52] Barbara Lafuente, Robert T Downs, Hexiong Yang, Nate Stone, Thomas Armbruster, Rosa Micaela Danisi, et al. The power of databases: the RRUFF project. *Highlights in mineralogical crystallography*, 1:25, 2015.
- [5.53] F Vereda, J de Vicente, and R Hidalgo-Álvarez. Colloidal characterization of micron-sized rod-like magnetite particles. *Colloids and Surfaces A: Physicochemical and Engineering Aspects*, 319(1-3):122–129, 2008.
- [5.54] Jane Cathleen Gabunada, Mohanraj Vinothkannan, Dong Hee Kim, Ae Rhan Kim, and Dong Jin Yoo. Magnetite nanorods stabilized by polyaniline/reduced graphene oxide as a sensing platform for selective and sensitive non-enzymatic hydrogen peroxide detection. *Electroanalysis*, 31(8):1507–1516, 2019.
- [5.55] Masahiro Rikukawa and K Sanui. Proton-conducting polymer electrolyte membranes based on hydrocarbon polymers. *Progress in Polymer Science*, 25(10):1463–1502, 2000.
- [5.56] Jinjin Shi, Hongling Zhang, Lei Wang, Lulu Li, Honghong Wang, Zhenzhen Wang, Zhi Li, Chengqun Chen, Lin Hou, Chaofeng Zhang, et al. Pei-derivatized fullerene drug delivery using folate as a homing device targeting to tumor. *Biomaterials*, 34(1):251–261, 2013.
- [5.57] Nehar Celikkin, Lucie Jakubcová, Martin Zenke, Mareike Hoss, John Erik Wong, and Thomas Hieronymus. Polyelectrolyte coating of ferumoxytol nanoparticles for labeling of dendritic cells. *Journal of Magnetism and Magnetic Materials*, 380:39–45, 2015.

- [5.58] Kinga Grenda, Alexander Idström, Lars Evenäs, Michael Persson, Krister Holmberg, and Romain Bordes. An analytical approach to elucidate the architecture of polyethyleneimines. *Journal of Applied Polymer Science*, 139(7):51657, 2022.
- [5.59] Daniel Ortega and Quentin A Pankhurst. Magnetic hyperthermia. *Nanoscience*, 1(60):e88, 2013.
- [5.60] Dirk H Ortgies, Leonor De La Cueva, Blanca Del Rosal, Francisco Sanz-Rodríguez, Nuria Fernandez, M Carmen Iglesias-De La Cruz, Gorka Salas, David Cabrera, Francisco J Teran, Daniel Jaque, et al. In vivo deep tissue fluorescence and magnetic imaging employing hybrid nanostructures. *ACS Applied Materials & Interfaces*, 8(2):1406–1414, 2016.
- [5.61] Julian Carrey, Boubker Mehdaoui, and Marc Respaud. Simple models for dynamic hysteresis loop calculations of magnetic single-domain nanoparticles: Application to magnetic hyperthermia optimization. *Journal of Applied Physics*, 109(8), 2011.
- [5.62] G Iglesias, AV Delgado, M Kujda, and MM Ramos-Tejada. Magnetic hyperthermia with magnetite nanoparticles: Electrostatic and polymeric stabilization. *Colloid and Polymer Science*, 294:1541–1550, 2016.
- [5.63] Ylenia Jabalera, Alberto Sola-Leyva, Ana Peigneux, Federica Vurro, Guillermo R Iglesias, Jesus Vilchez-Garcia, Inmaculada Pérez-Prieto, Francisco J Aguilar-Troyano, Luisa C López-Cara, María P Carrasco-Jiménez, et al. Biomimetic magnetic nanocarriers drive choline kinase alpha inhibitor inside cancer cells for combined chemo-hyperthermia therapy. *Pharmaceutics*, 11(8):408, 2019.
- [5.64] Héctor L Rodríguez-Luccioni, Magda Latorre-Esteves, Janet Méndez-Vega, Orlando Soto, Ana R Rodríguez, Carlos Rinaldi, and Madeline Torres-Lugo. Enhanced reduction in cell viability by hyperthermia induced by magnetic nanoparticles. *International Journal of Nanomedicine*, pages 373–380, 2011.
- [5.65] Ana Espinosa, Jelena Kolosnjaj-Tabi, Ali Abou-Hassan, Anouchka Plan Sangnier, Alberto Curcio, Amanda KA Silva, Riccardo Di Corato, Sophie Neveu, Teresa Pellegrino, Luis M Liz-Marzán, et al. Magnetic (hyper) thermia or photothermia? progressive comparison of iron oxide and gold nanoparticles heating in water, in cells, and in vivo. *Advanced Functional Materials*, 28(37):1803660, 2018.
- [5.66] Huiyul Park, Jaemoon Yang, Jaemin Lee, Seungjoo Haam, In-Hong Choi, and Kyung-Hwa Yoo. Multifunctional nanoparticles for combined doxorubicin and photothermal treatments. *ACS Nano*, 3(10):2919–2926, 2009.

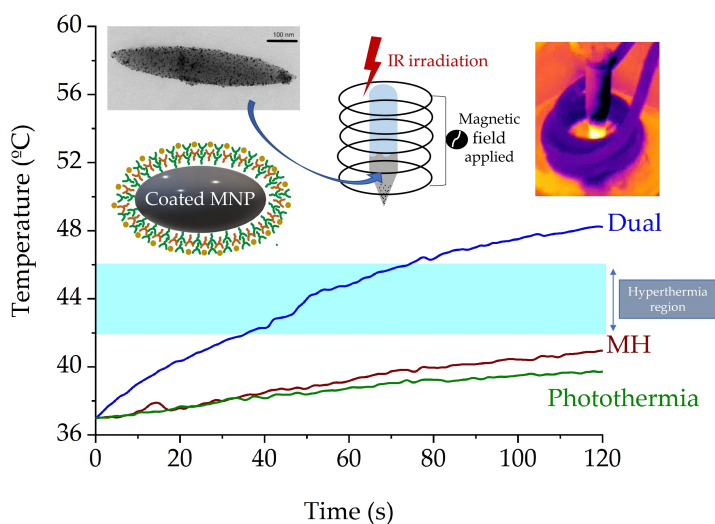
Chapter 6

Combined magnetic hyperthermia and photothermia with polyelectrolyte/gold-coated magnetic nanorods

M. Lázaro, P. Lupiáñez, JL. Arias, MP. Carrasco-Jiménez, ÁV. Delgado, GR. Iglesias, *Polymers* **2022**, *14*(22), 4913.

Abstract

Magnetite nanorods (MNRs) are synthesized based on the use of hematite nanoparticles of the desired geometry and dimensions as templates. The nanorods are shown to be highly monodisperse, with a 5:1 axial ratio, and with 275 nm long semiaxis. The MNRs are intended to be employed as magnetic hyperthermia and photothermia agents, and as drug vehicles. To achieve a better control of their photothermia response, the particles are coated with a layer of gold, after applying a branched polyethyleneimine (PEI, 2 kDa molecular weight) shell. Magnetic hyperthermia is performed by application of alternating magnetic fields with frequencies in the range 118-210 kHz and amplitudes up to 22 kA/m. Photothermia is carried out by subjecting the particles to a near-infrared (850 nm) laser, and three monochromatic lasers in the visible with wavelengths 480 nm, 505 nm, and 638 nm. Best results are obtained with the 505 nm laser, because of the proximity between this wavelength and that of the plasmon resonance. A so-called dual therapy is also tested, and the heating of the samples is found to be faster than with either method separately, so that the strengths of the individual fields can be reduced. Because of toxicity concerns with PEI coatings, viability of human hepatoblastoma HepG2 cells was tested after contact with nanorods suspensions up to 500 $\mu\text{g/mL}$ concentration. It was found that the cell viability was indistinguishable from control systems, so the particles can be considered non-cytotoxic *in vitro*. Finally, the release of the antitumor drug doxorubicin is investigated for the first time in the presence of the two external fields, and of their combination, with a clear improvement in the rate of drug release in the latter case.



6.1. Introduction

Magnetic nanoparticles (MNPs) are widely used in many different fields, but their potential in biomedicine stands out, particularly in the investigation of cancer treatment and diagnosis [6.1–6.3]. Although some are based on cobalt, nickel or zinc and thus have moderate biotoxicity, those based on iron oxides (maghemite, magnetite) are recognized as applicable nanomaterials for theranostic purposes.

The large variety of particles that have been synthesized opens a varied range of applications, going from the possibility of being used as contrast media in MRI [6.4], to that of becoming effective, directed, and specific drug transport vehicles [6.5]. Their response to magnetic fields capable of directing them to specified parts of the body and keep them there while carrying out their therapeutic role is another feature explaining their significance in the area. Furthermore, and this is the core of the present contribution, if the applied magnetic field is alternating, another application shows up, in which a lot of confidence has been deposited for at least two decades. This is the possibility of generating localized heat leading to the so-called magnetic hyperthermia, which has become an innovative treatment, considered a potential adjuvant to other cancer therapies. The application of such fields (of proper frequency and amplitude) produces energy loss in the form of heat which can be localized in the tumor, leading to cancer cell death. In fact, in magnetic hyperthermia, if MNPs are suspended in an aqueous medium, it is possible to raise their temperature by applying ac fields with frequencies of 100-200 kHz and intensities around 20 kA/m, although results have been shown whereby frequencies as high as 600 kHz and field strengths up to 59 kA/m have been applied [6.6, 6.7].

Another source of local heating has been devised in which MNPs (eventually modified) are subjected to the action of a light beam of suitable wavelength and intensity. By different mechanisms, particles can absorb part of that (visible or IR) radiation and re-emit it in the form of heat. The method is called photothermia, and, interestingly, both electro-magnetic stimuli (ac magnetic fields or light irradiation) can be used separately or together to improve the sought response [6.8]. Although photothermia has been tested with different materials [6.9, 6.10], we focus on the use of the same magnetic particles for both heating techniques.

The basis of both therapies is the fact that tumor cells do not survive temperatures above 41–46 °C, even for a short period of time [6.11]. It is well known that such cells have accelerated metabolism, as well as a disorganized vascular structure, that is, they are highly vascularized but with poor quality vessels. Therefore, when they are subjected to heating, the blood flow is not efficient enough to dissipate the heat and it is possible to cause apoptosis by temperature elevation without significantly affecting the surrounding healthy tissue. Moreover, it is difficult to eliminate nanometric objects that enter the tumor cell, which will allow them to spend more time inside it. This effect is therefore called EPR (Enhanced Permeability and Retention [6.12]).

In addition, it should also be noted that the pores of the vessels determine the size of the particles that can be extravasated: the windows are of the order of, at most, 300-700 nm [6.13].

The amount of heat produced is evaluated by the quantity called SAR (Specific Absorption Rate, or amount of heat released per unit mass of magnetic material) parameter. When MNPs are exposed to an electromagnetic stimulus, the SAR is affected by extrinsic factors like the frequency and strength of the applied field, as well as the particles intrinsic properties such as stability, saturation magnetization, anisotropy energy, and rate of magnetic relaxation [6.14]. It is usual to also define the ILP or Intrinsic Loss Power (ratio of SAR to the product of the squared field strength and the frequency), which normalizes the heating rate values and makes them almost independent of the frequency and strength of the applied field, thus allowing comparison between different devices, particles, and laboratories [6.15].

Size determines the optimum frequency for magnetic hyperthermia application, and it is also an essential factor for the stability of the MNPs dispersion. Morphology is also important; most works with biomedical focus have been performed with spherical magnetite particles, but an increasing number of contributions demonstrate the advantage of nanorods, particularly in drug transport and release. Truong *et al.* [6.16] have recently reviewed the field, suggesting exciting possibilities in the use of nanorods, mainly considering the flexibility in sizes and axial ratios that can be achieved, confirmed by works demonstrating that the tumor cells can capture elongated particles with short dimensions very efficiently, without increased biotoxicity [6.17–6.19]. Some drawbacks must also be mentioned: in the case of very elongated particles, the only route for membrane penetration is mechanical disruption, because of hindered endocytosis [6.19]. However, it may be worth pointing out that such mechanical penetration may be used with advantage for tumor cell destruction if rotating magnetic fields are applied [6.20–6.22].

Several studies have thus concentrated on anisotropic forms to improve the magnetic behavior of the particles (increased anisotropy related to shape is beneficial for our heating objectives) and drug delivery [6.23–6.25]. The most frequently used materials are magnetite (Fe_3O_4) and maghemite ($\gamma\text{-Fe}_2\text{O}_3$) since they are magnetic particles accepted for clinical use in Europe and USA. This is because of their strong magnetization and minimal toxicity, the latter being greatly improved by proper surface treatments of the particles [6.26]. In fact, although the magnetic core plays a fundamental role in the pursued applications, the easy aggregation and degradation of iron oxides in biological fluids prevents the use of the bare particles in biomedical uses. Ideally, particles should have diameters below 6 nm in order to be excreted through the kidney [6.27]. However, few syntheses produce such small particles, and their use by injection and transport by an externally applied magnet would be difficult due to their Brownian random motions. Whatever the size, untreated particles are prone to adsorb plasma proteins (opsonins) that make them targets for macrophages

of the mononuclear phagocyte system, leading to changes in the particles themselves and in the pH of the medium, affecting cell viability [6.28–6.30]. Coating with inert or biocompatible shells, including polymers, silica, or inert metals such as gold or silver [6.27, 6.30–6.33], appears necessary for reducing the potential toxicity of the particles.

Many tests of cell toxicity are performed *in vivo*, clearly simpler, and more accessible than *in vivo* evaluations, but this brings about the issue of the correspondence between both types of results, with poor correlation found in most cases. Mahmoudi *et al.* [6.29] analyzed the possible routes to increase the applicability of *in vitro* toxicity evaluations as predictor of *in vivo* results. Focusing on the particles of interest in this work, Maniglio *et al.* [6.34] recently demonstrated that magnetite/gold composite nanoparticles 12 nm in diameter did not show any significant toxicity against MG63 and NIH/3T3 cell lines, confirming results from other authors [6.35, 6.36] in relation to the negligible cytotoxicity of gold-coated magnetite. A one-year lasting study performed by Kolojsnaj-Tabi and coworkers [6.37] disclosed many aspects of the fate of gold/magnetite nanocomposites *in vivo*, after injection in laboratory mice. It is worth noting that the degradation of magnetite may enter the route of iron metabolism by cells and be finally managed by the organism of the living animal without provoking further harm, although at the price of losing the original magnetic properties. These authors found that particles accumulated in lysosomes of Kupffer cells in liver and macrophages in spleen. After long-time observations, gold particles were found to remain rather stable (with some reduction in diameter), whereas only traces of iron oxide were appreciable. This was hence eliminated by dissolution, and not as solid nanoparticles.

Coating with gold has an additional advantage. Although magnetite NPs by themselves have a photothermal response to a $\lambda \approx 800$ nm laser excitation, as demonstrated by Espinosa *et al.* [6.38] pursuing multi-functional uses of these nanosystems, the combination of MNPs with metallic surfaces, especially gold layers, has gained importance in recent years. This is due to the possibility of adding an extra optical response to the magnetic one and hence, maximizing the power absorption when exposed to an electromagnetic field. It should be noted that *in vivo* experiments are already being carried out with these types of techniques. One relevant example of combination of physical therapies is a study based on patients with glioblastoma multiforme, which presented relevant results using magnetic hyperthermia in combination with radiotherapy [6.39].

It is worth mentioning that it has recently been shown that some ferrites may show photoluminescent behavior: the substitution of Fe^{2+} by Mn^{2+} in magnetite or in cobalt ferrite gives rise to such optical activity [6.40, 6.41]. Interestingly, this may open an additional functionality to the MNPs as sensors and active devices. Thus, Ortgies *et al.* [6.42] make use of hybrid structures (MNPs and infrared emitting PbS quantum dots) to track, and thus observe deep tissue images with higher

penetration by magnetic resonance and luminescence. However, the role of such structural changes in the photothermal response can also be a field of application, yet unexplored.

The attachment of gold nanoparticles to magnetite has been investigated by different authors, and the stability of the coating and its uniformity and thickness are always an issue to consider. In the present approach, the core particles were coated with a cationic polyelectrolyte, poly(ethylene imine) (PEI), in order to promote the adhesion of negatively charged gold nanoparticles, as well as increasing the stability of the composite particles against aggregation [6.43, 6.44]. This improved stability has been taken advantage of in magnetic hyperthermia, using different stabilizing routes [6.45, 6.46].

The use of this polymer in the biomedical field has been strengthened by its application in gene delivery as a therapy in the treatment of different diseases due to its ability to electrostatically bind DNA [6.47], as an alternative to viral vectors presently showing the best performance in this task [6.48, 6.49]. There are, however, concerns about the cytotoxicity of PEI [6.47, 6.50, 6.51]. For instance, Hu *et al.* [6.52] found that cardiovascular toxicity in zebra fish embryos was associated with branched PEI with a molecular weight of 25 kDa, and that toxicity increased with molecular weight. Although this is the most usual vehicle of DNA for gene transfection, lower molecular weights appear less toxic to cells, with a safe limit around 2 kDa [6.53, 6.54], at the price of reducing transfection efficiency.

Interestingly, Wang *et al.* [6.55] found that building a layer-by-layer assembly of citric acid and PEI significantly reduced the cytotoxicity of the polymer. This is an argument in favor of coating the gold particles attached to the magnetite cores investigated in this work with citrate anions to make them negatively charged. Another advantage of attaching gold to the particles was demonstrated by Arsianti *et al.* [6.28], who found that cellular viability in the presence of magnetite/gold/PEI used as DNA vehicles was significantly higher than that measured in the absence of the gold layer.

In this work, we present the synthesis and characterization of magnetic nanorods (MNRs). Thanks to the use of highly controllable hematite templates, the particles obtained are very homogeneous in size and shape, a feature that hydrothermal methods often used cannot guarantee. They are coated with a triple polymeric layer, and the cytotoxicity of the nanorods for the HepG2 cell line is evaluated. Furthermore, gold seed nanoparticles are also adsorbed as a final layer, to attempt improving the optical response of the MNRs when irradiated with less penetrating wavelengths, specifically those close to the surface plasmon. The composite particles are subjected to magnetic hyperthermia, photothermia, and both techniques simultaneously applied, in a sort of dual therapy, never attempted with this kind of particles. In addition, their doxorubicin release rates are evaluated, also for the first time in presence of the two external agents simultaneously applied.

6.2. Materials and methods

Materials

All reactants used were commercially available: iron (III) chloride hexahydrate, potassium dihydrogen phosphate, sodium citrate tribasic dihydrate, sodium borohydride, branched polyethyleneimine (PEI, $M_w \approx 2000$ g/mol), poly(styrenesulfonate) (PSS, $M_w \approx 7 \times 10^4$ g/mol), and doxorubicin hydrochloride (DOX) were purchased from Sigma-Aldrich (Spain).

Absolute ethanol was provided by Scharlau, Germany. The water used was deionized and filtered through a $0.2 \mu\text{m}$ filter in a Milli-Q Academic equipment (Millipore, Spain).

Methods

Synthesis of magnetite nanorods

The synthesis of magnetite nanorods (MNRs) was carried out in two stages. First, hematite rods were obtained, which were subsequently transformed by reduction at high temperatures into magnetite. For the preparation of the hematite templates, 0.02 mol of $\text{FeCl}_3 \cdot 6\text{H}_2\text{O}$ were mixed with 4.5×10^{-4} mol of KH_2PO_4 and dissolved in 1 L of Milli-Q water [6.56]. The solution was kept at 100°C in a Pyrex bottle sealed with Teflon for 6 days. Thereafter, the hematite suspensions were cleaned by centrifugation at 21000 rpm for 15 minutes, and the supernatant was discarded and replaced by water. This process was repeated 3 times. Finally, the sample was redispersed in water and dried overnight at 50°C .

Subsequently, it was necessary to transform the hematite nanoparticles into magnetite. This process was carried out by reduction at high temperatures in an H_2 atmosphere [6.57]. For this purpose, a tube furnace (Hobersal, Spain) was set at 350°C while passing nitrogen-carrying ethanol. The nitrogen flow was bubbled in pure ethanol and passed along the tube at a rate of 3.83 L/h. At the selected temperature, the ethanol was oxidized releasing hydrogen, which, in turn, reduced the hematite powder. The powder was introduced once the temperature was reached and kept in the ethanol/ N_2 atmosphere for 6 hours.

It is important to note that to ensure maximum exposure of NPs to the gas flow, a glass tube with a flat and porous base (fritted glass) was used as the sample container inside the tube.

Preparation of polymer-coated nanoparticles

In order to improve MNPs polymer coating, the layer-by-layer method was used, as nanoparticles were coated with 3 successive layers of polyelectrolyte (cationic-anionic-cationic [6.45]). The procedure involved the addition of 5 mL of MNPs suspension (with 1 g/L particle concentration) dropwise into 5 mL of PEI (2 g/L) under ultrasonic agitation. The obtained suspension was kept for 90 min in an ultrasound bath and then it was left undisturbed for 30 min. The final step consisted of cleaning several times by magnetic decantation and redispersion in 5 mL MilliQ water, maintaining the initial concentration. This procedure was repeated for the successive PSS and PEI coatings.

Gold shell on polymer-coated nanoparticles

Gold seeds were synthesized by adding 0.5 mL HAuCl_4 0.01 M and 0.5 mL sodium citrate 0.01 M to 18 mL of MilliQ water under stirring. Afterwards, 0.5 mL of freshly prepared (and kept at 0 °C) NaBH_4 0.1 M was added. Sodium borohydride acts as a reducing agent, causing the reduction of Au^{3+} to neutral gold atoms, changing the solution from yellowish to reddish color. The mixture was kept at 30 °C in a thermostatic bath for 15 minutes and left unperturbed for 2 hours [6.45].

The procedure to attach the gold nanoparticles to the surface of the PEI/PSS/PEI-coated MNRs started by diluting the starting magnetite and gold suspensions. This was done by adding 20 mL of water up to a final concentration of 0.25 mg/mL, and they were added dropwise to a dilution of 30 mL of gold seeds and 10 mL of water, in an ultrasound bath. The resulting solution was maintained under sonication for 15 minutes and left unperturbed for half an hour. Finally, the particles were cleaned by magnetic decantation and redispersed in 2 mL of water, reaching a concentration of 2.5 mg/mL.

HRTEM Characterization: Morphology

The size and shape of dried nanoparticles were determined using a high-resolution transmission electron microscope (HRTEM) (Thermo Fisher Scientific TALOS F200X, USA), all images being provided by the CIC-UGR Microscopy Service. The sizes were measured using JImage software (University of Wisconsin, Madison, WI, USA).

Electrophoretic mobility and hydrodynamic diameter measurements

The determination of the surface electrical properties was carried out by measuring the electrophoretic mobility of dilute MNPs suspensions using a Zetasizer Nano-ZS (from Malvern Instruments, UK). The same instrument was used for the measurement of particle hydrodynamic diameters by dynamic light scattering (DLS).

Structural characterization

Crystal structures were identified from X-ray powder diffraction patterns (XRD) of the samples using a Bruker D8 Advance diffractometer (Berlin, Germany) equipped with a Bruker LINXEYE detector and a $\text{CuK}\alpha$ radiation source. Micro-Raman spectroscopy was performed using a JASCO NRS-5100 Dispersive Micro-Raman (Japan) equipped with a green diode laser of 532 nm, with 30 mW power (Elforlight G4-30; Nd: YAG), covering a spectral range from 50 to 8000 cm^{-1} . Thermogravimetric analysis was carried out in a Shimadzu TGA-50H (Japan) with a vertical furnace design, providing a maximum precision of 0.001 mg, and operating within a temperature range between $25\text{ }^{\circ}\text{C}$ and $950\text{ }^{\circ}\text{C}$ (CIC-UGR).

Magnetic properties

Magnetization cycles were obtained at room temperature ($20\text{ }^{\circ}\text{C}$) in an AC magnetometer AC Hyster Series (Spain). It works at a frequency of 1 kHz, and it can apply field strengths in the range -1.5 to $+1.5$ kOe (-119.4 to $+119.4$ kA/m).

Cytotoxicity determinations of PEI/PSS/PEI coated MNRs

The human hepatoblastoma cell line HepG2, supplied by European Collection of Animal Cell Cultures (Salisbury, U.K.), was used to perform cell viability experiments in order to assess the negligible toxicity of the triple polymer-layer-coated MNPs. The cells were seeded into 96-well plates (10,000 cells/well) and cultured in a cell culture medium for 24 hours with different concentrations of polymer-coated MNRs (25, 50, 100, 200, 300, 500 $\mu\text{g}/\text{mL}$) in a CO_2 (5%) atmosphere. After the treatment, the medium was aspirated from each well, and the cells were fixed with 100 μL of glutaraldehyde. The plate was stirred for 15 minutes at 50 rpm and then washed with distilled water eight times. After drying, 200 μL of 0.1% crystal violet was added and stirred for 20 minutes at 30 rpm. Again, the plate was washed and dried. Finally, the dye was solubilized with 100 μL of 10% acetic acid. The plates were stirred for 10 minutes and then analyzed using a plate reader set at a wavelength of 590 nm to quantify live cells [6.58].

Optical absorbance

UV/VIS optical absorbance of all samples was determined using a Jenway Series 67 (UK) spectrophotometer.

Magnetic hyperthermia

The magnetic hyperthermia device was built in our laboratory. The AC magnetic field was applied to the samples using a double four-turn coil 32.40 ± 0.05 mm in diameter, made of 6.00 ± 0.05 mm copper tube. An AC current of frequency f was passed along the coils using a parallel LC resonant circuit. The inductance of the coil was $L = 2.48 \pm 0.01$ mH, with resistance $R = 300 \pm 1$ m Ω , and the device contained a capacitor bank for selecting the frequency in the range 100-300 kHz.

In this work, the coil remained unchanged, and only the capacitance of the circuit capacitors was adjusted to select the frequency of the AC magnetic field. The copper tube of the coil allowed circulating water from a thermostatic bath, which is crucial as Joule heating can be significant (currents as high as 40 A pass through the coil) and could obscure any temperature changes associated with true magnetic hyperthermia. The resulting magnetic field strength could reach up to 22 kA/m at most. Field strength and frequency measurements at the sample location were determined by a NanoScience Laboratories Ltd. Probe (Staffordshire, UK), with a sensitivity of 10 μ T.

An Eppendorf tube containing the sample (200 μ L) was placed centrally inside the coil, after being thermostated at an initial temperature of 20°C. Sample and bath temperatures were recorded using two optical fiber sensors (Optocon AG, Germany) every 3 seconds, with a resolution of 0.01 °C.

Photothermia

The setup consisted of an infrared laser (Laserland, China, 850 nm, maximum power 1.6 W) pointing towards the support where the Eppendorf was located with the sample (200 μ L). A thermal imaging camera (Flir 60, USA) capable of taking temperature measurements every 0.0625 s with 0.045 °C thermal resolution was used for sensing the sample temperature.

To compare with the results obtained from the determination of the optical absorbance, less powerful red, green, and blue lasers with respective wavelengths 638 nm, 505 nm, and 480 nm (RGB Combined White Laser, Laserland, China) were also used.

Dual magnetic hyperthermia and photothermia device

When magnetic field and laser light were applied simultaneously, the laser was directed towards the top of the uncapped Eppendorf containing the sample. In this case, only the thermographic camera could be used for temperature measurements. Infrared laser irradiation and a constant frequency (100 kHz) field were used in this combined setup.

Drug loading and release

For the first step, drug loading on the MNRs, 1 mg of gold-coated nanoparticles was kept in contact with 1 mL DOX (doxorubicin hydrochloride) solutions of different concentrations and maintained for 72 hours under shaking. In order to determine the DOX concentration after adsorption, a calibration set of absorbance vs. concentration data was obtained by measuring optical absorbance at 483 nm (wavelength of maximum absorbance for DOX) for the concentrations used (0.02, 0.04, 0.06, 0.08, 0.10, and 0.12 mM DOX).

The second step was drug release experiments. For this purpose, 1 mL of 5 mg/mL suspension of gold-coated MNPs was placed in 1 mL 0.6 mM DOX and kept under shaking for 72 hours. After this time, the particles were magnetically decanted, and the DOX solution was substituted by acetate buffer at pH 5, a value selected considering that the tumor tissue environment is acidic [6.59]. At specified intervals, the particles were decanted, and the absorbance of the supernatant was measured to evaluate the amount of released DOX, using the calibration data. Fresh buffer was added, and the release process was continued (sink conditions [6.45]). Release experiments were carried out in four different experimental conditions, namely, under magnetic hyperthermia, in photothermia, with dual therapy, and in standard conditions (no field applied).

6.3. Results and discussion

Size and shape characterization

Figure 6.1A,B shows HRTEM images of the MNRs synthesized. It clearly demonstrates their geometry, spheroidal, as determined by the hematite template NPs.

In order to carry out the geometric characterization, the length of at least 100 particles was determined on different pictures, and the value obtained for the average length was 550 ± 90 nm, with an aspect ratio of 1:5 (a detailed size distribution can be found in the Supporting Information file, Fig. 6.14).

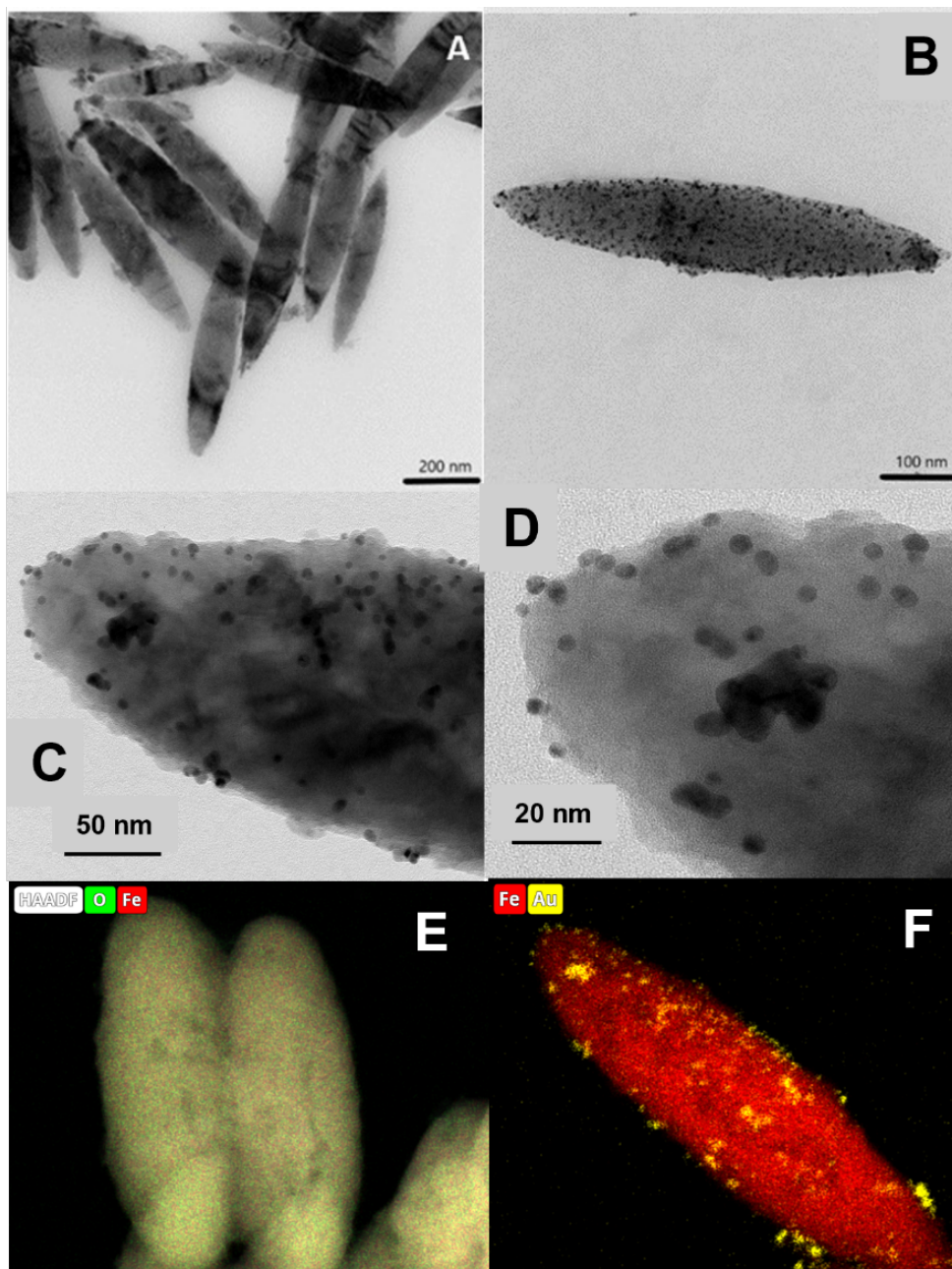


Figure 6.1: HRTEM images of magnetite nanorods; (A): bare particles; (B): gold-coated particles (the darker dots are Au NPs incorporated into the polymer shell); (C, E) high-magnification of gold particles-coated nanorods, with observation of the polymer layer with gold embedded in it; (E,F): EDX composition maps of bare (iron and oxygen) and gold-coated (iron and gold) nanorods.

Concerning the gold seeds, HRTEM pictures showed mostly spherical particles, quite monodisperse (Fig. 6.1C,D). Their average diameter was estimated by DLS, obtaining a value of 6.00 ± 0.10 nm. In addition, Fig. 6.1C,D demonstrates that a uniform coating of the magnetic nanorods was achieved, most likely a consequence of the PEI/PSS/PEI layer on magnetite, which enabled electrostatic bonds between the MNPs and the gold particles.

It is worth noting that the gold shell is not continuous but particles are deposited individually or forming gold islands. This has been found by other authors when coating magnetic particles with gold [6.45, 6.60] or silver [6.61], and calculations based on the density functional theory, performed by Sokolov *et al.* [6.62], demonstrated recently that the wetting parameter of the magnetite/gold interface happens to be negative, so that gold does not wet magnetite and it rather forms drops on its surface. In addition to morphological evaluation of the gold shell, EDX composition maps of the bare and gold-coated particles were also obtained, as shown in Fig. 6.1E,F for bare and gold-coated MNRs.

Electrophoretic measurements

Measurements of electrophoretic mobility as a function of pH served as a qualitative assessment of the surface structure of the NPs. The use of branched, low-MW PEI has initially been justified as a biocompatible polymer. However, one of the questions we can ask ourselves is whether the polyelectrolyte layer would detach over time, i.e., whether the particles might not be stable and gradually increase their cytotoxicity by release of free polymer, since it has been shown that a single layer can detach partially as time passes [6.45].

To verify if this was the case with our particles, the electrophoretic mobility of magnetite/PEI particles was measured first right after their preparation, finding that it was positive throughout the pH range. However, when the same measurements were taken a few days later, the loss of positive charge was evident, indicating detaching of the PEI layer. That is why the particles were coated with a triple layer using the layer-by-layer technique, in the order PEI (cationic)/PSS (anionic)/PEI (cationic) leading to an increased stability over time. By following this procedure, this third PEI layer remained attached to the particle, as is shown in Figure 6.2.

Coatings with the two polyelectrolytes change the surface charge of the bare particles, as expected. The electrostatic bond between the layers allows the generation of this type of multilayered particles and finally their decoration with gold seeds through attraction between positive PEI and negative citrate-capped gold.

In general, in all cases (bare, polymer and gold coated magnetite), the isoelectric point was found at acidic pH (around 5 for the gold-coated sample, and 6 for the multilayered sample). This finding is significant for particles aimed at DOX delivery,

considering that this drug is positively charged at that pH range, and that the tumor environment is typically acidic [6.63–6.65]: this means that DOX will tend to be released from the particles not only by diffusion, but also by electrostatic repulsion. These mobility data can be found in the Supporting Information Fig. 6.15.

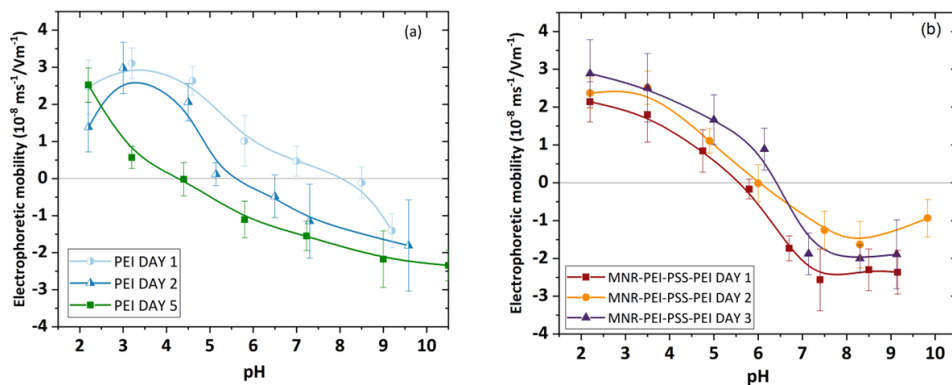


Figure 6.2: Electrophoretic mobility of magnetite nanorods at different aging times with one (a) and three (b) polyelectrolyte layers.

Structural characterization

It can be seen in Figure 6.3a that a complete transformation of hematite into magnetite appears to be achieved in view of the XRD results (magnetite reference data taken from RRUFF database [6.66]).

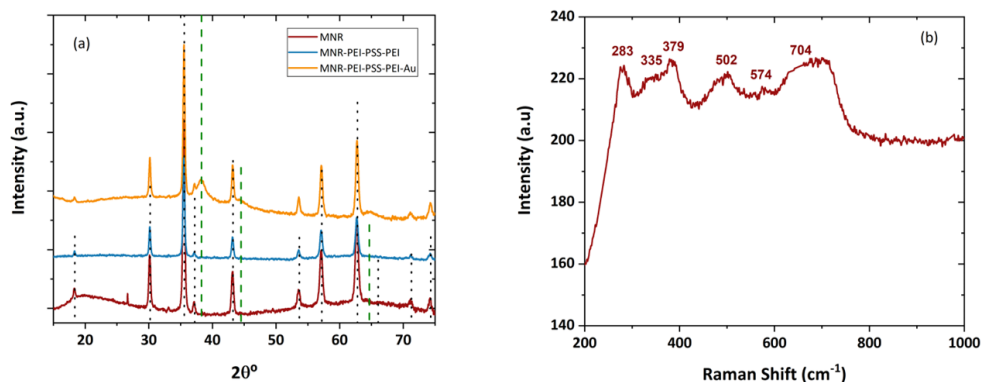


Figure 6.3: (a): X-ray diffraction patterns of bare, polymer-coated and polymer/gold-coated MNRs; (b) micro-Raman spectroscopy of the bare particles. The vertical lines in (a) are the reference lines for magnetite [6.31]; dotted black lines: magnetite; dashed green lines: gold.

It can also be noted that the diffraction pattern is not modified by the coating with polyelectrolytes, and that when gold is added, its characteristic peaks, although weak (because of the small amount of gold, see Fig. 6.1), are also appreciated. However, since the XRD diffraction pattern of magnetite and maghemite are very similar, other methods must be used to ascertain the structure.

In addition to XPS, Raman spectroscopy is one possibility. The Micro-Raman spectroscopy results obtained with our sample of MNRs are plotted in Figure 3b: the bands observed correspond [6.66] to magnetite (309, 560, and 690 cm^{-1} , RRuff ID R060656.3) and maghemite (288, 406, and 495 cm^{-1} reference data, RRuff ID R140712), indicating that our particles are in fact a mixture of maghemite and magnetite, although the magnetite denomination will be used throughout the manuscript for simplicity.

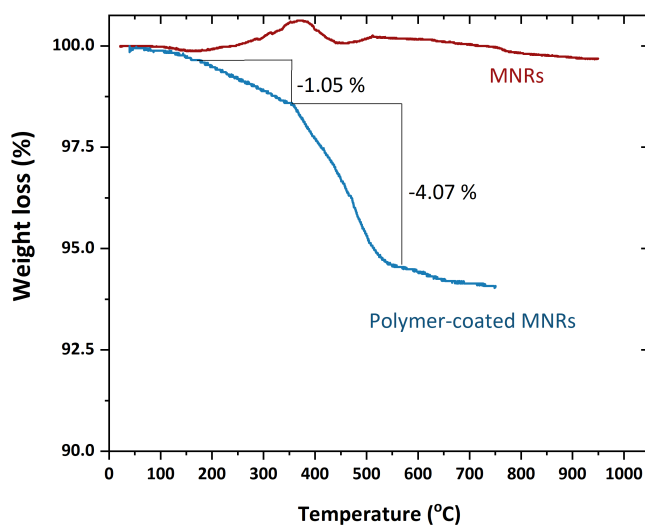


Figure 6.4: Thermogravimetric analysis of naked and polymer-coated MNRs.

Thermogravimetric analysis (TGA) was performed to estimate the amount of polymer forming the triple layer around the particle. Fig. 6.4 shows the evolution with temperature of the sample mass for both naked and PEI/PSS/PEI-coated nanorods. The bare particles do not show any special feature, except for a slight weight gain above 300 °C, which can be ascribed to partial oxidation of magnetite to hematite or maghemite [6.67].

In the case of the coated particles, the first significant weight change happens around 150 °C and must correspond to the loss of hydration water, while the next event extends up to 367 °C. Since the decomposition temperature of PSS is around 470

°C [6.68], it can be argued that this stage was the loss of PSS, which amounts to about 1.05%. The same TGA data show a weight loss of 4.07% in a process that finishes around 605 °C. Literature information on PEI polymer indicates that it decomposes at around 600 °C [6.69], with the TGA curves showing a pronounced weight loss.

The data in Figure 6.4 confirm the coating of the particles by the polyelectrolytes, especially PEI. An estimation of the thickness of the respective layers has been carried out by assuming that the density of such layers is at most 1/10 of that of the free polymers (1.1 g/cm³ and 1.08 g/cm³, respectively). If a uniform coating is assumed (as suggested by the pictures in Figure 6.1C and 6.1D), it can be estimated that the thickness of the PSS layer is 2.4 nm, and that of the PEI rises to about 10 nm (compare the layer appreciated in Figure 6.1C with the size of the Au NPs).

Magnetic characterization

The magnetization cycles of MNRs, both bare and coated by polymer or polymer/gold, are displayed in Figure 6.5. As observed, the bare MNR sample showed a high saturation magnetization, typical of that of good magnetite samples, namely 71.2 ± 3.0 emu/g.

The facts that the measurements were performed in AC magnetic fields, and that the particles are multidomain, produce open hysteresis cycles. As expected, a decrease in magnetization is observed with successive coatings (polymer-coated MNRs present a maximum magnetization of 21.3 ± 1.8 emu/g, and 12.1 ± 0.7 emu/g is found for gold-coated ones).

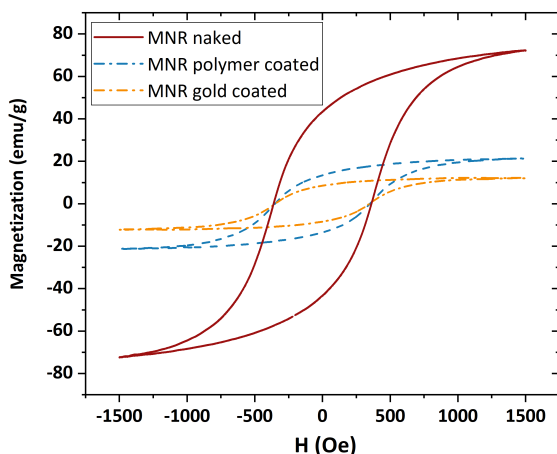


Figure 6.5: Magnetization curves of naked, polymer- and polymer-gold-coated magnetite nanoparticles.

Cell viability experiments

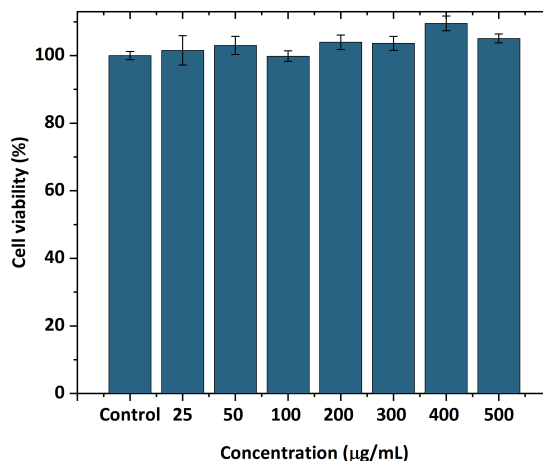


Figure 6.6: Effects of PEI-PSS-PEI coated MNRs on HepG2 cells proliferation. The concentration of nanorods as indicated.

Cell viability experiments were performed to determine whether the coatings provided the necessary biocompatibility of the systems. For this purpose, HepG2 cells were seeded for 24 hours with different concentrations (25, 50, 100, 200, 300, 400, 500 µg/mL) of PEI-PSS-PEI coated nanoparticles. The experiments were conducted in triplicate, and the viability, normalized with respect to the control cells, is evaluated as the mean \pm SD of these experiments.

As can be seen in Figure 6.6, the preliminary data are very promising. The cytotoxicity of polyelectrolyte-coated MNRs particles is negligible, even at the highest concentrations. No significant differences were observed between cells cultured with the concentration sweep and control cells (within statistical error).

Optical absorbance

The results of the optical absorbance determinations are depicted in Fig. 6.16: the shoulder shown by the absorbance of gold-coated sample indicated the presence of gold, since such an absorbance maximum can be ascribed to the surface plasmon of gold particles, observed at 564 nm. This is another proof that an efficient coating was achieved.

Magnetic hyperthermia experiments

The magnetic hyperthermia performance of the different nanorods was evaluated for different frequencies and intensities of the AC magnetic field. The results are presented in Figures 6.7 (SAR and ILP) and 6.8 (temperature vs. time).

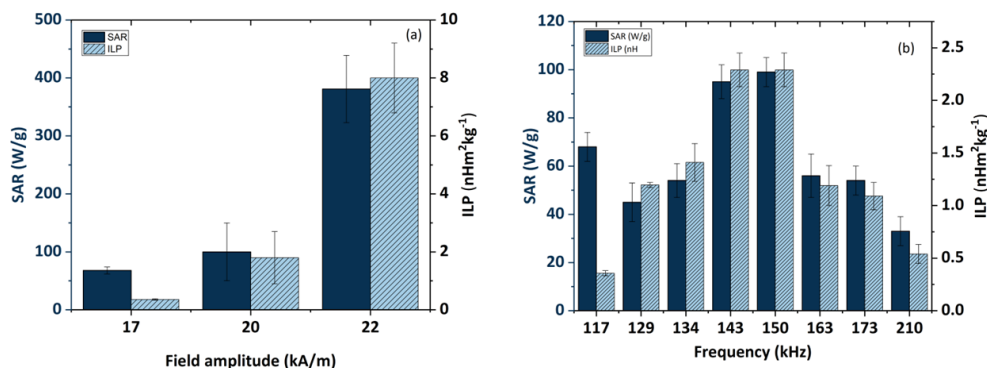


Figure 6.7: SAR and ILP values for magnetite nanorods. (a) Field strength sweep keeping the frequency at 100 kHz; (b) frequency sweep for a 17 kA/m field amplitude.

As can be seen from the SAR values, the best frequency for this application and this sample was 150 kHz. This means that the phase shift between magnetization and field strength is largest at this frequency, thus producing the maximum heat dissipation.

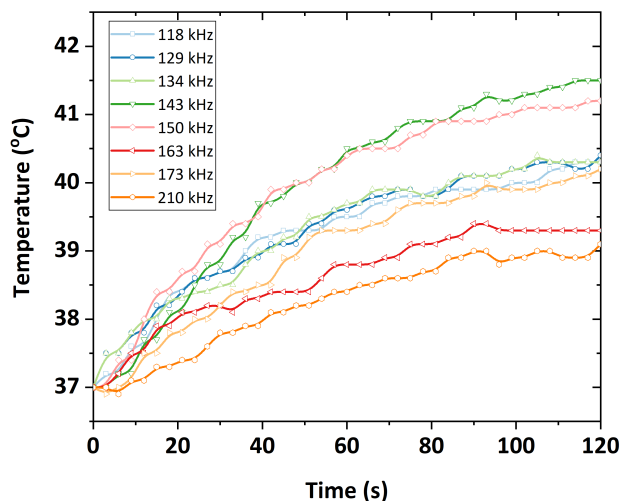


Figure 6.8: Frequency sweep for the MNR sample. Field intensity maintained at 17 kA/m.

Magnetic hyperthermia experiments were also carried out with the gold-coated particles (Figure 6.9a). As expected, given the magnetization cycles described above, the efficiency with gold coating decreased, as confirmed by the significant reduction in SAR (Figure 6.9b).

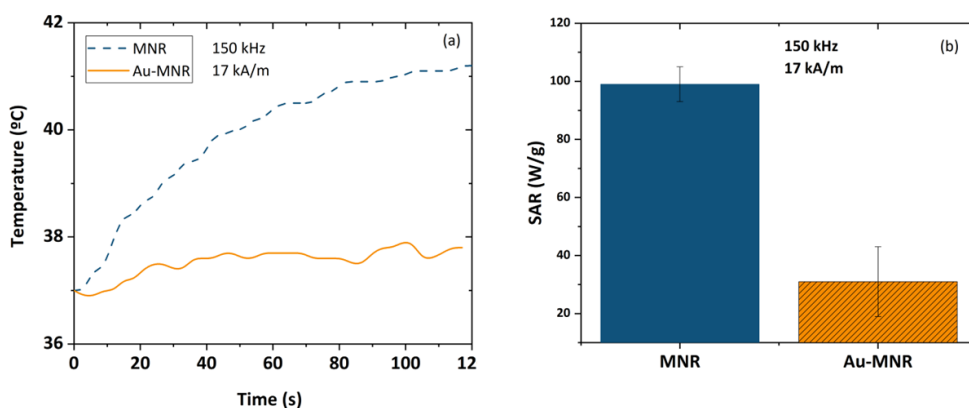


Figure 6.9: Temperature increases for polymer-coated and gold-coated MNRs (a), and SAR values (b).

Photothermia

In photothermia, two approaches were followed: the first, considering the presence of the surface plasmon of gold in the visible spectrum (Figure 6.16), consisted of irradiating with wavelengths close to it, using the RGB laser. Although penetration is lower, it may still be useful in certain cases of superficial cancer [6.70], and, in our case, as a proof of the improvement achieved by coating with gold NPs. The second was to irradiate the sample with a near-infrared (NIR) laser due to its great penetration through human skin.

Figure 6.10 shows the results of the first approach: note that for monochromatic laser the coating with Au improved the photothermia response, as compared to that of MNRs with the triple polymer shell. Taking into account that the laser powers were not identical for the three wavelengths tested, we could calculate the ratios SAR/(power density) for each of the lasers. The results were (in units of cm^2/g) 0.21, 0.22 and 0.17 for 480, 505, and 638 nm, respectively, so that the 480-505 nm illumination source produce the best photothermia performance, as one would expect given the proximity between this wavelength and that of the surface plasmon resonance (SPR) of gold nanospheres.

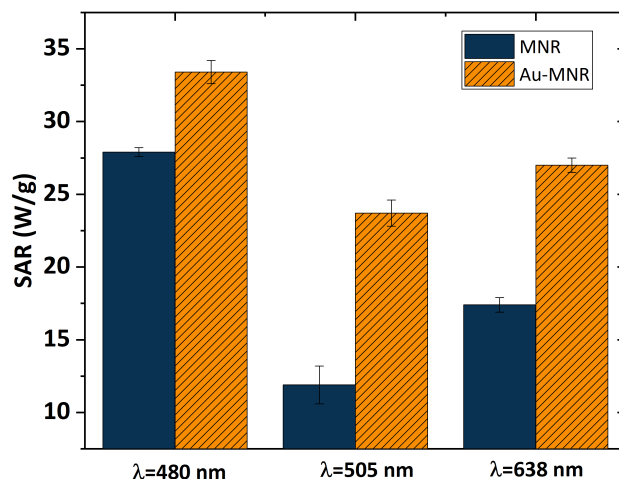


Figure 6.10: SAR values for RGB laser irradiation of polymer- and gold-coated magnetite samples. The respective laser power densities were 159 mW/cm^2 (480 nm), 109 mW/cm^2 (505 nm), and 161 mW/cm^2 (638 nm).

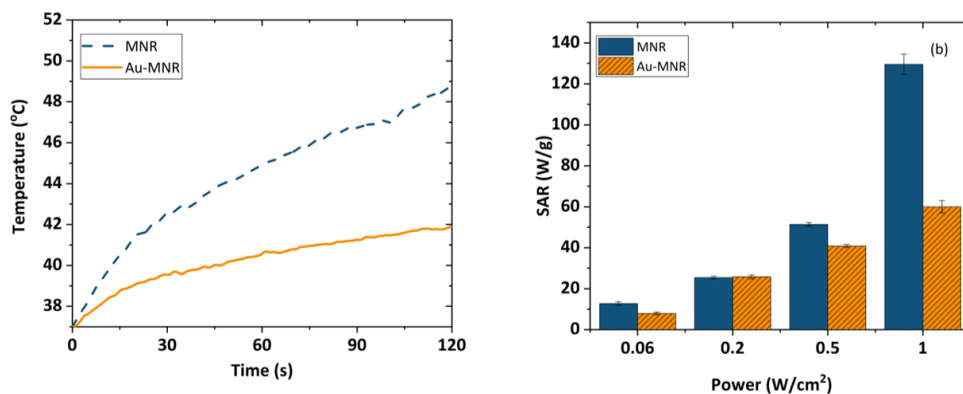


Figure 6.11: (a) Temperature evolution as a function of time in photothermia experiments (NIR laser, 850 nm wavelength, and 1 W/cm^2 power density in the sample location), for polymer-coated and gold-coated MNRs. (b) SAR values as a function of laser power density for the two samples.

In the case of NIR irradiation (Figure 6.11), it is observed that when the MNR particles are coated with gold NPs the rate of heating is reduced in comparison with that reached with polymer coated MNRs, mainly at high laser power density. Considering that the plasmon resonance of our gold nanoparticles is around 570 nm

(Figure 6.16), it can be explained that the presence of gold seeds does not help in heating by the SPR effect, but apparently reduces the heat transfer by radiation without actively participating in heating. In contrast, Rincón-Iglesias *et al.* [6.71] recently reported significant photothermal heating with 140 nm magnetite rods coated by a continuous layer of gold, using a 0.2 W/cm² NIR led source of 735 nm wavelength. These experiments demonstrate that controlling the thickness and uniformity of the coating is an essential aspect of hyperthermia with composite magnetic nanorods.

Dual Therapy

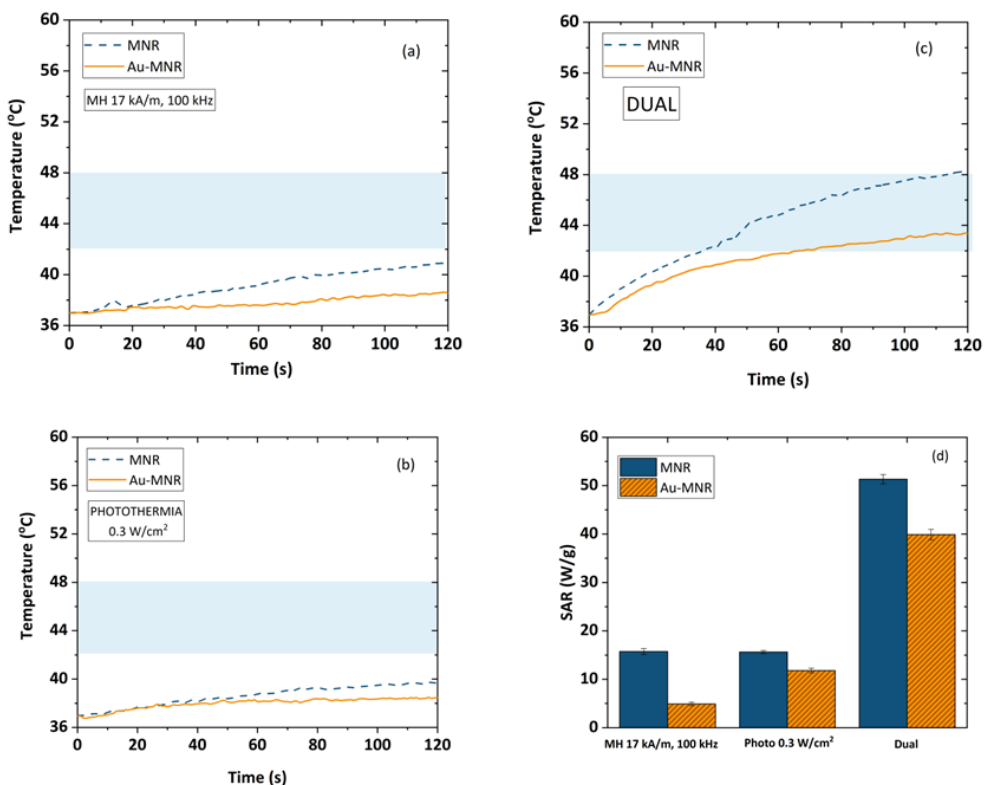


Figure 6.12: Magnetic hyperthermia (a), photothermia (b) and dual therapy (c) curves for MNR magnetite. (d) Comparison between SAR values of magnetic hyperthermia, photothermia and dual techniques. The magnetic field frequency used is 100 kHz. The blue band marks the desired hyperthermia range.

As mentioned, by dual therapy we mean the situation in which an AC magnetic field is applied simultaneously to the photothermia laser, with the aim of reaching a given therapeutic response while decreasing the energy inputs from both the magnetic

field (17 kA/m amplitude instead of 21 kA/m) and the laser (0.3 W/cm^2 instead of 1 W/cm^2). The combination can thus be thought of as a potentially less harmful, although equally efficient, treatment. The experimental data can be found in Figure 6.17.

This is in contrast with the results achieved when both therapies are superimposed. As Figure 6.12, shows, when the samples are irradiated with 0.3 W/cm^2 while being subjected to a magnetic field of 17 kA/m, the rate of temperature increase is significantly faster, and as a result, the SAR values reached with the dual therapy are three times larger than those corresponding to either technique separately. This is a very important result, as it opens a way of optimizing the treatment while minimizing unwanted side effects.

Drug release

As repeatedly mentioned in this contribution, one possible application of the particles described is drug release alone or in combination with the hyperthermia effects. To this aim, polyelectrolyte-gold coated MNRs were first contacted with a doxorubicin solution of 0.6 mM concentration, as described. Optical absorbance of the supernatant at the end of this time indicated a DOX concentration of 0.146 mM. This means that the adsorption was $0.308 \mu\text{mol}/0.005 \text{ g}$, equivalent to $61 \mu\text{mol}$ per gram of magnetic particles or 33 mg/g . This adsorption density is of the same order of the values found in other works for adsorption of DOX on functionalized magnetic particles. Thus, Reyes Ortega *et al.* [6.72] reported 20 mg/g for spheroidal magnetite particles coated with PEI/PSS, and Rudzka *et al.* [6.73] obtained a saturation adsorption of 25 mg/g using particles with a maghemite/silica/gold composite structure. Using a different particle structure (carbon dots and magnetite on carbon nanohorns), Su *et al.* [6.74] measured up to 66 mg/g DOX payload. Comparable values can be found in other works [6.75–6.77].

The mechanism of DOX adsorption on the investigated Au-coated MNRs must be mostly electrostatic. It is well known that the amino group in the DOX molecule is characterized by a pKa value of 9.93 [6.78], so that the molecule will be positively charged at acidic pH. The presence of a carbonyl group in the molecule makes that the drug presents a low positive charge in neutral conditions. The fact that the adsorbed gold nanoparticles are negative leads to an electrostatic attraction between such particles and DOX as predominant adsorption mechanism. Optical absorbance data reported by Rudzka *et al.* [6.73] demonstrate that the surface plasmon resonance of gold is quenched after contact with DOX in solution, a proof of the proposed mechanism of interaction, also confirmed by the data from other investigators [6.79, 6.80].

In order to evaluate the release of this drug, absorbance measurements were performed under sink conditions at pH 5. Figure 6.13 shows the results in the form of accumulated drug release as a function of time during application of magnetic hyperthermia (17 kA/m, 100 kHz), photothermia (850 nm wavelength, 0.3 W/cm²) and both, as well as without treatment (the latter data are extended to longer times in Supporting Information Fig. 6.18). Assuming the mechanisms above described, it is expected that at neutral pH the release is slow and very limited, due to the reduced tendency of the drug to be solubilized, and in fact most published works have focused on acidic media for passive release, as in the present work. In such conditions, DOX is strongly positively charged and prone to be solubilized and released to the solution by diffusion. In addition, Fig. 6.2 shows that the coated MNRs become increasingly positive, leading to electrostatic repulsion between DOX and the substrate, easing the release. The main result in Figure 6.13 is the improvement in the rate of drug release when both fields are applied simultaneously. In this case almost 10 % of the DOX available was released in less than one hour. Furthermore, this rate can be easily tuned by controlling the field parameters.

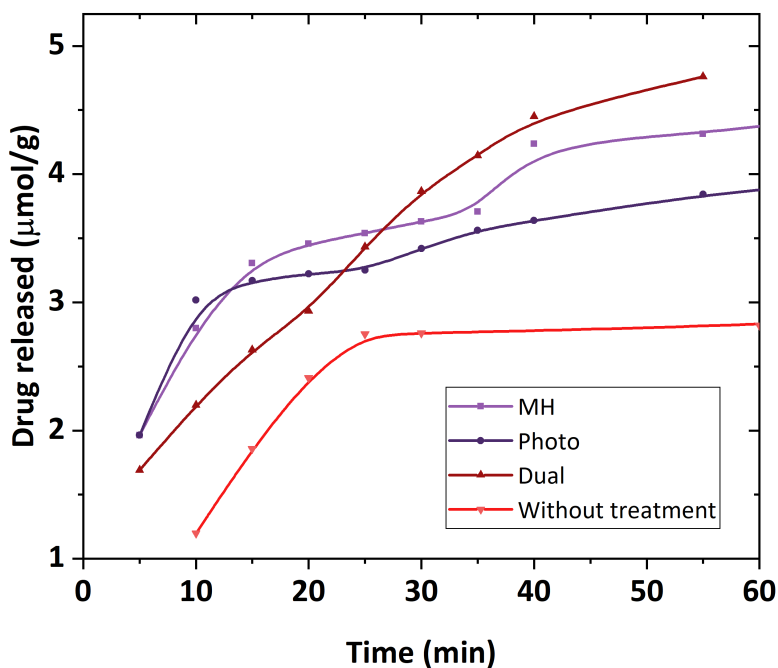


Figure 6.13: DOX release from magnetic nanoparticles in a pH 5 buffer and sink conditions. MH: under magnetic hyperthermia; Photo: with applied laser; Dual: both laser and magnetic field applied

6.4. Conclusions

Magnetite/maghemite nanorods 550 nm long have been successfully synthesized based on hematite templates, and they have been coated with a triple PEI/PSS/PEI polyelectrolyte layer, allowing the final adsorption of gold nanoparticles. The particles were designed to be applied under alternating magnetic fields and produce magnetic hyperthermia as an adjuvant therapy against malignant cells. They are also demonstrated to be very efficient heating sources when subjected to laser beams (photothermia) both in the near infrared and in the visible, the former being preferred because of its better penetration in the body, and the latter because of proximity with the wavelength of the surface plasmon resonance of gold nanoparticles. The nanorods coated by polymer respond very efficiently to either of the external (magnetic or electromagnetic) actions, whereas the coating by gold was only beneficial if the laser was in the visible window of the spectrum. In this work we also describe a sort of dual therapy, consisting of the simultaneous application of a magnetic field and an infrared laser. The temperature window in which cancer cells are supposed to undergo destruction is reached with this kind of therapy in a shorter time and with lower (safer) strengths of the magnetic field or the laser power. The gold-coated magnetite nanorods are also used as drug vehicles for doxorubicin, and it is also shown that dual therapy provides better results for the drug release. The particles could be a multitask tool in fighting cancer cells. In future works, their use for cell hyperthermia *in vitro*, and the possibility of using them for mechanical disruption of the cells by applying rotating magnetic fields will also be explored.

Acknowledgments

This research was funded by Junta de Andalucía, Spain, Consejería de Economía y Conocimiento/ Proyectos de I + D + I del Plan Andaluz de Investigación, Desarrollo e Innovación/ Grants P20 00346, P20 00233. Ministerio de Ciencia e Innovación, Spain, Plan Estatal I+D+I 2017-2020/ Grant EQC2019 005930 P. Ministerio de Economía y Competitividad, Spain, Grant PID2019 109294RB 100. We acknowledge the assistance of the technical personnel in the Centro de Instrumentación Científica, University of Granada.

Appendix. Supplementary Information

Geometrical characterization of the magnetic nanorods

To analyze the length and width of the nanorods (Figure 6.14), a total of 100 nanoparticles were measured and their size was estimated from the microscopy images and JImage software. The value obtained for the length was 550 ± 90 nm (1:5 ratio).

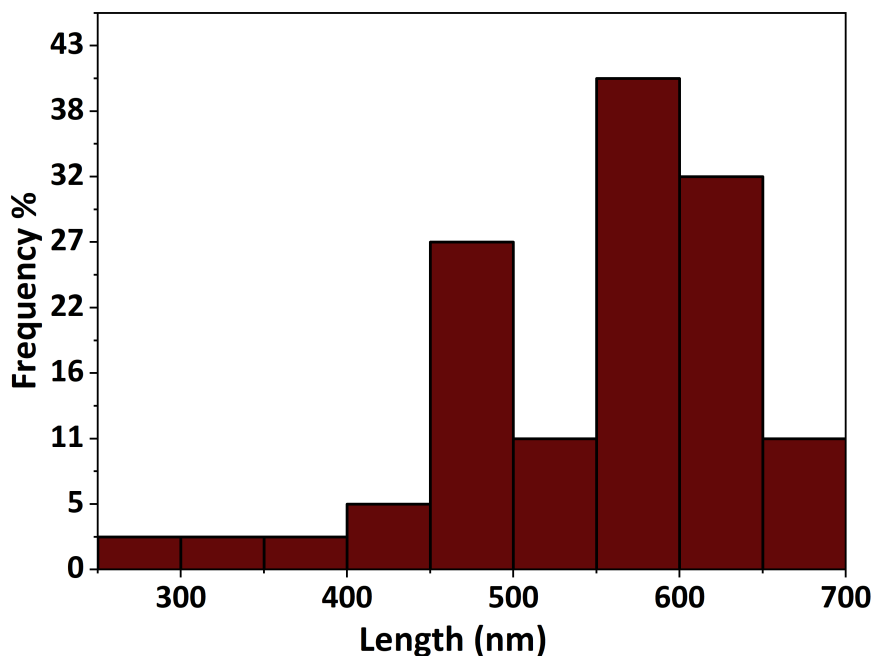


Figure 6.14: Histogram of magnetic nanorods length distribution.

Electrophoretic mobility of the MNRs

To check whether the different coating layers had been deposited, the electrophoretic mobility of the samples was measured (Figure 6.15). In the case of the PEI layer (cationic), the shift towards positive values of the mobility over the entire pH range due to a complete coating is observed. In the case of the gold seed coating (negatively charged) this effect is not so visible, evidencing that it is just a partial coating.

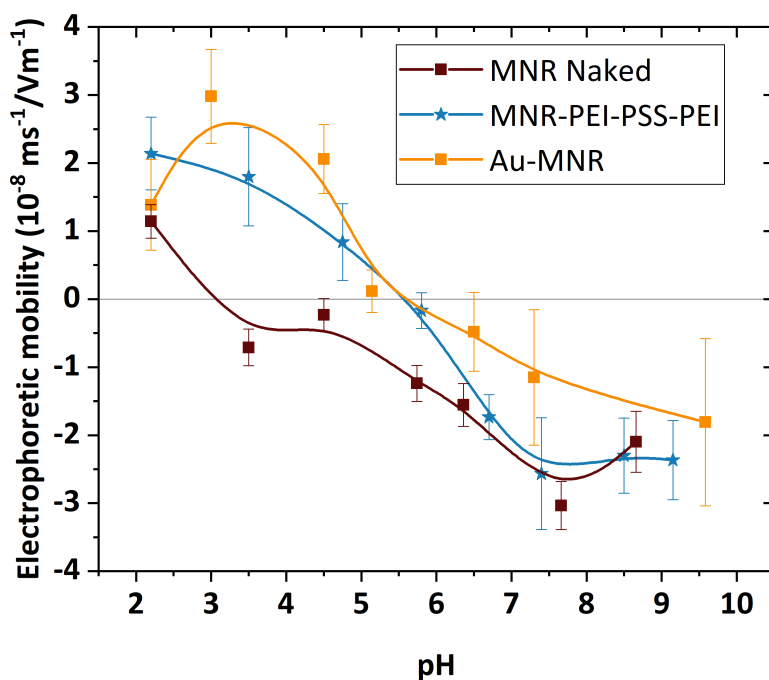


Figure 6.15: Electrophoretic mobility of MNR, coated with PEI-PSS-PEI and PEI-PSS-PEI-Au.

Optical absorbance

Figure 6.16 shows the optical absorbance spectra of pure magnetite and Au-coated nanorods.

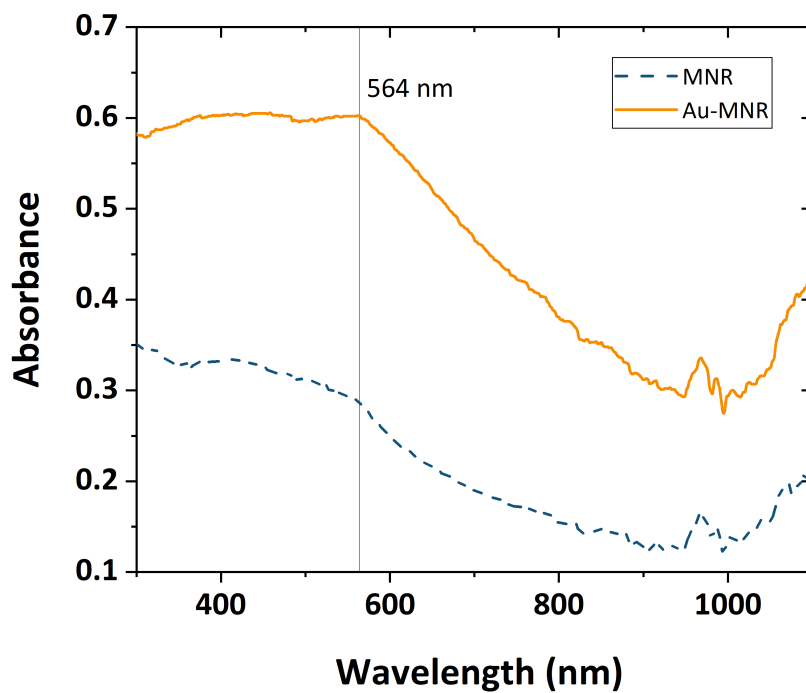


Figure 6.16: Optical absorbance of magnetite and gold coated nanoparticles.

Dual therapy

The first advantage in applying dual therapy is to achieve a decrease of the field strength and the irradiation power required to reach the therapeutic heating level. Figure 6.17 shows the temperature evolution when the two techniques were separately applied with the reduced intensities just mentioned. As observed, none of them could rise the sample temperature to the target value of 41-46 °C, after reducing the field and laser powers to the values found optimal in dual application.

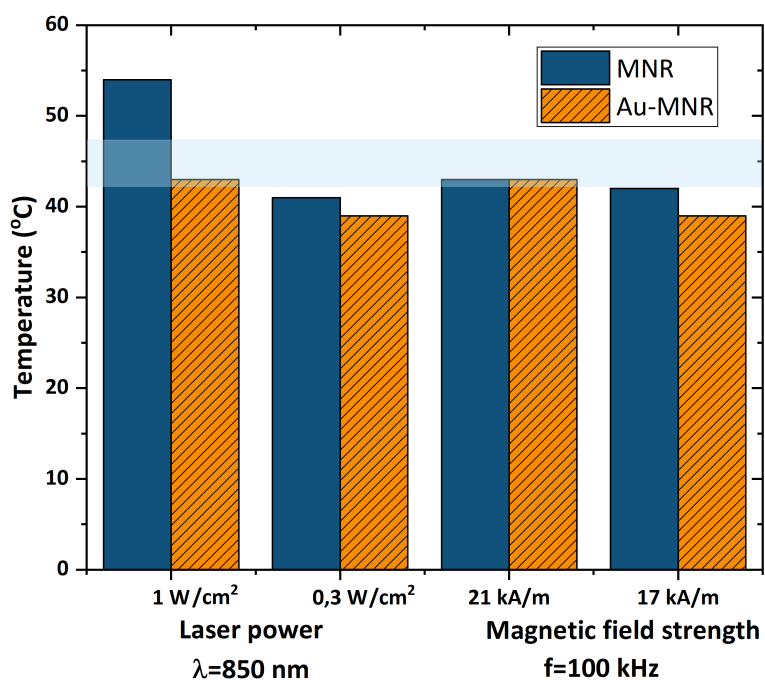


Figure 6.17: Maximum temperatures reached for magnetic hyperthermia and photothermia. Time of application 3 min. The blue band marks the desired temperature interval for hyperthermia.

Drug release

Figure 6.18 shows the experimental results of the accumulated drug release as a function of time without treatment, showing that even for times longer than those shown in the main text (Figure 6.12), the results obtained with hyperthermia, photothermia or dual therapy techniques are not achieved.

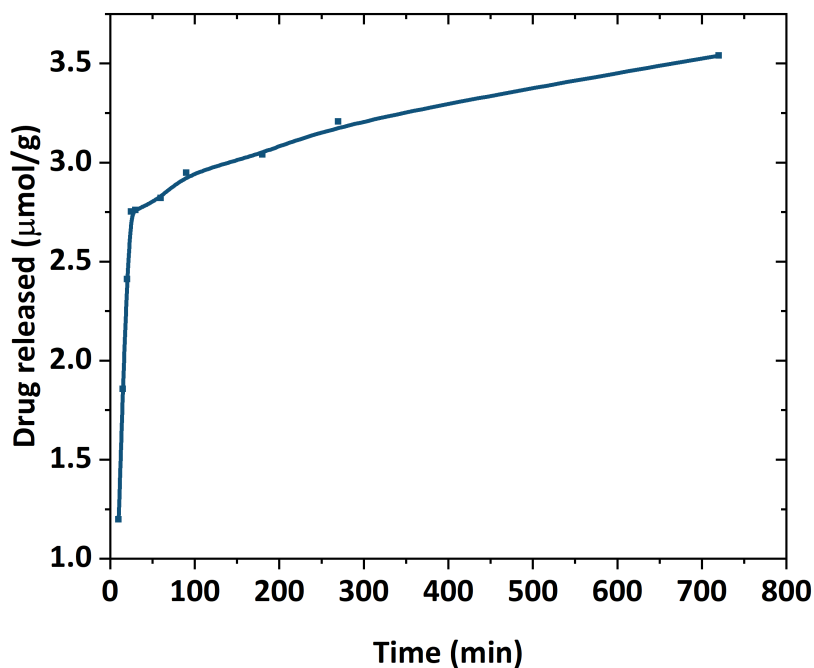


Figure 6.18: DOX release from magnetic nanoparticles in a pH 5 buffer and sink conditions. Extension of the time scale for the data obtained without hyperthermia treatment, as shown in Figure 6.12.

Bibliography

- [6.1] Catalano Enrico and Tiwari Asuthosh. Magnetic nanomaterial-based anticancer therapy. *Advanced Magnetic and Optical Materials*; Tiwary, A., Paramesvar, KI, Kumar, V., Hendrick, S., Eds, pages 141–164, 2017.
- [6.2] D Stanicki, T Vangijzegem, I Ternad, and S Laurent. An update on the applications and characteristics of magnetic iron oxide nanoparticles for drug delivery. *Expert Opinion on Drug Delivery*, 19(3):321–335, 2022.
- [6.3] Hung-Vu Tran, Nhat M Ngo, Riddhiman Medhi, Pannaree Srinoi, Tingting Liu, Supparesk Rittikulstichai, and T Randall Lee. Multifunctional iron oxide magnetic nanoparticles for biomedical applications: A review. *Materials*, 15(2):503, 2022.
- [6.4] RY Hong, B Feng, LL Chen, GH Liu, HZ Li, Y Zheng, and DG Wei. Synthesis, characterization and MRI application of dextran-coated Fe_3O_4 magnetic nanoparticles. *Biochemical Engineering Journal*, 42(3):290–300, 2008.
- [6.5] GR Iglesias, AV Delgado, F González-Caballero, and MM Ramos-Tejada. Simultaneous hyperthermia and doxorubicin delivery from polymer-coated magnetite nanoparticles. *Journal of Magnetism and Magnetic Materials*, 431:294–296, 2017.
- [6.6] Olivia L Lanier, Olena I Korotych, Adam G Monsalve, Dayita Wable, Shehaab Savliwala, Noa WF Grooms, Christopher Nacea, Omani R Tuitt, and Jon Dobson. Evaluation of magnetic nanoparticles for magnetic fluid hyperthermia. *International Journal of Hyperthermia*, 36(1):686–700, 2019.
- [6.7] Pablo Guardia, Riccardo Di Corato, Lenaic Lartigue, Claire Wilhelm, Ana Espinosa, Mar Garcia-Hernandez, Florence Gazeau, Liberato Manna, and Teresa Pellegrino. Water-soluble iron oxide nanocubes with high values of specific absorption rate for cancer cell hyperthermia treatment. *ACS Nano*, 6(4):3080–3091, 2012.

- [6.8] Ana Espinosa, Riccardo Di Corato, Jelena Kolosnjaj-Tabi, Patrice Flaud, Teresa Pellegrino, and Claire Wilhelm. Duality of iron oxide nanoparticles in cancer therapy: amplification of heating efficiency by magnetic hyperthermia and photothermal bimodal treatment. *ACS Nano*, 10(2):2436–2446, 2016.
- [6.9] H Belkahla, R Boudjemaa, V Caorsi, D Pineau, A Curcio, JS Lomas, P Decorse, A Chevillot-Biraud, T Azaïs, C Wilhelm, et al. Carbon dots, a powerful non-toxic support for bioimaging by fluorescence nanoscopy and eradication of bacteria by photothermia. *Nanoscale Advances*, 1(7):2571–2579, 2019.
- [6.10] Mariano Ortega-Muñoz, Paula Vargas-Navarro, Simona Plesselova, M Dolores Giron-Gonzalez, Guillermo R Iglesias, Rafael Salto-Gonzalez, Fernando Hernandez-Mateo, Angel V Delgado, F Javier Lopez-Jaramillo, and Francisco Santoyo-Gonzalez. Amphiphilic-like carbon dots as antitumoral drug vehicles and phototherapeutic agents. *Materials Chemistry Frontiers*, 5(23):8151–8160, 2021.
- [6.11] Daniel Jaque, L Martínez Maestro, Blanca del Rosal, P Haro-Gonzalez, Antonio Benayas, JL Plaza, E Martín Rodríguez, and J García Solé. Nanoparticles for photothermal therapies. *Nanoscale*, 6(16):9494–9530, 2014.
- [6.12] Jun Wu. The enhanced permeability and retention (EPR) effect: the significance of the concept and methods to enhance its application. *Journal of Personalized Medicine*, 11(8):771, 2021.
- [6.13] P Stephen Williams, Francesca Carpino, and Maciej Zborowski. Magnetic nanoparticle drug carriers and their study by quadrupole magnetic field-flow fractionation. *Molecular pharmaceuticals*, 6(5):1290–1306, 2009.
- [6.14] Sheng Tong, Christopher A Quinto, Linlin Zhang, Priya Mohindra, and Gang Bao. Size-dependent heating of magnetic iron oxide nanoparticles. *ACS Nano*, 11(7):6808–6816, 2017.
- [6.15] RR Wildeboer, P Southern, and QA Pankhurst. On the reliable measurement of specific absorption rates and intrinsic loss parameters in magnetic hyperthermia materials. *Journal of Physics D: Applied Physics*, 47(49):495003, 2014.
- [6.16] Nghia P Truong, Michael R Whittaker, Catherine W Mak, and Thomas P Davis. The importance of nanoparticle shape in cancer drug delivery. *Expert Opinion on Drug Delivery*, 12(1):129–142, 2015.
- [6.17] Julie A Champion and Samir Mitragotri. Role of target geometry in phagocytosis. *Proceedings of the National Academy of Sciences*, 103(13):4930–4934, 2006.

- [6.18] Julie A Champion, Yogesh K Katare, and Samir Mitragotri. Particle shape: a new design parameter for micro-and nanoscale drug delivery carriers. *Journal of Controlled Release*, 121(1-2):3–9, 2007.
- [6.19] Samir Mitragotri and Joerg Lahann. Physical approaches to biomaterial design. *Nature Materials*, 8(1):15–23, 2009.
- [6.20] Yong Qian, Dongmei Wang, Xiaofei Tian, Hongji Liu, Xingyu Wang, Hai Li, Qianwang Chen, Xin Zhang, and Hui Wang. Synthesis of urchin-like nickel nanoparticles with enhanced rotating magnetic field-induced cell necrosis and tumor inhibition. *Chemical Engineering Journal*, 400:125823, 2020.
- [6.21] Kexin Hou, Yandong Zhang, Meili Bao, Chao Xin, Zengyan Wei, Guochang Lin, and Zhenyu Wang. A multifunctional magnetic red blood cell-mimetic micromotor for drug delivery and image-guided therapy. *ACS Applied Materials & Interfaces*, 14(3):3825–3837, 2022.
- [6.22] Yajing Shen, Congyu Wu, Taro QP Uyeda, Gustavo R Plaza, Bin Liu, Yu Han, Maciej S Lesniak, and Yu Cheng. Elongated nanoparticle aggregates in cancer cells for mechanical destruction with low frequency rotating magnetic field. *Theranostics*, 7(6):1735, 2017.
- [6.23] Z Nemati, J Alonso, LM Martinez, H Khurshid, E Garaio, JA Garcia, MH Phan, and H Srikanth. Enhanced magnetic hyperthermia in iron oxide nano-octopods: size and anisotropy effects. *The Journal of Physical Chemistry C*, 120(15):8370–8379, 2016.
- [6.24] Jeetikanta Mohapatra, Meiyang Xing, Julian Beatty, Jacob Elkins, Takele Seda, Sanjay R Mishra, and J Ping Liu. Enhancing the magnetic and inductive heating properties of Fe₃O₄ nanoparticles via morphology control. *Nanotechnology*, 31(27):275706, 2020.
- [6.25] Raquel GD Andrade, Sérgio RS Veloso, and Elisabete MS Castanheira. Shape anisotropic iron oxide-based magnetic nanoparticles: Synthesis and biomedical applications. *International Journal of Molecular Sciences*, 21(7):2455, 2020.
- [6.26] Hiren Jethva, Omar Torres, Robert D Field, Alexei Lyapustin, Ritesh Gautam, and Vinay Kayetha. Connecting crop productivity, residue fires, and air quality over northern india. *Scientific Reports*, 9(1):16594, 2019.
- [6.27] Yukina Kobayashi, Michi Nagatsuka, Keisuke Akino, Noriko Yamauchi, Kouichi Nakashima, Tomoya Inose, Chihiro Nishidate, Keisuke Sato, Kohsuke Gonda, and Yoshio Kobayashi. Development of methods for fabricating nanoparticles composed of magnetite, gold, and silica toward diagnostic imaging. *Colloids and Surfaces A: Physicochemical and Engineering Aspects*, 643:128773, 2022.

- [6.28] Maria Arsianti, May Lim, Shi Nee Lou, Ian Y Goon, Christopher P Marquis, and Rose Amal. Bi-functional gold-coated magnetite composites with improved biocompatibility. *Journal of Colloid and Interface Science*, 354(2):536–545, 2011.
- [6.29] Morteza Mahmoudi, Abdolreza Simchi, Mohammad Imani, Mohammad A Shokrgozar, Abbas S Milani, Urs O Häfeli, and Pieter Stroeve. A new approach for the in vitro identification of the cytotoxicity of superparamagnetic iron oxide nanoparticles. *Colloids and Surfaces B: Biointerfaces*, 75(1):300–309, 2010.
- [6.30] Morteza Mahmoudi, Heinrich Hofmann, Barbara Rothen-Rutishauser, and Alke Petri-Fink. Assessing the in vitro and in vivo toxicity of superparamagnetic iron oxide nanoparticles. *Chemical Reviews*, 112(4):2323–2338, 2012.
- [6.31] SV Saikova, TV Trofimova, A Yu Pavlikov, DV Karpov, DI Chistyakov, and Yu L Mikhlin. Synthesis of magnetic hybrid magnetite—gold nanoparticles. *Russian Chemical Bulletin*, 69:1284–1289, 2020.
- [6.32] B Kalska-Szostko, M Rogowska, A Dubis, and K Szymański. Enzymes immobilization on Fe_3O_4 –gold nanoparticles. *Applied Surface Science*, 258(7):2783–2787, 2012.
- [6.33] Daozhen Chen, Qiusha Tang, Xiangdong Li, Xiaojin Zhou, Jia Zang, Wen-qun Xue, Jing-ying Xiang, and Cai-qin Guo. Biocompatibility of magnetic Fe_3O_4 nanoparticles and their cytotoxic effect on MCF-7 cells. *International journal of nanomedicine*, pages 4973–4982, 2012.
- [6.34] D Maniglio, F Benetti, L Minati, J Jovicich, Aldo Valentini, G Speranza, and C Migliaresi. Theranostic gold-magnetite hybrid nanoparticles for mri-guided radiosensitization. *Nanotechnology*, 29(31):315101, 2018.
- [6.35] Dickson K Kirui, Diego A Rey, and Carl A Batt. Gold hybrid nanoparticles for targeted phototherapy and cancer imaging. *Nanotechnology*, 21(10):105105, 2010.
- [6.36] Dickson K Kirui, Ildar Khalidov, Yi Wang, and Carl A Batt. Targeted near-ir hybrid magnetic nanoparticles for in vivo cancer therapy and imaging. *Nanomedicine: Nanotechnology, Biology and Medicine*, 9(5):702–711, 2013.
- [6.37] Jelena Kolosnjaj-Tabi, Yasir Javed, Lénaïc Lartigue, Jeanne Volatron, Dan Elgrabli, Iris Marangon, Giammarino Pugliese, Benoit Caron, Albert Figuerola, Nathalie Luciani, et al. The one year fate of iron oxide coated gold nanoparticles in mice. *ACS Nano*, 9(8):7925–7939, 2015.
- [6.38] Ana Espinosa, Jelena Kolosnjaj-Tabi, Ali Abou-Hassan, Anouchka Plan Sangnier, Alberto Curcio, Amanda KA Silva, Riccardo Di Corato, Sophie

- Neveu, Teresa Pellegrino, Luis M Liz-Marzán, et al. Magnetic (hyper) thermia or photothermia? progressive comparison of iron oxide and gold nanoparticles heating in water, in cells, and in vivo. *Advanced Functional Materials*, 28(37):1803660, 2018.
- [6.39] Klaus Maier-Hauff, Frank Ulrich, Dirk Nestler, Hendrik Niehoff, Peter Wust, Burghard Thiesen, Helmut Orawa, Volker Budach, and Andreas Jordan. Efficacy and safety of intratumoral thermotherapy using magnetic iron-oxide nanoparticles combined with external beam radiotherapy on patients with recurrent glioblastoma multiforme. *Journal of Neuro-oncology*, 103:317–324, 2011.
- [6.40] Prashant Kumar, Saurabh Pathak, Komal Jain, Arjun Singh, GA Basheed, RP Pant, et al. Low-temperature large-scale hydrothermal synthesis of optically active PEG-200 capped single domain MnFe_2O_4 nanoparticles. *Journal of Alloys and Compounds*, 904:163992, 2022.
- [6.41] Prashant Kumar, Saurabh Pathak, Arjun Singh, Komal Jain, Himani Khanduri, Lan Wang, Sang-Koog Kim, and RP Pant. Observation of intrinsic fluorescence in cobalt ferrite magnetic nanoparticles by Mn^{2+} substitution and tuning the spin dynamics by cation distribution. *Journal of Materials Chemistry C*, 10(35):12652–12679, 2022.
- [6.42] Dirk H Ortgies, Leonor De La Cueva, Blanca Del Rosal, Francisco Sanz-Rodríguez, Nuria Fernandez, M Carmen Iglesias-De La Cruz, Gorka Salas, David Cabrera, Francisco J Teran, Daniel Jaque, et al. In vivo deep tissue fluorescence and magnetic imaging employing hybrid nanostructures. *ACS Applied Materials & Interfaces*, 8(2):1406–1414, 2016.
- [6.43] Ian Y Goon, Leo MH Lai, May Lim, Paul Munroe, J Justin Gooding, and Rose Amal. Fabrication and dispersion of gold-shell-protected magnetite nanoparticles: systematic control using polyethyleneimine. *Chemistry of Materials*, 21(4):673–681, 2009.
- [6.44] Lei Li, Fumei Gao, Weiwei Jiang, Xueliang Wu, Yuanyuan Cai, Jintian Tang, Xueyun Gao, and Fuping Gao. Folic acid-conjugated superparamagnetic iron oxide nanoparticles for tumor-targeting MR imaging. *Drug Delivery*, 23(5):1726–1733, 2016.
- [6.45] María del Mar Ramos-Tejada, Julian L Viota, Katarzyna Rudzka, and Angel V Delgado. Preparation of multi-functionalized $\text{Fe}_3\text{O}_4/\text{Au}$ nanoparticles for medical purposes. *Colloids and Surfaces B: Biointerfaces*, 128:1–7, 2015.
- [6.46] Takeshi Kobayashi. Cancer hyperthermia using magnetic nanoparticles. *Biotechnology Journal*, 6(11):1342–1347, 2011.

- [6.47] Bogdan Florin Craciun, Gabriela Gavril, Dragos Peptanariu, Laura Elena Ursu, Lilia Clima, and Mariana Pinteala. Synergistic effect of low molecular weight polyethylenimine and polyethylene glycol components in dynamic nonviral vector structure, toxicity, and transfection efficiency. *Molecules*, 24(8):1460, 2019.
- [6.48] Qing Ji, Yuchen Wu, Andreas Albers, Meiyu Fang, and Xu Qian. Strategies for advanced oncolytic virotherapy: current technology innovations and clinical approaches. *Pharmaceutics*, 14(9):1811, 2022.
- [6.49] Muhammad Hammad Butt, Muhammad Zaman, Abrar Ahmad, Rahima Khan, Tauqeer Hussain Mallhi, Mohammad Mehedi Hasan, Yusra Habib Khan, Sara Hafeez, Ehab El Sayed Massoud, Md Habibur Rahman, et al. Appraisal for the potential of viral and nonviral vectors in gene therapy: A review. *Genes*, 13(8):1370, 2022.
- [6.50] M Khansarizadeh, A Mokhtarzadeh, M Rashedinia, SM Taghdisi, P Lari, KH Abnous, and M Ramezani. Identification of possible cytotoxicity mechanism of polyethylenimine by proteomics analysis. *Human & Experimental Toxicology*, 35(4):377–387, 2016.
- [6.51] Lian Xue, Yunfeng Yan, Petra Kos, Xiaoping Chen, and Daniel J Siegwart. Pei fluorination reduces toxicity and promotes liver-targeted sirna delivery. *Drug Delivery and Translational Research*, 11:255–260, 2021.
- [6.52] Qinglian Hu, Fengliang Guo, Fenghui Zhao, Guping Tang, and Zhengwei Fu. Cardiovascular toxicity assessment of poly (ethyleneimine)-based cationic polymers on zebrafish model. *Journal of Biomaterials Science, Polymer Edition*, 28(8):768–780, 2017.
- [6.53] Rui Deng, Yanan Yue, Fan Jin, Yangchao Chen, Hsiang-Fu Kung, Marie CM Lin, and Chi Wu. Revisit the complexation of PEI and DNA—how to make low cytotoxic and highly efficient PEI gene transfection non-viral vectors with a controllable chain length and structure? *Journal of Controlled Release*, 140(1):40–46, 2009.
- [6.54] Yongsheng Gao, Jian-Yuan Huang, Jonathan O’Keeffe Ahern, Lara Cutlar, Dezhong Zhou, Feng-Huei Lin, and Wenxin Wang. Highly branched poly (β -amino esters) for non-viral gene delivery: High transfection efficiency and low toxicity achieved by increasing molecular weight. *Biomacromolecules*, 17(11):3640–3647, 2016.
- [6.55] Yaqiong Wang, Ping Cao, Shicui Li, Xiaofeng Zhang, Jin Hu, Mingyue Yang, Sujuan Yao, Feng Gao, Ao Xia, Jian Shen, et al. Layer-by-layer assembled PEI-based vector with the upconversion luminescence marker for gene delivery.

- Biochemical and Biophysical Research Communications*, 503(4):2504–2509, 2018.
- [6.56] Manuel Ocaña, Maria P Morales, and Carlos J Serna. The growth mechanism of α -Fe₂O₃ ellipsoidal particles in solution. *Journal of Colloid and Interface Science*, 171(1):85–91, 1995.
- [6.57] Weijie Huang, Fengchang Yang, Lu Zhu, Rui Qiao, and Yiping Zhao. Manipulation of magnetic nanorod clusters in liquid by non-uniform alternating magnetic fields. *Soft Matter*, 13(20):3750–3759, 2017.
- [6.58] Ylenia Jabalera, Alberto Sola-Leyva, Ana Peigneux, Federica Vurro, Guillermo R Iglesias, Jesus Vilchez-Garcia, Inmaculada Pérez-Prieto, Francisco J Aguilar-Troyano, Luisa C López-Cara, María P Carrasco-Jiménez, et al. Biomimetic magnetic nanocarriers drive choline kinase alpha inhibitor inside cancer cells for combined chemo-hyperthermia therapy. *Pharmaceutics*, 11(8):408, 2019.
- [6.59] Michele Iafisco, Josè Manuel Delgado-Lopez, Elena Maria Varoni, Anna Tampieri, Lia Rimondini, Jaime Gomez-Morales, and Maria Prat. Cell surface receptor targeted biomimetic apatite nanocrystals for cancer therapy. *Small*, 9(22):3834–3844, 2013.
- [6.60] H Maleki, A Simchi, M Imani, and BFO Costa. Size-controlled synthesis of superparamagnetic iron oxide nanoparticles and their surface coating by gold for biomedical applications. *Journal of Magnetism and Magnetic Materials*, 324(23):3997–4005, 2012.
- [6.61] DA Petrov, C-R Lin, RD Ivantsov, SG Ovchinnikov, SM Zharkov, G Yu Yurkin, DA Velikanov, Yu V Knyazev, MS Molokeev, Y-T Tseng, et al. Characterization of the iron oxide phases formed during the synthesis of core-shell Fe_xO_y@C nanoparticles modified with ag. *Nanotechnology*, 31(39):395703, 2020.
- [6.62] AE Sokolov, OS Ivanova, Aleksandr S Fedorov, Evgeniya Andreevna Kovaleva, MA Vysotin, C-R Lin, and Sergei Gennad'evich Ovchinnikov. Why the magnetite–gold core–shell nanoparticles are not quite good and how to improve them. *Physics of the Solid State*, 63(10):1536–1540, 2021.
- [6.63] German Garcia Rubia, Ana Peigneux, Ylenia Jabalera, Javier Puerma, Francesca Oltolina, Kerstin Elert, Donato Colangelo, Jaime Goémez Morales, Maria Prat, and Concepcion Jimenez-Lopez. pH-dependent adsorption release of doxorubicin on MamC-biomimetic magnetite nanoparticles. *Langmuir*, 34(45):13713–13724, 2018.

- [6.64] Francesca Oltolina, Donato Colangelo, Ivana Miletto, Nausicaa Clemente, Marta Miola, Enrica Verné, Maria Prat, and Antonia Follenzi. Tumor targeting by monoclonal antibody functionalized magnetic nanoparticles. *Nanomaterials*, 9(11):1575, 2019.
- [6.65] Miao Guo, Yu Yan, Hongkai Zhang, Husheng Yan, Youjia Cao, Keliang Liu, Shourong Wan, Junsheng Huang, and Wei Yue. Magnetic and pH-responsive nanocarriers with multilayer core-shell architecture for anticancer drug delivery. *Journal of Materials Chemistry*, 18(42):5104–5112, 2008.
- [6.66] Barbara Lafuente, Robert T Downs, Hexiong Yang, Nate Stone, Thomas Armbruster, Rosa Micaela Danisi, et al. The power of databases: the RRUFF project. *Highlights in mineralogical crystallography*, 1:25, 2015.
- [6.67] Zimin Li, Corinne Chanéac, Gilles Berger, Sophie Delaunay, Anaïs Graff, and Grégory Lefèvre. Mechanism and kinetics of magnetite oxidation under hydrothermal conditions. *RSC Advances*, 9(58):33633–33642, 2019.
- [6.68] Qiang Yao and Charles A Wilkie. Thermal degradation of blends of polystyrene and poly (sodium 4-styrenesulfonate) and the copolymer, poly (styrene-co-sodium 4-styrenesulfonate). *Polymer Degradation and Stability*, 66(3):379–384, 1999.
- [6.69] Nehar Celikkin, Lucie Jakubcová, Martin Zenke, Mareike Hoss, John Erik Wong, and Thomas Hieronymus. Polyelectrolyte coating of ferumoxytol nanoparticles for labeling of dendritic cells. *Journal of Magnetism and Magnetic Materials*, 380:39–45, 2015.
- [6.70] Pinar Avci, Asheesh Gupta, Magesh Sadasivam, Daniela Vecchio, Zeev Pam, Nadav Pam, and Michael R Hamblin. Low-level laser (light) therapy (lllt) in skin: stimulating, healing, restoring. In *Seminars in cutaneous medicine and surgery*, volume 32, page 41. NIH Public Access, 2013.
- [6.71] Mikel Rincón-Iglesias, Irati Rodrigo, Leixuri B. Berganza, Esraa Samy Abu Serea, Fernando Plazaola, Senentxu Lanceros-Méndez, Erlantz Lizundia, and Javier Reguera. Core-shell Fe₃O₄@ Au nanorod-loaded gels for tunable and anisotropic magneto-and photothermia. *ACS Applied Materials & Interfaces*, 14(5):7130–7140, 2022.
- [6.72] Felisa Reyes-Ortega, Blanca Luna Checa Fernández, Angel V Delgado, and Guillermo R Iglesias. Hyperthermia-triggered doxorubicin release from polymer-coated magnetic nanorods. *Pharmaceutics*, 11(10):517, 2019.
- [6.73] Katarzyna Rudzka, Angel V Delgado, and Julian L Viota. Maghemite functionalization for antitumor drug vehiculization. *Molecular pharmaceutics*, 9(7):2017–2028, 2012.

- [6.74] Chin-Hao Su, Andree Soendoro, Shinya Okayama, Fitriani Jati Rahmania, Takashi Nagai, Toyoko Imae, Kaname Tsutsumiuchi, and Noriyasu Kawai. Drug release stimulated by magnetic field and light on magnetite-and carbon dot-loaded carbon nanohorn. *Bulletin of the Chemical Society of Japan*, 95(4):582–594, 2022.
- [6.75] Nasrin Zohreh, Sakineh Alipour, Seyed Hassan Hosseini, Morena S Xaba, Reinout Meijboom, Mahdi Fasihi Ramandi, Nazila Gholipour, and Mehdi Akhlaghi. Natural salep/PEGylated chitosan double layer toward a more sustainable pH-responsive magnetite nanocarrier for targeted delivery of DOX and hyperthermia application. *ACS Applied Nano Materials*, 2(2):853–866, 2019.
- [6.76] Parisa Eslami, Martin Albino, Francesca Scavone, Federica Chiellini, Andrea Morelli, Giovanni Baldi, Laura Cappiello, Saer Doumett, Giada Lorenzi, Costanza Ravagli, et al. Smart magnetic nanocarriers for multi-stimuli on-demand drug delivery. *Nanomaterials*, 12(3):303, 2022.
- [6.77] Ali Dabbagh, Ziba Hedayatnasab, Hamed Karimian, Masoud Sarraf, Chai Hong Yeong, Hamid Reza Madaah Hosseini, Noor Hayaty Abu Kasim, Tin Wui Wong, and Noorsaadah Abdul Rahman. Polyethylene glycol-coated porous magnetic nanoparticles for targeted delivery of chemotherapeutics under magnetic hyperthermia condition. *International Journal of Hyperthermia*, 2018.
- [6.78] Sung-Wook Choi, Woo-Sik Kim, and Jung-Hyun Kim. Surface modification of functional nanoparticles for controlled drug delivery. *Journal of Dispersion Science and Technology*, 24(3-4):475–487, 2003.
- [6.79] Jian You, Guodong Zhang, and Chun Li. Exceptionally high payload of doxorubicin in hollow gold nanospheres for near-infrared light-triggered drug release. *ACS Nano*, 4(2):1033–1041, 2010.
- [6.80] Agha Zeeshan Mirza and Hina Shamshad. Preparation and characterization of doxorubicin functionalized gold nanoparticles. *European Journal of Medicinal Chemistry*, 46(5):1857–1860, 2011.

Chapter 7

Magnetic activated carbon as stimuli-responsive vehicles for methotrexate

J. Mater. Chem. B, submitted.

Abstract

This work explores the possibility of using porous particles based on activated carbon (AC) as drug delivery vehicles for methotrexate (MTX). In order to broaden the range of applications and improve performance, these particles are coated with magnetic nanoparticles, which give them a superparamagnetic character and the ability to respond to magnetic forces for transport and localisation. The resulting composites are positively charged by adsorbing a layer of cationic polymer, branched low molecular weight polyethyleneimine (PEI). Once the particles have been characterised in terms of size, composition and magnetic hysteresis, they are brought into contact with MTX solutions, to test their possible use as vehicles for this anti-tumour drug. Electrophoretic mobility and infrared absorption data qualitatively demonstrate the presence of magnetite, polymer and drug in the systems studied. It is proposed to first analyse whether the final particles respond to the action of infrared laser radiation, producing local heating as expected in photothermal therapy (PTT), and it is demonstrated that the mixed MAC-PEI particles produce up to 180 W/g of specific absorbed power (SAR). Since the particles are anisotropic in shape, another possible stimulus affecting their performance as drug delivery vehicles is the application of a rotating magnetic field (RMF) at low frequency, which will produce a torque on the particles and hence induce their rotation. Recent studies have suggested the possibility of increasing the efficiency of drug delivery is raised, which is an even less explored technique. As a prelude to investigating their adsorption and drug release capacity, their biocompatibility is assessed using human skin M1 fibroblasts. MAC-PEI particles do not significantly impair cell viability at concentrations below 700 $\mu\text{g/ml}$, as determined by crystal violet assay. The porosity of the activated carbon and the attractive interaction between the MAC-PEI particles and MTX result in strong drug adsorption onto the particles, to the extent that more than 80% of the drug contained in 0.6 mM solution is loaded by particles at a concentration of 6 mg/mL. The release is studied as a function of time by maintaining a pH of 5.8 both without external stimulus and applying photothermia and rotating magnetic fields during release. The results show that the amount of MTX released is twice that obtained without stimuli, with negligible difference between both stimuli, so that in both cases they could be used with the designed particles as an active vehicle for MTX transport and release.

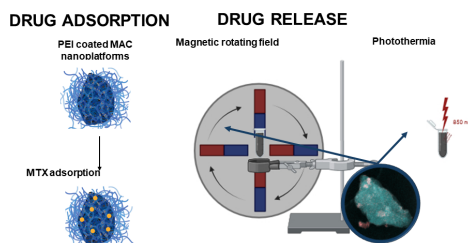


Figure 7.1: Figure created with Biorender.com.

7.1. Introduction

Cancer is one of the world's leading causes of death and its incidence is expected to triple by 2050, largely due to the world's ageing population [7.1, 7.2]. It is therefore evident that novel approaches are required to overcome the forthcoming challenges in cancer treatment. A promising strategy to address this challenge involves the use of advanced carriers with the objective of optimising conventional treatments (e.g. chemotherapy) and/or the implementation of novel therapeutic approaches such as antitumour hyperthermia [7.3–7.9].

Methotrexate (MTX) is a standard anticancer drug employed in the treatment of a range of cancers, including acute lymphoblastic leukemia [7.10], osteosarcoma [7.11], and lymphoma malignancies [7.12], among others. However, MTX is subject to rapid plasma clearance and poor solubility [7.13], necessitating the administration of high doses over an extended infusion period to achieve effective treatment. Consequently, this dosage regimen is frequently associated with toxic effects and the development of resistance [7.14, 7.15]. Therefore, the controlled delivery of MTX is being investigated as a means of enhancing the safety and efficacy of therapy [7.16].

Among the potential advanced materials for MTX delivery, carbon-based nanoporous particles have shown promise [7.17–7.19]. The nanoporous structure of AC materials is responsible for a high surface area to volume ratio, which renders them potential candidates for high drug payloads, as has been previously reported [7.20, 7.21]. Moreover, AC nanoporous particles are cost-effective and safe, as they are already being employed in clinical settings [7.22]. In addition to their potential for drug delivery, they are capable of absorbing light within the NIR-I window, where tissues are nearly transparent, and converting it into heat. For example, Shahcheragh *et al.* [7.23] demonstrated a strong absorbance in the 300–1100 nm wavelength range. Furthermore, Li *et al.* [7.24] developed an innovative approach whereby the incorporation of carbon nanoparticles (NPs) facilitated the enhanced absorption of laser irradiation on a suspension of (low-absorbance) alumina, resulting in the production of particles with precisely controlled geometry. The elevation of temperature achieved when a system is subjected to an external stimulus and is capable of converting it into heat is generally referred to as hyperthermia. When induced by a near-infrared (NIR) laser, it is termed photothermia, or PTT. While other potential applications exist, the majority of research efforts in the field of PTT are concentrated on the biomedical domain. The objective is to achieve localised heating, which can effectively eliminate malignant cells without affecting surrounding healthy tissue. This can be achieved through direct application of an infrared laser to skin tumours or indirectly to deeper tumours using techniques such as optical fibres, which can guide the light directly into the malignant area. While PTT has been the subject of extensive preclinical investigation (see, for example, references [7.25, 7.26]), ongoing research is aimed at facilitating its translation into clinical applications [7.27].

Iron oxide NPs (magnetite and maghemite) have been the subject of extensive investigation due to their superparamagnetic and biocompatible character, with applications in drug delivery, magnetic resonance imaging (MRI), and magnetic hyperthermia agents [7.28]. It is noteworthy that magnetite NPs also demonstrate a photothermal therapy (PTT) response, as evidenced in previous studies [7.29–7.31]. It has recently been reported that a low-frequency magnetic field applied to drug-loaded magnetic particles has the potential to induce a prompt release of the drug. In such circumstances, the magnetic particles align themselves with the direction of the rotation field, thereby generating a strong mechanical force that is capable of producing a rapid release of the drug [7.32,7.33]. In addition, *in vivo* [7.34] antitumor effect of magnetic particles under a low-frequency magnetic field have been recently demonstrated.

Polyethyleneimine (PEI) has been shown to be an effective coating agent for inorganic nanoparticles in a number of studies [7.31, 7.35–7.37]. It is a versatile, highly positive charge-density polycation that creates a cationic surface, which has particular interest in the field of anticancer drug delivery. A positive surface can facilitate enhanced biological interactions with cellular surfaces, thereby improving cellular uptake. Additionally, it can facilitate interactions with tumour vasculature proteoglycans, which could improve tumour targeting [7.38]. Furthermore, the characteristics of this polymer are highly advantageous for drug delivery, particularly due to its hydrophilic nature and its capacity to load negatively charged drugs such as MTX, as previously reported [7.39]. Furthermore, and of greater relevance to the intended application, it endows the system with biocompatibility, given that low-molecular-weight branched PEI exhibits low cytotoxicity [7.37, 7.40].

This article proposes a method for the production of activated carbon (AC) microporous particles that are magnetisable (Magnetic Activated Carbons, or MAC) through the incorporation of magnetite NPs. The physicochemical and magnetic characterisation of the particles confirms their structure, demonstrating an appropriate size, composition, and PTT and magnetic character. The PEI surface coating of MAC was employed to enhance the particles' interaction with MTX, given that it exhibited a negative charge. Moreover, the MAC-PEI structures demonstrated preliminary biocompatibility, as evidenced by the absence of cytotoxic effects in the human skin fibroblast cell line M1 in a broad concentration range (0-700 µg/mL).

Finally, drug release studies demonstrated the potential of MTX-loaded MAC-PEI for stimuli-responsive drug delivery when an external NIR-I light and/or a low-frequency magnetic field was applied. To the best of our knowledge, this is the first instance of a hybrid nanomaterial based on AC, magnetic nanoparticles and PEI having been engineered. To date, no studies have focused on the release of this material and the effect of PTT and low-strength rotating magnetic field (RMF) stimuli. It is the objective of this research to facilitate the clinical translation of MAC particles as anticancer agents under external stimuli.

7.2. Materials and methods

Materials

YP50F AC particles were purchased from Kuraray Europe GmbH (Finland). The iron salts $\text{FeSO}_4 \cdot 7\text{H}_2\text{O}$ and $\text{FeCl}_3 \cdot 6\text{H}_2\text{O}$ from Merck Sigma Aldrich (Germany), and a 32% ammonia solution from Scharlau, Spain were used for the preparation of the magnetic NPs, together with water from a Milli-Q Academic device (Millipore, Spain). For the polymer coating, branched polyethyleneimine (PEI, MW \approx 2000 g/mol) was used, and for the drug adsorption and release experiments methotrexate (MTX) was chosen, both compounds from Sigma Aldrich (Germany).

Phosphate buffer saline (PBS), glutaraldehyde, acetic acid, crystal violet solution (1%, aqueous solution) and antibiotic-antimycotic solution (10,000 units penicillin, 10 mg streptomycin and 25 μg amphotericin B per mL) for cell culture and biocompatibility tests were also from Merck Sigma-Aldrich (Germany), and Dulbecco's modified Eagle's medium (DMEM), Fetal Bovine Serum (FBS), 0.05% trypsin-EDTA were supplied by Gibco™ (ThermoFisher Scientific, USA).

Methods

Preparation of polyethyleneimine-coated magnetic activated carbon particles preparation

The synthesis of Fe_3O_4 colloids was conducted in accordance with the chemical co-precipitation methodology previously reported in reference [7.41]. Magnetic activated carbon (MAC) particles were produced by the addition of YP50F AC to the aqueous media in which the Fe_3O_4 colloids were formed. The methodology commenced with the mechanical stirring of two aqueous solutions, comprising 0.9 g of $\text{FeSO}_4 \cdot 7\text{H}_2\text{O}$ in 8.6 mL and 1.7 g of $\text{FeCl}_3 \cdot 6\text{H}_2\text{O}$ in 10 mL, respectively, at room temperature. Subsequently, 5.2 g of YP50F AC was dispersed in 100 mL of water and added to the aforementioned solutions. The resulting suspension was then stirred for a period of 30 minutes (Figure 7.2a).

To induce the precipitation of Fe_3O_4 onto the surface of the AC particles, 4.4 mL of the ammonia solution was added. Following a period of one hour under mechanical stirring, the resulting MAC particles were subjected to three cycles of centrifugation (10 minutes at 15,000 rpm, using a Sigma 3-30KS centrifuge, Germany), followed by magnetic decanting and redispersion in water. Subsequently, the product was subjected to drying in an oven at a temperature of 50 °C.

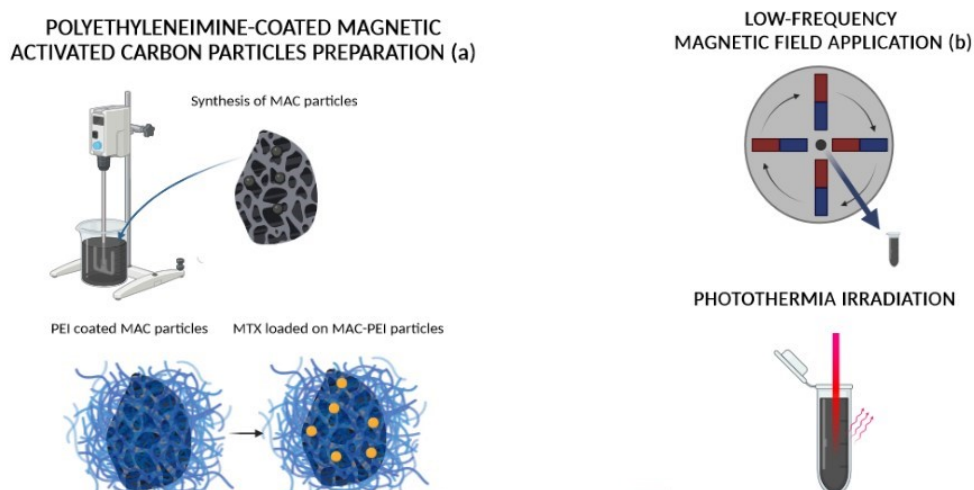


Figure 7.2: (a) Scheme of the synthesis procedures of MAC particles, their coating with PEI, and the incorporation of pharmacophore. (b) Diagram of the operation of the low-frequency rotating magnetic field device (top) and of the photothermia experiment (below). Images created with Biorender.com.

In order to obtain the MAC particles coated with the PEI polymer, 0.5 g of MAC particles were diluted in 30 mL of PEI, and MilliQ water was added to complete a solution of 250 mL. The mixture was then subjected to rigorous mechanical stirring for the duration of the night. Subsequently, the particles were purified by centrifugation at 21,000 rpm for 20 minutes, with this process repeated until the supernatant reached a pH range of 7–7.5.

Adsorption of methotrexate onto the surface of polyethyleneimine-coated magnetic activated carbon particles

MTX-loaded MAC-PEI nanoporous particles were produced by the incubation of MAC particles (6 mg/ml) in an aqueous solution containing MTX (0.6 mM) under mild stirring using a Stuart rotator SB3 (United States) at 30 rpm (Figure 7.2a). Samples were centrifuged for 45 minutes at 14000 rpm (Mikro 220R, Hettich Zentrifugen, Germany) to remove the non-attached drug molecules. Two adsorption kinetics experiments were performed, the first one at a fixed concentration (the one chosen for the rest of the experiments, 0.6 mM MTX) versus time, in the range of 1, 2, 24, 72, 144 hours. The second one, at a fixed time (24 hours of adsorption) varying the drug concentration (between 0.2 mM–10 mM). Figure 7.2a provides a schematic representation of the process of MAC particle synthesis, coating with PEI, and drug incorporation.

Size and shape of the particles

Evaluation of the size of the MAC nanoplateforms was carried out by electron microscopy analysis. Fe_3O_4 and MAC particles were studied by high-resolution transmission electron microscopy (HRTEM) and high-angle annular dark field scanning transmission electron microscopy (HAADF-STEM) (HAADF TALOS F200X, Thermofisher Scientific Inc., United States; accelerating voltage of 200 kV).

Elemental analysis was performed during these electron microscopy observations [energy dispersive X-ray (EDX) spectrometer, Bruker Nano GmbH, Germany].

Particle size was also evaluated by Dynamic Light Scattering (DLS) using a Zetasizer Nano-ZS (Malvern Pananalytical, UK).

The specific surface area of AC YP50F is $1692 \text{ m}^2/\text{g}$, and the micropore size distribution peaks at 1 nm (according to Kuraray Europe GmbH). These characteristics make it an ideal drug vehicle [7.41].

Electrophoretic mobility

The determination of the surface electrical properties of AC, bare Fe_3O_4 , MAC-PEI and MTX-loaded MAC-PEI was carried out by measuring their electrophoretic mobility using the Zetasizer Nano-ZS device. A qualitative follow-up of the PEI coating of the MAC surface and the subsequent MTX adsorption was carried out by determining the influence of pH on their electrophoretic mobility in the presence of 1 mM KCl.

FTIR analysis

The structure of MAC-PEI was confirmed by Fourier transform infrared (FTIR) spectroscopy (FT/IR-6200 spectrometer, JASCO, United States; resolution of 0.25 cm^{-1}). For that purpose, the MAC-PEI spectrum was compared to those obtained for MAC, Fe_3O_4 and PEI.

Magnetic properties

The magnetization cycles were obtained at $(20.0 \pm 0.5) \text{ }^\circ\text{C}$, in both a Vibrating Sample Magnetometer (PPMS DynaCool, Quantum Design, USA, maximum applied field strength 4700 kA/m) and an AC Hyster Series magnetometer (Nanotech Solutions S.L., Spain), operating at a frequency of 1.5 kHz and a maximum field strength of 120 kA/m.

Low-frequency rotating magnetic field application

The technique entails exposing the sample to a low-frequency RMF, thereby circumventing the heating phenomenon that occurs in magnetic hyperthermia. This approach facilitates drug release by rotating the particles, which enhances the diffusion process. This is accomplished through the utilisation of four permanent magnets positioned in a face-to-face configuration. The magnets are made to rotate in synchrony around the sample, with opposite polarities (Figure 7.2b). The synchronised rotation of the magnetic field induces a corresponding rotation of the magnetic particles within the sample. The field strength was 65 mT and the rotation speed 300 ± 10 rpm.

Thermal measurements

The photothermal (PTT) capacity of the various samples was evaluated using an 850 nm laser at powers of 0.5, 1, and 1.5 W/cm². The particle concentrations were 5 mg/mL. Eppendorf tubes containing 100 μ L of the nanoparticles (Fe₃O₄, AC, MAC, and MAC-PEI particles) in water were used.

Irradiation was conducted from the top, and the temperature was recorded with a thermographic camera (FLIR E60, 320 \times 240 pixel IR resolution, FLIR Systems, Inc., United States) throughout the experiment (Fig. 7.2b).

The amount of heat transferred from the particles to their surrounding environment is determined by the Specific Absorption Rate (SAR), which is calculated through experimental means as follows:

$$SAR = \frac{C_{liq}\rho_{liq}}{\phi} \frac{dT}{dt} \quad (7.1)$$

where C_{liq} is the mass specific heat, ρ_{liq} is the density of the suspension, and ϕ is the NPs concentration (w/v). The essential quantity is the rate of temperature increase, $\frac{dT}{dt}$, which is determined by the linear model [7.42]. The densities of magnetite ($\rho_{MAG} = 5.2 \times 10^3$ g/L) and of AC ($\rho_{AC} = 0.3 \times 10^3$ g/L, provided by Kuraray Europe GmbH), as well as the magnetite-to-carbon ratio for the MAC sample, were used for the SAR determination.

Magnetic activated carbon platforms as methotrexate delivery systems

In order to determine the concentration of MTX after adsorption, a calibration set of absorbance versus concentration data was obtained by measuring the optical absorbance at 305 nm (maximum absorbance wavelength for MTX) using a

BioSpectrometer kinetic UV/Vis spectrophotometer (Eppendorf AG, Germany) for the concentrations used in the range of 0.001-0.2 mM of MTX.

Drug release experiments were conducted using MTX-loaded MAC-PEI particles (1.5 mL suspensions containing 6 mg/mL of particles) under two different conditions: physiological (pH 7.4 phosphate buffer) and tumour-like (pH 5.8 phosphate buffer).

To this end, 1.3 mL of the medium was withdrawn at predetermined intervals for UV spectrophotometric analysis. An equal volume of the release medium, maintained under the same conditions, was added after sampling to maintain the final volume (sink conditions [7.37]), and the release process was continued. When necessary, the laser for photothermia and/or the RMF were applied while the release process was taking place.

Cell culture and cytotoxicity assay

Cells from the human fibroblast-derived, non-tumor epithelial cells and not commercial M1 cell line were cultured in DMEM pH 7.4, supplemented with 10% (v/v) FBS and antibiotic-antimycotic solution (0.2%) as previously described [7.43]. Cells were incubated at 37°C with 5% CO₂. Medium was changed every 48 h, unless stated.

MAC-PEI particles potential cytotoxicity was determined by crystal violet, following a previously described protocol [7.31]. M1 cells were grown in a 96-well plate (25,000 cells per well) at 37°C with 5% CO₂ for 24 h. Then, cells were exposed to a broad concentration range (0–1000 µg/mL) of previously UV- and ethanol-sterilized MAC-PEI particles.

After 24 h incubation, the medium was removed from each well by aspiration, cells were washed with sterile PBS, and were fixed with glutaraldehyde (1%) for 15 min. Glutaraldehyde was then washed with PBS 4 times. Excess PBS was removed by plate decantation and crystal violet (0.1% v/v) was added, incubated for 20 min, and repeatedly washed with deionized water until no color was leaking from the plate. The plate was dried overnight, the remaining dye was solubilized with 10% acetic acid and loaded in triplicates into a new 96-well plate. Absorbance was measured in each well at 590 nm with a microplate reader spectrophotometer (INNO, LTeK, Korea).

Statistical analysis was carried out using one-way ANOVA followed by Bonferroni test to determine statistical significance ($p \leq 0.05$). All statistical analyses were performed using GraphPad Prism (version 10.1.2, La Jolla, CA, USA).

7.3. Results and discussion

Characterization

Particle geometry

Fe_3O_4 and MAC particle sizes determined by HRTEM were found to be (6.59 ± 0.22) nm (Figure 7.2a) and (230 ± 170) nm, respectively (Figure 7.3b,c). These average sizes were determined by measuring at least 20 particles in different pictures using JImage software. EDX mapping of Fe and C employing HAADF-STEM imaging demonstrated that the magnetite (represented by the Fe element) is uniformly distributed over specific areas of the carbon surface (represented by the C element) in the MAC particles (Figure 7.3d,e,f).

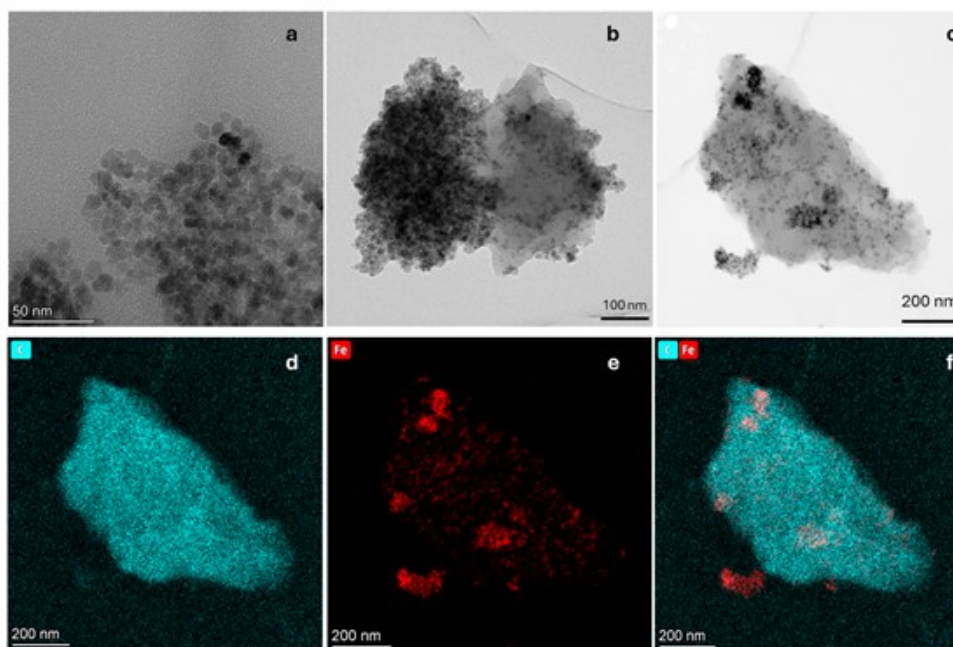


Figure 7.3: HRTEM pictures of bare Fe_3O_4 and MAC platforms. (a) bare Fe_3O_4 ; (b and c) MAC; (d) EDX mapping analysis of C element of MAC particles; (e) EDX mapping analysis of Fe element of MAC particles; (f) EDX mapping analysis of overlapped C and Fe elements of magnetic carbon activated nanoplateforms.

The sizes obtained by DLS were also measured (Figure 7.10, Supplementary Information), obtaining (74 ± 28) nm for magnetite, (355 ± 74) nm for carbon, (388 ± 170) nm for MAC, and (593 ± 121) nm for MAC-PEI [7.44].

Electrical surface characteristics

Electrophoretic mobility measurements of bare magnetite Fe_3O_4 , AC, MAC, and MTX-loaded MAC in 1 mM KCl served as qualitative assessment of the surface changes during the preparation procedure steps (Figure 7.4).

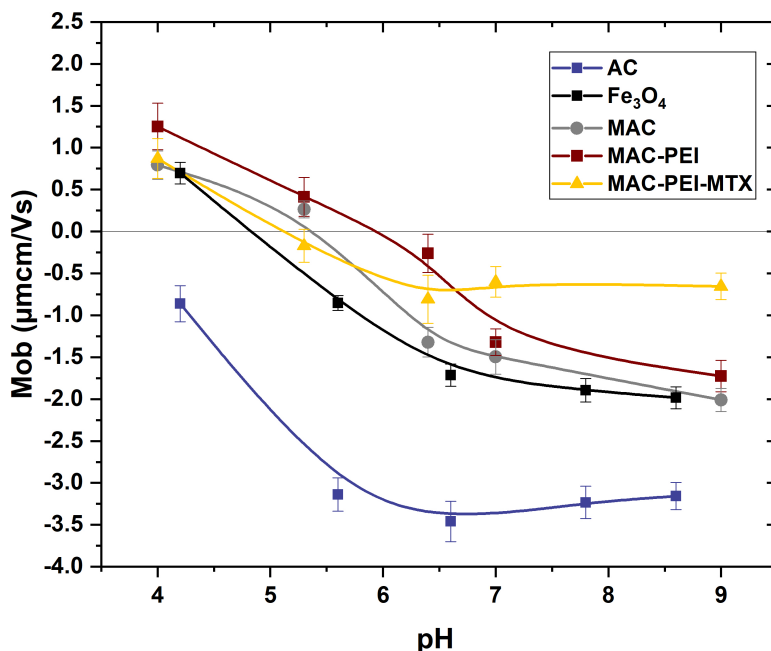


Figure 7.4: Electrophoretic mobility measurements of bare Fe_3O_4 , AC, MAC and MTX-loaded MAC (1 mM KCl).

In accordance with previous studies, negative and neutral electrophoretic mobility was found for AC and bare Fe_3O_4 , respectively [7.45]. When AC particles were decorated with Fe_3O_4 colloids following the coprecipitation method, the zeta potential values of the particles shifted from highly negative to moderate values, closer to those obtained for bare Fe_3O_4 . This could be explained by the coverage of Fe_3O_4 onto the AC surface, as demonstrated by EDX mapping analysis (Figure 7.3f). As expected, the PEI coating causes the mobility to move towards slightly more positive values, this being in fact a qualitative proof of the achieved coating [7.37]. Finally, MTX-loaded MAC particles depicted more moderately negative values than non-loaded ones [7.37]. Potential conjugation between MAC $-\text{COOH}$ groups and MTX $-\text{NH}_2$ groups could explain that behavior, as it has been previously reported [7.19].

Infrared analysis

The MAC-PEI nanoporous particles were characterized by FTIR (Figure 7.5). The IR transmittance spectra matched well with the data already reported in the literature [7.46–7.49]. The following analysis focuses on the most significant peaks that enable the identification of each material used. Symmetric and asymmetric C-H stretching vibrations of the fatty CH_2 on the PEI backbone signal were identified in the IR spectrum of MAC-PEI and PEI, at 2970 and 2894 cm^{-1} . Then, at 1635 cm^{-1} , the stretching vibration of C=O in the carboxyl group appeared for MAC and MAC-PEI. AC presence in MAC and MAC-PEI was also confirmed by the absorption peak located at 1020 cm^{-1} , as it is characteristic of some oxygen-containing functional groups. Because of that, this peak can also be observed in the Fe_3O_4 spectrum. PEI coating was again identified at 881 cm^{-1} , as an absorption peak appeared corresponding to the stretching vibration of the N-H bond in the PEI amine group. Finally, the absorption bands of the region around $\approx 550\text{ cm}^{-1}$ are attributed to the stretching vibrations of metal oxide (Fe-O) bonds.

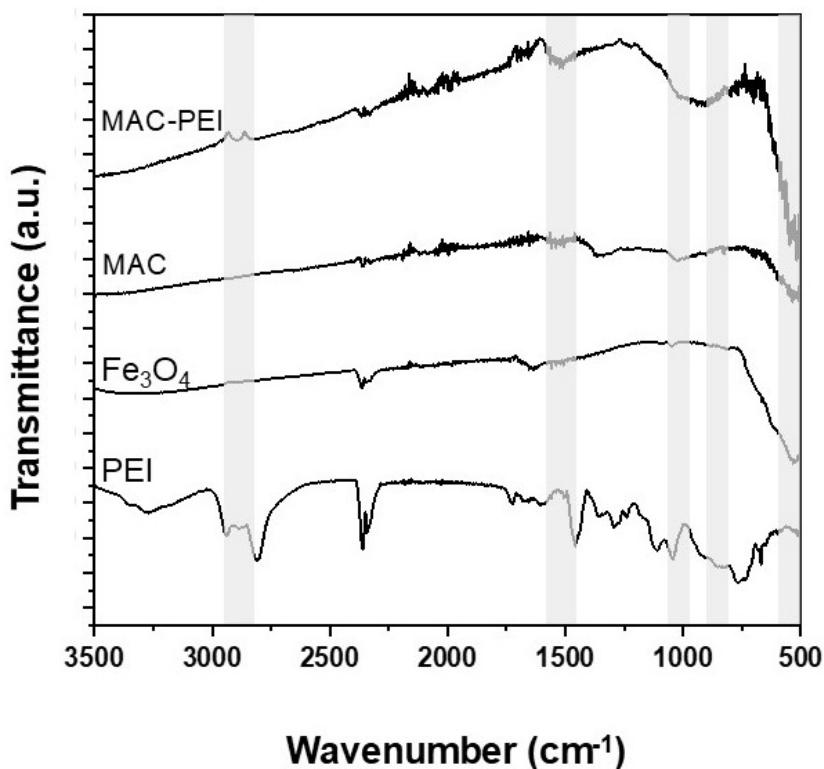


Figure 7.5: FTIR analysis of the particles investigated.

Magnetic characterization

Magnetic characterization results of bare Fe_3O_4 , MAC, and PEI-coated particles are depicted in Figure 7.6a. It can be observed that the magnetization of magnetite nanoparticles is 65 emu/g, somewhat lower than that of bulk magnetite and the value reported by other authors [7.50], probably due to a slight oxidation to maghemite, since the synthesis process is carried out in the presence of oxygen. The results obtained by the two methods are coherent, except for the range of magnetic field applied. In all cases, the increasing and decreasing field ramps are almost coincident, suggesting a superparamagnetic character of the magnetite NPs, a feature that is transferred to the magnetic carbon hybrid particles, as depicted in the low-field detail of Figure 7.6b. The low magnetic hysteresis of the composites suggests a potential application of the MAC particles for biomedical purposes, given their moderate magnetization and their expectedly negligible risk of aggregation in blood vessels due to magnetic forces [7.28]. This is also an indication of an efficient coating of the AC particles by magnetite, although the saturation magnetization of the former (6.0 ± 0.2 emu/g) is considerably lower due to the comparatively small mass of magnetic material.

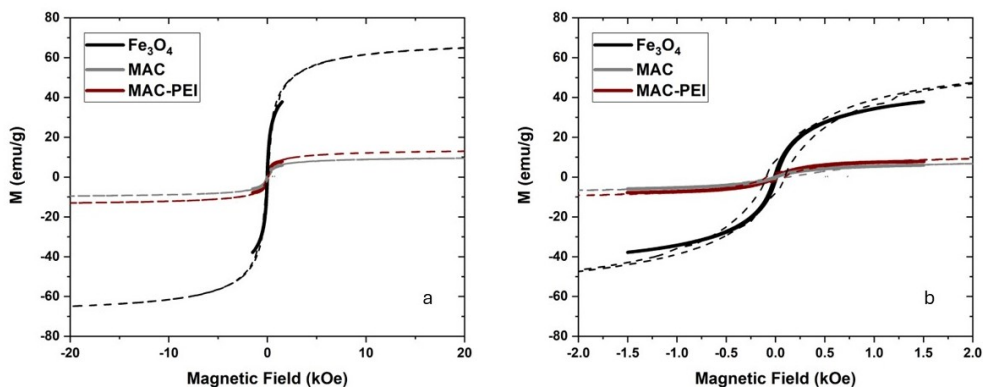


Figure 7.6: Magnetic characterization of the obtained MAC nanoporous particles. (a) Magnetization curves of the bare Fe_3O_4 , MAC and PEI coated particles using VSM (dotted lines) and AC magnetometry (solid lines); (b) Low-field detail of the plots in (a). Hysteresis cycles carried out at 300 K.

In addition, the AC magnetization of PEI-coated MAC particles was also determined, obtaining a very similar value (7.9 ± 0.3 emu/g), although slightly higher, probably due to the increased stability of the suspension (MAC particles tended to sediment quickly) (Figures 7.6a and 7.6b). This is because PEI is a sterically branched polymer with numerous amino groups, which are hydrophilic and capable of forming hydrogen bonds with water [7.51–7.53]. This characteristic provides stability to the NPs in the dispersion medium, due to the strong electrostatic repulsion forces between

them, thus preventing their aggregation. Note in Figure 7.10 the narrower size distribution of MAC-PEI composites, as compared to bare activated carbon particles. The slightly increased average size of MAC-PEI suggests that the PEI layer is thin enough to provide stability and biocompatibility without significantly increasing the particle dimensions.

Results

Photothermal response

Experimental conditions were carefully selected regarding clinical safety limits for photothermia. A wavelength in the first biological transparency window (NIR-I) was chosen, in addition to laser power densities within the range of acceptable values previously reported [7.25, 7.54–7.56]. Therefore, our research was focused on evaluating the impact of heating induced by NPs at mild conditions where the impact of tissue damage caused solely by the laser power irradiation would be negligible.

As can be seen in Figure 7.7a,b,c, magnetic NPs are an excellent heating agent in photothermal therapy, as has been demonstrated previously by several authors [7.25, 7.57, 7.58]. Moreover, their magnetic properties allow them to be directed with an external field. In the case of activated carbon alone, the temperature rise and hence the SAR achieved is certainly lower, although considering its advantageous high surface area, AC particles cannot be neglected as tools in photothermia [7.59]. What is particularly interesting is the PTT behavior of MAC particles. These retain the photothermal response of magnetite and, thanks to their content of AC, also have a high specific surface area. It is worth mentioning that for bare Fe_3O_4 , MAC and MAC-PEI samples, the results obtained are always very similar, MAC-PEI always presenting a slightly better performance. This demonstrates the advantage of the polymer coating, since the layer is thin enough not to affect the amount of magnetite or carbon present in the sample, but provides greater stability, resulting in better PTT results, as was also observed in the electrophoretic mobility, and in the magnetic characterization.

On the other hand, the SAR determination (Figure 7.7d), becomes another evidence of how the incorporation of magnetite is necessary to improve the photothermal response of activated carbon, obtaining in most cases a higher SAR for magnetite/carbon composite particles than for magnetite by itself. It should be mentioned that for the determination of the SAR of MAC and MAC-PEI samples it has been taken into account that approximately 86% of the sample is activated carbon, while 14% is magnetic material (as estimated from the saturation magnetization in Figure 7.6a).

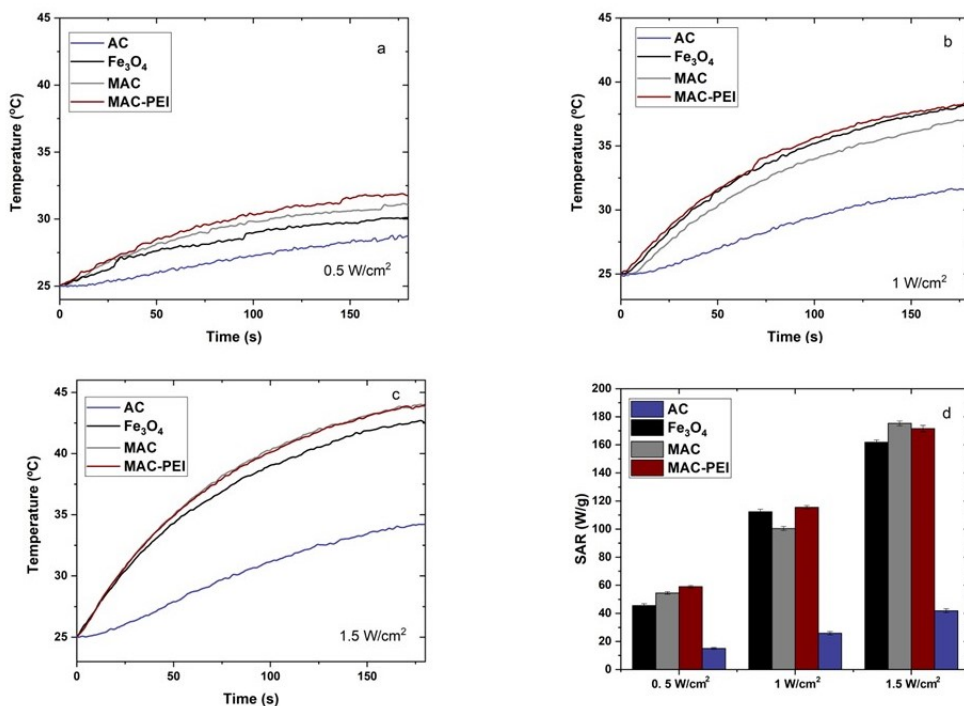


Figure 7.7: Temperature increases for PTT therapy, at a power irradiation of 0.5 W/cm² (a), 1 W/cm² (b), and 1.5 W/cm² (c), using 100 μ L of sample at 5 mg/mL. Determination of the SAR obtained (d).

In addition to the characterization performed, it is important to consider that drug release experiments are carried out with a much larger sample volume, which can affect the heating produced. Therefore, a comparative test was performed using 1.5 mL of sample (Figure 7.11), in which it was observed that the temperature increase obtained is again sufficient to reach the hyperthermia region (between 42 and 46 °C, Figure 7.11).

Cell viability of the magnetic activated carbon nanoporous particles

Cell viability experiments were performed to determine whether the MAC-PEI nanoporous particles obtained provided the necessary biocompatibility for anticancer purposes.

For this purpose, human skin M1 fibroblasts were plated. After 24 h, cells were exposed to different concentrations (from 25 to 1000 μ g/mL) of MAC-PEI particles. The evaluation of the potential cytotoxic effects of MAC-PEI on human skin M1 fibroblasts was based on the quantification of viable cells by crystal violet. Viable cells are stained with the dye, in contrast to non-viable cells. Increasing

concentrations of MAC-PEI nanoporous particles did not significantly affect the viability of the fibroblasts in a broad range of concentrations (from 25 to 500 $\mu\text{g}/\text{mL}$; Figure 7.8). Only concentrations higher than 700 $\mu\text{g}/\text{mL}$ significantly reduced cell viability (29.76% compared to untreated control levels).

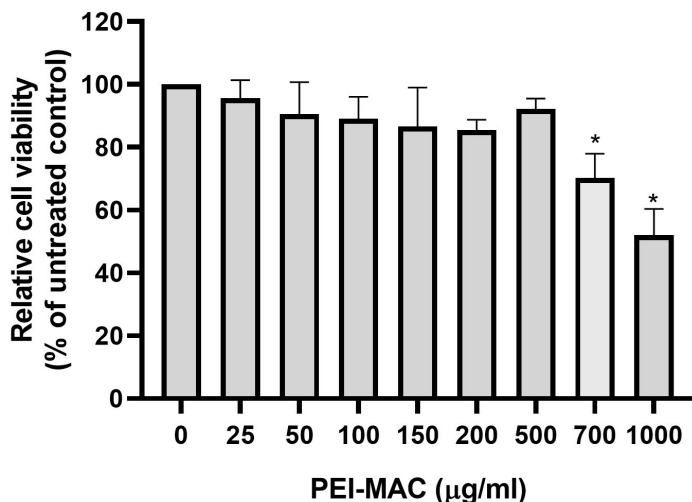


Figure 7.8: Effects of MAC-PEI on M1 human skin fibroblasts viability. Cell viability in M1 fibroblasts was tested after 24 h exposure with MAC-PEI (0-1000 $\mu\text{g}/\text{mL}$). Data are shown as the mean \pm SEM of 3 independent experiments and expressed as a percentage of untreated control levels. Cytotoxicity assays were performed in triplicates per experimental condition. Data are presented as mean \pm standard error of the mean (SEM), of at least three independent experiments. Statistical significance was established at p values below or equal to 0.05 (*).

Thus, we can conclude that MAC-PEI nanoporous particles at concentrations intended for biomedical applications exert negligible cytotoxic effects.

Methotrexate vehiculation and controlled drug release. Effect of external stimuli

As mentioned above, a calibration was performed to determine the concentration of adsorbed and released MTX (available in Figure 7.12). In addition, adsorption kinetics tests (0.6 mM MTX) were performed in the range of 1, 2, 24, 72, 144 h, showing that adsorption in the first two hours exceeded 80%, a result of the high porosity of the MAC particles (Figure 7.13). Further evidence of this porosity is provided by drug adsorption tests (up to 10 mM) in which the MAC-PEI sample adsorbed almost all of the drug brought into contact with the sample (Figure 7.14).

As can be seen in Figure 7.9, drug release at pH 5.8, which mimics the tumour environment, is significantly enhanced by the application of external stimuli such as photothermia and rotating fields. Drug release induced by laser irradiation on magnetic particles has been described by other authors with different drugs such as AS-48 [7.60] or doxorubicin [7.61]. In the latter study, mesoporous silica particles with a magnetic core loaded between 20% and 40% of the drug, which allows us to conclude that: (1) MAC particles are a more effective alternative for drug loading than conventional magnetic particles and even mesoporous silica with a magnetic core, since they load almost all the drug available in the solution due to their high specific surface area, and (2) although the release may seem low (around 4%), the large amount of drug adsorbed is sufficient to optimise future anti-tumour treatments compared to other studies such as the one mentioned above or to our previous work with doxorubicin and PEI-coated magnetite particles [7.31].

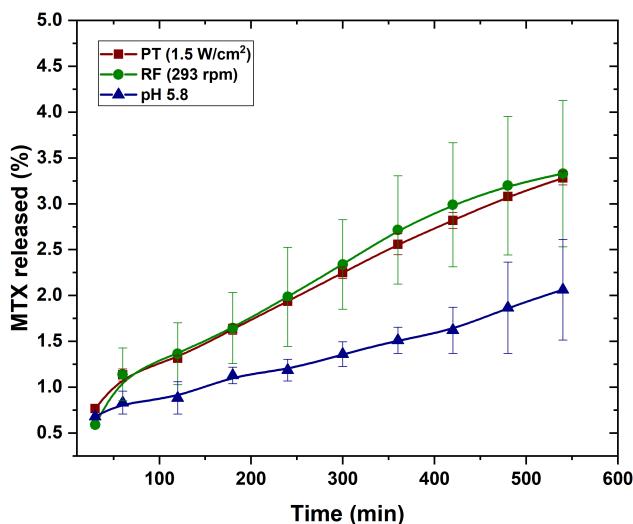


Figure 7.9: Release of MTX with respect to the amount previously adsorbed on PEI-coated MAC particles using different stimuli: photothermia (PT), rotating fields (RF), and with no stimuli applied, all of them in phosphate buffer at pH 5.8.

Figure 7.9 also shows that drug release using rotating fields (RF) (at the highest rotational speed available in our equipment, 293 rpm) slightly improves PT performance, probably due to mechanically enhanced diffusion.

In general, the release achieved under either PT or rotating field is significantly higher compared to our results under nonstimulated conditions. Similar results have been reported by Nappini *et al.* [7.62], who observed that magnetoliposomes loaded with carboxyfluorescein experienced a significantly enhanced release of the

fluorescent agent under the influence of a low-frequency alternating magnetic field (5.8 kHz). This is a very interesting result, as this technique has been less studied and could be more effective than photothermia for biomedical applications requiring high tissue penetration.

Finally, it is worth noting the comparison with the neutral pH (pH 7.4) results, depicted in Figure 7.15. Although at this pH the drug tends to be released more rapidly initially, this is not of great interest, as the treatment delivery times are long compared to the time it takes the human body to renew all the blood (approximately one minute under normal resting conditions). Assuming that the particles are injected intravenously and accumulate in the tumour area due to their magnetic properties, this process would occur rapidly. However, it should be noted that after 6 hours of application, the drug release using photothermia and rotating fields is greater at tumour pH than at pH 7.4.

7.4. Conclusions

This work describes the utilisation of porous activated carbon particles as vehicles for the anti-tumour drug MTX. The particles are coated with magnetite nanoparticles, which confer them superparamagnetic behaviour, thus extending the field of application to situations where it is possible to use external magnetic fields to transport the particles to their action site or eventually produce heating if the field is alternating, or torque if the magnetic field is rotating. In order to enhance the stability of the particles and their interaction with the anti-tumour agent, a cationic polymer, low molecular weight PEI, is employed for their coating. The MAC-PEI particles demonstrate high biocompatibility at concentrations suitable for biomedical applications, and exhibit a photothermal response to infrared laser irradiation, whereby local heating is generated. This phenomenon is exploited in this research as a stimulus to enhance MTX release. The photothermal response is markedly elevated for the activated carbon-magnetite (MAC) composites, and it is little affected by the application of the polymer coating. The synthesised MAC-PEI composite particles demonstrated the capacity to adsorb up to 80% of the drug from a 0.6 mM MTX solution after 20 hours of contact. The drug release was conducted at pH 5.8 with and without the application of external photothermal and rotating magnetic field stimuli. The process is gradual and can be controlled using stimuli of different intensity, resulting in a considerable increase in the amount of drug released. The designed porous particles thus appear to be excellent platforms for the transport and release of MTX, as they are capable of loading significant quantities of drug and releasing it gradually at a rate that can be controlled by both PTT and RMF external stimuli, while preserving biocompatibility.

Acknowledgements

Financial support of this investigation by the grant TED2021-131855BI00/AEI/10.13039/501100011033 Unión Europea Next Generation EU/PRTR is gratefully acknowledged. We also thank Juan M. Falcón-Perez (Metabolomics Unit, Centro de Investigación Cooperativa en Biociencias, Derio, Vizcaya 48160, Spain) for providing M1 human fibroblasts.

Appendix. Supplementary Information

Size obtained by DLS

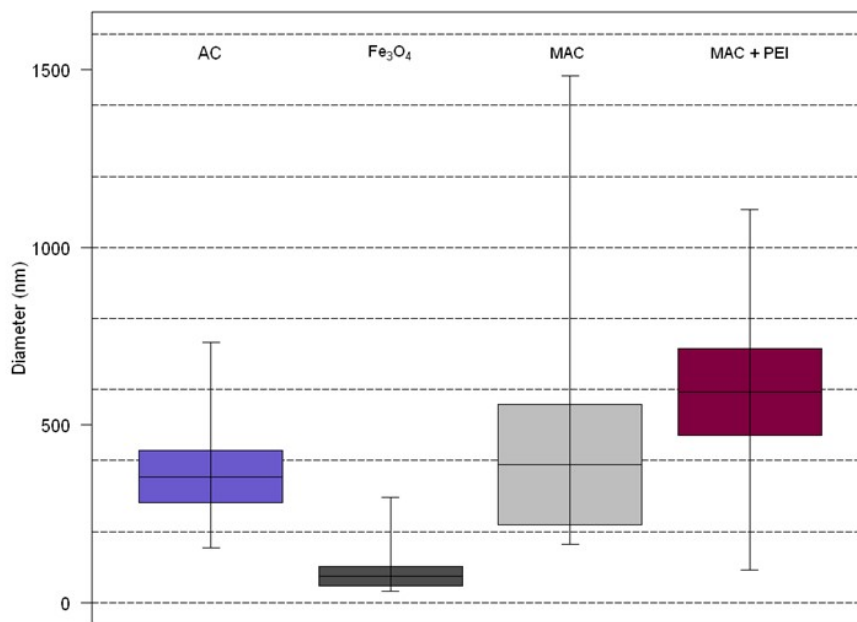


Figure 7.10: Boxplot of size determinations using DLS technique of bare magnetite (MAG), activated carbon (AC), magnetic activated carbon naked (MAC) and polymer coated sample (PEI-MAC).

Photothermia characterization for drug release

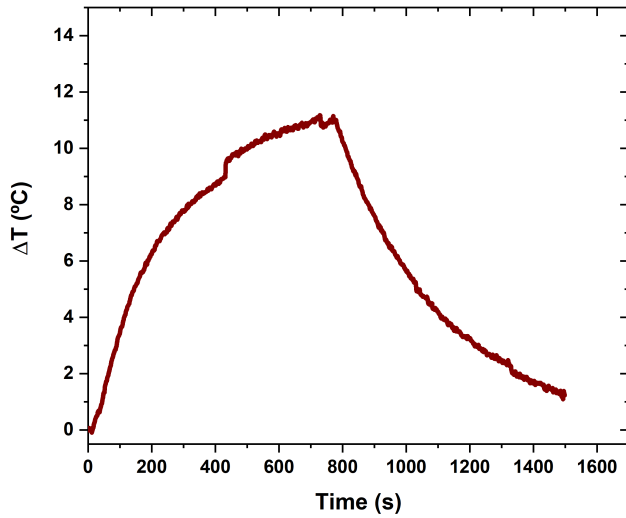


Figure 7.11: Photothermia experiment performed by irradiating with 850 nm for 15 minutes at 1.5 W/cm^2 the MAC-PEI sample at 5 mg/mL (1.5 mL).

Calibration of MTX concentrations

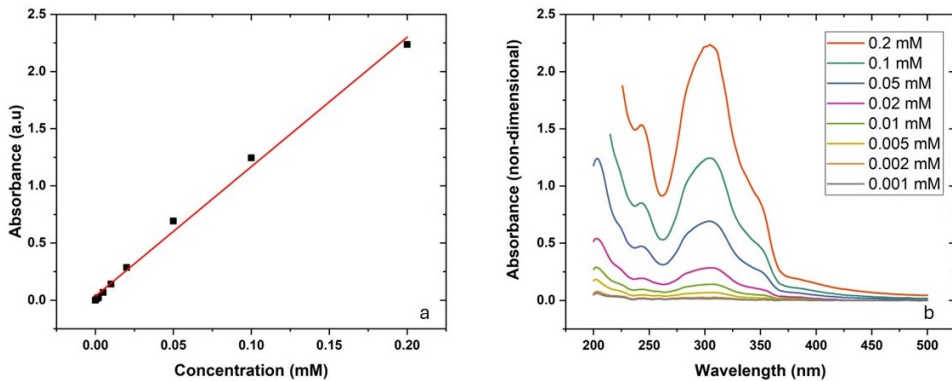


Figure 7.12: Calibration of MTX concentrations performed at 305 nm (a) Calibration line (b) MTX adsorption peaks.

Adsorption kinetics experiments

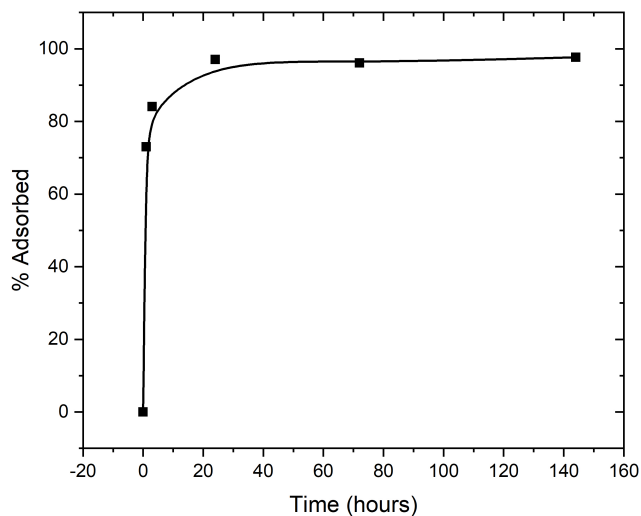


Figure 7.13: Adsorption of MTX (0.6 mM) on the MAC-PEI sample over time.

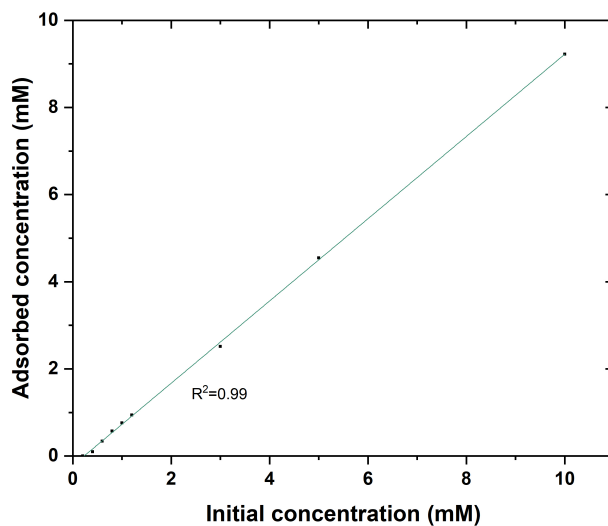


Figure 7.14: Adsorption of different amounts of MTX on the PEI coated MAC sample after 24 hours in contact.

MTX release at pH 7.4

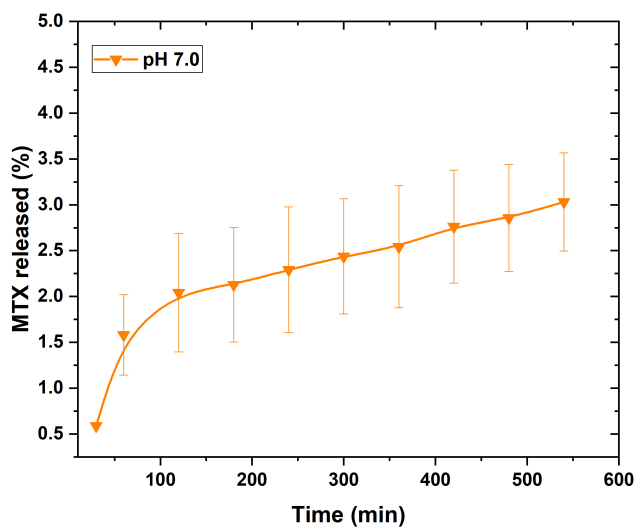


Figure 7.15: MTX release without stimuli application in phosphate buffer at pH 7.4.

Bibliography

- [7.1] Ezio Laconi, Fabio Marongiu, and James DeGregori. Cancer as a disease of old age: changing mutational and microenvironmental landscapes. *British Journal of Cancer*, 122(7):943–952, 2020.
- [7.2] Sophie Pilleron, Enrique Soto-Perez-de Celis, Jerome Vignat, Jacques Ferlay, Isabelle Soerjomataram, Freddie Bray, and Diana Sarfati. Estimated global cancer incidence in the oldest adults in 2018 and projections to 2050. *International Journal of Cancer*, 148(3):601–608, 2021.
- [7.3] Fátima Fernández-Álvarez, Carlos Caro, Gracia García-García, María Luisa García-Martín, and José L Arias. Engineering of stealth (maghemite/PLGA)/chitosan (core/shell)/shell nanocomposites with potential applications for combined MRI and hyperthermia against cancer. *Journal of Materials Chemistry B*, 9(24):4963–4980, 2021.
- [7.4] Fátima Fernández-Álvarez, Gracia García-García, and José L Arias. A tri-stimuli responsive (maghemite/plga)/chitosan nanostructure with promising applications in lung cancer. *Pharmaceutics*, 13(8):1232, 2021.
- [7.5] Tiago P Ribeiro, J Agostinho Moreira, Fernando J Monteiro, and Marta S Laranjeira. Nanomaterials in cancer: Reviewing the combination of hyperthermia and triggered chemotherapy. *Journal of Controlled Release*, 347:89–103, 2022.
- [7.6] Kristin Loomis, Kathleen McNeeley, and Ravi V Bellamkonda. Nanoparticles with targeting, triggered release, and imaging functionality for cancer applications. *Soft Matter*, 7(3):839–856, 2011.
- [7.7] Ki Young Choi, Gang Liu, Seulki Lee, and Xiaoyuan Chen. Theranostic nanoplatfoms for simultaneous cancer imaging and therapy: current approaches and future perspectives. *Nanoscale*, 4(2):330–342, 2012.
- [7.8] Mark E Davis. Fighting cancer with nanoparticle medicines—the nanoscale matters. *MRS bulletin*, 37(9):828–835, 2012.

- [7.9] Ruibing Wang, Paul S Billone, and Wayne M Mullett. Nanomedicine in action: an overview of cancer nanomedicine on the market and in clinical trials. *Journal of Nanomaterials*, 2013(1):629681, 2013.
- [7.10] Linea N Toksvang, Shawn HR Lee, Jun J Yang, and Kjeld Schmiegelow. Maintenance therapy for acute lymphoblastic leukemia: basic science and clinical translations. *Leukemia*, 36(7):1749–1758, 2022.
- [7.11] Zheng Li, Xingye Li, Derong Xu, Xin Chen, Shugang Li, Lin Zhang, Matthew TV Chan, and William KK Wu. An update on the roles of circular rnas in osteosarcoma. *Cell Proliferation*, 54(1):e12936, 2021.
- [7.12] Jori May, Kenneth R Carson, Sara Butler, Weijian Liu, Nancy L Bartlett, and Nina D Wagner-Johnston. High incidence of methotrexate associated renal toxicity in patients with lymphoma: a retrospective analysis. *Leukemia & Lymphoma*, 55(6):1345–1349, 2014.
- [7.13] Hanifeh Shariatifar, Fateme Ranjbarian, Fahimeh Hajiahmadi, and Alireza Farasat. A comprehensive review on methotrexate containing nanoparticles; an appropriate tool for cancer treatment. *Molecular Biology Reports*, 49(11):11049–11060, 2022.
- [7.14] Laura B Ramsey, Frank M Balis, Maureen M O'Brien, Kjeld Schmiegelow, Jennifer L Pauley, Archie Bleyer, Brigitte C Widemann, David Askenazi, Sharon Bergeron, Anushree Shirali, et al. Consensus guideline for use of glucarpidase in patients with high-dose methotrexate induced acute kidney injury and delayed methotrexate clearance. *The Oncologist*, 23(1):52–61, 2018.
- [7.15] Fang-Li Zhang. *The ene reaction of aminonitrosopyrimidines: a novel synthesis of pterins, homopterins, and related heterocycles*. PhD thesis, ETH Zurich, 2008.
- [7.16] Zulfequar Ahamad Khan, Rahul Tripathi, and Brahmeshwar Mishra. Methotrexate: a detailed review on drug delivery and clinical aspects. *Expert Opinion on Drug Delivery*, 9(2):151–169, 2012.
- [7.17] Goeun Choi, Tae-Hyun Kim, Jae-Min Oh, and Jin-Ho Choy. Emerging nanomaterials with advanced drug delivery functions; focused on methotrexate delivery. *Coordination Chemistry Reviews*, 359:32–51, 2018.
- [7.18] Muthukumar Thangavelu, Aravinthan Adithan, Sastry Thotapalli Parvathaleswara, and Chamundeeswari Munusamy. Morphological modification of carbon nanoparticles after interacting with methotrexate as a potential anticancer agent. *Pharmaceutical Research*, 35:1–10, 2018.

- [7.19] Tzu-Han Hsin, Namasivayam Dhenadhayalan, and King-Chuen Lin. Ligusticum striatum-derived carbon dots as nanocarriers to deliver methotrexate for effective therapy of cancer cells. *ACS Applied Bio Materials*, 3(12):8786–8794, 2020.
- [7.20] F Guo, X Mao, J Wang, F Luo, and Z Wang. Gemcitabine adsorbed onto carbon particles increases drug concentrations at the injection site and in the regional lymph nodes in an animal experiment and a clinical study. *Journal of International Medical Research*, 39(6):2217–2227, 2011.
- [7.21] Nikhila Miriyala, Defang Ouyang, Yvonne Perrie, Deborah Lowry, and Daniel J Kirby. Activated carbon as a carrier for amorphous drug delivery: Effect of drug characteristics and carrier wettability. *European Journal of Pharmaceutics and Biopharmaceutics*, 115:197–205, 2017.
- [7.22] Kent R Olson. Activated charcoal for acute poisoning: one toxicologist’s journey. *Journal of Medical Toxicology*, 6:190–198, 2010.
- [7.23] SK Shahcheragh, MM Bagheri Mohagheghi, and A Shirpay. Effect of physical and chemical activation methods on the structure, optical absorbance, band gap and urbach energy of porous activated carbon. *SN Applied Sciences*, 5(12):313, 2023.
- [7.24] Xiangyou Li, Yoshiki Shimizu, Alexander Pyatenko, Hongqiang Wang, and Naoto Koshizaki. Carbon-assisted fabrication of submicrometre spheres for low-optical-absorbance materials by selective laser heating in liquid. *Journal of Materials Chemistry*, 21(38):14406–14409, 2011.
- [7.25] Ana Espinosa, Jelena Kolosnjaj-Tabi, Ali Abou-Hassan, Anouchka Plan Sangnier, Alberto Curcio, Amanda KA Silva, Riccardo Di Corato, Sophie Neveu, Teresa Pellegrino, Luis M Liz-Marzán, et al. Magnetic (hyper) thermia or photothermia? progressive comparison of iron oxide and gold nanoparticles heating in water, in cells, and in vivo. *Advanced Functional Materials*, 28(37):1803660, 2018.
- [7.26] H Belkahla, R Boudjemaa, V Caorsi, D Pineau, A Curcio, JS Lomas, P Decorse, A Chevillot-Biraud, T Azaïs, C Wilhelm, et al. Carbon dots, a powerful non-toxic support for bioimaging by fluorescence nanoscopy and eradication of bacteria by photothermia. *Nanoscale Advances*, 1(7):2571–2579, 2019.
- [7.27] Xingshu Li, Jonathan F Lovell, Juyoung Yoon, and Xiaoyuan Chen. Clinical development and potential of photothermal and photodynamic therapies for cancer. *Nature Reviews Clinical Oncology*, 17(11):657–674, 2020.

- [7.28] L Harivardhan Reddy, José L Arias, Julien Nicolas, and Patrick Couvreur. Magnetic nanoparticles: design and characterization, toxicity and biocompatibility, pharmaceutical and biomedical applications. *Chemical Reviews*, 112(11):5818–5878, 2012.
- [7.29] Tsai-Jung Yu, Po-Han Li, Te-Wei Tseng, and Yu-Chie Chen. Multifunctional $\text{Fe}_3\text{O}_4/\text{alumina}$ core/shell mnps as photothermal agents for targeted hyperthermia of nosocomial and antibiotic-resistant bacteria. *Nanomedicine*, 6(8):1353–1363, 2011.
- [7.30] Mei-Yi Liao, Ping-Shan Lai, Hsiu-Ping Yu, Hong-Ping Lin, and Chih-Chia Huang. Innovative ligand-assisted synthesis of nir-activated iron oxide for cancer theranostics. *Chemical Communications*, 48(43):5319–5321, 2012.
- [7.31] Marina Lázaro, Pablo Lupiáñez, José L Arias, María P Carrasco-Jiménez, Ángel V Delgado, and Guillermo R Iglesias. Combined magnetic hyperthermia and photothermia with polyelectrolyte/gold-coated magnetic nanorods. *Polymers*, 14(22):4913, 2022.
- [7.32] Xin Hua, Qin Yang, Zhimin Dong, Jiashuo Zhang, Wanjiang Zhang, Qiudong Wang, Shengnan Tan, and Hugh DC Smyth. Magnetically triggered drug release from nanoparticles and its applications in anti-tumor treatment. *Drug Delivery*, 24(1):511–518, 2017.
- [7.33] Tíffany Marín, Paula Montoya, Oscar Arnache, Rodolfo Pinal, and Jorge Calderón. Development of magnetite nanoparticles/gelatin composite films for triggering drug release by an external magnetic field. *Materials & Design*, 152:78–87, 2018.
- [7.34] Yu Cheng, Megan E Muroski, Dorothée CMC Petit, Rhodri Mansell, Tarun Vemulkar, Ramin A Morshed, Yu Han, Irina V Balyasnikova, Craig M Horbinski, Xinlei Huang, et al. Rotating magnetic field induced oscillation of magnetic particles for in vivo mechanical destruction of malignant glioma. *Journal of Controlled Release*, 223:75–84, 2016.
- [7.35] Xiao Sun, Chuanjie Cai, Qian Wang, Dongqing Cai, Junchao Qian, Yu Chi, Kang Zheng, Xin Zhang, Guilong Zhang, Kai Zhong, et al. A polyethylenimine functionalized porous/hollow nanoworm as a drug delivery system and a bioimaging agent. *Physical Chemistry Chemical Physics*, 18(11):7820–7828, 2016.
- [7.36] M Lázaro, A Sola-Leyva, M Jimenez-Carretero, MP Carrasco Jiménez, ÁV Delgado, and GR Iglesias. The role of biocompatible coatings of magnetic nanorods on their thermal response in hyperthermia. consequences on tumor cell survival. *Journal of Drug Delivery Science and Technology*, 95:105622, 2024.

- [7.37] María del Mar Ramos-Tejada, Julian L Viota, Katarzyna Rudzka, and Angel V Delgado. Preparation of multi-functionalized Fe₃O₄/Au nanoparticles for medical purposes. *Colloids and Surfaces B: Biointerfaces*, 128:1–7, 2015.
- [7.38] Beata Chertok, Allan E David, and Victor C Yang. Polyethyleneimine-modified iron oxide nanoparticles for brain tumor drug delivery using magnetic targeting and intra-carotid administration. *Biomaterials*, 31(24):6317–6324, 2010.
- [7.39] Emanuell dos Santos-Silva, Mariana F Alves-Silva, Juliana S de Medeiros, Rômulo dos Santos-Cavalcante, Alianda M Cornelio, Matheus F Fernandes-Pedrosa, Eryvaldo ST do Egito, Raimundo F de Araújo-Júnior, and Arnóbio A da Silva-Júnior. Colloidal properties of self-assembled cationic hyperbranched-polyethyleneimine covered poly lactide-co-glycolide nanoparticles: Exploring modified release and cell delivery of methotrexate. *Journal of Molecular Liquids*, 315:113721, 2020.
- [7.40] Ritu Goyal, Sushil K Tripathi, Esther Vazquez, Pradeep Kumar, and Kailash C Gupta. Biodegradable poly (vinyl alcohol)-polyethylenimine nanocomposites for enhanced gene expression in vitro and in vivo. *Biomacromolecules*, 13(1):73–83, 2012.
- [7.41] Zhanna K Nazarkina, Tatyana A Savostyanova, Boris P Chelobanov, Irina V Romanova, Pavel A Simonov, Ren I Kvon, Andrey A Karpenko, and Pavel P Laktionov. Activated carbon for drug delivery from composite biomaterials: The effect of grinding on sirolimus binding and release. *Pharmaceutics*, 14(7):1386, 2022.
- [7.42] Beatriz Sanz, M Pilar Calatayud, Nicolás Cassinelli, M Ricardo Ibarra, and Gerardo F Goya. Long-term stability and reproducibility of magnetic colloids are key issues for steady values of specific power absorption over time. *European Journal of Inorganic Chemistry*, 2015(27):4524–4531, 2015.
- [7.43] Pedro Urquiza, Ana Laín, Arantza Sanz-Parra, Jorge Moreno, Ganeko Bernardo-Seisdedos, Pierre Dubus, Esperanza González, Virginia Gutiérrez-de Juan, Sandra García, Hasier Eraña, et al. Repurposing ciclopirox as a pharmacological chaperone in a model of congenital erythropoietic porphyria. *Science translational medicine*, 10(459):eaat7467, 2018.
- [7.44] Sourav Bhattacharjee. DIs and zeta potential—what they are and what they are not? *Journal of Controlled Release*, 235:337–351, 2016.
- [7.45] Gracia García-García, Marina Lázaro-Callejón, Fátima Fernández-Álvarez, Guillermo R Iglesias, and José L Arias. (magnetite/poly (ϵ -caprolactone))/chitosan (core/shell)/shell nanocomposites with potential

- applications in hyperthermia cancer therapy. *Journal of Magnetism and Magnetic Materials*, 588:171500, 2023.
- [7.46] Hamedreza Javadian, Forough Ghorbani, Habib-allah Tayebi, and SeyedMostafa Hosseini Asl. Study of the adsorption of cd (ii) from aqueous solution using zeolite-based geopolymer, synthesized from coal fly ash; kinetic, isotherm and thermodynamic studies. *Arabian Journal of Chemistry*, 8(6):837–849, 2015.
- [7.47] Gracia García-García, Fátima Fernández-Álvarez, Laura Cabeza, Ángel V Delgado, Consolación Melguizo, José C Prados, and José L Arias. Gemcitabine-loaded magnetically responsive poly (ϵ -caprolactone) nanoparticles against breast cancer. *Polymers*, 12(12):2790, 2020.
- [7.48] Thawatchai Maneerung, Johan Liew, Yanjun Dai, Sibudjing Kawi, Clive Chong, and Chi-Hwa Wang. Activated carbon derived from carbon residue from biomass gasification and its application for dye adsorption: kinetics, isotherms and thermodynamic studies. *Bioresource Technology*, 200:350–359, 2016.
- [7.49] Shepherd S Sambaza, Monaheng L Masheane, Soraya P Malinga, Edward N Nxumalo, and Sabelo D Mhlanga. Polyethyleneimine-carbon nanotube polymeric nanocomposite adsorbents for the removal of Cr^{6+} from water. *Physics and Chemistry of the Earth, Parts A/B/C*, 100:236–246, 2017.
- [7.50] Scott J Kemp, R Matthew Ferguson, Amit P Khandhar, and Kannan M Krishnan. Monodisperse magnetite nanoparticles with nearly ideal saturation magnetization. *RSC Advances*, 6(81):77452–77464, 2016.
- [7.51] Niamh Bayliss and Bernhard VKJ Schmidt. Hydrophilic polymers: Current trends and visions for the future. *Progress in Polymer Science*, page 101753, 2023.
- [7.52] Justice Delali Akoto, Fei Chai, Eveliina Repo, Zhihui Yang, Danyang Wang, Feiping Zhao, Qi Liao, and Liyuan Chai. Polyethyleneimine stabilized nanoscale zero-valent iron-magnetite ($\text{Fe}_3\text{O}_4@ \text{nzvi-pe}$) for the enhanced removal of arsenic from acidic aqueous solution: Performance and mechanisms. *Journal of Environmental Chemical Engineering*, 10(6):108589, 2022.
- [7.53] Raúl Megías, Maialen Arco, Jesús Ciriza, Laura Saenz Del Burgo, Gustavo Puras, Margarita López-Viota, Ángel V Delgado, Jon P Dobson, José L Arias, and José L Pedraz. Design and characterization of a magnetite/pei multifunctional nanohybrid as non-viral vector and cell isolation system. *International Journal of Pharmaceutics*, 518(1-2):270–280, 2017.
- [7.54] Alla Bucharskaya, Galina Maslyakova, Georgy Terentyuk, Alexander Yakunin, Yuri Avetisyan, Olga Bibikova, Elena Tuchina, Boris

- Khlebtsov, Nikolai Khlebtsov, and Valery Tuchin. Towards effective photothermal/photodynamic treatment using plasmonic gold nanoparticles. *International Journal of Molecular Sciences*, 17(8):1295, 2016.
- [7.55] Steven L Jacques. Laser-tissue interactions. photochemical, photothermal, and photomechanical. *The Surgical Clinics of North America*, 72(3):531–558, 1992.
- [7.56] André M Gobin, Min Ho Lee, Naomi J Halas, William D James, Rebekah A Drezek, and Jennifer L West. Near-infrared resonant nanoshells for combined optical imaging and photothermal cancer therapy. *Nano Letters*, 7(7):1929–1934, 2007.
- [7.57] Sonia Cabana, Alberto Curcio, Aude Michel, Claire Wilhelm, and Ali Abou-Hassan. Iron oxide mediated photothermal therapy in the second biological window: A comparative study between magnetite/maghemite nanospheres and nanoflowers. *Nanomaterials*, 10(8):1548, 2020.
- [7.58] Agnieszka Włodarczyk, Szymon Gorgoń, Adrian Radoń, and Karolina Bajdak-Rusinek. Magnetite nanoparticles in magnetic hyperthermia and cancer therapies: Challenges and perspectives. *Nanomaterials*, 12(11):1807, 2022.
- [7.59] Maoquan Chu, Yuxiang Shao, Jinliang Peng, Xiangyun Dai, Haikuo Li, Qingsheng Wu, and Donglu Shi. Near-infrared laser light mediated cancer therapy by photothermal effect of Fe_3O_4 magnetic nanoparticles. *Biomaterials*, 34(16):4078–4088, 2013.
- [7.60] Salvatore Calogero Gaglio, Ylenia Jabalera, Manuel Montalbán-López, Ana Cristina Millán-Placer, Marina Lázaro-Callejón, Mercedes Maqueda, María Paz Carrasco-Jimenez, Alejandro Laso, José A Aínsa, Guillermo R Iglesias, et al. Embedding biomimetic magnetic nanoparticles coupled with peptide AS-48 into PLGA to treat intracellular pathogens. *Pharmaceutics*, 14(12):2744, 2022.
- [7.61] Alexandre Adam and Damien Mertz. Iron oxide@ mesoporous silica Core-Shell nanoparticles as multimodal platforms for magnetic resonance imaging, magnetic hyperthermia, near-infrared light photothermia, and drug delivery. *Nanomaterials*, 13(8):1342, 2023.
- [7.62] Silvia Nappini, Francesca Baldelli Bombelli, Massimo Bonini, Bengt Nordèn, and Piero Baglioni. Magnetoliposomes for controlled drug release in the presence of low-frequency magnetic field. *Soft Matter*, 6(1):154–162, 2010.

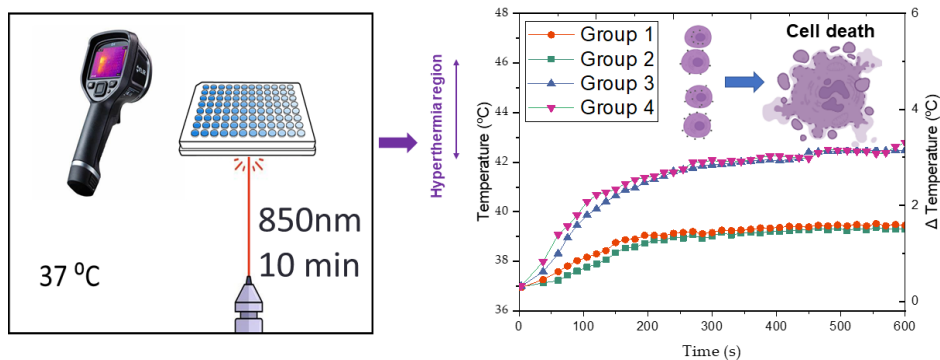
Chapter 8

The importance of cell uptake in photothermal treatments mediated by biomimetic magnetic nanoparticles

M. Lázaro, P. Lupiáñez, A. Sola-Leyva, T. Pozo-Gualda, F. Oltolina, M. Jimenez-Carretero, C. Jimenez-Lopez, MP Carrasco-Jiménez, GR. Iglesias, *Colloids Surf. B.* **2024**, 234, 113722.

Abstract

Biomimetic magnetic nanoparticles (BMNPs) mediated by MamC have proven to be photothermal agents able to allow an optimized cytotoxicity against tumoral cells when used simultaneously as drug nanotransporters and as hyperthermia agents. However, it remains unclear whether BMNPs need to be internalized by the cells and/or if there is a threshold for internal Fe concentration for the photothermal therapy to be effective. In this study, three different situations for photothermal treatments have been simulated to disentangle the effect of BMNPs cell uptake on cell viability after photothermal treatments. Human hepatoblastoma (HepG2) cell line was treated with suspensions of BMNPs, and protocols were developed to have only intracellular BMNPs, only extracellular BMNPs or both, followed by photothermal exposure of the treated cell cultures. Our data demonstrate that: (1) Although the heating efficiency of the photothermal agent is not altered by its location (intra/extracellular), the intracellular location of BMNPs is crucial to ensure the cytotoxic effect of photothermal treatments, especially at low Fe concentration. In fact, the concentration of BMNPs needed to reach the same cytotoxic effect following upon laser irradiation of 0.2 W/cm^2 is three times larger if BMNPs are located extracellularly compared to that needed if BMNPs are located intracellularly; (2) For a given location of the BMNPs, cell death increases with BMNPs (or Fe) concentration. When BMNPs are located intracellularly, there is a threshold for Fe concentration ($\sim 0.5 \text{ mM}$ at laser power intensities of 0.1 W/cm^2) needed to affect cell viability following upon cell exposure to photothermia. (3) Bulk temperature rise is not the only factor accounting for cell death. Actually, temperature increases inside the cells cause more damage to cell structures and trigger cell death more efficiently than an increase in the temperature outside the cell.



8.1. Introduction

According to the Global Cancer Observatory (<https://gco.iarc.fr/>), the last data of cancer incidence over the world is an estimate of over 18 million cases. At the present, surgery, chemo- and radio-therapy are the usual treatments for primary cancers. However, many of these therapies are still insufficient due to, for instance, heterogeneities in the tumor microenvironment, drug efflux via multi-drug resistance proteins among other causes, and usually cause adverse secondary effect [8.1]. Therefore, it is crucial to optimize new therapies to increase the efficiency of the treatments while decreasing the undesirable secondary effects.

Among these new therapies, hyperthermia mediated by nanoparticles (either magnetic hyperthermia or photothermia) is being explored at the present as physical trigger of tumor cell apoptosis. Temperature increases generated by magnetic hyperthermia or photothermia have been observed to reduce the viability of cells, in particular tumoral ones, which are more sensitive to heat rises than healthy cells [8.2–8.4]. But hyperthermia can also be used to enhance drug release in drug delivery therapies [8.5–8.8] and/or, particularly photothermia, to generate pores in the cell wall allowing gene therapy [8.9–8.11]. Photothermal effects are induced by laser irradiation of a photothermal agent in the first biological window (NIR-1, 700–1000 nm) where tissues become partially transparent [8.11–8.13]. Depending on the laser energy and the irradiation time, cell structural damages induced by photothermia occur as a result of temperature increases, photochemical reactions and/or laser-induced water vapor nanobubbles [8.11, 8.14, 8.15].

Still, some questions remain unclear for which no experimental data have been provided up to date. One of them is how important is the location of the hyperthermia agent for the effectiveness of the treatment. Some authors have studied this issue in the context of magnetic hyperthermia [8.16–8.20], but a consensus has not still been reached. Since the ultimate reason for cell death (i.e., temperature increase, reactive oxygen species (ROS) production, mechanical damage) is not well understood [8.21–8.25], there is no agreement on whether or not the nanoparticles must be internalized by the cells for these hyperthermia therapies to be effective. If there is no agreement on this specific issue in the context of magnetic hyperthermia, there is even less information in the context of photothermia. Depending on the location, the photothermal effect could range from just cell damage in the outer structures (if the agent is located extracellularly) to additional internal cell damage (if the agent has been internalized by the cell) and/or the triggering of different cellular responses leading to a decrease in the cellular viability. Therefore, although the cellular uptake of the photothermal agent is expected to play a crucial role in the success of the treatment, it has not yet been demonstrated. Moreover, whether or not there is a certain internalization threshold needed for the photothermal treatment to be effective has never been determined. This issue is important because if internalization proves to

be crucial, the success of the photothermal treatments could be improved by designing strategies to increase the internalization of the photothermal agent.

Different photothermal nanoagents have been used. These nanomaterials can be both organic (dyes, conjugated polymers) or inorganic (metallic nanostructures, metal oxide nanoparticles, hybrid gold-iron oxide nanoparticles carbon-based nanoparticles, nanoscale metal chalcogenides and/or transition metal dichalcogenide nanostructures) [8.26–8.30]. Gold nanoparticles (nanorods, nanoshells, nanostars, nanocages) were the first successfully used photothermal agents. They are easy to produce, exhibit high conjugation ability and great photothermal response. However, they become easily fragmented upon pulsed laser irradiation, posing potential safety risks if the fragments intercalate in DNA [8.11]. Iron oxide magnetic nanoparticles (MNP), on the contrary, are photothermal agents preferred for clinical uses due to their enhanced biocompatibility, their great heat conversion efficiency [8.5,8.8–8.11] and their ability to be guided and concentrated at the target by using magnetic fields [8.31].

Among them, biomimetic magnetic nanoparticles (BMNPs) mediated by MamC, a magnetosome membrane-associated protein from *Magnetococcus marinus* MC-1, have proven to be photothermal agents that adsorb the electromagnetic energy of the laser at $\lambda = 850$ nm and convert it into heat, causing cytotoxicity in tumoral cells [8.31–8.35]. They have also shown to be internalized by cells by endocytosis [8.24] and their uptake can be varied by controlling the time they are incubated with cells. Therefore, they are good candidates to study the importance of their internalization in the success of photothermal therapies in terms of the viability of treated cells. Moreover, their advantages compared to other magnetite nanoparticles make them attractive candidates for future potential directed drug delivery therapies in combination with photothermia. In fact, BMNPs have already proven to be efficient drug nanotransporters able to be guided to the target by magnetic fields, and efficient tumor reducers when local drug delivery is combined with magnetic hyperthermia [8.31]. The advantages of BMNPs over other MNPs reside in the control that MamC exerts over the nucleation of magnetite, acting as a template of crystal growth [8.36]. As a result, this MamC-mediated magnetite formation results in superparamagnetic nanoparticles with an average size of 40 nm with a magnetic saturation of ~ 52 emu/g [8.37, 8.38]. Moreover, this protein strongly adsorbs to the surface of the magnetite nanoparticles, changing their surface properties and providing them with functional groups that allow nanoparticle functionalization without the need of a further postproduction covering, otherwise needed for most MNPs [8.38, 8.39].

Therefore, the goal of the present work is to analyze the effect of the localization (intracellular and/or extracellular) of the photothermal agent (BMNPs chosen as a model agents) on tumoral cell viability (HepG2 chosen as a model cell line) following upon irradiation with a laser in the NIR.

8.2. Materials and methods

BMNP synthesis and characterization

MamC was expressed in *Escherichia coli* TOP10 (Life Technologies, Invitrogen, Grand Island, NY, USA) as a recombinant protein and purified under denaturing conditions (6 M urea) following the protocol of Valverde-Tercedor *et al.* [8.39]. Isopropyl- β -D-thiogalactopyranoside (IPTG, Fisher BioReagents, Pittsburgh, PA, USA) was used to induce the expression of the recombinant MamC. The protein was purified using a HiTrap Chelating HP column (GE Healthcare) in an ÄKTA Prime Plus FPLC System (GE Healthcare). Successive dialyses were performed to remove the urea, thus allowing the refolding of MamC. The isolated protein was stored at 4°C until used in the biomineralization process. Details of the production process are given in Reference [8.39].

BMNPs were synthesized inside an anaerobic COY chamber (Coy Laboratory Products, Grass Lake, MI) from the following master solution: 2.78 mM Fe(ClO₄)₂, 3.5 mM NaHCO₃, 3.5 mM Na₂CO₃, and 5.56 mM FeCl₃, at pH 9, to which 10 µg/mL MamC were added. The formation of the nanoparticles occurred in free-drift experiments for 30 days at 25°C and 1 atm total pressure. The precipitates were magnetically concentrated and rinsed with oxygen-free MilliQ water at least ten times until the supernatant remained clear.

Transmission electron microscopy (TEM) analyses (STEM Philips Model CM20 microscope) were performed on ultrathin sections (50–70 nm) prepared by embedding the nanoparticles in Embed 812 resin, which were later cut with a Reichert Ultracut S microtome (Leica Microsystems GmbH, Wetzlar, Germany). Particle sizes were measured using ImageJ 1.47 software on multiple micrographs, with more than 1000 nanoparticles measured to ensure reproducibility. Optical spectra of BMNPs were obtained using a UV–vis spectrometer, the JenwayTM 6705 (Jenway, Staffordshire, United Kingdom), in the 200–900 nm spectral range. The hydrodynamic radius of the nanoparticles was measured at physiological pH (25 °C) in a Zetasizer Nano-ZS (Malvern Instruments, Malvern, UK). BMNPs were suspended in 10 mL of 10 mM NaClO₄ pH 7.4 and sonicated for 2 min before the measurement. Powder X-ray diffraction (XRD) analysis was carried out with an Xpert Pro X-ray diffractometer (PANalytical) using Cu K α radiation, 20°–60° in 2 θ (0.01° per step; 3s per step). Precipitates were identified using X Powder software [8.40].

MNPs as photothermia agents: BMNPs suspensions in aqueous solutions

Experiments were performed in a 96 well plate that contained 200 μL of suspension of nanoparticles in HEPES (2-[4-(2-hydroxyethyl)piperazin-1-yl]ethanesulfonic acid) buffer, pH 7.4. The concentration of nanoparticles was adjusted to 0.75 mg/mL, equivalent to a concentration of $[\text{Fe}] = 9.5 \text{ mM}$. Each sample was exposed to a NIR laser ($\lambda = 850 \text{ nm}$), from the bottom, for a duration of 360 seconds at different power densities (0.1, 0.2, 0.45, 0.63, 0.83 and 1 W/cm^2) of incident light. Simultaneously, each sample was monitored with a thermographic camera Flir 60 with 320×240 pixels, IR resolution and thermal sensitivity $< 0.045^\circ\text{C}$; (FLIR Systems, Inc., Wilsonville, USA), with the purpose of measuring temperature variations. To characterize the thermal properties of BMNPs, the Specific Absorption Rate (SAR) for each laser power intensity was determined using the following equation:

$$SAR = \frac{C_{\text{liq}}\rho_{\text{liq}}}{\phi} \frac{dT}{dt} \quad (8.1)$$

Where ϕ is the concentration of BMNPs, C_{liq} and ρ_{liq} are the mass specific heat and the density of the suspension, respectively, and $\frac{dT}{dt}$ is the temperature increase rate in the sample [8.32, 8.41]. The SAR values obtained have been calculated using the non-adiabatic Box Lucas model [8.42].

Cell culture

The HepG2, human hepatoblastoma cell line, was acquired by the European Collection of Animal Cell Cultures (Salisbury, UK). Cells were cultured using Minimum Essential Medium (MEM) supplemented with fetal bovine serum (FBS) at 10%, 2 mM L-glutamine, 100 U/mL penicillin and 100 μg /streptomycin, at 37°C in a 5% CO_2 and in a humidified atmosphere.

Uptake of BMNPs

To evaluate the amount of internalized BMNPs, HepG2 cells were seeded in 12-well plates (300,000 cells per well) and treated with BMNPs 100, 200, 300 and 400 μg /mL in medium for 24 h, equivalent to $[\text{Fe}] = 1.26, 2.53, 3.8$ and 5 mM , respectively. After 24h incubation, cells were washed 3 times with PBS to remove the non-internalized BMNPs. Aliquots of these washed samples were observed by inverted microscope (IX50; Olympus Corporation, Tokyo, Japan) to confirm the absence of extracellular BMNPs in the samples. Then, cells were trypsinized and centrifuged at 1,000 rpm for 5 min. Afterward, to dissolve the cell pellet, 37% HCl/10% H_2O_2 was

added and maintained for 20 min at room temperature. One milliliter of 1% potassium thiocyanate in Milli-Q water was immediately added to the tubes. As a final step, the absorbance at 490 nm was measured, and a standard calibration curve was used to obtain the endogenous iron content of the cells.

Photothermal assays *in vitro*

HepG2 cells were seeded onto 12 well-plates (300,000 cells per well) in medium. The cells were divided into five different groups, one for each treatment [here referred as *Intracellular* (Group 1), *Extracellular* (Group 2 and Group 4) and *Intracellular and Extracellular* (Group 3)] and one acting as control, where no BMNP were used. Figure 8.1 provides a schematic representation of the procedures applied to each group.

Group 1: Intracellular. 1 mL of BMNPs (300 $\mu\text{g/mL}$, $[\text{Fe}]=3.8 \text{ mM}$) in medium was added per well where HepG2 cells were seeded (300,000 cells/well). The treatment was maintained for 24 h to allow for BMNPs internalization. After the 24 h treatment, the medium was removed by washing the cells 3 times with PBS to eliminate extracellular BMNPs. The efficiency of the washing was checked by inverted microscope. After removing the extracellular BMNPs, the concentration of BMNPs inside the cells was 90 $\mu\text{g/mL}$. Following the washing, cells were trypsinized and resuspended in 120 μL of fresh medium. Total BMNPs concentration (BMNPs TC) was 0.75 mg/mL ($[\text{Fe}]=9.5 \text{ mM}$).

Group 2: Extracellular. HepG2 cells (300,000 cells/well) were incubated for 24 h in 1 mL of medium. Cells were trypsinized, resuspended in 60 μL of fresh medium and immediately added with a volume of 60 μL of BMNPs (1.5 mg/mL in MEM/10% FBS) per well. BMNPs TC was 0.75 mg/mL ($[\text{Fe}]=9.5 \text{ mM}$).

Group 3: Intra + Extracellular. 1 mL of BMNPs (300 $\mu\text{g/mL}$, $[\text{Fe}]=3.8 \text{ mM}$) in medium was added per well in which HepG2 cells were seeded (at 300,000 cells/well) and the treatment was maintained for 24 h to allow for BMNPs internalization. After the 24 h treatment, the extracellular medium was removed by washing 3 times with PBS to remove the extracellular BMNPs, which were collected from the PBS by using a magnet. These collected BMNPs were resuspended in 60 μL of fresh medium (here referred as fraction B). Then, cells were trypsinized and resuspended in 60 μL of fresh medium (referred as fraction A). Fractions A and B were mixed. BMNPs TC was 2.5 mg/mL ($[\text{Fe}]=31 \text{ mM}$), with intracellular BMNPs accounting for 0.75 mg/mL and extracellular BMNPs for 1.75 mg/mL.

Group 4: Extracellular. HepG2 cells (300,000 cells/well) were incubated for 24 h. Cells were trypsinized, resuspended in 60 μL of fresh medium, and immediately added with a volume of 60 μL of BMNPs (5 mg/mL in MEM/10% FBS medium) per well. BMNPs TC was 2.5 mg/mL, $[\text{Fe}]=31 \text{ mM}$.

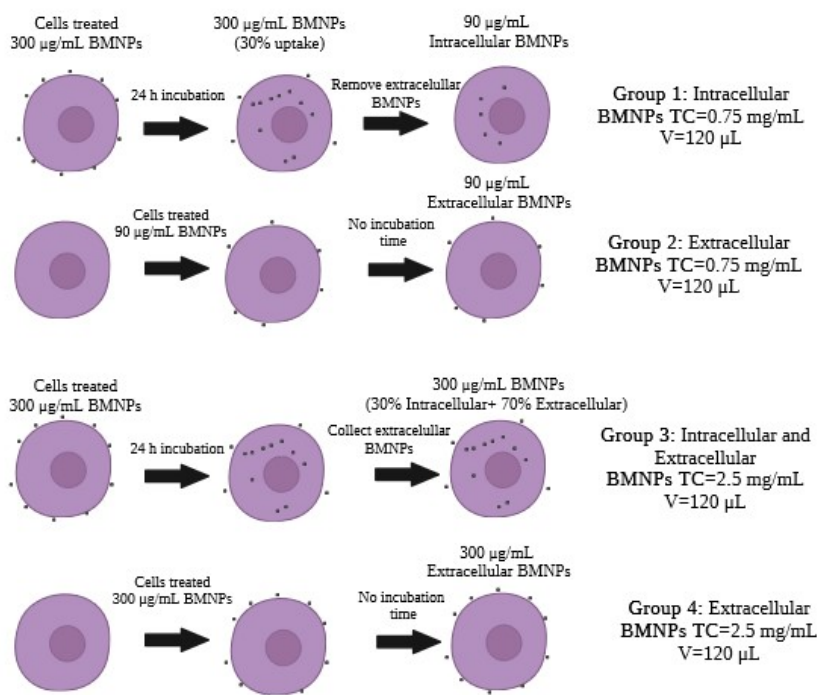


Figure 8.1: Schematic representation of the different BMNP treatments applied in the four different groups. The differences between groups include the location and the total concentration of BMNPs (BMNPs TC).

The procedures were set to achieve an identical BMNPs concentration in Groups 1 and 2, and in Groups 3 and 4. Thus, Group 1 will be compared with Group 2, and Group 3 will be compared with Group 4, as BMNPs concentration within these groups (1-2 and 3-4) is identical, but BMNPs localization (intra- and/or extracellular) is different.

TEM imaging was performed to examine BMNP localization and the structural damage in cells. To do this, HepG2 cells were cultivated in 6-well plates at a density of 10^6 cells/well. Subsequently, the relevant treatments were administered as described above (Groups 1-4). Then, cell pellets were fixed in 2.5% glutaraldehyde and 2% paraformaldehyde in 0.05 M cacodylate buffer for 4 h, at 4°C. The samples were washed three times with cacodylate buffer and postfixed in an aqueous solution of 1% OsO₄ containing 1% potassium ferrocyanide for 1 h at 4°C in darkness. The following washes were performed at 25°C: 0.15% tannic acid in cacodylate buffer, cacodylate buffer, and H₂O. The samples were then exposed to 2% uranyl acetate for 2 h and washed several times with H₂O. Dehydration in ethanol solutions ranging from 50% to 100% was carried out at 4°C. Subsequently, the samples were embedded firstly in resin (EMbed 812/100% ethanol (1/1)) for 60 min at room temperature, following by the same resin at a 2:1 ratio for 60 min, and then, in resin without ethanol

overnight. For polymerization, the samples were incubated in pure resin for 48 h at 60°C. Ultrafine sections (50–70 nm) were cut using a Leica Ultramicrotome R and contrasted using 1% aqueous uranyl acetate for 5 min and lead citrate in a CO₂-depleted atmosphere for 4 min [8.43]. A Zeiss Libra Plus 120 electron microscope was used to visualize the sections.

Laser irradiation

All the samples from each group (three replicas per group) were transferred to a 96-well plate and exposed to a NIR laser from the bottom, for a duration of 600 s and at a power density of 0.2 W/cm² of incident light. In parallel, cells from the four groups were maintained without applying laser irradiation as control experiments. The irradiation was carried out on six samples concurrently using a 6-head, 850 nm multimode IR infrared laser diode (Model RLD85NZJ4-00A, Mouser Electronics, Inc. Texas, USA), which was previously calibrated using an Optical Power Meter, PM160T (Thorlabs, Inc. USA). Temperature changes during the irradiation were monitored and measured using the previously mentioned thermographic camera, Flir 60. Throughout the process, the environmental temperature was maintained at 37°C.

Viability assay

Following laser exposure, a volume of 90 µL of each sample was transferred to a well of a 96-well black plate, and 9 µL of resazurin (R7017, Sigma-Aldrich, Spain) 1 mM in PBS was added. The reaction was incubated in darkness for 40 min, and the fluorescence intensity was subsequently measured at $\lambda_{Ex} = 535/\lambda_{Em} = 590$ nm, making use of a microplate reader (HTX Microplate Reader BioTek Instruments, Vermont, USA).

Transmission electron microscopy

TEM imaging was performed to examine the BMNP localization and the structural damage in cells. To do this, HepG2 cells were cultivated in 6-well plates at a density of 106 cells/well. Subsequently, the respective treatments with BMNPs and laser irradiation were administered as described above (Groups 1-4). Then, cell pellets were [8.42] prepared for TEM observation as detailed above.

Photothermal assays at different cell uptakes: threshold for Fe concentration

The purpose of this experiment was to get an approximation of the minimum Fe concentration in the cells (proportional to BMNPs cell uptake) that was necessary for the photothermal treatment to be effective. If the location of the photothermal agent is important, then such a location must be fixed in order to disentangle the effect of the Fe concentration from the effect of the location of the photothermal agent. For this experiment, it was chosen to work only with internalized BMNPs (Group 1). By doing this, and by varying the amount of internalized BMNPs, the photothermal effect and the Fe concentration in the cells could finally be related.

As stated above, HepG2 cells were seeded onto well-plates at a concentration of 300,000 cells/mL in MEM/10% FBS. This experiment was performed identically to that of Group 1, but incubating the cells with BMNPs for different times, up to 24 h, to allow for different uptakes. Control experiments were performed without the use of BMNPs. After the treatment, a fraction of the cells from each experiment was used to quantify BMNP uptake (as described above). The remaining cell fraction was prepared for exposure to laser irradiation (0.1 W/cm^2 of incident light for 600 seconds), also identically to that explained above. In these experiments, lower laser power intensities were used (compared to the experiments described above) to avoid a strong photothermal effect that might have interfered with the resolution of the experiment. Upon irradiation, cell viability was determined by using resazurin, as already detailed.

Statistical analysis

To determine whether there were significant differences in photothermal experiments, the t-student test was carried out for two unpaired samples. The two-tailed test with a 95% confidence interval was employed. The statistically significant differences were obtained as follows: * $p < 0.05$; ** $p < 0.01$; *** $p < 0.001$.

8.3. Results and discussion

TEM analyses of BMNPs reveal 2D morphologies, including rectangular, square, and rhombic geometries with some missing corners (Fig. 8.2a). The average size is $39 \pm 7 \text{ nm}$, although crystal sizes ranging from 10 to 70 nm can be found (Figure 8.2b). At pH 7.4, BMNPs present a hydrodynamic diameter of $500 \pm 100 \text{ nm}$. Being the average size of the BMNPs $\sim 40 \text{ nm}$, this means that at physiological pH most BMNPs are aggregated in clusters of about 10 to 15 nanoparticles. The

XRD diffraction data shows the characteristic reflections for magnetite (Figure 8.2c). BMNPs have the capability to elevate the temperature of the surrounding medium upon laser irradiation in the NIR, making them effective hyperthermia agents (Fig. 8.2d). Temperature increases can be observed across the entire range of laser power density studied, with ΔT increasing proportionally to the laser power density. At a laser power density of 1 W/cm^2 , ΔT can reach up to 40°C . Therapeutic temperature ($42^\circ\text{C} < T < 46^\circ\text{C}$) can be achieved at laser power densities $> 0.2 \text{ W/cm}^2$, in less than 240 seconds (Fig. 8.2d). SAR values (Figure 8.2e) are consistent with the data reported in literature for other magnetic nanoparticles [8.44]. Additional information regarding the achieved temperatures and SAR values can be found in Table 8.1.

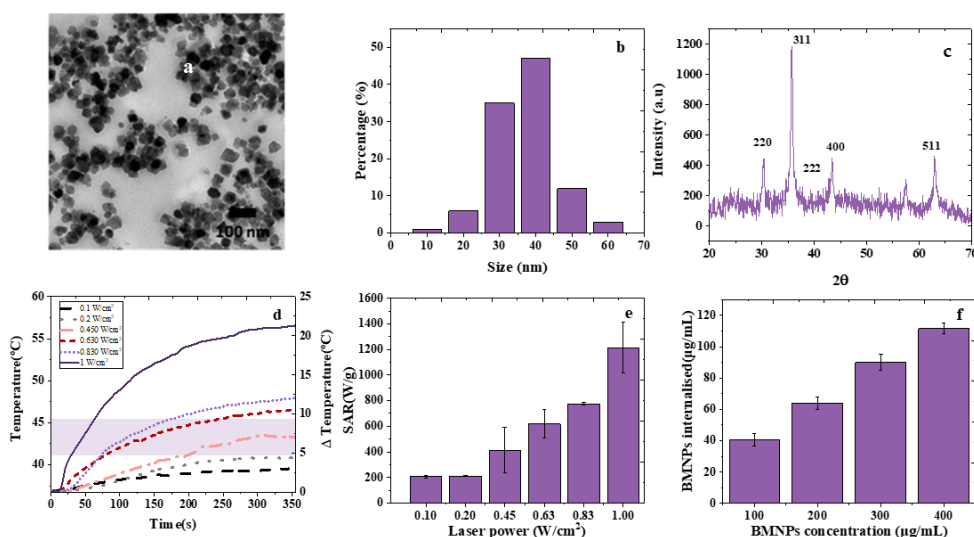


Figure 8.2: BMNPs characterization. (a) Transmission electron microscopy (TEM), (b) BMNPs size distribution. (c) X-ray diffraction. Photothermal response of suspensions of BMNPs in HEPES using a BMNPs concentration of 0.75 mg/mL ($[\text{Fe}] = 9.5 \text{ mM}$) (d) as a function of irradiation time at $0.1, 0.2, 0.45, 0.63, 0.83,$ and 1 W/cm^2 . Semi-transparent violet box is highlighted the hyperthermia temperature range. (e) SAR values obtained at different laser densities. (f) BMNPs uptake after treating HepG2 cells with different BMNPs concentrations ($100\text{-}400 \text{ }\mu\text{g/mL}$).

It can also be found how the SAR varies as a function of concentration (Figure 8.6), decreasing as the concentration increases, as described by other authors [8.45]. This is probably caused by a shadow effect that prevents laser penetration and, therefore, the irradiation of the total mass of nanoparticles [8.46]. As the concentration of the photothermal agent increases, so does the number of nanoparticles generating heat following upon radiation. However, as the concentration of the nanoparticles increases, they may start shadowing others, thus preventing their irradiation and, so, heat generation. As the SAR parameter is a normalization of the

heat production by the concentration of the photothermal agent, if shadow effects are important, the SAR value will decrease, since the heat generated by those that have been irradiated is normalized by the total mass of the photothermal agent (including irradiated and non-irradiated nanoparticles) [8.44].

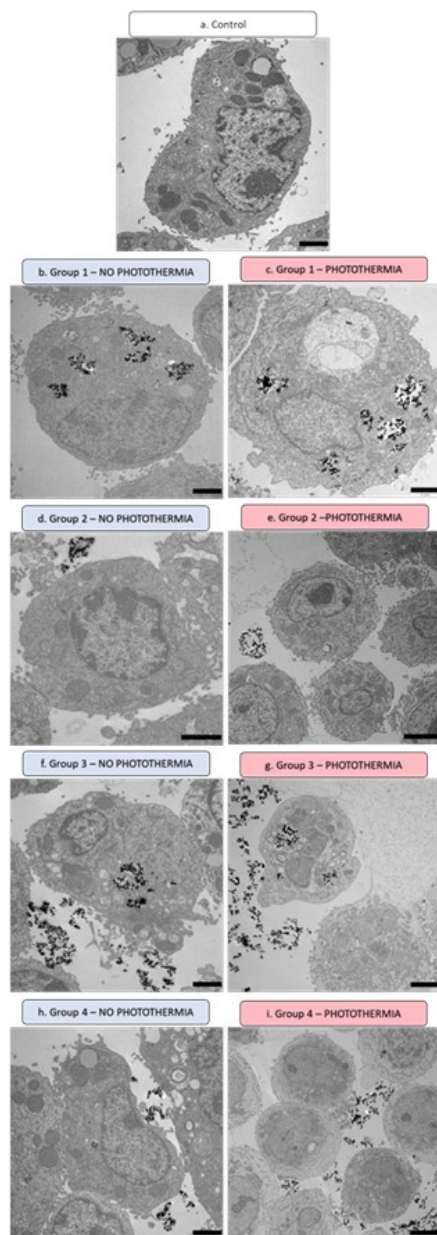


Figure 8.3: TEM images of HepG2 (controls and groups 1-4) exposed or not to photothermal treatment. Scale bar corresponds to 2 μm (a, b, c, d, f) and 5 μm (e, i).

As described in previous works, BMNPs internalize in HepG2 via endocytosis [8.24, 8.25]. Figure 8.2f demonstrates that, at the minimum concentration tested (100 $\mu\text{g/mL}$, $[\text{Fe}] = 1.26 \text{ mM}$), the percentage of BMNPs uptake was near to 40% ($40 \pm 4 \mu\text{g/mL}$ of BMNPs) and this uptake increased by increasing the concentration of BMNP in the cell treatment. In fact, when HepG2 cells were treated at the maximum concentration of BMNP, 400 $\mu\text{g/mL}$ ($[\text{Fe}] = 5 \text{ mM}$), the uptake was $112 \pm 4 \mu\text{g/mL}$. According to these data, we chose a BMNP concentration for cell treatment of 300 $\mu\text{g/mL}$, at which a 90% internalization and low toxicity were observed. This chosen concentration was a compromise to achieve high uptake, cytocompatibility and no interferences of BMNPs with the protocol for measuring cell viability, otherwise observed at higher BMNP concentrations [8.24, 8.25].

TEM analyses of HepG2 cells from Group 1 to 4 are shown in Figure 8.3. HepG2 cells from Group 1 (Figure 8.3b) show internalized BMNPs and no signs of cell damage. Conversely, when BMNP treatment was adjusted to prevent internalization (Groups 2 and 4), no internalization was detected in any of the observed cells. BMNPs were visualized in the bulk medium with little interaction with the cell outer structures (Figures 8.3d and 8.3e). In the Group 3 (Figure 8.3d) high BMNPs internalization as well as extracellular BMNPs were observed. In any case, regardless of whether or not BMNPs were internalized, structural cell damage was not observed in any of the groups.

Data for the effect of photothermia on HepG2 cells treated with BMNPs (Groups 1 to 4) are reported in Figure 8.4a.

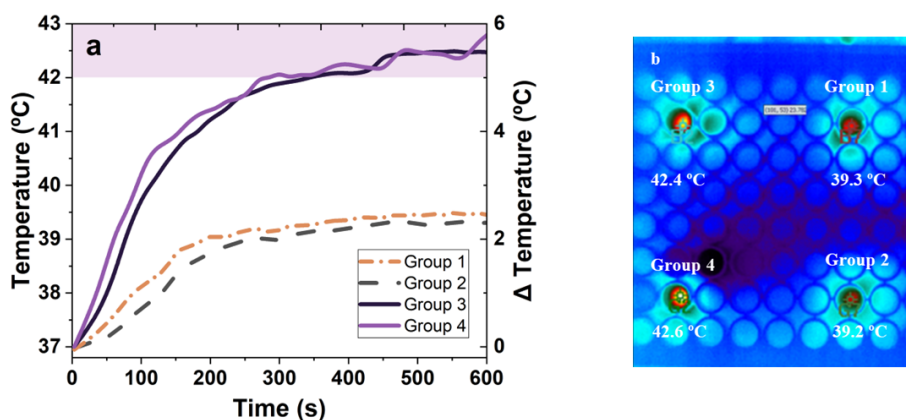


Figure 8.4: (a) Temperatures reached for BMNPs TC from Groups 1 to 4 following upon laser exposure at 0.2 W/cm^2 (therapeutic temperature in blue) (b) IR temperature image capture of a 96-well plate. Temperature data are available in Table 8.2.

The groups with lower BMNPs concentration (Group 1 and Group 2, TC 0.75 mg/mL) reached a lower temperature following upon laser exposure ($\sim 40^\circ\text{C}$),

compared to that ($\sim 43^{\circ}\text{C}$) reached by Groups 3 and 4 (TC 2.5 mg/mL). These results are confirmed by thermographic determinations shown in Figure 8.4b and it is consistent with previously observations from many authors that an increase on the photothermal agent concentration induces a higher thermal efficiency (that understood as the ability of BMNPs to increase the temperature). Detailed temperature data from this experiment can be found in Table 8.2.

However, it is interesting to note that the increase in temperature in treated cells does not depend on the location of BMNPs, since no differences in temperature elevation were observed between Group 1 (intracellular BMNPs) and Group 2 (extracellular BMNPs). Based on this data, it can be concluded that temperature increases following photothermia treatments depend solely on Fe concentration and not on the location of BMNPs.

Another remarkable point showed when Figure 8.2d and Figure 8.4 is that cell internalization does not shield BMNPs thermal efficiency. Figure 8.2d shows the temperature profile in aqueous suspension of BMNPs at a concentration of 0.75 mg/mL and different irradiation powers. When this irradiation power is 0.2 W/cm^2 and irradiation time 350 s, the temperature reached by BMNPs in aqueous suspension is 40.8°C . Cells treated with BMNPs and concentrated to 0.75 mg BMNPs/mL (Figure 8.4a, Groups 1 and 2), at identical laser power intensity as that for BMNPs in suspension (0.2 W/cm^2) and irradiation time (350 s), reach 39.4°C for Group 1 experiments (intracellular BMNPs) and 39.1°C for Group 2 experiments (extracellular BMNPs). Differences between the thermal efficiency of BMNPs in aqueous solution and in cells are not significant. Contrary to what happens in magnetic hyperthermia, where the mechanisms of heat generation can be blocked if the hyperthermal agent is internalized [8.5, 8.28, 8.33, 8.45], internalization of the photothermal agent does not affect heat generation following upon laser irradiation. In fact, some authors have observed that heat generation is improved if the photothermal agent is internalized [8.5, 8.28, 8.33, 8.45].

However, and although the location of the photothermia agent did not affect the thermal efficiency of BMNPs, such location did affect cell viability, especially at lower BMNPs concentration (Figure 8.5a). While BMNPs were cytocompatible in all non-irradiated treated cells (from Group 1 to Group 4), laser exposure induced HepG2 cell death, and the effect was strongly dependent on the location of the BMNPs. The viability of HepG2 cells from Group 1 (BMNP intracellular) decreased to 26%, while that for cells in Group 2 (BMNP extracellular) remained at 93%. These values were significantly different (it is worth noting that both groups have the same BMNP concentration and differ only in BMNP location). When BMNPs concentration increased (Groups 3 and 4), HepG2 cells viability after laser exposure decreased to 10% for Group 3 and to 29% for Group 4.

These results of viability loss are consistent with the noticeable cell damage observed by TEM following upon photothermia treatments in cells from Group 1,

Group 3 and Group 4 (Figures 8.3f-i). Cells show disorganization of the cytoplasm and subcellular organelles. In particular, disorganized mitochondria and endoplasmic reticulum and vacuolization can be observed, which is consistent with the loss of cell viability observed in Figure 8.5a or these Groups.

Figures 8.5a and 8.5b also show that, for a given location of the photothermal agent, cell viability is significantly reduced by increasing the concentration of this photothermal agent. In fact, when BMNPs are located extracellularly (Figure 8.5a) cell viability after irradiation decreases from 93% (Group 2, extracellular [Fe] = 1.2 mM) to 29% (Group 4, extracellular [Fe] = 3.8 mM). When BMNPs are located intracellularly (Figure 8.5b), cell viability after irradiation also decreases as the concentration of intracellular Fe increases. In fact, a significant cell loss (cell viability < 80%) is only reached when the intracellular Fe concentration is higher than ~ 0.5 mM under the conditions studied (0.1 W/cm^2), being that a threshold. It is also worth noting that much higher BMNP concentrations and twice the laser power intensities are needed for extracellular BMNPs to reach equivalent cell death than that achieved when BMNPs are located intracellularly.

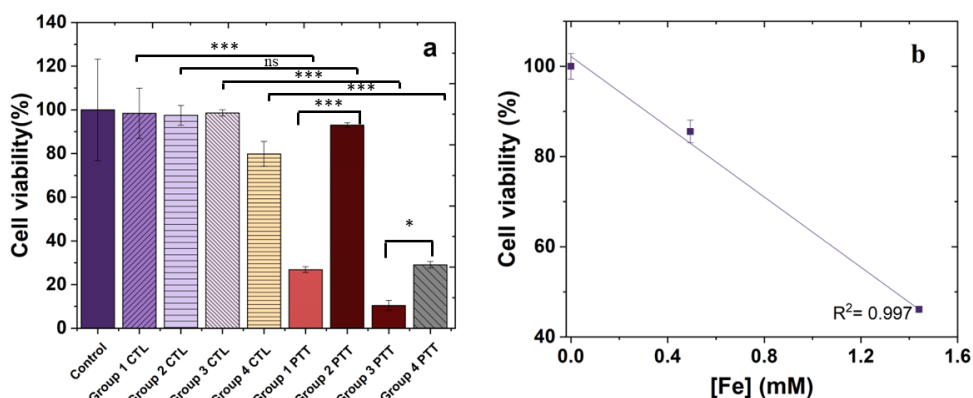


Figure 8.5: (a) HepG2 cell viability with and without photothermia treatment (0.2 W/cm^2) *in vitro*. p-value $* < 0.05$; $*** p < 0.001$. (b) HepG2 cell viability following upon photothermia treatment (0.1 W/cm^2) as a function of internalized Fe (proportional to BMNPs uptake).

These experiments demonstrate three important facts:

1. The intracellular location of BMNPs is crucial to ensure the effectiveness of photothermia treatments under all tested conditions, especially at low Fe concentration. In fact, data from Group 1 and Group 4 show that, to induce the same level of cell death as intracellular BMNPs (Group 1), the concentration of extracellular BMNPs (Group 4) needs to be at least three times higher ($300 \mu\text{g/mL}$ versus $90 \mu\text{g/mL}$).

2. For a given location of the photothermia agent (i.e., extracellular: Group 2 and Group 4), cell viability strongly depends on the Fe concentration. With extracellular location of BMNPs and at the laser power density used (0.2 W/cm^2), no significant loss in cell viability was detected when $[\text{Fe}]$ was of 0.75 mg/mL (Group 2), while $\sim 70\%$ cell loss was observed when $[\text{Fe}]$ was of 2.5 mg/mL . Moreover, when photothermia treatments (0.1 W/cm^2) were applied to HepG2 cells with different BMNPs uptake (and so, different intracellular Fe concentration; Figure 8.5b), cell viability was only affected when the concentration of intracellular Fe was higher than $\sim 0.5 \text{ mM}$. This data show that there is a threshold for Fe internalization needed to be reached to ensure effectiveness of the treatment and that this threshold is lower if this Fe is located intracellularly vs extracellularly. Nanoformulations that increase BMNPs cell uptake [i.e., liposomes, PLGA, for example [8.47, 8.48]], are thus expected to increase the efficiency of photothermia treatments, especially at low Fe concentrations.
3. Bulk temperature rise is not the only factor accounting for cell death (see Fig. 8.5a vs Fig. 8.5b), and other factors need to be considered. In this context, the importance of the intracellular location of BMNPs may indicate that the temperature increase, induced by the laser energy adsorption by BMNPs and energy release in the form of heat, may damage and disorganize internal cell organelles. It is well described that the main organelle affected by intracellular heat is mitochondria [8.49, 8.50], which is involved in ROS generation. Significant disruption of mitochondrial membranes results in an alteration of oxidative status inside the cells, sensitizing the cells and causing significant cell death [8.51, 8.52]. Therefore, BMNPs located intracellularly may induce cell death by temperature increase, alteration of organelles, and ROS production. This observation aligns with studies from other authors [8.52] and with previous studies from our group, where it was observed that BNMPs subjected to alternating magnetic field, without triggering measurable temperature increase in the bulk medium, could still induce cell death through ROS production [?, 8.25, 8.47]. When BMNPs are located extracellularly, the temperature increase could only affect the cell plasmatic membrane [8.53].

Furthermore, it is important to mention that at the low laser power intensity used here, photothermia damages are mainly attributed to heat transfer. Additional cell damages could be provoked by applying other protocols for laser irradiation, such as laser pulses of higher laser power intensity. Under these conditions, the formation of water vapor nanobubbles is reported following upon irradiation of an extracellular photothermal agent, resulting in damage in cell outer structures that lead to photoporation [8.11].

8.4. Conclusions

The data here presented demonstrate that the location of the photothermal agent, specially at low concentrations, is crucial to ensure the effectiveness of a photothermia treatment. Particularly, when BMNPs are used as photothermal agents on HepG2 cells, roughly three times the concentration of BMNPs are needed if they are located extracellularly versus intracellularly to have the same efficiency in terms of cell death. Moreover, for a given location, cell death increases as BMNPs concentration increases and, even when BMNPs are internalized, there is a threshold on Fe concentration (~ 0.5 mM at laser power intensities of 0.1 W/cm²) needed to affect cell viability following upon cell exposure to photothermia. The rise in bulk temperature is not the sole factor contributing to cell death but structural damage, especially that of internal organelles, also accounts for such cell death.

These findings emphasize the importance of designing photothermia treatments that achieve the necessary threshold of local Fe concentration in the target cells. Furthermore, the development of nanoformulations to enhance cell uptake, particularly at low Fe concentrations, would significantly improve the efficiency of photothermia treatments for tumors.

Acknowledgments

Financial support of this investigation by Ministerio de Economía y Competitividad (PID2019-109294RB-100 and PDC2021-121135.100), Instituto de Salud Carlos III (PI20-01658), FEDER/Junta de Andalucía-Consejería de Transformación Económica, Industria, Conocimiento y Universidades, Spain (Grant No. P20_00346 and P20_00233) and Consejería de Conocimiento, Investigación y Universidad, Junta de Andalucía, Spain (Grants No B-BIO-432-UGR20, B-CTS-216-UGR20, A-FQM492-UGR20) are gratefully acknowledged. CJL thanks UCE-PP2016-05 and Biotechnology Institute (University of Granada). G.R.I and M.L thanks grant TED2021-131855BI00/Unión Europea Next Generation EU/PRTR. European Union's Horizon 2020 research and innovation programme under the Marie Skłodowska-Curie grant agreement No 10106426 and F.O No 754446 and UGR Research and Knowledge Transfer Found-Athenea3i. M.J.-C thanks FPU2021 grant (ref. FPU21_01529) from the Ministerio de Universidades (Spain). C.J.-L. thanks UCE-PP2016-05, Biotechnology Institute (University of Granada). G.R.I and M.L thanks Instituto de Investigación Biosanitaria ibs. GRANADA, España. M.J.-C. wants to acknowledge a FPU2021 grant (ref. FPU21_01529) from the Ministerio de Universidades (Spain). We also acknowledge the assistance of the technical personnel in the Centro de Instrumentación Científica, University of Granada.

Appendix. Supplementary Information

Laser Intensity (W/cm ²)	Δ Temperature (°C \pm 0.2)	SAR (W/g)
0.1	2.7	206.9 \pm 8.3
0.2	4.9	264.8 \pm 41.4
0.45	7.4	412.8 \pm 126.5
0.63	10.4	619.6 \pm 80.5
0.83	12.5	775.4 \pm 6.1
1	21.8	1214 \pm 139

Table 8.1: Temperature increase during aqueous solution photothermia using a BMNPs concentration of 0.75 mg/mL ([Fe]=9.5mM).

Cell Group	Δ Temperature (°C \pm 0.2)	Reached Temperature (°C \pm 0.2)
Group 1	2.3	39.3
Group 2	2.2	39.2
Group 3	5.4	42.4
Group 4	5.6	42.6

Table 8.2: Temperature increase of cells from Group 1 to 4 following upon laser irradiation at 0.2 W/cm² for 600 seconds

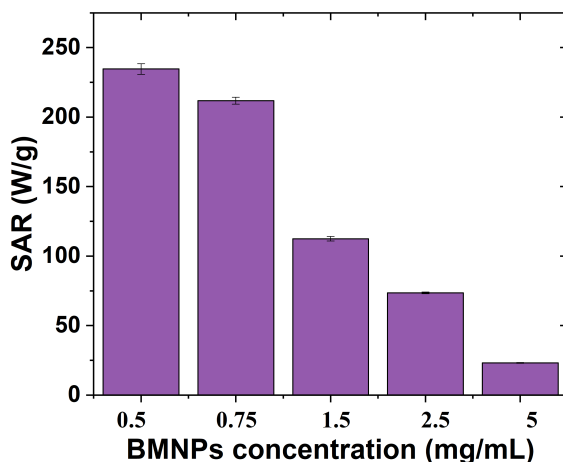


Figure 8.6: SAR values obtained from suspensions of BMNPs at different irradiated for 600 seconds at a power laser intensity of 0.2 W/cm².

Bibliography

- [8.1] Preeti Kumari, Balaram Ghosh, and Swati Biswas. Nanocarriers for cancer-targeted drug delivery. *Journal of Drug Targeting*, 24(3):179–191, 2016.
- [8.2] David Chang, May Lim, Jeroen ACM Goos, Ruirui Qiao, Yun Yee Ng, Friederike M Mansfeld, Michael Jackson, Thomas P Davis, and Maria Kavallaris. Biologically targeted magnetic hyperthermia: Potential and limitations. *Frontiers in Pharmacology*, 9:831, 2018.
- [8.3] Arunima Rajan and Niroj Kumar Sahu. Review on magnetic nanoparticle-mediated hyperthermia for cancer therapy. *Journal of Nanoparticle Research*, 22:1–25, 2020.
- [8.4] Hira Fatima, Tawatchai Charinpanitkul, and Kyo-Seon Kim. Fundamentals to apply magnetic nanoparticles for hyperthermia therapy. *Nanomaterials*, 11(5):1203, 2021.
- [8.5] Sebastjan Nemeč, Slavko Kralj, Claire Wilhelm, Ali Abou-Hassan, Marie-Pierre Rols, and Jelena Kolosnjaj-Tabi. Comparison of iron oxide nanoparticles in photothermia and magnetic hyperthermia: Effects of clustering and silica encapsulation on nanoparticles' heating yield. *Applied Sciences*, 10(20):7322, 2020.
- [8.6] Aldo Isaac Martínez-Banderas, Antonio Aires, Marta Quintanilla, Jorge A Holguín-Lerma, Claudia Lozano-Pedraza, Francisco J Teran, Julián A Moreno, Jose E Perez, Boon S Ooi, Timothy Ravasi, et al. Iron-based core-shell nanowires for combinatorial drug delivery and photothermal and magnetic therapy. *ACS Applied Materials & Interfaces*, 11(47):43976–43988, 2019.
- [8.7] Xiaomeng Guo, Wei Li, Lihua Luo, Zuhua Wang, Qingpo Li, Fenfen Kong, Hanbo Zhang, Jie Yang, Chunqi Zhu, Yongzhong Du, et al. External magnetic field-enhanced chemo-photothermal combination tumor therapy via iron oxide nanoparticles. *ACS Applied Materials & Interfaces*, 9(19):16581–16593, 2017.

- [8.8] Shun Shen, Sheng Wang, Rui Zheng, Xiaoyan Zhu, Xinguo Jiang, Deliang Fu, and Wuli Yang. Magnetic nanoparticle clusters for photothermal therapy with near-infrared irradiation. *Biomaterials*, 39:67–74, 2015.
- [8.9] Jana Ramon, Ranhua Xiong, Stefaan C De Smedt, Koen Raemdonck, and Kevin Braeckmans. Vapor nanobubble-mediated photoporation constitutes a versatile intracellular delivery technology. *Current Opinion in Colloid & Interface Science*, 54:101453, 2021.
- [8.10] Ranhua Xiong, Sangram Keshari Samal, Jo Demeester, Andre G Skirtach, Stefaan C De Smedt, and Kevin Braeckmans. Laser-assisted photoporation: fundamentals, technological advances and applications. *Advances in Physics: X*, 1(4):596–620, 2016.
- [8.11] Ranhua Xiong, Félix Sauvage, Juan C Fraire, Chaobo Huang, Stefaan C De Smedt, and Kevin Braeckmans. Photothermal nanomaterial-mediated photoporation. *Accounts of Chemical Research*, 56(6):631–643, 2023.
- [8.12] Rafael Inácio Barbosa, Elaine Caldeira de Oliveira Guirro, Luciano Bachmann, Hugo Evangelista Brandino, and Rinaldo Roberto de Jesus Guirro. Analysis of low-level laser transmission at wavelengths 660, 830 and 904 nm in biological tissue samples. *Journal of Photochemistry and Photobiology B: Biology*, 209:111914, 2020.
- [8.13] Louise Finlayson, Isla RM Barnard, Lewis McMillan, Sally H Ibbotson, C Tom A Brown, Ewan Eadie, and Kenneth Wood. Depth penetration of light into skin as a function of wavelength from 200 to 1000 nm. *Photochemistry and Photobiology*, 98(4):974–981, 2022.
- [8.14] Andreas Siems, Stefan AL Weber, Johannes Boneberg, and Anton Plech. Thermodynamics of nanosecond nanobubble formation at laser-excited metal nanoparticles. *New Journal of Physics*, 13(4):043018, 2011.
- [8.15] Dmitri Lapotko. Optical excitation and detection of vapor bubbles around plasmonic nanoparticles. *Optics Express*, 17(4):2538–2556, 2009.
- [8.16] Lara K Bogart, Arthur Taylor, Yann Cesbron, Patricia Murray, and Raphaël Lévy. Photothermal microscopy of the core of dextran-coated iron oxide nanoparticles during cell uptake. *ACS Nano*, 6(7):5961–5971, 2012.
- [8.17] Qiangqiang Liu, Jinxing Huang, Qiyi Feng, Ting Zhang, Xuanming Chen, Xiaojie Li, Xinyi Liu, Hongxia Li, Zhihui Zhong, and Kai Xiao. Multi-modal visualization of uptake and distribution of iron oxide nanoparticles in macrophages, cancer cells, and xenograft models. *Journal of Biomedical Nanotechnology*, 15(8):1801–1811, 2019.

- [8.18] Deepak B Thimiri Govinda Raj and Niamat Ali Khan. Surface functionalization dependent subcellular localization of superparamagnetic nanoparticle in plasma membrane and endosome. *Nano Convergence*, 5(1):4, 2018.
- [8.19] Thomas Kirkegaard and Marja Jäätelä. Lysosomal involvement in cell death and cancer. *Biochimica et Biophysica Acta (BBA)-Molecular Cell Research*, 1793(4):746–754, 2009.
- [8.20] Boris Turk, Veronica Stoka, Jerica Rozman-Pungercar, Tina Cirman, Gabriela Droga-Mazovec, K Oreic, and Vito Turk. Apoptotic pathways: involvement of lysosomal proteases. *Biological Chemistry*, (383):1035–1044, 2002.
- [8.21] Gary Hannon, Anna Bogdanska, Yuri Volkov, and Adriele Prina-Mello. Comparing the effects of intracellular and extracellular magnetic hyperthermia on the viability of BxPC-3 cells. *Nanomaterials*, 10(3):593, 2020.
- [8.22] Lilianne Beola, Laura Asín, Catarina Roma-Rodrigues, Yilian Fernández-Afonso, Raluca M Fratila, David Serantes, Sergiu Ruta, Roy W Chantrell, Alexandra R Fernandes, Pedro V Baptista, et al. The intracellular number of magnetic nanoparticles modulates the apoptotic death pathway after magnetic hyperthermia treatment. *ACS Applied Materials & Interfaces*, 12(39):43474–43487, 2020.
- [8.23] Lilianne Beola, Laura Asín, Raluca M Fratila, Vanessa Herrero, Jesús M De La Fuente, Valeria Grazué, and Lucía Gutiérrez. Dual role of magnetic nanoparticles as intracellular hotspots and extracellular matrix disruptors triggered by magnetic hyperthermia in 3d cell culture models. *ACS Applied Materials & Interfaces*, 10(51):44301–44313, 2018.
- [8.24] Ylenia Jabalera, Alberto Sola-Leyva, Ana Peigneux, Federica Vurro, Guillermo R Iglesias, Jesus Vilchez-Garcia, Inmaculada Pérez-Prieto, Francisco J Aguilar-Troyano, Luisa C López-Cara, María P Carrasco-Jiménez, et al. Biomimetic magnetic nanocarriers drive choline kinase alpha inhibitor inside cancer cells for combined chemo-hyperthermia therapy. *Pharmaceutics*, 11(8):408, 2019.
- [8.25] Alberto Sola-Leyva, Ylenia Jabalera, María A Chico-Lozano, María P Carrasco-Jiménez, Guillermo R Iglesias, and Concepción Jimenez-Lopez. Reactive oxygen species (ROS) production in HepG2 cancer cell line through the application of localized alternating magnetic field. *Journal of Materials Chemistry B*, 8(34):7667–7676, 2020.
- [8.26] Jing Liu, Ranhua Xiong, Toon Brans, Saskia Lippens, Eef Parthoens, Francesca Cella Zancacchi, Raffaella Magrassi, Santosh K Singh, Sreekumar Kurungot, Sabine Szunerits, et al. Repeated photoporation with graphene

- quantum dots enables homogeneous labeling of live cells with extrinsic markers for fluorescence microscopy. *Light: Science & Applications*, 7(1):47, 2018.
- [8.27] Jieli Wang, Aranit Harizaj, Yongbo Wu, Xiaofang Jiang, Toon Brans, Juan C Fraire, Julián Mejía Morales, Stefaan C De Smedt, Zhilie Tang, Ranhua Xiong, et al. Black phosphorus mediated photoporation: a broad absorption nanoplatform for intracellular delivery of macromolecules. *Nanoscale*, 13(40):17049–17056, 2021.
- [8.28] Joan Estelrich and Maria Antònia Busquets. Iron oxide nanoparticles in photothermal therapy. *Molecules*, 23(7):1567, 2018.
- [8.29] MA Dheyab, AA Aziz, MS Jameel, PM Khaniabadi, B Mehrdel, and BM Khaniabadi. Gold-coated iron oxide nanoparticles as a potential photothermal therapy agent to enhance eradication of breast cancer cells. In *Journal of Physics: Conference Series*, volume 1497, page 012003. IOP Publishing, 2020.
- [8.30] Achalla Vaishnav Pavan Kumar, Sunil K Dubey, Sanjay Tiwari, Anu Puri, Siddhanth Hejmady, Bapi Gorain, and Prashant Kesharwani. Recent advances in nanoparticles mediated photothermal therapy induced tumor regression. *International Journal of Pharmaceutics*, 606:120848, 2021.
- [8.31] Ylenia Jabalera, Francesca Oltolina, Ana Peigneux, Alberto Sola-Leyva, Maria P Carrasco-Jiménez, Maria Prat, Concepcion Jimenez-Lopez, and Guillermo R Iglesias. Nanoformulation design including mamc-mediated biomimetic nanoparticles allows the simultaneous application of targeted drug delivery and magnetic hyperthermia. *Polymers*, 12(8):1832, 2020.
- [8.32] Ylenia Jabalera, Alberto Sola-Leyva, María P Carrasco-Jiménez, Guillermo R Iglesias, and Concepcion Jimenez-Lopez. Synergistic photothermal-chemotherapy based on the use of biomimetic magnetic nanoparticles. *Pharmaceutics*, 13(5):625, 2021.
- [8.33] Sonia Cabana, Alberto Curcio, Aude Michel, Claire Wilhelm, and Ali Abou-Hassan. Iron oxide mediated photothermal therapy in the second biological window: A comparative study between magnetite/maghemite nanospheres and nanoflowers. *Nanomaterials*, 10(8):1548, 2020.
- [8.34] Robert JG Johnson, Jonathan D Schultz, and Benjamin J Lear. Photothermal effectiveness of magnetite nanoparticles: Dependence upon particle size probed by experiment and simulation. *Molecules*, 23(5):1234, 2018.
- [8.35] Ana Espinosa, Riccardo Di Corato, Jelena Kolosnjaj-Tabi, Patrice Flaud, Teresa Pellegrino, and Claire Wilhelm. Duality of iron oxide nanoparticles in cancer therapy: amplification of heating efficiency by magnetic hyperthermia and photothermal bimodal treatment. *ACS Nano*, 10(2):2436–2446, 2016.

- [8.36] Rafael Lopez-Moreno, Antonia Fernaéndez-Vivas, Carmen Valverde-Tercedor, Ana I Azuaga Fortes, Salvador Casares Atienza, Alejandro B Rodriguez-Navarro, Raz Zarivach, and Concepcion Jimenez-Lopez. Magnetite nanoparticles biomineralization in the presence of the magnetosome membrane protein MamC: effect of protein aggregation and protein structure on magnetite formation. *Crystal Growth & Design*, 17(4):1620–1629, 2017.
- [8.37] Ana Peigneux, Francesca Oltolina, Donato Colangelo, Guillermo R Iglesias, Angel V Delgado, Maria Prat, and Concepcion Jimenez-Lopez. Functionalized biomimetic magnetic nanoparticles as effective nanocarriers for targeted chemotherapy. *Particle & Particle Systems Characterization*, 36(6):1900057, 2019.
- [8.38] German Garcia Rubia, Ana Peigneux, Ylenia Jabalera, Javier Puerma, Francesca Oltolina, Kerstin Elert, Donato Colangelo, Jaime Goémez Morales, Maria Prat, and Concepcion Jimenez-Lopez. pH-dependent adsorption release of doxorubicin on MamC-biomimetic magnetite nanoparticles. *Langmuir*, 34(45):13713–13724, 2018.
- [8.39] C Valverde-Tercedor, M Montalbán-López, T Perez-Gonzalez, MS Sanchez-Quesada, T Prozorov, E Pineda-Molina, MA Fernandez-Vivas, AB Rodriguez-Navarro, D Trubitsyn, Dennis A Bazylnski, et al. Size control of in vitro synthesized magnetite crystals by the MamC protein of *Magnetococcus marinus* strain MC-1. *Applied Microbiology and Biotechnology*, 99:5109–5121, 2015.
- [8.40] JD Martín Ramos. Xpovder, a software package for powder x-ray diffraction analysis. *Legal Deposit GR*, 1001(04), 2004.
- [8.41] L León Félix, B Sanz, V Sebastián, TE Torres, Marcelo Henrique Sousa, JAH Coaquira, MR Ibarra, and Gerardo Fabian Goya. Gold-decorated magnetic nanoparticles design for hyperthermia applications and as a potential platform for their surface-functionalization. *Scientific Reports*, 9(1):4185, 2019.
- [8.42] Beatriz Sanz, M Pilar Calatayud, Nicolás Cassinelli, M Ricardo Ibarra, and Gerardo F Goya. Long-term stability and reproducibility of magnetic colloids are key issues for steady values of specific power absorption over time. *European Journal of Inorganic Chemistry*, 2015(27):4524–4531, 2015.
- [8.43] Edward S Reynolds. The use of lead citrate at high ph as an electron-opaque stain in electron microscopy. *The Journal of cell biology*, 17(1):208, 1963.
- [8.44] Anouchka Plan Sangnier, Sandra Preveral, Alberto Curcio, Amanda KA Silva, Chistopher T Lefèvre, David Pignol, Yoann Lalatonne, and Claire Wilhelm. Targeted thermal therapy with genetically engineered magnetite magnetosomes@ RGD: Photothermia is far more efficient than magnetic hyperthermia. *Journal of Controlled Release*, 279:271–281, 2018.

- [8.45] Ana Espinosa, Jelena Kolosnjaj-Tabi, Ali Abou-Hassan, Anouchka Plan Sangnier, Alberto Curcio, Amanda KA Silva, Riccardo Di Corato, Sophie Neveu, Teresa Pellegrino, Luis M Liz-Marzán, et al. Magnetic (hyper) thermia or photothermia? progressive comparison of iron oxide and gold nanoparticles heating in water, in cells, and in vivo. *Advanced Functional Materials*, 28(37):1803660, 2018.
- [8.46] Ana Espinosa, Javier Reguera, Alberto Curcio, Álvaro Muñoz-Noval, Christian Kuttner, Aurore Van de Walle, Luis M Liz-Marzán, and Claire Wilhelm. Janus magnetic-plasmonic nanoparticles for magnetically guided and thermally activated cancer therapy. *Small*, 16(11):1904960, 2020.
- [8.47] Ylenia Jabalera, Alberto Sola-Leyva, Salvatore Calogero Gaglio, María P Carrasco-Jiménez, Guillermo R Iglesias, Massimiliano Perduca, and Concepcion Jimenez-Lopez. Enhanced cytotoxic effect of TAT-PLGA-embedded DOXO carried by biomimetic magnetic nanoparticles upon combination with magnetic hyperthermia and photothermia. *Pharmaceutics*, 13(8):1168, 2021.
- [8.48] Federica Vurro, Ylenia Jabalera, Silvia Mannucci, Giulia Glorani, Alberto Sola-Leyva, Marco Gerosa, Alessandro Romeo, Maria Grazia Romanelli, Manuela Malatesta, Laura Calderan, et al. Improving the cellular uptake of biomimetic magnetic nanoparticles. *Nanomaterials*, 11(3):766, 2021.
- [8.49] Hyo Sung Jung, Jiyoun Han, Jae-Hong Lee, Ji Ha Lee, Jong-Min Choi, Hee-Seok Kweon, Ji Hye Han, Jong-Hoon Kim, Kyung Min Byun, Jong Hwa Jung, et al. Enhanced NIR radiation-triggered hyperthermia by mitochondrial targeting. *Journal of the American Chemical Society*, 137(8):3017–3023, 2015.
- [8.50] Ranran Guo, Haibao Peng, Ye Tian, Shun Shen, and Wuli Yang. Mitochondria-targeting magnetic composite nanoparticles for enhanced phototherapy of cancer. *Small*, 12(33):4541–4552, 2016.
- [8.51] Da-Yong Yu, Yuji Matsuya, Qing-Li Zhao, Kanwal Ahmed, Zheng-Li Wei, Hideo Nemoto, and Takashi Kondo. Enhancement of hyperthermia-induced apoptosis by a new synthesized class of furan-fused tetracyclic compounds. *Apoptosis*, 12:1523–1532, 2007.
- [8.52] Joseph L Roti Roti. Cellular responses to hyperthermia (40–46 °C): Cell killing and molecular events. *International Journal of Hyperthermia*, 24(1):3–15, 2008.
- [8.53] M Pilar Calatayud, Elisa Soler, Teobaldo E Torres, Enrique Campos-Gonzalez, Concepción Junquera, M Ricardo Ibarra, and Gerardo F Goya. Cell damage produced by magnetic fluid hyperthermia on microglial BV2 cells. *Scientific Reports*, 7(1):8627, 2017.

Part IV

Summary and conclusions

Chapter 9

Conclusions

The main objective of this work was the synthesis of magnetic nanoparticles with different sizes, geometries, and polymer surface coatings (both anionic and cationic). Their application in magnetic hyperthermia and photothermia has been investigated, as well as the release of antitumor agents incorporated in the nanoparticles, using both the aforementioned electromagnetic stimuli and low frequency rotating magnetic fields. From the results obtained, the following conclusions can be drawn:

1. Throughout Chapters 5-7, four types of nanoparticles have been synthesized: 70 nm diameter magnetic nanospheres, magnetic nanorods of length around 40 nm (1:8 aspect ratio) and 550 nm (1:5 aspect ratio), as well as carbon/magnetite hybrid particles 230 nm in length. All of them have been coated with PEI polymer, or with a PEI/PSS/PEI polymeric triple layer in the case of the nanorods. Their biocompatibility was demonstrated in the cases studied (both groups of nanorods and hybrid particles) at least up to a concentration of 300 $\mu\text{g/mL}$.
2. In all magnetic samples obtained, a high magnetic response has been achieved, around 80 emu/g for spherical nanoparticles and smaller size nanorods, and around 70 emu/g for 550 nm long nanorods. For activated carbon/magnetite particles, the magnetization is considerably lower, with saturation at 6 emu/g.
3. All the synthesized samples are shown to act as photothermal agents. In addition, both nanospheres and nanorods also function as magnetic hyperthermia agents. In the case of the smaller-sized nanorods, it was shown that when exposed to an alternating magnetic field of 23 kA/m and 114 kHz, a significant reduction in the viability of MCF7 (breast cancer) cell line was achieved, down to $73.3 \pm 5.3\%$. In addition, by applying photothermia, temperatures of 42-46 $^{\circ}\text{C}$ were maintained for 10 minutes, resulting in a cell death of $64.4 \pm 3.7\%$.

4. Both nanospheres and 550 nm long nanorods have been coated with gold seeds. In the case of magnetic hyperthermia, the gold coating reduces the effectiveness of the treatment. Similarly, when irradiating with a wavelength of 850 nm, gold-coated particles show slightly lower photothermal behavior. However, using wavelengths closer to the plasmon of the gold nanospheres (in the blue-green regions), the temperature increases by a factor of 10. This suggests that, although these wavelengths are less penetrating than NIR, they may be useful for treating superficial tumors or those accessible by optical fiber.
5. One of the most relevant results obtained is related to the application of a so-called dual therapy, in which an alternating magnetic field is applied simultaneously with laser irradiation, with the aim of achieving a specific therapeutic response. This strategy makes it possible to reduce the magnetic field strength (17 kA/m instead of 21 kA/m) and laser power density (0.3 W/cm² instead of 1 W/cm²) for obtaining the desired temperature increase. This combination is emerging as a potentially less damaging, but equally effective treatment. In this approach, the rate of temperature rise is significantly faster and, as a result, the SAR values obtained with dual therapy are three times higher than those achieved with each technique separately. This finding is extremely important, as it opens up the possibility of optimizing treatment while minimizing unwanted side effects.
6. With regard to the drug release experiments, the following conclusions can be drawn:
 - It has been shown that larger nanorods can be applied as drug carrier vehicles (adsorbing around 24% of the drug in solution). The most relevant result obtained is that they are able to release about 10% of adsorbed doxorubicin in one hour applying dual therapy, improving the release rate compared to the separate application of each of the electromagnetic stimuli.
 - In the case of magnetic activated carbon, it has been shown to be an efficient drug transporting agent, since it is capable of adsorbing around 80% of the drug (methotrexate) available in solution in only 2 hours, reaching higher amounts when left in contact for 24 hours. Furthermore, with respect to drug release, one of the most relevant results is that is considerably improved with the application of photothermal techniques and low frequency rotating magnetic fields.
7. Finally Chapter 8 is devoted to *in vitro* experiments, in which the location of the photothermal agent is essential to ensure the effectiveness of a photothermal treatment. In particular, when biomimetic MNPs (BMNPs) are used as photothermal agents in HepG2 (liver cancer) cell line, approximately three

times the concentration of BMNPs is required if they are located extracellularly compared to their intracellular location, to achieve the same efficiency in terms of cell death. Furthermore, for a specific location, cell death increases as the concentration of BMNPs increases, and even if BMNPs are internalized, there is a threshold Fe concentration (0.5 mM using laser power intensities of 0.1 W/cm^2) required to affect cell viability after exposure to photothermia. Moreover, it should be noted that increased global temperature is not the only factor contributing to cell death; structural damage, especially to internal organelles, also plays a crucial role in this process.

Capítulo 10

Resumen

10.1. Introducción

El cáncer es una de las principales causas de muerte y un gran obstáculo para mejorar la calidad y esperanza de vida en todo el mundo [10.1]. Para hacer frente a esta enfermedad, pese a los avances realizados, los tratamientos convencionales presentan importantes limitaciones debido a su alta toxicidad y agresividad. En este contexto, la nanotecnología ofrece nuevas y prometedoras alternativas. Un ejemplo de dichas alternativas es el uso de las nanopartículas magnéticas (NPMs), las cuales constituyen una herramienta de gran interés debido a sus múltiples aplicaciones, que incluyen desde la eliminación de contaminantes en entornos medioambientales e industriales. [10.2–10.4], a distintas aplicaciones en el campo de la biomedicina por su respuesta magnética, que les permite ser guiadas hacia zonas específicas del cuerpo y cumplir la función terapéutica deseada [10.5–10.7]. Además, ellas mismas pueden ser los agentes terapéuticos (en el caso de la hipertermia), o diagnósticos (en imagen por RMN).

En la actualidad, existen diferentes métodos de producción de NPMs (coprecipitación, descomposición termal, métodos hidrotermales, pirólisis...), así como estrategias biomiméticas que utilizan microorganismos y bacterias [10.8, 10.9].

Estas nanopartículas (NPs), además de ser funcionales, deben ser biocompatibles. Por este motivo, las NPs más empleadas son aquellas compuestas por magnetita (Fe_3O_4) y/o maghemita ($\gamma\text{-Fe}_3\text{O}_4$), que destacan sus excelentes propiedades magnéticas y su baja toxicidad [10.10, 10.11]. En particular, la magnetita es un material ferrimagnético caracterizado por una estructura de espinela cúbica inversa y un parámetro de celda de 8.39 Å [10.12]. Además, tiene una alta magnetización de saturación (92-100 emu/g), aunque las NPs de magnetita muestran una magnetización ligeramente inferior, un hecho que ha sido ampliamente investigado [10.11, 10.13, 10.14]. Específicamente, la magnetización de saturación aumenta con el tamaño de

las partículas, mientras que la reducción del tamaño disminuye la temperatura de Curie, donde la magnetización cambia de ferrimagnética a paramagnética [10.12]. A temperatura ambiente, el tamaño crítico para una estructura multidominio en NPs esféricas de Fe_3O_4 es teóricamente de 128 nm [10.13].

Las características de las NPMs también tienen importantes implicaciones biológicas. En primer lugar, cabe destacar que pueden ser administradas tanto por vía intravenosa, subcutánea u oral, aunque la administración oral plantea dificultades por la baja adsorción [10.15]. Posteriormente, es necesario que las NPs lleguen al órgano o tejido diana y, para ello, escapen del torrente sanguíneo, lo que requiere un campo magnético no homogéneo con un gradiente elevado para contrarrestar el flujo sanguíneo. Los factores clave que influyen en la administración de NPs son el tipo de tumor y el tamaño de las partículas. El efecto de permeabilidad y retención mejoradas (EPR), impulsado por la neoangiogénesis inducida por el tumor [10.16], permite que las NPs se acumulen en los tumores debido a vasos sanguíneos defectuosos. En particular, para un EPR eficaz, los tamaños óptimos de las NPs oscilan entre 100 y 200 nm [10.17], aunque pueden ser de hasta una micra [10.18].

Una vez fuera del torrente sanguíneo, las NPs deben interactuar con las células diana e, idealmente, ser internalizadas por ellas [10.18], para aumentar la eficacia del tratamiento, como se ha demostrado en esta tesis doctoral. Por último, también es importante saber qué ocurre con las NPs una vez cumplida su función. Dependiendo de su tamaño y capacidad de biodegradación, algunas NPs se excretan en la bilis y se eliminan en las heces, mientras que otras son filtradas por los riñones y eliminadas en la orina. Las partículas más pequeñas son eliminadas rápidamente por los riñones, mientras que las más grandes quedan retenidas en el hígado, el bazo y la médula ósea [10.15].

Otro aspecto relacionado con el tamaño es el superparamagnetismo de las NPMs. Esta característica garantiza tanto la seguridad como la eficacia, ya que impide las interacciones magnéticas entre las NPMs, además de mantener la estabilidad coloidal y evitar la agregación, minimizando el riesgo de formación de trombos. Aún así, en condiciones fisiológicas (pH ligeramente básico, fuerza iónica elevada) la carga superficial es pequeña, y la agregación es difícil de evitar [10.19, 10.20]. Para contrarrestar esta situación, el recubrimiento de las NPs con cubiertas poliméricas, capas lipídicas o metales puede mejorar su estabilidad, dispersión y funcionalización [10.19]. En concreto, el polímero catiónico polietilenoimina (PEI) es especialmente eficaz como recubrimiento debido a su elevada carga, que resulta beneficiosa para la administración de tratamientos contra el cáncer y para mejorar las interacciones biológicas [10.21]. Otro ejemplo son las partículas magnéticas biomiméticas, como las mediadas por la proteína MamC, que imitan de forma natural las estructuras biológicas, lo que proporciona compatibilidad inherente sin necesidad de recubrimientos adicionales [10.22, 10.23].

Entre las aplicaciones biomédicas de las NPMs, una de las más notables es su

capacidad para convertirse en transportadores de fármacos, reduciendo la distribución sistémica y mejorando la captación en la zona diana, lo que posibilita un tratamiento eficaz con dosis de fármaco más bajas. Por lo tanto, es de gran interés conocer la adsorción de fármaco, así como una vez administrado y dirigido a la zona específica con un gradiente magnético, si se produce la liberación controlada y localizada durante periodos de tiempo prolongados [10.24]. Dicha liberación puede llevarse a cabo mediante actividad enzimática o cambios fisiológicos (pH, osmolalidad o temperatura) o terapias basadas en estímulos electromagnéticos [10.25, 10.26].

Otra posibilidad es emplear las NPMs como agentes de calentamiento localizado, o agentes de hipertermia [10.27]. Se ha demostrado que al elevar la temperatura de las células tumorales hasta un rango de 41-46°C durante un cierto periodo de tiempo, éstas no sobreviven [10.28]. Las células tumorales tienen un metabolismo acelerado y una estructura vascular desorganizada. Por este motivo, cuando son sometidas a calor, el flujo sanguíneo no es lo suficientemente eficiente para disipar el calor de manera uniforme, lo que puede inducir a la apoptosis mediante el aumento de la temperatura.

El núcleo de la presente contribución es el estudio y aplicación de terapias térmicas en NPMs. En primer lugar, se destaca la hipertermia magnética, un potencial tratamiento en el que se confía desde hace dos décadas. Consiste en la generación de calor localizado mediante la aplicación de campos magnéticos alternos [10.29]. Para que se produzca el calentamiento, es imprescindible que exista un mecanismo capaz de generar pérdidas de energía, que a su vez produzca el calor suficiente para inducir la muerte celular [10.29]. Si las partículas son ferromagnéticas, el aumento de temperatura observado se atribuye a la histéresis. Sin embargo, si son superparamagnéticas, se produce un desfase entre la dirección del campo magnético alterno y el momento magnético de las partículas. En partículas uniaxiales (una única forma de imanación fácil) pueden darse dos mecanismos que retrasan \mathbf{M} respecto de \mathbf{B} . El primero (mecanismo de Néel) se relaciona con el tiempo finito que el momento magnético de la NPM necesita para orientarse de un sentido a otro de la imanación fácil. Este tiempo se conoce como tiempo de relajación de Néel, τ_N : la orientación está dificultada por la anisotropía magnética y la energía se transfiere a la red cristalina siendo absorbida por los fonones [10.29]. El segundo proceso es el la relajación de Brown (tiempo característico τ_B) y consiste en la rotación de la partícula (no del momento magnético dentro de ella), de modo que la disipación es ahora por fricción viscosa con el medio [10.29]. Ambos actúan en paralelo, pero el tiempo de relajación de Brown predomina (es más corto que el de Néel) para partículas con radio superior a 22 nm.

Otra alternativa es la aplicación de la terapia conocida como fototerapia, que consiste en aumentar la temperatura mediante irradiación láser de una longitud de onda específica [10.30]. Es importante mencionar que, en el caso de la fototerapia, su limitación radica en la localización del tumor, siendo la penetración de la radiación visible e infrarroja limitada en el cuerpo humano. Sin embargo, es posible

aprovechar ciertos rangos del espectro, denominados ventanas biológicas, en los que la transmitancia óptica a través de los tejidos, el agua y la hemoglobina se hace mucho mayor. Este es el caso de las regiones NIR de 650-1350 nm [10.31]. Este tipo de terapia puede ser de gran interés para cánceres superficiales, como los tumores de carcinoma basocelular, que tienen una profundidad de invasión de 0.68 mm de media [10.32]. Además, esta limitación en la penetración se puede superar mediante el uso de fibras ópticas, que son capaces de guiar estas longitudes de onda.

Por último, una posibilidad menos estudiada es el uso de campos magnéticos rotantes de baja frecuencia. Estos campos no generan calor, pero pueden romper membranas o células de forma magneto-mecánica, o potenciar la difusión del fármaco transportado por las NPM [10.33–10.35]. Además, las tres técnicas presentadas pueden utilizarse juntas o por separado, no sólo para provocar la muerte de células cancerosas por aumento de temperatura (en el caso de la hipertermia magnética y la fototerapia), sino también para liberar fármacos, actuando así como agentes multifuncionales.

Para finalizar esta sección se destaca el creciente interés en nanoestructuras híbridas que responden a múltiples estímulos, desde la perspectiva física como biológica. Desde el punto de vista físico, estas nanoestructuras optimizan las propiedades y el rendimiento en aplicaciones específicas. Desde el punto de vista biológico, pretenden minimizar los efectos secundarios y maximizar la eficacia de los tratamientos.

Se ha demostrado que la magnetita actúa como agente tanto en hipertermia magnética como en fototerapia [10.36, 10.37]. Sin embargo, existen otros materiales con una mejor respuesta óptica, como el oro y la plata [10.37, 10.38] debido a sus propiedades plasmónicas [10.39]. En particular, el oro destaca por su alta biocompatibilidad, demostrando ser un agente fototerapia altamente eficaz [10.37, 10.40].

Además de la mejora de las propiedades ópticas, es importante tener en cuenta la anisotropía de las partículas. Por ejemplo, Mohapatra y col. [10.41] demostraron que a medida que aumenta la relación de aspecto de las NPs (esferas < cubos < octaedros < varillas < hilos), aumenta la eficiencia térmica, a pesar de tener una menor susceptibilidad magnética (hilos < varillas < esferas < cubos < octaedros), probablemente debido a la alta anisotropía de los nanohilos, que aumenta significativamente la pérdida por histéresis, mejorando así la eficiencia de calentamiento [10.41]. Además, las NPs anisotrópicas también pueden ejercer acciones magnetomecánicas y tratar de inducir muerte celular [10.42].

La última posibilidad mencionada es otro enfoque prometedor que consiste en la combinación de materiales porosos para la adsorción de fármacos, con materiales magnéticos que imparten direccionalidad o hipertermia a la partícula porosa, en sí misma un excelente transportador de ciertos fármacos. Esta idea se ha aplicado a la

sílice mesoporosa [10.43–10.46] o el carbón activo [10.47, 10.48].

10.2. Resultados

Nanoesferas con recubrimiento de nanopartículas de oro: Efecto del recubrimiento en las terapias de hipertermia magnética y fototermia

En este capítulo se describe la síntesis de nanoesferas de magnetita (de diámetro 70 ± 12 nm), incorporando el polímero biocompatible polietilenimina (NPM-PEI) directamente durante el proceso de síntesis de las NPs [10.49, 10.50]. Además, también se adhirieron semillas de oro en la superficie de las NPMs (Au-NPM), con el objetivo de mejorar su respuesta óptica (Figura 10.1). De este modo, se obtuvieron las primeras NPMs híbridas magnetita/oro descritas en esta tesis doctoral.

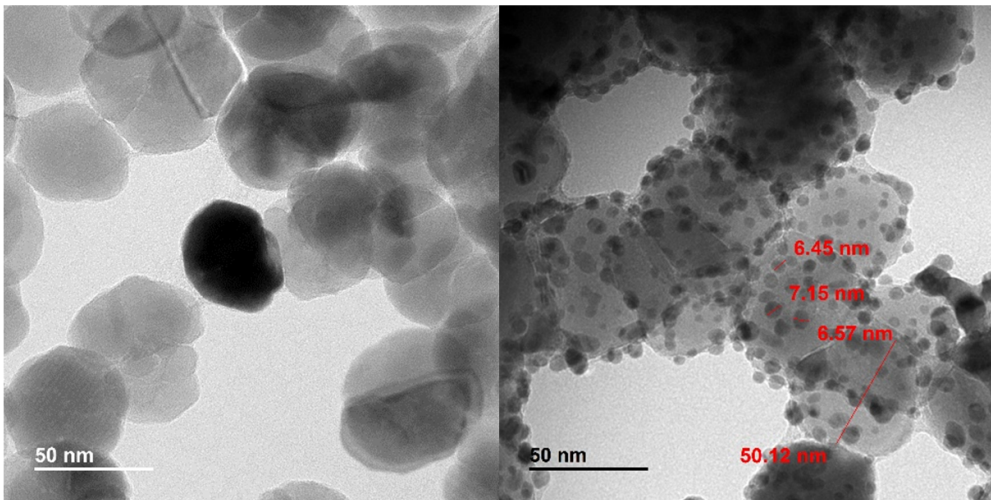


Figura 10.1: Imágenes HRTEM de NPMs antes (izquierda) y después (derecha) del recubrimiento de oro.

Ambas muestras, con y sin recubrimiento de oro, fueron completamente caracterizadas. Los resultados de la caracterización estructural confirmaron la presencia de la estructura cristalina de la magnetita, con trazas de maghemita. Posteriormente, se verificó exitosamente la incorporación tanto del recubrimiento polimérico como del recubrimiento de semillas de oro, basado en el análisis de la movilidad electroforética y la termogravimetría, en el caso del primero. En cuanto a las propiedades ópticas, se observó un ligero incremento en la absorbancia en la

muestra recubierta, probablemente debido a un desplazamiento del plasmón del oro, entre 530 y 620 nm. Además, se obtuvieron buenas propiedades magnéticas, con valores de 81.3 ± 2.2 emu/g para las muestras NPM-PEI y 36.1 ± 1.7 emu/g para las recubiertas con semillas de oro.

A continuación, las muestras de NPM-PEI y Au-NPMs fueron analizadas con las técnicas de hipertermia magnética (HM) y fototerapia (PT). La Figura 10.2A demuestra que, aunque la elevación de la temperatura conseguida con las Au-MNP alcanza el rango deseado para la actividad antitumoral, tarda más que con las partículas recubiertas únicamente de PEI. En el caso de la hipertermia magnética este efecto era de esperar teniendo en cuenta la mejor respuesta magnética de dichas NPs. Además, esto se manifiesta en los cálculos de SAR (Specific Absorption Rate, o potencia disipada por unidad de masa de NPs, Figura 10.2B) en los que se compara un valor de SAR de 87 W/g (NPM-PEI) con 27 W/g (Au-NPM). Estas estimaciones de SAR son comparables a los resultados previamente obtenidos por otros investigadores utilizando otros tipos de MNPs bajo frecuencias e intensidades de campo similares [10.51].

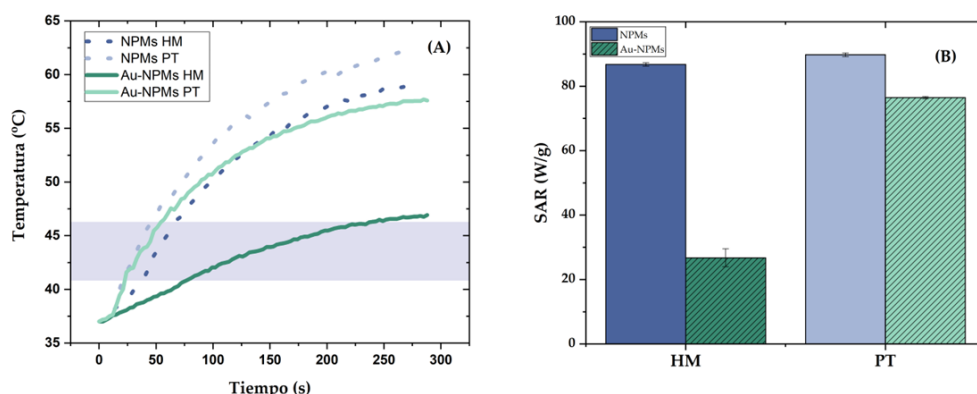


Figura 10.2: Incremento de temperatura de NPMs tratadas con PEI y recubiertas de oro (Au-NPMs). (A) Hipertermia magnética (HM) bajo la aplicación de un campo magnético alterno de 110 kHz y 20 kA/m y fototerapia (PT) por irradiación láser de 850 nm (1 W/cm^2) de potencia. (B) Valores de SAR para las situaciones presentadas en (A). La concentración de partículas utilizada fue de 10 mg/mL.

Por otro lado, es importante destacar que con la aplicación de 110 kHz, y 20 kA/m de intensidad de campo, en ambas muestras se alcanza el régimen de hipertermia antes de los 5 minutos de tratamiento (en el caso de la muestra recubierta con polielectrolito antes de los primeros 40 s), manteniendo la intensidad de campo y la frecuencia de aplicación por debajo de los límites de seguridad para el cuerpo humano propuestos por Hergt y Dutz [10.52]. Esto demuestra la potencial utilidad de las NPs como herramientas de hipertermia magnética, si bien es cierto que el recubrimiento de oro disminuye el rendimiento en hipertermia magnética, ya que el SAR obtenido es

menor. Sin embargo, a pesar de ello, se alcanza la región de hipertermia magnética (42-46°C) en menos de dos minutos.

Por otro lado, se obtuvieron resultados similares en la elevación de temperatura y los valores de SAR al aplicar la técnica de fototerapia con un láser infrarrojo (IR) de 850 nm (1 W/cm² de potencia específica o 0.2 W de potencia nominal) en muestras con y sin recubrimiento de oro, aunque las muestras sin recubrimiento demostraron ser más eficientes. Esto se debe a dos factores: en primer lugar, la densidad del oro es considerablemente mayor que la de la magnetita, por lo que habrá menos nanopartículas en un volumen dado a la misma concentración nominal; por otro lado, el aumento de absorbancia de las nanoesferas de oro incorporadas en la superficie de las NPMs no se observa en el infrarrojo cercano, sino en el visible (donde está el plasmon superficial).

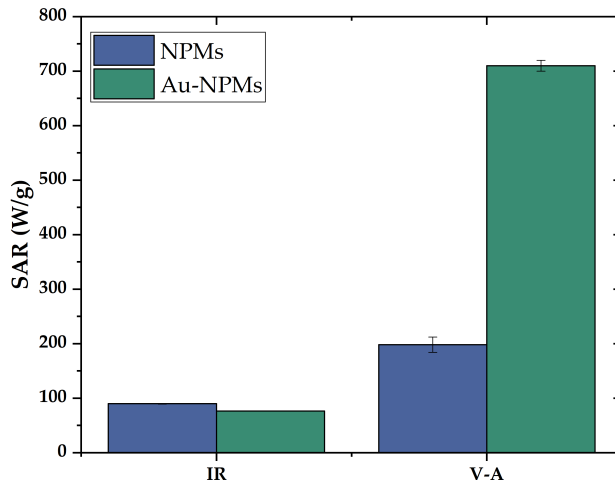


Figura 10.3: Determinación del SAR de las NPM recubiertas de PEI y oro a una irradiación láser de 0.2 W utilizando un láser NIR (850 nm, IR), y un láser RGB (verde azul V-A, 0.65 mW de $\lambda_{verde}=505$ nm, y 0.35 mW de $\lambda_{azul}=450$ nm).

Por este motivo, las partículas también se irradiaron con el láser RGB, con longitudes de onda verde (0.65 W) y azul (0.35 W) (V-A en la Figura 10.3). Curiosamente, la eficiencia térmica, medida por el SAR, aumenta en casi un factor 10 (en el caso del recubrimiento de oro) y de 2 (recubrimiento de PEI) en comparación con los resultados bajo láser IR. Aunque estas longitudes de onda están fuera de la primera ventana biológica [10.53], y tienen una penetración más limitada que un láser IR (hasta 1 mm frente a 3 mm de penetración), por lo que se estima que puedan ser útiles para algunas enfermedades superficiales [10.54]. Este es el

caso de los tumores celulares de carcinoma basocelular, en los que la profundidad media global de invasión es de 0.68 mm [10.32]. Además, podrían utilizarse fibras ópticas para aumentar significativamente la penetración. Alternativamente, el futuro uso terapéutico de estas NPs híbridas de magnetita/oro en fototerapia mediante IR podría diseñarse con otro tipo de estructuras plasmónicas (nanovarillas de oro, nanoestrellas...), que puedan desplazar la resonancia plasmónica al NIR.

Nanovarillas magnéticas biocompatibles: Evaluación de la muerte celular tras la aplicación de hipertermia magnética y fototerapia

En la sección anterior se estudiaron NPs esféricas. El siguiente objetivo de este trabajo fue ir un paso más allá y centrarnos en la síntesis y aplicación de geometrías más complejas, como las nanovarillas, que fueran biocompatibles y actuaran como agentes para hipertermia, con el fin de evaluar su impacto *in vitro*.

Por este motivo, se sintetizaron nanovarillas de magnetita de 40 ± 15 nm de largo, y relación de aspecto 1:8 (denominadas NR2), siguiendo los pasos descritos por Sugimoto y Muramatsu [10.55].

En primer lugar, se realizó una caracterización completa, determinando su tamaño y geometría a partir de microscopía HRTEM (Figura 10.4), y sus características estructurales (mezcla de magnetita y maghemita) se analizaron mediante difracción de rayos X (DRX) y espectroscopía Micro Raman.

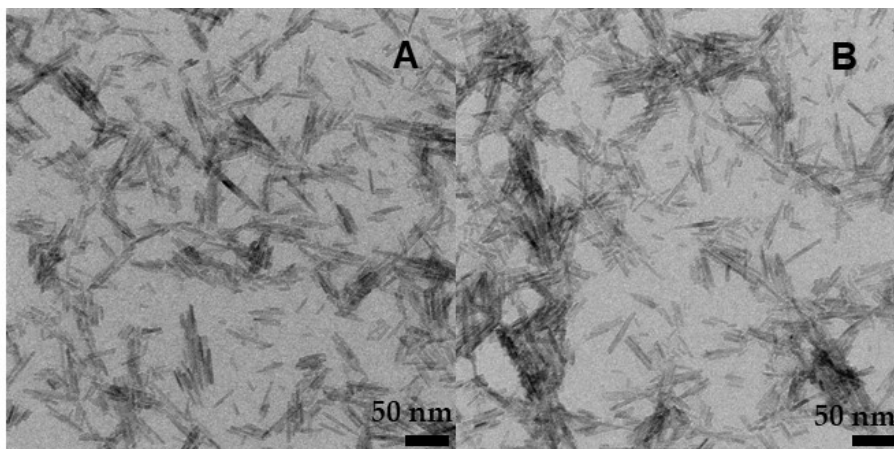


Figura 10.4: Imágenes HRTEM de las nanovarillas magnéticas (A y B).

Una característica a destacar fue la alta respuesta magnética obtenida, con magnetización de saturación superior a 80 emu/g. En este caso, se aseguró que

el recubrimiento de las partículas se mantuviera a lo largo del tiempo y, por lo tanto, garantizara la biocompatibilidad, mediante una triple capa polimérica catiónica/aniónica/catiónica formada por los polímeros polietilenimina (catiónico, PEI) y poliestirenosulfonato (aniónico, PSS). La estabilidad del recubrimiento se verificó a través de la movilidad electroforética. Posteriormente, se comprobó la viabilidad celular de la muestra recubierta con la línea celular MCF7 (de cáncer de mama), de hasta 300 $\mu\text{g/mL}$. Otro resultado crucial obtenido, es la alta tasa de internalización de la muestra NR2 recubierta poliméricamente en las células, de un $82.41 \pm 0.99\%$.

El siguiente propósito fue determinar si las nanovarillas se comportaban como agentes de hipertermia magnética y fototermia. El resultado obtenido fue que ambas muestras demostraron su eficacia, tanto en ausencia de recubrimiento, como con la capa polimérica, a concentraciones de 5 mg/mL .

Una vez logrado dicho objetivo, finalmente se evaluó *in vitro* el efecto de las nanovarillas recubiertas con polímero sobre la línea celular MCF7, en respuesta a los estímulos electromagnéticos mencionados. En el caso del tratamiento de hipertermia magnética, se realizó por triplicado, manteniendo las muestras durante 2 horas en un campo magnético alterno de 23 kA/m y 114 kHz .

Por otro lado, en el caso de la fototermia, las células se mantuvieron en el rango de hipertermia (42-46 $^{\circ}\text{C}$) durante 10 minutos, irradiando los triplicados con una longitud de onda de 850 nm y una potencia de 0.7 W/cm^2 , que se encuentra dentro de los límites tolerables y en el rango utilizado por otros autores [10.37, 10.56, 10.57]. Es importante señalar que los experimentos *in vitro* se realizaron a una concentración de 300 $\mu\text{g/mL}$ ya que, como se mencionó anteriormente, la muestra NR2 recubierta con la capa polimérica no mostró citotoxicidad.

Como se puede ver en la Figura 10.5, tras exponer NR2s a la técnica de hipertermia magnética, se consigue una reducción significativa de la viabilidad de las células MCF7 (hasta $73.3 \pm 5.3\%$), mientras que la aplicación de fototermia se produjo una muerte celular de $64.4 \pm 3.7\%$.

Por lo tanto, el resultado clave de este estudio es la evidencia de una muerte celular significativa cuando las células se incuban con 300 $\mu\text{g/mL}$ y se tratan con hipertermia magnética o fototermia, sin diferencias notables en la mortalidad celular entre ambas técnicas. Esto es particularmente relevante, ya que sugiere la posibilidad de combinar estas técnicas de forma separada o simultánea, como se detallará a continuación.

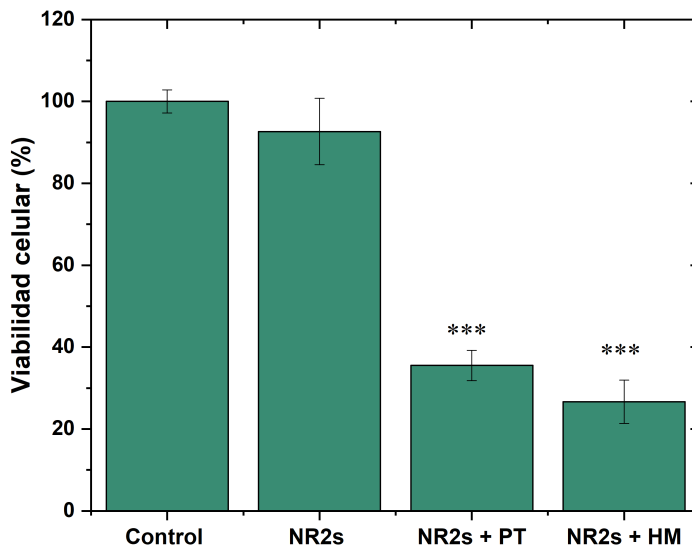


Figura 10.5: Viabilidad celular de las células MCF7 tras el tratamiento con medio EMEM (control) y nanovarillas recubiertas de polímero NR2s (300 $\mu\text{g}/\text{mL}$) en ausencia o tras la aplicación de hipertermia magnética (HM) y fototerapia (PT). Los datos representan las medias \pm SEM de tres experimentos independientes realizados por triplicado; $p \leq 0.001$ (***)

Nanovarillas magnéticas biocompatibles con recubrimiento de nanopartículas de oro: Impacto de la terapia dual y su influencia en la liberación controlada de fármacos

Una vez demostrada la eficacia de las nanovarillas recubiertas con la triple capa PEI/PSS/PEI como agentes de hipertermia *in vitro*, capaces de inducir la muerte en células MCF7 gracias a su biocompatibilidad e internalización, se procedió a un nuevo estudio. En este, se evaluó el comportamiento de nanovarillas más grandes, igualmente recubiertas con dicha capa, pero con la incorporación de oro en su superficie, tanto para hipertermia como para el transporte de fármacos.

Considerando estos objetivos, en esta investigación se sintetizaron nanovarillas de magnetita, siguiendo el trabajo de Ocaña y col. [10.58]. A través de microscopía electrónica HRTEM se determinó su tamaño, obteniendo nanovarillas con una longitud promedio de 550 ± 90 nm y una relación de aspecto de 1:5 (denominadas MNR, Figura 10.6A). La Figura 10.6B,C y D también muestra el recubrimiento con semillas de oro (Au-MNR).

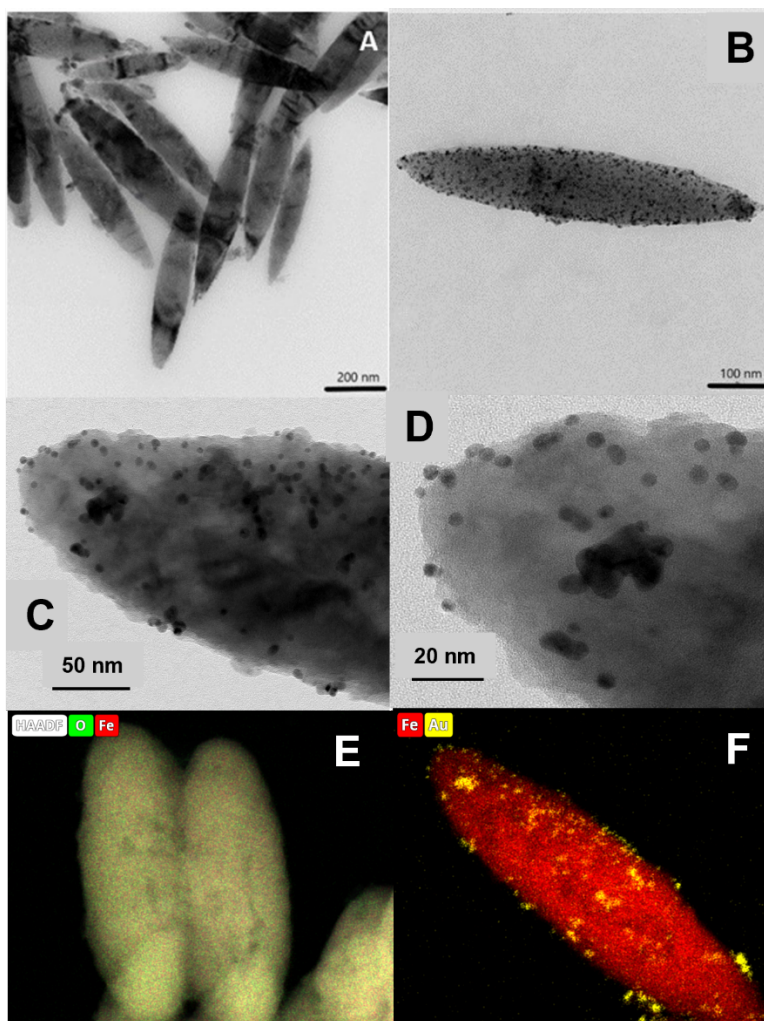


Figura 10.6: Imágenes HRTEM de nanovarillas de magnetita; (A): partículas desnudas; (B): partículas recubiertas de oro (los puntos más oscuros son NPs de Au incorporadas a la cubierta de polímero); (C, E) aumento de las nanovarillas recubiertas de partículas de oro, con observación de la capa de polímero con oro incrustado en ella; (E,F): Mapas de composición a partir de la técnica de espectroscopia de rayos X de energía dispersiva (EDX) de nanovarillas sin recubrimiento (hierro y oxígeno) y recubiertas de oro (hierro y oro).

El análisis DRX confirmó que la estructura cristalina puede identificarse con la de la magnetita, mientras que la espectroscopía Raman reveló la presencia de trazas de maghemita. Por otro lado, los resultados de la movilidad electroforética confirmaron tanto la adhesión de la triple capa de PEI/PSS/PEI como su estabilidad a lo largo del tiempo. Asimismo, el análisis termogravimétrico permitió estimar el grosor de la capa de PEI (10 nm) y de PSS (2.4 nm), correspondiéndose con el recubrimiento observado en la Figura 10.6C y D.

Además, los ensayos de magnetización demostraron alta imanación para las nanovarillas sin recubrimiento (saturación de 71.2 ± 0.3 emu/g), y la disminución con el recubrimiento polimérico y la incorporación de oro en la superficie (21.3 ± 1.8 y 12.1 ± 0.7 emu/g, respectivamente). Finalmente, se evaluó la viabilidad celular de la muestra recubierta con polímero en la línea celular HepG2 (cáncer de hígado), demostrando biocompatibilidad hasta una concentración de 500 $\mu\text{g/mL}$.

Una vez completada la caracterización, se evaluó la respuesta térmica. En hipertermia magnética, las nanovarillas sin recubrimiento de oro mostraron una mayor eficacia. Por otra parte, en los ensayos de fototermia, se probaron dos enfoques. El primero de ellos implicó irradiar con longitudes de onda cercanas a la resonancia del plasmón superficial del oro (480, 505 y 638 nm), donde el recubrimiento con oro mejoró el rendimiento, especialmente a 480-505 nm, debido a su proximidad a la resonancia del plasmón de las NPs de oro.

El segundo enfoque utilizó un láser de infrarrojo cercano (NIR), que mostró que la muestra recubierta con oro producía una menor velocidad de calentamiento en comparación con las recubiertas solo con polímero, lo que sugiere que el oro reduce la transferencia de calor por radiación sin contribuir al calentamiento. Estos resultados destacan la importancia de controlar el grosor y la uniformidad del recubrimiento para la eficacia de la hipertermia con nanovarillas magnéticas.

Tras evaluar el comportamiento con ambas técnicas llegamos a uno de los resultados clave de esta tesis doctoral: la terapia dual. Consiste en aplicar un campo magnético alterno simultáneamente al láser de fototermia, con el objetivo de alcanzar una respuesta terapéutica determinada, al mismo tiempo que se disminuye tanto la intensidad del campo magnético (17 kA/m en lugar de 21 kA/m) como del láser (0.3 W/cm^2 en lugar de 1 W/cm^2). Así pues, la combinación puede considerarse un tratamiento potencialmente menos nocivo, aunque igualmente eficaz.

Como muestra la Figura 10.7, cuando las muestras son irradiadas con 0.3 W/cm^2 mientras son sometidas a un campo magnético de 17 kA/m, la velocidad de aumento de temperatura es mayor que cuando se usan las técnicas separadamente, y en consecuencia, los valores de SAR alcanzados con la terapia dual son tres veces mayores que los correspondientes a cualquiera de las dos técnicas por separado. Se trata de un resultado de gran relevancia, ya que abre una vía para optimizar el tratamiento minimizando al mismo tiempo los efectos secundarios no deseados.

Finalmente, se evaluó el comportamiento de las nanovarillas magnéticas recubiertas de oro como agentes multifuncionales para la liberación de fármacos, específicamente doxorubicina (DOX), un conocido agente antitumoral. El objetivo era que estas nanovarillas pudieran liberar el fármaco en respuesta a estímulos electromagnéticos, como la hipertermia magnética, la fototermia y la combinación de ambos.

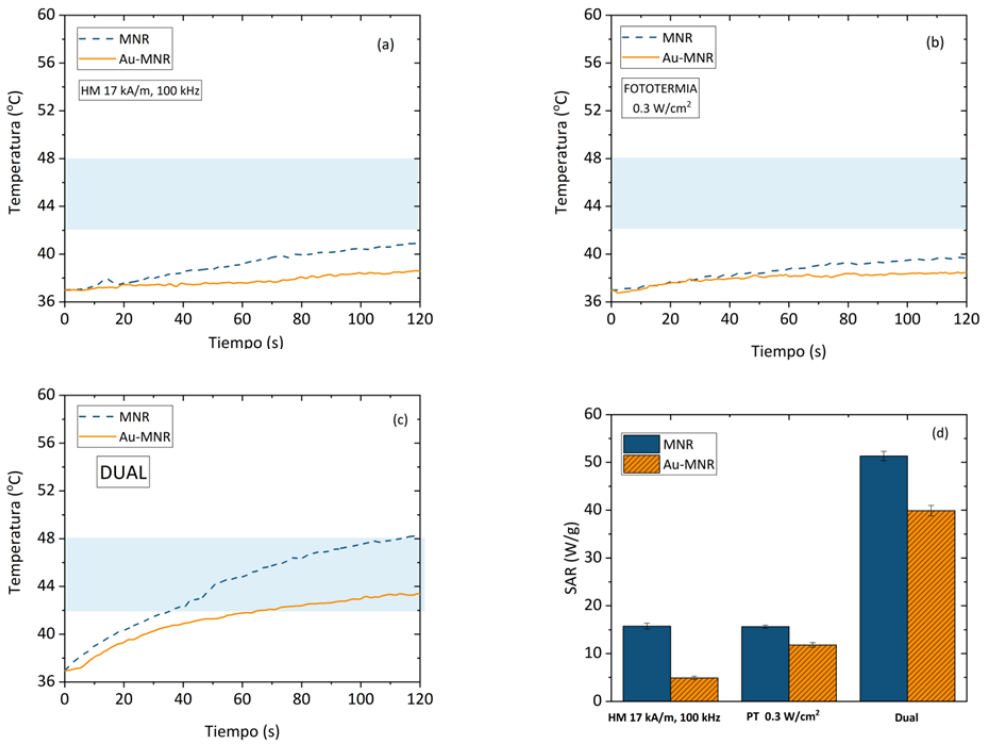


Figura 10.7: Curvas de hipertermia magnética (a), fototermia (b) y terapia dual (c). (d) Comparación entre sus valores de SAR. La frecuencia del campo magnético utilizada es de 100 kHz. La banda azul marca el rango de hipertermia deseado.

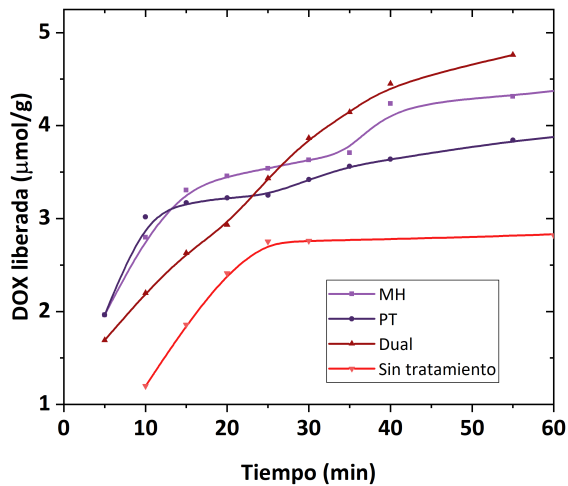


Figura 10.8: Liberación de DOX a partir de nanopartículas magnéticas en un tampón de pH 5 y en condiciones "sink". HM: bajo hipertermia magnética; PT: con láser aplicado; Dual: tanto láser como campo magnético aplicados simultáneamente.

La adsorción de DOX fue de 33 mg/g, y debido principalmente a interacciones electrostáticas, dado que este fármaco antitumoral tiene una carga positiva a pH ácido. La liberación de DOX se evaluó a pH 5 (representativo del entorno tumoral) bajo diferentes condiciones: hipertermia magnética, fototermia y la combinación de ambos tratamientos (Figura 10.8). Los resultados mostraron que la liberación de DOX es lenta a pH neutro, pero mejora significativamente con la aplicación de hipertermia magnética y fototermia, especialmente cuando ambos tratamientos se aplican simultáneamente, alcanzando casi el 10 % de liberación en menos de una hora.

Por lo tanto, se determinó que, además de reducir los parámetros utilizados en hipertermia magnética y fototermia, minimizando así los efectos del tratamiento, la terapia dual demostró ser ligeramente más eficaz en la liberación del fármaco antitumoral.

Partículas de carbón activo con magnetita: Transportadores de fármaco eficientes con liberación controlada mediante fototermia y campos magnéticos rotantes de baja frecuencia

Tras verificar que las NPs híbridas magnetita/oro constituyen posibles nanosistemas de transporte y de liberación de fármaco, la finalidad fue determinar si era posible emplear estructuras porosas/magnéticas, que ofreciesen la posibilidad de adsorber mayor cantidad de antitumoral, y, al mismo tiempo, ser dirigidas mediante campos magnéticos. Además, se buscó evaluar si la liberación del fármaco se mejoraba con la aplicación de campos magnéticos rotantes de baja frecuencia.

En este contexto, se desarrollaron partículas de carbón activo magnético (MAC, por su nombre en inglés) de longitud media 230 ± 170 nm, obtenidas mediante la incorporación de carbón activo comercial YP50F en la síntesis de nanopartículas de magnetita (Figura 10.9). Posteriormente, estas partículas fueron recubiertas con PEI para asegurar su biocompatibilidad (MAC-PEI), y la efectividad del recubrimiento se confirmó mediante los resultados de la movilidad electroforética y el análisis por espectroscopía infrarroja por transformada de Fourier. Por otro lado, los resultados de caracterización magnética señalaron una baja magnetización, de 6.0 ± 0.2 emu/g para las partículas sin recubrimiento de PEI, y ligeramente superior (probablemente debido al incremento producido en la estabilidad de la suspensión) para aquellas recubiertas de polímero (7.9 ± 0.3 emu/g). También se verificó que las partículas recubiertas con polímero no presentan citotoxicidad en fibroblastos dérmicos humanos M1 hasta una concentración de 500 $\mu\text{g/mL}$.

En cuanto al comportamiento en fototermia, tanto el carbón activo como las NPs de magnetita demostraron sus propiedades fototérmicas, siendo la magnetita más eficaz. Tras incorporar la magnetita y obtener las muestras MAC y MAC-PEI, se observó una mejora general en su respuesta térmica.

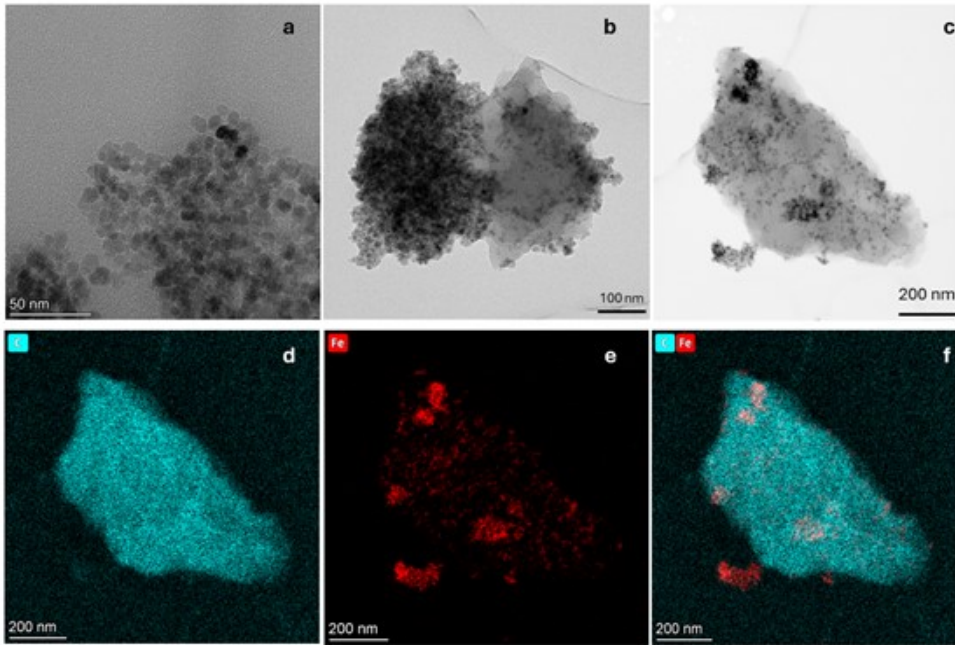


Figura 10.9: Imágenes de HRTEM de las muestras Fe_3O_4 y carbón magnético (MAC). (a) Fe_3O_4 ; (b y c) MAC; (d) mapa EDX del elemento C de las partículas MAC; (e) mapa EDX del elemento Fe de las partículas MAC; (f) mapa EDX de los elementos C y Fe superpuestos en la muestra MAC.

Posteriormente, se puso en contacto el fármaco escogido (metotrexato, o MTX) con la partículas recubiertas de PEI, mostrando que la adsorción en las dos primeras horas superó el 80 %, resultado de la alta porosidad de las partículas MAC. Es por este motivo, que estas demuestran ser más eficaces para la carga de fármacos que las partículas magnéticas convencionales, o que las partículas de sílice mesoporosa con núcleo magnético [10.59], dado que pueden adsorber casi todo el fármaco disponible debido a su alta superficie específica.

Finalmente, se realizaron ensayos de liberación de fármacos. Como se muestra en la Figura 10.10, la liberación de MTX a pH 5.8, que simula el entorno tumoral, aumenta notablemente con la aplicación de fototerapia y campos rotantes. Tras la obtención de estos resultados, es importante recalcar que, aunque la liberación de fármaco puede parecer baja (alrededor del 4%), la cantidad adsorbida de fármaco es alta, y por tanto, incluso esa baja liberación podría ser suficiente para optimizar tratamientos antitumorales futuros.

Por otro lado, la Figura 10.10 también indica que el uso de campos rotantes (a 293 rpm) aumenta ligeramente la liberación en comparación con la fototerapia, probablemente debido a una difusión mecánicamente mejorada. En general, la

liberación ante los estímulos de fototermia o campos rotantes es significativamente mayor que en condiciones no estimuladas. Autores como Nappini et al. [10.35] obtuvieron resultados similares, encontrando que los magnetoliposomas liberaban más carboxifluoresceína bajo un campo magnético alterno de baja frecuencia. Este hallazgo sugiere que los campos rotantes podrían ser más eficaces que la fototermia para aplicaciones biomédicas con alta penetración en tejidos.

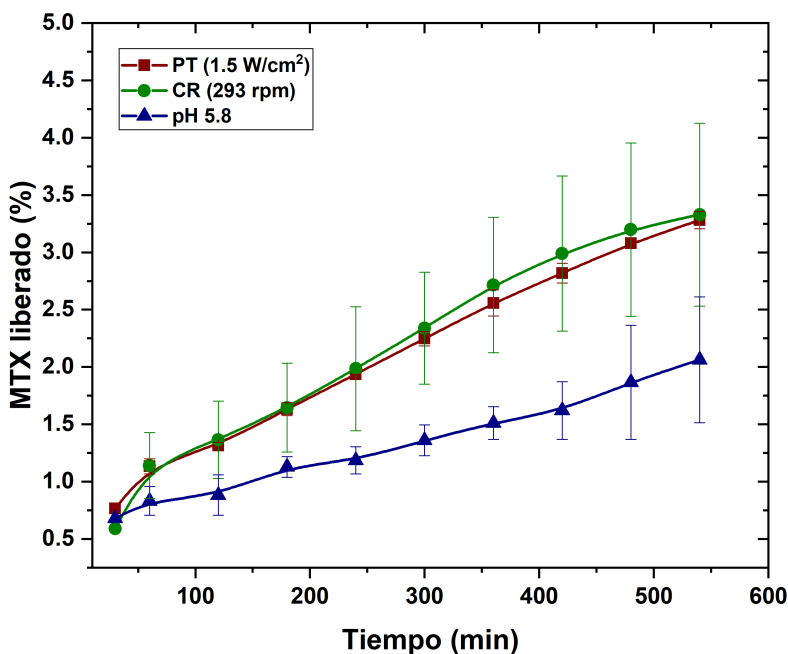


Figura 10.10: Liberación de MTX con respecto a la cantidad previamente adsorbida en partículas MAC recubiertas de PEI utilizando diferentes estímulos: fototermia (PT), campos rotantes (CR), y sin estímulos aplicados, todos ellos en tampón fosfato a pH 5.8.

Por último, es importante mencionar que a pH 7.4, el fármaco se libera inicialmente más rápidamente. Este hecho no tiene gran interés, ya que los tiempos de administración del tratamiento son largos en comparación con el tiempo que tarda el cuerpo humano en renovar toda la sangre (aproximadamente un minuto en condiciones normales de reposo). Suponiendo que las partículas se inyecten por vía intravenosa y se acumulen en la zona del tumor debido a sus propiedades magnéticas, este proceso se produciría rápidamente. Además, tras 6 horas de aplicación, la liberación del fármaco mediante fototermia y campos rotantes es mayor a pH tumoral que a pH 7.4.

Impacto de la internalización de nanopartículas magnéticas biomiméticas en tratamientos fototérmicos

En el último capítulo de esta tesis doctoral se enmarcan los resultados más significativos desde el punto de vista biológico. En este caso, la meta fue determinar si es necesario que las NPMs sean internalizadas por las células y/o si existe un umbral de concentración interna de Fe para que la terapia fototérmica sea eficaz.

Para ello, en este caso se llevó a cabo el estudio con un tipo de nanopartículas magnéticas: las llamadas biomiméticas (denominadas BMNPs por su nombre en inglés), mediadas por la proteína MamC. Las BMNPs han demostrado ser efectivas como agentes fototérmicos, capaces de lograr una citotoxicidad optimizada contra células tumorales cuando se utilizan como nanotransportadores de fármacos y/o agentes de hipertermia [10.26, 10.60].

Con el objetivo anteriormente mencionado, se simularon cuatro situaciones diferentes de tratamientos fototérmicos para desentrañar el efecto de la captación celular de BMNPs sobre la viabilidad celular tras el tratamiento. La línea celular de hepatoblastoma humano (HepG2) fue tratada con suspensiones de BMNPs, y se desarrollaron protocolos para tener sólo BMNPs intracelulares, sólo BMNPs extracelulares o ambas, seguidos de la exposición fototérmica de los cultivos celulares tratados. De este modo, se obtuvieron cuatro grupos diferentes: (i) BMNPs intracelulares (0.75 mg/mL, Grupo 1), (ii) BMNPs extracelulares (0.75 mg/mL, Grupo 2), (iii) BMNPs intracelulares+extracelulares (2.5 mg/mL, Grupo 3) y (iv) BMNPs extracelulares (2.5 mg/mL, Grupo 4).

Como resultado de este estudio, y tras la evaluación de los ensayos de fototermia realizados *in vitro*, se demostraron tres aspectos clave:

1. Aunque la eficiencia de calentamiento del agente fototérmico no se ve alterada por su localización (intra/extracelular, Figura 10.11A)), la localización intracelular de las BMNPs es crucial para asegurar el efecto citotóxico de los tratamientos fototérmicos, especialmente a baja concentración de Fe. De hecho, la concentración de BMNPs necesaria para alcanzar el mismo efecto citotóxico tras una irradiación láser de 0.2 W/cm^2 es tres veces mayor si se localizan extracelularmente en comparación con la necesaria si las BMNPs se localizan intracelularmente (Figura 10.11A).

2. Para una localización dada de las BMNPs, la muerte celular aumenta con la concentración de BMNPs (o Fe). Cuando las BMNPs están situadas intracelularmente, existe un umbral de concentración de Fe ($\sim 0.5 \text{ mM}$ a intensidades de potencia láser de 0.1 W/cm^2) necesario para afectar a la viabilidad celular tras la exposición de las células a la fototermia (Figura 10.11B).

3. Por último, es importante destacar que el aumento de la temperatura no es el único factor que provoca la muerte celular. En realidad, los aumentos de

temperatura en el interior de las células causan más daños a las estructuras celulares y desencadenan la muerte celular de forma más eficiente que un aumento de la temperatura en el exterior de la célula.

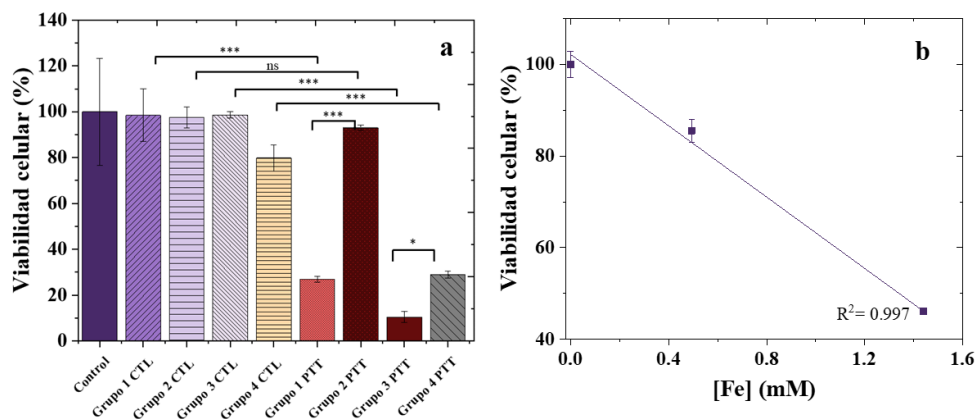


Figura 10.11: (a) Viabilidad de células HepG2 con y sin tratamiento de fototerapia (0.2 W/cm^2) in vitro. Valor-p $* < 0.05$; $*** p < 0.001$. (b) Viabilidad de células HepG2 tras el tratamiento con fototerapia (0.1 W/cm^2) en función del Fe internalizado (proporcional a la captación de BMNPs).

10.3. Conclusiones

El objetivo central de este trabajo ha sido la síntesis de nanopartículas magnéticas de distintos tamaños y geometrías, así como sus recubrimientos superficiales poliméricos (catiónicos y aniónicos). Estas partículas se han desarrollado con el fin de ser aplicadas en las técnicas de hipertermia magnética y fototerapia, así como para liberación de agentes antitumorales incorporados en las nanopartículas, utilizando los estímulos electromagnéticos mencionados y campos magnéticos rotantes de baja frecuencia. De los resultados obtenidos se pueden extraer las siguientes conclusiones:

- A lo largo de los Capítulos 5-7 se han sintetizado cuatro tipos de nanoestructuras: nanoesferas magnéticas de 70 nm de diámetro, nanovarillas magnéticas de longitud en torno a 40 nm (relación de aspecto 1:8) y 550 nm (relación de aspecto 1:5), así como partículas híbridas de partículas de carbón activo con magnetita, de 230 nm de longitud. Todas ellas han sido recubiertas con el polímero PEI, o con una triple capa polimérica PEI/PSS/PEI en el caso de las nanovarillas. Su biocompatibilidad se ha demostrado en los casos estudiados (ambos grupos de nanovarillas y partículas de carbón activo con magnetita) hasta concentraciones de $300 \mu\text{g/mL}$ en diversas líneas celulares.

- En todas las muestras magnéticas obtenidas se ha conseguido una elevada respuesta magnética, en torno a 80 emu/g para las nanopartículas esféricas y las nanovarillas de menor tamaño, disminuyendo ligeramente a los 70 emu/g para las nanovarillas de 550 nm de longitud. En el caso de las partículas de carbón activado/magnetita, la magnetización es considerablemente inferior, con saturación de 6 emu/g.

- Se ha demostrado que todas las muestras sintetizadas actúan como agentes fototérmicos. Además, tanto las nanoesferas como las nanovarillas funcionan también como agentes de hipertermia magnética.

Concretamente, en el caso de las nanovarillas de menor tamaño, se demostró que tras la exposición a un campo magnético alterno de 23 kA/m y 114 kHz, se conseguía una reducción significativa de la viabilidad de la línea celular MCF7 (cáncer de mama) de un $73.3 \pm 5.3\%$. Por otro lado, aplicando fototermia y manteniendo temperaturas de 42-46 °C durante 10 minutos, produjo una muerte celular del $64.4 \pm 3.7\%$.

- Tanto las nanoesferas como las nanovarillas de 550 nm de longitud han sido recubiertas con semillas de oro. En el caso de la hipertermia magnética, el recubrimiento de oro reduce la eficacia del tratamiento. Del mismo modo, al irradiar con una longitud de onda de 850 nm, las partículas recubiertas de oro muestran un comportamiento fototérmico ligeramente inferior. Sin embargo, utilizando longitudes de onda más cercanas al plasmón de las nanoesferas de oro (en las regiones azul-verde), la temperatura aumenta 10 veces más. Esto sugiere que, aunque estas longitudes de onda son menos penetrantes que las del NIR, pueden ser útiles para tratar tumores superficiales o accesibles por fibra óptica.
- Uno de los resultados más relevantes obtenidos está relacionado con la aplicación de la llamada terapia dual, en la que se aplica un campo magnético alterno simultáneo a la irradiación láser. Esta estrategia permite reducir tanto la intensidad del campo magnético (17 kA/m en lugar de 21 kA/m) como de la densidad de potencia del láser ($0,3 \text{ W/cm}^2$ en lugar de 1 W/cm^2), para obtener el aumento de temperatura deseado. Esta combinación se perfila como un tratamiento potencialmente menos dañino, pero igualmente eficaz. En este enfoque, el ritmo de aumento de la temperatura es significativamente más rápido y, en consecuencia, los valores de SAR obtenidos con la terapia dual son tres veces superiores a los logrados con cada técnica por separado. Este hallazgo es extremadamente importante, ya que abre la posibilidad de optimizar el tratamiento minimizando al mismo tiempo los efectos secundarios no deseados.
- En cuanto a los experimentos de liberación del fármaco, pueden extraerse las siguientes conclusiones:

- Se ha demostrado que las nanovarillas de mayor tamaño pueden ser empleados como vehículos portadores de fármaco (adsorbiendo alrededor del 24 % del fármaco en disolución). El resultado más relevante obtenido es que son capaces de liberar alrededor del 10 % de doxorubicina adsorbida en una hora aplicando terapia dual, mejorando la tasa de liberación ligeramente en comparación con la aplicación de estímulos electromagnéticos por separado.
 - En el caso de las partículas de carbón activo con magnetita, se ha demostrado que constituyen eficientes transportadores de fármacos, capaces de adsorber alrededor del 80 % del fármaco (metotrexato) disponible en disolución en tan sólo 2 horas, alcanzando cantidades superiores cuando se dejan en contacto durante 24 horas. Además, respecto a la liberación de fármaco, uno de los resultados más relevantes es que la liberación mejora considerablemente con la aplicación de técnicas fototérmicas y campos magnéticos rotantes de baja frecuencia.
- Finalmente, el Capítulo 8 se dedica a los experimentos *in vitro*, en los que la localización del agente fototérmico es esencial para garantizar la eficacia de un tratamiento fototérmico. En particular, cuando las NPMs biomiméticas (BMNPs) se utilizan como agentes fototérmicos en la línea celular HepG2, se requiere aproximadamente tres veces la concentración de BMNPs si se localizan extracelularmente en comparación con su localización intracelular, para conseguir la misma eficacia en términos de muerte celular. Además, para una localización específica, la muerte celular aumenta a medida que aumenta la concentración de BMNPs, e incluso si las BMNPs se internalizan, existe una concentración umbral de Fe (0.5 mM utilizando intensidades de potencia láser de 0.1 W/cm²) necesaria para afectar a la viabilidad celular tras la exposición a la fototermia. Por último, debe tenerse en cuenta que el aumento de la temperatura global no es el único factor que contribuye a la muerte celular; el daño estructural, especialmente en los orgánulos internos, también desempeña un papel crucial en este proceso.

Bibliografía

- [10.1] Tadeusz Dyba, Giorgia Randi, Freddie Bray, Carmen Martos, Francesco Giusti, Nicholas Nicholson, Anna Gavin, Manuela Flego, Luciana Neamtii, Nadya Dimitrova, et al. The european cancer burden in 2020: Incidence and mortality estimates for 40 countries and 25 major cancers. *European Journal of Cancer*, 157:308–347, 2021.
- [10.2] Leena Mohammed, Hassan G Gomaa, Doaa Ragab, and Jesse Zhu. Magnetic nanoparticles for environmental and biomedical applications: A review. *Particuology*, 30:1–14, 2017.
- [10.3] Saurabh Shukla, Ramsha Khan, and Achlesh Daverey. Synthesis and characterization of magnetic nanoparticles, and their applications in wastewater treatment: A review. *Environmental Technology & Innovation*, 24:101924, 2021.
- [10.4] Sheila Shahidi. Magnetic nanoparticles application in the textile industry—a review. *Journal of Industrial Textiles*, 50(7):970–989, 2021.
- [10.5] Seipati Rosemary Mokhosi, Wendy Mdlalose, Amos Nhlapo, and Moganavelli Singh. Advances in the synthesis and application of magnetic ferrite nanoparticles for cancer therapy. *Pharmaceutics*, 14(5):937, 2022.
- [10.6] D Stanicki, T Vangijzegem, I Ternad, and S Laurent. An update on the applications and characteristics of magnetic iron oxide nanoparticles for drug delivery. *Expert Opinion on Drug Delivery*, 19(3):321–335, 2022.
- [10.7] Hung-Vu Tran, Nhat M Ngo, Riddhiman Medhi, Pannaree Srinoi, Tingting Liu, Supparesk Rittikulsittichai, and T Randall Lee. Multifunctional iron oxide magnetic nanoparticles for biomedical applications: A review. *Materials*, 15(2):503, 2022.
- [10.8] Laís Salomão Arias, Juliano Pelim Pessan, Ana Paula Miranda Vieira, Taynara Maria Toito de Lima, Alberto Carlos Botazzo Delbem, and Douglas Roberto Monteiro. Iron oxide nanoparticles for biomedical applications: a perspective on synthesis, drugs, antimicrobial activity, and toxicity. *Antibiotics*, 7(2):46, 2018.

- [10.9] C Valverde-Tercedor, M Montalbán-López, T Perez-Gonzalez, MS Sanchez-Quesada, T Prozorov, E Pineda-Molina, MA Fernandez-Vivas, AB Rodriguez-Navarro, D Trubitsyn, Dennis A Bazylinski, et al. Size control of in vitro synthesized magnetite crystals by the MamC protein of *Magnetococcus marinus* strain MC-1. *Applied Microbiology and Biotechnology*, 99:5109–5121, 2015.
- [10.10] Lokesh Srinath Ganapathe, Mohd Ambri Mohamed, Rozan Mohamad Yunus, and Dilla Duryha Berhanuddin. Magnetite nanoparticles (Fe_3O_4) in biomedical application: From synthesis to surface functionalisation. *Magnetochemistry*, 6(4):68, 2020.
- [10.11] Kirill D Petrov and Alexey S Chubarov. Magnetite nanoparticles for biomedical applications. *Encyclopedia*, 2(4):1811–1828, 2022.
- [10.12] Lee Blaney. Magnetite (Fe_3O_4): Properties, synthesis, and applications. *Lehigh Preserve*, 15, 2007.
- [10.13] Qing Li, Christina W Kartikowati, Shinji Horie, Takashi Ogi, Toru Iwaki, and Kikuo Okuyama. Correlation between particle size/domain structure and magnetic properties of highly crystalline Fe_3O_4 nanoparticles. *Scientific Reports*, 7(1):9894, 2017.
- [10.14] Arati G Kolhatkar, Andrew C Jamison, Dmitri Litvinov, Richard C Willson, and T Randall Lee. Tuning the magnetic properties of nanoparticles. *International Journal of Molecular Sciences*, 14(8):15977–16009, 2013.
- [10.15] Manuel Arruebo, Rodrigo Fernández-Pacheco, M Ricardo Ibarra, and Jesús Santamaría. Magnetic nanoparticles for drug delivery. *Nano Today*, 2(3):22–32, 2007.
- [10.16] Rakesh K Jain. Normalization of tumor vasculature: an emerging concept in antiangiogenic therapy. *Science*, 307(5706):58–62, 2005.
- [10.17] Jun Wu. The enhanced permeability and retention (EPR) effect: the significance of the concept and methods to enhance its application. *Journal of Personalized Medicine*, 11(8):771, 2021.
- [10.18] Xiaopin Duan and Yaping Li. Physicochemical characteristics of nanoparticles affect circulation, biodistribution, cellular internalization, and trafficking. *Small*, 9(9-10):1521–1532, 2013.
- [10.19] L Harivardhan Reddy, José L Arias, Julien Nicolas, and Patrick Couvreur. Magnetic nanoparticles: design and characterization, toxicity and biocompatibility, pharmaceutical and biomedical applications. *Chemical Reviews*, 112(11):5818–5878, 2012.

- [10.20] Ajay Kumar Gupta and Mona Gupta. Synthesis and surface engineering of iron oxide nanoparticles for biomedical applications. *Biomaterials*, 26(18):3995–4021, 2005.
- [10.21] Ritu Goyal, Sushil K Tripathi, Esther Vazquez, Pradeep Kumar, and Kailash C Gupta. Biodegradable poly (vinyl alcohol)-polyethylenimine nanocomposites for enhanced gene expression in vitro and in vivo. *Biomacromolecules*, 13(1):73–83, 2012.
- [10.22] Michael T Klem, Mark Young, and Trevor Douglas. Biomimetic magnetic nanoparticles. *Materials Today*, 8(9):28–37, 2005.
- [10.23] Ylenia Jabalera, Alberto Sola-Leyva, María P Carrasco-Jiménez, Guillermo R Iglesias, and Concepcion Jimenez-Lopez. Synergistic photothermal-chemotherapy based on the use of biomimetic magnetic nanoparticles. *Pharmaceutics*, 13(5):625, 2021.
- [10.24] Joanna Kurczewska and Bernadeta Dobosz. Recent progress and challenges regarding magnetite-based nanoparticles for targeted drug delivery. *Applied Sciences*, 14(3):1132, 2024.
- [10.25] Jon Dobson. Magnetic nanoparticles for drug delivery. *Drug Development Research*, 67(1):55–60, 2006.
- [10.26] Salvatore Calogero Gaglio, Ylenia Jabalera, Manuel Montalbán-López, Ana Cristina Millán-Placer, Marina Lázaro-Callejón, Mercedes Maqueda, María Paz Carrasco-Jimenez, Alejandro Laso, José A Aínsa, Guillermo R Iglesias, et al. Embedding biomimetic magnetic nanoparticles coupled with peptide AS-48 into PLGA to treat intracellular pathogens. *Pharmaceutics*, 14(12):2744, 2022.
- [10.27] Zhila Shaterabadi, Ángel Delgado, and Guillermo R Iglesias. Solvothermally synthesized magnetite nanorods for application in magnetic hyperthermia and photothermia. *Journal of Magnetism and Magnetic Materials*, 596:171990, 2024.
- [10.28] Daniel Jaque, L Martínez Maestro, Blanca del Rosal, P Haro-Gonzalez, Antonio Benayas, JL Plaza, E Martín Rodríguez, and J García Solé. Nanoparticles for photothermal therapies. *Nanoscale*, 6(16):9494–9530, 2014.
- [10.29] Daniel Ortega and Quentin A Pankhurst. Magnetic hyperthermia. *Nanoscience*, 1(60):e88, 2013.
- [10.30] Anouchka Plan Sangnier, Sandra Preveral, Alberto Curcio, Amanda KA Silva, Chistopher T Lefèvre, David Pignol, Yoann Lalatonne, and Claire Wilhelm. Targeted thermal therapy with genetically engineered magnetite

- magnetosomes@ RGD: Photothermia is far more efficient than magnetic hyperthermia. *Journal of Controlled Release*, 279:271–281, 2018.
- [10.31] Louise Finlayson, Isla RM Barnard, Lewis McMillan, Sally H Ibbotson, C Tom A Brown, Ewan Eadie, and Kenneth Wood. Depth penetration of light into skin as a function of wavelength from 200 to 1000 nm. *Photochemistry and Photobiology*, 98(4):974–981, 2022.
- [10.32] Megan Wetzel, John Strickley, M Tye Haeberle, and Timothy S Brown. Depth of invasion of aggressive and nonaggressive basal cell carcinoma. *The Journal of Clinical and Aesthetic Dermatology*, 12(3):12, 2019.
- [10.33] Yajing Shen, Congyu Wu, Taro QP Uyeda, Gustavo R Plaza, Bin Liu, Yu Han, Maciej S Lesniak, and Yu Cheng. Elongated nanoparticle aggregates in cancer cells for mechanical destruction with low frequency rotating magnetic field. *Theranostics*, 7(6):1735, 2017.
- [10.34] Sara Lopez, Nicolas Hallali, Yoann Lalatonne, Arnaud Hillion, Joana C Antunes, Nizar Serhan, Pascal Clerc, Daniel Fourmy, Laurence Motte, Julian Carrey, et al. Magneto-mechanical destruction of cancer-associated fibroblasts using ultra-small iron oxide nanoparticles and low frequency rotating magnetic fields. *Nanoscale Advances*, 4(2):421–436, 2022.
- [10.35] Silvia Nappini, Francesca Baldelli Bombelli, Massimo Bonini, Bengt Nordèn, and Piero Baglioni. Magnetoliposomes for controlled drug release in the presence of low-frequency magnetic field. *Soft Matter*, 6(1):154–162, 2010.
- [10.36] Agnieszka Włodarczyk, Szymon Gorgoń, Adrian Radoń, and Karolina Bajdak-Rusinek. Magnetite nanoparticles in magnetic hyperthermia and cancer therapies: Challenges and perspectives. *Nanomaterials*, 12(11):1807, 2022.
- [10.37] Ana Espinosa, Jelena Kolosnjaj-Tabi, Ali Abou-Hassan, Anouchka Plan Sangnier, Alberto Curcio, Amanda KA Silva, Riccardo Di Corato, Sophie Neveu, Teresa Pellegrino, Luis M Liz-Marzán, et al. Magnetic (hyper) thermia or photothermia? progressive comparison of iron oxide and gold nanoparticles heating in water, in cells, and in vivo. *Advanced Functional Materials*, 28(37):1803660, 2018.
- [10.38] Karthikeyan Manivannan, Chih-Chia Cheng, Rajeshkumar Anbazhagan, Hsieh-Chih Tsai, and Jem-Kun Chen. Fabrication of silver seeds and nanoparticle on core-shell Ag@SiO₂ nanohybrids for combined photothermal therapy and bioimaging. *Journal of Colloid and Interface Science*, 537:604–614, 2019.
- [10.39] Yingjie Hang, Anyang Wang, and Nianqiang Wu. Plasmonic silver and gold nanoparticles: shape-and structure-modulated plasmonic functionality for point-

- of-caring sensing, bio-imaging and medical therapy. *Chemical Society Reviews*, 2024.
- [10.40] Rua J Kadhim, Esraa H Karsh, Zainab J Taqi, and Majid S Jabir. Biocompatibility of gold nanoparticles: In-vitro and in-vivo study. *Materials Today: Proceedings*, 42:3041–3045, 2021.
- [10.41] Jeotikanta Mohapatra, Meiyong Xing, Julian Beatty, Jacob Elkins, Takele Seda, Sanjay R Mishra, and J Ping Liu. Enhancing the magnetic and inductive heating properties of Fe₃O₄ nanoparticles via morphology control. *Nanotechnology*, 31(27):275706, 2020.
- [10.42] Aleksey A Nikitin, Victor A Arkhipov, Nelly S Chmelyuk, Anna V Ivanova, Stepan S Vodopyanov, Anastasiia S Garanina, Mikhail A Soldatov, Maksim A Gritsai, Valeriy M Cherepanov, Natalia N Barbotina, et al. Multifunctional Anisotropic Rod-Shaped CoFe₂O₄ Nanoparticles for Magnetic Resonance Imaging and Magnetomechanical Therapy. *ACS Applied Nano Materials*, 6(15):14540–14551, 2023.
- [10.43] Yuan Gao, Ming-Wei Chang, Zeeshan Ahmad, and Jing-Song Li. Magnetic-responsive microparticles with customized porosity for drug delivery. *RSC Advances*, 6(91):88157–88167, 2016.
- [10.44] Shanshan Huang, Chunxia Li, Ziyong Cheng, Yong Fan, Piaoping Yang, Cuimiao Zhang, Kuiyue Yang, and Jun Lin. Magnetic Fe₃O₄@mesoporous silica composites for drug delivery and bioadsorption. *Journal of Colloid and Interface Science*, 376(1):312–321, 2012.
- [10.45] Cuilian Tao and Yufang Zhu. Magnetic mesoporous silica nanoparticles for potential delivery of chemotherapeutic drugs and hyperthermia. *Dalton Transactions*, 43(41):15482–15490, 2014.
- [10.46] Baisong Chang, Jia Guo, Congying Liu, Ji Qian, and Wuli Yang. Surface functionalization of magnetic mesoporous silica nanoparticles for controlled drug release. *Journal of Materials Chemistry*, 20(44):9941–9947, 2010.
- [10.47] RV Ramanujan, S Purushotham, and MH Chia. Processing and characterization of activated carbon coated magnetic particles for biomedical applications. *Materials Science and Engineering: C*, 27(4):659–664, 2007.
- [10.48] Zhanna K Nazarkina, Tatyana A Savostyanova, Boris P Chelobanov, Irina V Romanova, Pavel A Simonov, Ren I Kvon, Andrey A Karpenko, and Pavel P Laktionov. Activated carbon for drug delivery from composite biomaterials: The effect of grinding on sirolimus binding and release. *Pharmaceutics*, 14(7):1386, 2022.

- [10.49] Ian Y Goon, Leo MH Lai, May Lim, Paul Munroe, J Justin Gooding, and Rose Amal. Fabrication and dispersion of gold-shell-protected magnetite nanoparticles: systematic control using polyethyleneimine. *Chemistry of Materials*, 21(4):673–681, 2009.
- [10.50] María del Mar Ramos-Tejada, Julian L Viota, Katarzyna Rudzka, and Angel V Delgado. Preparation of multi-functionalized Fe₃O₄/Au nanoparticles for medical purposes. *Colloids and Surfaces B: Biointerfaces*, 128:1–7, 2015.
- [10.51] Lucía Vizcaíno-Anaya, Carlos Herreros-Lucas, José M Vila-Fungueiriño, and María del Carmen Giménez-López. Magnetic hyperthermia enhancement in iron-based materials driven by carbon support interactions. *Chemistry—A European Journal*, 28(67):e202201861, 2022.
- [10.52] Rudolf Hergt and Silvio Dutz. Magnetic particle hyperthermia—biophysical limitations of a visionary tumour therapy. *Journal of Magnetism and Magnetic Materials*, 311(1):187–192, 2007.
- [10.53] Andrew M Smith, Michael C Mancini, and Shuming Nie. Second window for in vivo imaging. *Nature Nanotechnology*, 4(11):710–711, 2009.
- [10.54] Pinar Avci, Asheesh Gupta, Magesh Sadasivam, Daniela Vecchio, Zeev Pam, Nadav Pam, and Michael R Hamblin. Low-level laser (light) therapy (llt) in skin: stimulating, healing, restoring. In *Seminars in cutaneous medicine and surgery*, volume 32, page 41. NIH Public Access, 2013.
- [10.55] Tadao Sugimoto and Atsushi Muramatsu. Formation Mechanism of Monodispersed α -Fe₂O₃ Particles in Dilute FeCl₃ Solutions. *Journal of Colloid and Interface Science*, 184(2):626–638, 1996.
- [10.56] Héctor L Rodríguez-Luccioni, Magda Latorre-Esteves, Janet Méndez-Vega, Orlando Soto, Ana R Rodríguez, Carlos Rinaldi, and Madeline Torres-Lugo. Enhanced reduction in cell viability by hyperthermia induced by magnetic nanoparticles. *International Journal of Nanomedicine*, pages 373–380, 2011.
- [10.57] Huiyul Park, Jaemoon Yang, Jaemin Lee, Seungjoo Haam, In-Hong Choi, and Kyung-Hwa Yoo. Multifunctional nanoparticles for combined doxorubicin and photothermal treatments. *ACS Nano*, 3(10):2919–2926, 2009.
- [10.58] Manuel Ocaña, Maria P Morales, and Carlos J Serna. The growth mechanism of α -Fe₂O₃ ellipsoidal particles in solution. *Journal of Colloid and Interface Science*, 171(1):85–91, 1995.
- [10.59] Alexandre Adam and Damien Mertz. Iron oxide@ mesoporous silica Core-Shell nanoparticles as multimodal platforms for magnetic resonance imaging, magnetic hyperthermia, near-infrared light photothermia, and drug delivery. *Nanomaterials*, 13(8):1342, 2023.

-
- [10.60] German Garcia Rubia, Ana Peigneux, Ylenia Jabalera, Javier Puerma, Francesca Oltolina, Kerstin Elert, Donato Colangelo, Jaime Goómez Morales, Maria Prat, and Concepcion Jimenez-Lopez. pH-dependent adsorption release of doxorubicin on MamC-biomimetic magnetite nanoparticles. *Langmuir*, 34(45):13713–13724, 2018.

